The University of Nottingham

UNITED KINGDOM · CHINA · MALAYSIA

Shaohong, Zhu (2021) Fractional Slot Concentrated Winding PM Synchronous Motors for Transport Electrification Applications. PhD thesis, University of Nottingham.

Fractional Slot Concentrated Winding PM Synchronous Motors for Transport Electrification Applications

by

Shaohong Zhu

Thesis submitted to The University of Nottingham

for the degree of Doctor of Philosophy, September 2020

Abstract

Moving towards electrification of transport including electric vehicles (EV), more electric aircraft (MEA), and electric ships offers a crucial way in dealing with global carbon emissions and climate change. Electric motors are a key enabling technique in these applications, but their increased use is associated with requirements of extreme power/torque density, excellent fault-tolerance, high efficiency, and good manufacturability.

The main goal of this thesis is to study permanent magnet electric machine winding theory to determine the suitable electric machine winding topologies for different applications. Two separate vehicle transport applications are investigated, including an EV traction motor and a novel modular electromechanical actuator (EMA) for MEA.

The study of the EV traction motor involves the investigation of methods for reducing the significant stator MMF harmonics in fractional slot concentrated winding (FSCW) electric machines, and the development of novel FSCW topologies while keeping the benefits of easy manufacturing and the non-overlapping characteristic of concentrated windings. The novel FSCW topologies can be extended to multi-phase FSCW motors. A traction motor equipped with a novel 24 slots, 14 poles FSCW topology and interior PM (IPM) rotor is developed for evaluation. The performance under normal and fault conditions is fully explored and validated with simulation and experimental results, which demonstrates the applicability and strong potential of the proposed 24 slots, 14 poles IPM motor in fault-tolerant traction motor applications.

The second topic focuses on modular fault-tolerant EMAs for aircraft actuation systems which can meet a diverse range of requirements. The architecture and design

considerations of the actuator system are firstly determined considering reliability, fault-tolerance, and weight. The modular EMA scheme consisting of a direct-drive rotary motor and mechanical screw is identified. A dual 3-phase 24 slots, 22 poles FSCW motor with a surface-mounted permanent magnet (SPM) rotor is developed and evaluated in terms of electromagnetics, thermal management, and fault-tolerance. Experimental results of the modular EMA motor prototypes agree well with predicted results. All this confirms the applicability and satisfactory implementation of the modular EMA motor for aircraft actuation system applications.

Acknowledgement

Four years ago, when I made the decision to accept the offer to pursue a PhD in the University of Nottingham, UK, it was not easy. Now, when I look back at this long journey, I am glad I made this choice. The PhD journey is long and full of challenges. There are a lot of unknowns, struggles, and frustrations, but at the same time, it is also full of possibilities and happiness. Through four years of hard work and dedication, I made it through. I've grown a lot as both an individual and a researcher.

I am extremely grateful to my supervisors Dr Tom Cox, Dr Zeyuan Xu, and Professor Chris Gerada for their guidance and support on the research work. Their regular guidance and dedication are crucial towards the completion of the PhD journey.

I would like to thank my internal examiner Dr Gaurang Vakil for his valuable examination and feedback on improving the research work and his help in getting me the position of industrial placement with Cummins Inc. Also, thanks to Prof Michael Gala and Dr Michele Degano for their guidance and valuable support on the research activities.

Contents

Contents

Contents

Contents

Contents

Contents

Contents

List of Figures

List of Figures

List of Figures

List of Figures

List of Figures

List of Figures

List of Figures

List of Figures

List of Tables

List of Tables

List of Tables

List of Tables

Acronyms

AEA	All Electric Aircraft
DL	Double-layer
EV	Electric Vehicle
EM	Electromagnetic
EMA	Electromechanical Actuator
EHA	Electro-Hydrostatic Actuator
ECU	Electronic Control Unit
EMI	Electromagnetic Interference
EMF	Electromotive Force
FEM	Finite Element Method
FFT	Fast Fourier Transform
FCC	Flight Control Computer
FSCW	Fractional Slot Concentrated Winding
FSDW	Fractional Slot Distributed Winding
GCD	Greatest Common Divisor
HA	Hydraulic Actuator
ISDW	Integral Slot Distributed Winding
IM	Induction Motor

Acronyms

IPM	Interior Permanent Magnet
LCM	Least Common Multiple
MEA	More Electric Aircraft
MMF	Magnetomotive Force
MTPA	Maximum Torque Per Ampere
MS	Mechanical Screw
MLS	Magnetic Lead Screw
OC	Open-Circuit
PM	Permanent Magnet
PMSM	Permanent Magnet Synchronous Motor
PMA-SynRM	PM Assisted SynRM
PLOC	Probability of Loss of Control
RS	Roller Screw
RSM	Response Surface Methodology
SRM	Switched Reluctance Motor
SynRM	Synchronous Reluctance Motor
SPM	Surface-mounted Permanent Magnet
SC	Short-Circuit
SPP	Slots/Pole/Phase
SL	Single-layer
SF	Sizing Factor
TPMLM	Tubular PM Linear Motor
UMP	Unbalanced Magnetic Pull
VA	Voltage-Ampere
VSI	Voltage Source Inverter
WFSM	Wound Field Synchronous Motor

Symbols

α_s, b_s, c_s	Stator winding name
A	Electric loading, A/mm
B_r	Radial flux density
B_t	Tangential flux density
$B_{\delta av}$	Magnetic loading, T
B_{s0}	Slot opening, mm
B_{s1}	Width of top of slot, mm
B_{s2}	Width of bottom of slot, mm
C_f	Friction coefficient
D	Airgap diameter, mm
D_i	Stator inner diameter, mm
D_o	Stator outer diameter, mm
F	Force, N
$F(\theta, t)$	MMF function
f_r	Radial force density
$f_{s,v}$	Amplitude of vth order harmonic of stator MMF harmonic
$f_{r,v}$	Amplitude of vth order harmonic of rotor MMF harmonic
g	Physical airgap length, mm
g'	Equivalent airgap length, mm
$g(\theta_s - \theta_r)$	Airgap length function, mm

Symbols

G_{rs}	Gear ratio of roller screw
G_{mls}	Gear ratio of magnetic lead screw
$\boldsymbol{G_{abc}}$	Matrix in *abc* static frame, $\boldsymbol{G}$ can be current, flux linkage, voltage, and inductance
$\boldsymbol{G_{dq}}$	Matrix in *d-q* rotating frame, $\boldsymbol{G}$ can be current, flux linkage, voltage, and inductance
h_m	PM magnetization length, mm
h_{s0}	Slot opening depth, mm
h_{s1}	Slot wedge depth, mm
h_{s2}	Slot body depth, mm
i_s, i_r	Current in stator, rotor winding, A
i_a, i_b, i_c	Current of phase *a*, *b*, *c*, A
i_d, i_q	Current in *d-q* rotating frame, A
I_{max}	Maximum current, A
I_{ch}	Characteristic current, A
I_{sc}	Short-circuit current, A
I_{scmax}	Maximum short-circuit current, A
$I_{d,sc}, I_{q,sc}$	Short-circuit current in *d-q* rotating frame, A
j	Integer
J	Current density, A/mm^2
k	Integer
k_{wv}	Winding factor of vth harmonic
k_a	Attenuation factor due to winding shifting
K_ϕ	Waveform factor
K	Roughness coefficient
L_l, L_m	Leakage inductance, magnetizing inductance, mH
L_{xy}, L_{xyl}, L_{xym}	Mutual-inductance, leakage mutual-inductance, magnetizing mutual-inductance between phase *x* and *y*, mH
L_0, L_2	Average value and amplitude of second-order harmonic of self-inductance, mH
L_{diff}	Difference between *d-* and *q-* inductance, mH

Symbols

L_{aa}, L_{bb}, L_{cc}	Self-inductance of phase *a, b* and *c*, mH
L_d, L_q	Inductance in *d-q* rotating frame, mH
$L_{h\sigma}$	Harmonic leakage inductance
$L_{s\sigma}$	Slot leakage inductance
L_{tt}	Tooth-tip leakage inductance
L_{ew}	End-winding leakage inductance
l_{ef}	Active axial length of the motor, mm
m	Phase numbers
M_0, M_2	Average value and amplitude of second-order harmonic of mutual-inductance, mH
M_{sr}, M_{rs}	Mutual inductance between stator and rotor winding, mH
N_s	Number of turns in series per phase
N	Number of conductors per slot
N_1	Turn numbers of per coil
N_c	Coil numbers per phase
N_p	The LCM of number of slots and poles
$N(\theta)$	Winding turn function
$N_a(\theta_s), N_b(\theta_s), N_c(\theta_s)$	Winding turn function of phase *a*, *b* and *c*
N_v	Equivalent winding turns of vth harmonic
P	Rotor pole-pair numbers, mm
$\boldsymbol{P}$	Park transformation matrix
P_h	Lead of screw, mm
$P(x)$	Failure probability of *x*
P_f	Windage loss, W
Q	Slot numbers
r	Airgap radius, mm
R	Resistance, Ω
R_s, R_r	Resistance of stator, rotor winding, Ω
S	Surface area of tramslator of magnetic lead screw, mm^2
t	Time instant, s
t_m	Motor's electrical periodicity
T	Torque, Nm

Symbols

T_{em}	EM torque, Nm
T_r	Reluctance torque, Nm
T_{pm}	Magnet torque, Nm
T_{avg}	Average torque, Nm
T_{ripple}	Ripple torque, Nm
T_{sc}	SC braking torque, Nm
T_{scmax}	Maximum SC braking torque, Nm
T_{out}	Output torque, Nm
T_{max}	Maximum output torque, Nm
u_d, u_q	Voltage in d-q rotating frame, V
v	Order of harmonic
v_s, v_r	Voltage in stator, rotor winding, V
w_t	Tooth width, mm
w_{pm}	Width of PM, mm
W_c	Magnetic energy, J
α	Shift angle, degree
α_{pm}	PM arc coefficient
β	Angle between stator and rotor flux linkage phasor, degree
θ	Space angle, degree
θ_s	Angle between stator flux linkage and stator reference axis, degree
θ_r	Angle between stator and rotor reference axis, degree
φ	Phase advance angle of current, degree
ω	Angular speed, rad/s
ω_s, ω_r	Angular speed of stator, rotor flux linkage phasor, rad/s
ω_m^*	Critical speed, rpm
μ_0	Permeability of free space, H/m
τ	Pole pitch, mm
γ_d	Current phase advance angle measured from d-axis
η	Efficiency of motor
η_{screw}	Efficiency of screw

Symbols

δ_g	Shear stress, kN/m²
σ_g	Harmonic airgap leakage factor
$\lambda_{s\sigma}$	Slot leakage permeance factor
λ_s, λ_r	Flux linkage of stator, rotor winding, Wb
λ_d, λ_q	Flux linkage in *d-q* rotating frame, Wb
λ_f	PM Flux linkage, Wb
λ_l, λ_m	Leakage flux linkage, magnetizing flux linkage, Wb
λ_{tt}	Tooth-tip permeance factor
ρ	Mass density, kg/m³
ð	Model number

Chapter 1

Introduction

Climate change is one of the global challenges causing global warming and posing an existential threat to human civilization [1]. All the nations across the world have reached an agreement to reduce carbon footprint and combat climate change. Significant efforts have been made to deal with these issues at an international level, with agreements such as The Paris Agreement and the Copenhagen Accord. In responding to this, many countries' governments have set out specific carbon emission reduction goals. Some of them have even promised a net zero carbon emission and seek to legislate corresponding law, such as Norway (2030) and UK (2050).

According to the Emissions Database for Global Atmospheric Research (EDGAR), the transport sector has contributed 27% of total greenhouse gas emissions in 2016 in the EU. It was found that transport remains the major contributor to NOx emissions, which cause air pollution and result in premature mortality [2][3]. Figure 1.1 depicts the share of greenhouse gas emissions for different transportation methods, illustrating the fact that road, maritime, and aviation transport are the three most significant contributors, contributing 72.1%, 13.6%, and 12.3% of total emissions, respectively. Electric vehicles (EVs) are anticipated to be a key component in the future that offers great reduction in carbon and air pollutant emissions, consequently reducing impacts on climate change when coupled with renewable power generation [4]. Therefore, moving towards electrification of transport like EV, more electric aircraft (MEA), and electric ships offers a crucial way in dealing with global carbon emissions and climate change [4]-[6].
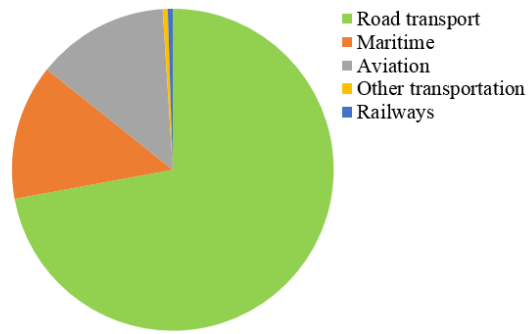
Figure 1.1 Share of transport greenhouse gas emissions [3]

Electric motor is a key enabling technique in EVs or MEA [7]. This implies an extreme power/torque density, high efficiency, and manufacturability requirements on electric motors as these factors will affect the range, cost and carbon emissions. Several technological advancements in the areas of electric motor operation theory, high-performance steel, advanced winding topology, and novel rare-earth magnets, have made the electric motor a crucial player in the electric transport industry. Reliability, on the other hand, is also a significant factor in safety-critical transport applications, which requires the electric motor or electric drive to offer fault-tolerance [8][9]. All these requirements raises a significant challenge in the design of electric motors.

In this thesis, permanent magnet electric machine winding theory is studied in order to determine the suitable electric machine winding topologies for different applications. Two vehicle transport applications are investigated, including a traction motor for EV and a modular electromechanical actuator (EMA) for aircraft actuation systems.

The study of EV traction motor aims to investigate permanent magnet (PM) electric motors with novel winding topologies. PM electric motors with conventional fractional slot concentrated winding (FSCW) offer benefits in terms of power density, fault-tolerant capability, and manufacturability but suffer from high stator space MMF harmonics which may result in significantly high rotor losses, localized saturation, unbalanced magnetic force, noise and vibrations [10]-[12]. Therefore, the main effort is towards studying the novel FSCW topologies with reduced stator space MMF harmonics and implementing them into electric traction motors.

The second topic focuses on modular fault-tolerant EMAs for aircraft actuation systems. Aircraft typically use many actuators with varying requirements. Having as few components as possible is a huge benefit for design, certification, construction and maintenance. Electric actuation system architecture and actuator configurations/envelopes are studied in terms of weight, reliability, and cost, and thereby are determined to develop modular electrical actuators capable of meeting a diverse range of actuation requirements. A modular fault-tolerant FSCW PM motor is developed to meet these strict requirements.

1.1   Electric motor technology in HEVs & EVs

Electric and hybrid electric vehicles have been rapidly developing in recent decades due to the increasing fuel economy/efficiency concerns and climate change challenges. The electric machine as a core part of electric vehicle propulsion technology including motor and generator has received much attention and has extreme requirements in terms of power/torque density, efficiency, reliability, fault tolerance, cost and manufacturability.

The selection of electric motor drives is a very crucial step in the development of the powertrain for EVs as the performance of EVs heavily depends on traction motors. This process normally involves three key factors: drive cycle, complete vehicle drive and energy system, which makes selecting the most suitable electric motor drive a challenging task. Generally, the EV traction motor must meet the following characteristics requirements:

- High torque/power density.
- Wide constant power speed range capability, typically 3-4 times of base speed.
- High efficiency in the wide speed and torque range or drive cycle.
- Desirable overload capability for a short period of 30-90s.
- High reliability and acceptable fault-tolerance.
- Reasonable cost and manufacturability.

The feasibility of a number of electric motor topologies, including DC motor, induction motor (IM), PM synchronous motor (PMSM), switched reluctance motor (SRM), axial-flux motor, wound field synchronous motor (WFSM), synchronous

reluctance (SynRM)motor, and stator-PM synchronous motor are investigated [13]-[17]. Five topologies are identified by the industry to be the most promising candidates for EVs/HEVs traction system, including IM, PMSM, SRM, WFSM, and PM SynRM. Table 1.1 lists some of the typical electric traction motor topologies adopted in the EVs and HEVs.

Table 1.1 Electric motor topologies adopted in EVs and HEVs

Motor topology	EVs or HEVs Model
IM [18]-[22]	GM EV1, Tesla Model S/X, Chevrolet Silverado Spark EV, and NIO ES6/8
PMSM [23]-[29]	Toyota Prius, Honda Insight, Nissan Leaf, Chevrolet Volt, Tesla Model 3, BYD EV Models, NIO ES6/8, and ROEWE E50
SRM [30]-[36]	Land Rover Defender EV and Holden ECOmmodore
WFSM [13][22], [37]-[52]	Renault Kangoo/Fluence/Zoe, and BRUSA

IM is widely used in EVs and railway traction systems due to low material cost, simple structure and high reliability [19]. Despite these advantages, the drawbacks of low efficiency, low power density, and low power factor limit its ability to meet the increasing demands. Although improvements can be achieved using a copper rotor cage, this will increase motor mass and manufacturing effort [22].

As the more strict requirement on high efficiency and power density is needed, the PMSM has gained more attention and has become the most popular candidate in the current electric vehicle market [23][24]. Due to the use of permanent magnets, high back EMF in the high speed range is a challenge, which makes field-weakening to the rotor magnet necessary and so sacrifices some efficiency [25].

SRMs can deliver high power density and overall high efficiency at a low cost, making them a cost-effective candidate for EVs and HEVs applications [30] [31]. However, the high torque ripple and vibration due to double-salient structure are the challenges [35]. A dedicated control drive system is also needed [31].

WFSM provide a flexible controllable rotor flux by adopting an independent rotor field coil excitation [37][38]. A reduced flux linkage can easily be implemented to reduce the no-load back EMF in high speed zone, which reduce the stator copper

losses and rotor iron losses and extend the constant power high speed range [39]. However, their efficiency and power density are not comparable to PMSMs and the rotor coil brings the issue of slip ring and rotor copper loss [40]. A self-excited machine using rotary transformer can be used to solve the rotor excitation issue [41].

1.2   Electric motor technology in more electric aircraft (MEA)

More electric aircraft (MEA) has been a general trend for the next generation of aircraft, with the ultimate goal of all electric aircraft (AEA). This is due to its characteristics of faster and simpler power-by-wire system, optimizing aircraft performance, improving efficiency and overall weight, reducing operating and maintenance cost and decreasing carbon emissions [42]-[45]. In the conventional aircraft, a combination of powers including hydraulic, pneumatic, mechanical and electrical power are usually used. Recent advancements in new technologies, specifically power electronics and electrical motors, enable the more electric aircraft. The MEA underlines the utilization of the electrical power to power the non-propulsive aircraft systems currently powered by hydraulic, pneumatic or mechanical methods, including flight control surfaces, landing gear systems, fuel pump, and numerous other utility applications, and potentially propulsion systems in the future.

The concept of MEA brings in challenges for the aircraft design, among which the most challenging three parts are aircraft electrical power systems, electric/hybrid propulsion and electrical actuation systems.

1.2.1 Aircraft electrical power system

For aircraft electrical power systems, the typical power rating of dozens of kW for traditional aircraft is largely increased to level of MW for MEA, e.g. Boeing 787. This increasing requirement in the electrical power system increases the demand for on-board generation systems, which results in the discussion of variable aircraft power systems including constant frequency, variable frequency, and importantly DC power system ($\pm$270V DC) [42][46]. The reliability of on-board electrical power systems and energy management are the challenges [5].

1.2.2 Electric/hybrid propulsion

Hybrid electric propulsion aircraft is a step advance in the MEA technology. In November 2017, the Airbus/Rolls-Royce/Siemens launched the E-Fan X (hybrid-electric aircraft demonstrator) project, by replacing one of its four turbofans in a BAe 146 airplane with a Siemens 2 MW electric motor [47]. The collaboration will pave the way to a hybrid single-aisle commercial aircraft that is safe, efficient, and cost-effective. On the other side, the United Technologies Corporation (UTC) unveiled its initial hybrid-electric demonstration aircraft in 2019 by using an electric motor to support one of its two turboprop engines during take-off and climb on a modified Bombardier Dash 8-100, which aims to fly by 2022. This hybrid-electric solution could yield 30 percent fuel savings on a typical one-hour mission [48].

A full-electric commercial regional aircraft seems to be out of reach in the short- to mid-term future based on current technology, principally due to the weight of required batteries. However, in the 2019 Paris Air show, an Israel plane maker Eviation Aircraft demonstrated its first pure electric airplane Dubbed Alice, which is a regional commuter designed to fly up to 650 miles at around 276mph. The airplane has a capability of up to 9 passengers and is powered by 3x260kW electric motor on tails and wingtips. The 900 kWh Li-ion battery is distributed throughout the airplane and accounts for 60% of MTOW. It is set to be in service in 2021 [49]. Obviously, the electric motor technology is shaping the aviation industry.

1.2.3 Electrical actuation system

One of the most challenging parts for aircraft is the electrical actuation system. Generally, modern aircraft actuation systems including primary control surfaces, secondary control surfaces, and landing gear systems are powered by a combination of hydraulic, pneumatic, and mechanical systems. Adopting electrically powered actuators, viz., electromechanical actuators (EMA), to replace the concentrated hydraulic actuators brings the benefits of weight reduction, improved maintainability, and the potential advantage of more flexible flight control by introducing distributed actuation system architecture [45].

This thesis will focus on the electrical actuation system, investigating using electromechanical actuators (EMAs) to replace conventionally concentrated hydraulic

actuators, which brings in the potential advantages of advanced distributed electrical actuation architecture [45] [50]. The electrically powered actuators have the advantages of 'power on demand', consuming power only when moving or holding a position. On top of this, the removal of high-pressure pipelines and utilization of 'power by wire' results in a weight reduction at system level, improved functionality and manufacturability, reduced installation efforts and easy maintenance. The flight control surfaces including primary and secondary control surfaces and landing gear systems are quite important parts of the aircraft, thus the electrically powered flight control surfaces and landing gear system is a significant step to advance the MEA.

1.3   Objectives, aims and outline of the thesis

This thesis focuses on two topics. The first is applying an IPM motor with novel FSCW topology to an EV traction motor application, and the second is developing a modular electromechanical actuator (EMA) for aircraft actuation systems.

The study of the EV traction motor is to investigate methods for reducing the significant stator MMF harmonics in the conventional FSCW electric motors and to propose novel FSCW topologies. The novel FSCW topologies feature reduced stator space MMF harmonics while keeping the benefits of easy manufacturing and good fault-tolerance of concentrated windings. A traction motor equipped with a novel 24 slots, 14 poles FSCW topology and an interior PM (IPM) rotor is developed for evaluation.

The second topic focuses on modular fault-tolerant EMAs for aircraft actuation systems which can meet a diverse range of requirements. This is done through evaluating novel modular actuator configuration and actuation system architecture considering reliability, fault-tolerance and weight. A FSCW motor with a surface-mounted PM (SPM) rotor designed for the modular fault-tolerant EMA is developed and evaluated in terms of electromagnetics, thermal management, and fault-tolerance.

In all, the thesis aims to

- Systematically analyze the issue of significant stator MMF harmonics of FSCW motor and stator MMF harmonic reduction techniques.

- Propose a generalized FSCW design method for electric motor with reduced stator MMF harmonics while keeping the concentrated winding characteristics, which can be extended to different slot/pole combinations for different phase numbers.

- Investigate the advantages and disadvantages of the proposed FSCW topologies with reduced stator MMF harmonics compared to the conventional FSCW counterparts.

- Investigate the applicability and prospect of the proposed FSCW topology in the traction motor applications.

- Systematically analyze the architecture and design considerations of electromechanical actuator (EMA) for aircraft actuation systems in terms of weight, reliability, and fault-tolerance.

- Propose a modular EMA configuration and develop a highly fault-tolerant rotatory motor solution for the modular EMA.

    To this end, the thesis is outlined as below:

- Chapter 1 presents a general introduction of electric motor technology in the area of electric vehicles (EVs) and more electric aircraft (MEA), while Chapter 2 gives a review of recent application examples and advancements of high-performance electric motor technology.

- In Chapter 3, the theory and design aspects of fractional slot concentrated winding (FSCW) motors are presented, with the impacts of significant stator MMF space harmonics highlighted. The stator MMF harmonic reduction techniques in the literature are systematically analyzed and compared.

- A generalized FSCW design method with reduced stator MMF space harmonics for electric motor is proposed in Chapter 4; the proposed winding design can cancel all stator MMF harmonics except for the working harmonic and its slot harmonics while keeping the concentrated winding characteristics.

- The behavior of an IPM motor with the proposed 24 slots, 14 poles FSCW topology with reduced stator MMF harmonics developed for an electric traction system is evaluated in Chapter 5 in terms of torque capability, efficiency, and fault-tolerant capability.

- Chapter 6 and Chapter 7 deal with the design considerations of a modular electromechanical actuator (EMA) for an aircraft actuation system. The actuation system architecture and actuator topology are firstly determined considering

reliability, weight and cost. Then, the detailed design of a 24 slots, 22 poles dual 3-phase FSCW SPM motor for the modular EMA is developed and evaluated considering the modular structure concept, EM performance, thermal management and fault-tolerant capability.

- Manufacturing, construction, and experimental validation of two kinds of prototypes, namely, the IPM traction motor with the proposed 24 slots, 14 poles FSCW topology and the 24 slots, 22 poles SPM motor, are presented in Chapter 8. The experimental results are reported and compared with analytical and finite element method (FEM) results, with good agreement between results.

- The final Chapter 9 presents general conclusions and considerations on the limitations of the work and further work to be done.

Chapter 2

Review of Electric Motor Technology

As has been introduced, the thesis focuses on two topics, including traction motors for EVs and modular EMAs for aircraft actuation systems. This chapter presents the electric motor technology advancements for these two applications, respectively.

2.1 Electric motor technologies in HEV&EVs

A number of electric motor topologies, including DC motor, induction motor (IM), PM synchronous motor (PMSM), switched reluctance motor (SRM), axial-flux motor, wound field synchronous motor (WFSM) and synchronous reluctance (SynRM)motor, and stator-PM synchronous motor have been investigated for traction applications [13]-[17]. There are some other electric motor topologies with special structure like double stator/rotor field-modulated motor or stator-PM synchronous motor. However, it is expected that they are still in early stage of research and development, and some of them are inherently constrained with structure complexity or performance limitation for traction applications [13].

Five electric motor topologies are identified by the industry to be the most promising candidates for EV/HEVs traction system, namely, IM, PMSM, SRM, WFSM, and SynRM. Each of them will be reviewed.

2.1.1 Induction motor (IM)

The induction motor or so-called asynchronous motor is a common AC motor with a conductive rotor formed from a conductive copper or aluminium cage, or occasionally rotor windings, which is widely used in industrial applications. It has been successfully utilized in many commercial EVs and HEVs such as GM EV1, BMW X5 and Tesla Model S [18]-[20]. An example is the GM EV1 rolled out in 1996, which equipped with a three-phase, 102kW AC induction motor that spins to 13,000rpm and weights 68kg [19]. The most recent exceptional example is the Tesla Model S which has a 225 kW 3-phase 4-pole AC induction motor with copper cage rotor [18]. Figure 2.1 shows a high-performance induction motor with a copper cage rotor [21].

(a) Induction motor   (b) Copper cage rotor [21]
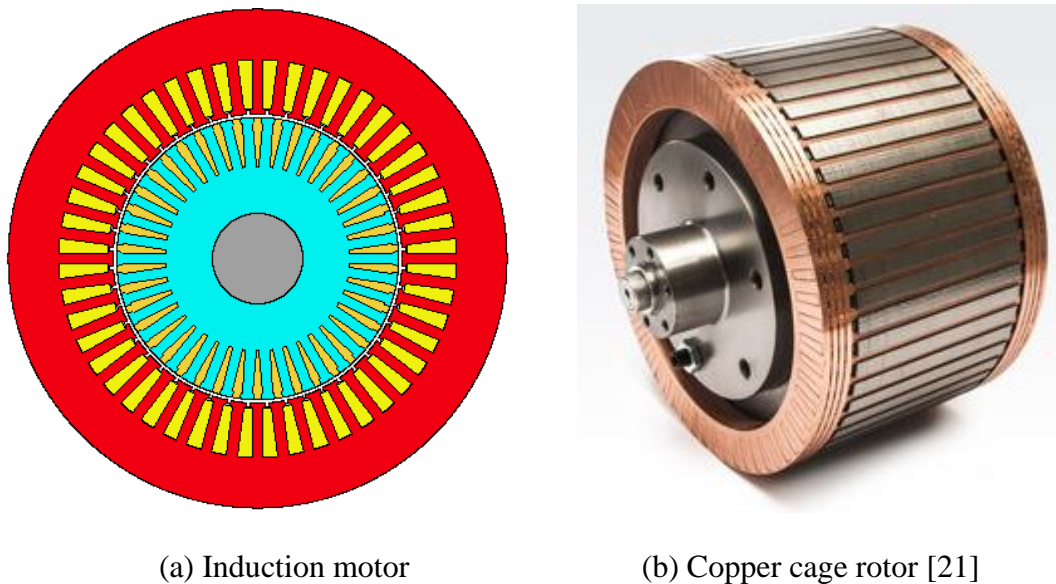
Figure 2.1 Induction motor with a copper rotor

The induction motor works by inducing current in the rotor to generate a rotor magnetic field. As a result, an electromagnetic (EM) torque can be produced by the interaction between stator and rotor magnetic field. As there is no rare-earth permanent magnet (PM) material, the material cost of the induction motor is low, and it is free from the impact of possible large price fluctuations of PM material. On top of this, the simple motor structure makes the manufacturing process simple and ensures a high reliability.

There are a few drawbacks facing the induction motor, including low efficiency, low power factor, low power/torque density, and low inverter usage compared to the

PM synchronous motor [20]. The induced current in the rotor will increase stator current and peak Voltage-Ampere (VA) rating in the power inverter. The induced rotor current and increased stator current will increase loss and reduce electric drive efficiency, which will in turn impact the endurance mileage of EVs and battery capacity. Much attention should be taken to tackle the thermal management challenge in the rotor as the high loss in the rotating rotor is normally difficult to dissipate and it may rapidly be over-heated during high power operation.

Although the induction motor does not have the high-power density and/or efficiency that a PM synchronous motor has, the rotor flux can be flexibly controlled by decoupled vector control as the induction motor contains no magnets in the rotor. In terms of high speed operation, flux-weakening can easily be implemented to restrain the high back EMF generated, which is normally a critical issue for PM synchronous motors. However, the constant power extended speed range operation is limited by the existence of break down torque which occurs when the rotor reaches the critical speed.

Several techniques have been pushing forward to improve the performance of the induction motor such as optimization during the design step, using copper cage rotors instead of aluminium alloy, and hairpin winding technology. Apart from the improvements from the motor design aspect, considerations have also been taken in the control techniques such as pole-changing and dual-inverter technology [22].

2.1.2 PM synchronous motor (PMSM)

The PM synchronous motor is a family of brushless synchronous motor normally with rare-earth PM in the rotor. The PMSM is the most popular candidate for automotive applications owing to its excellent power/torque density, high efficiency, and high power factor.

However, this kind of motor may have a short constant power range due to the high back EMF generated by the fixed PM excitation. Although the flux-weakening control technique can be adopted to reduce the back EMF when the speed is above the base speed and 4:1 or 5:1 extended speed operation can be achieved, the efficiency in the high speed range may drop down significantly and a demagnetization may happen to the sensitive magnet. Furthermore, rotor losses due to flux-weakening would be

considerably increased, this will result in a thermal management challenge in the rotor and thereby increase the magnet's demagnetization risk.

Depending on the position of the magnet in the rotor, the PMSM can be classified into surface-mounted PM (SPM) motor, interior PM (IPM) motor, and spoke PM motor.

The SPM motor may give the same torque as the interior PM motor, it is not considered as a good candidate for achieving an extended constant power operation range due to the high back EMF at the base speed and lower inductance resulting from the thick magnet on the rotor surface (which is literally like an air region in the magnetic circuit). It also can suffer from high magnet loss and mechanical stiffness problems. Nonetheless, there is an SPM motor equipped with FSCW configuration developed by A. M. El-Refaie, *et al.*, which confirms it can provide high performance and meet several of the very challenging FreedomCAR 2020 specifications, as in Figure 2.2 [51].
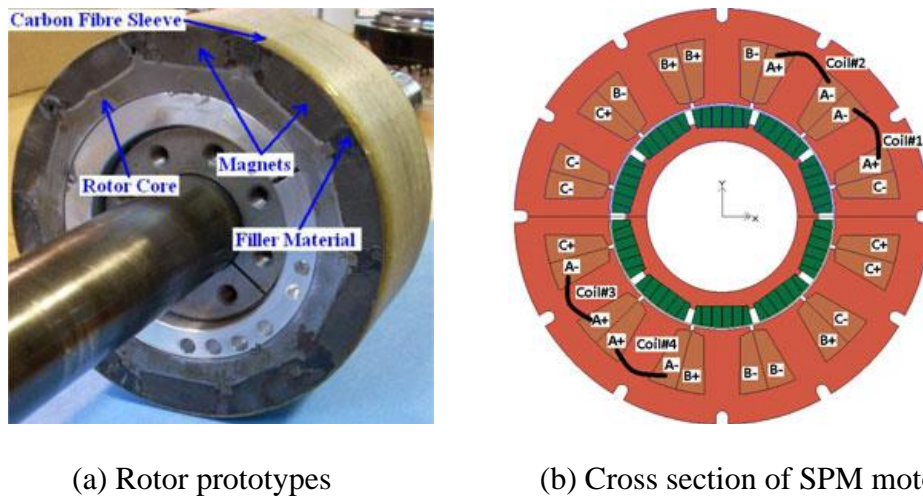
| (a) Rotor prototypes | (b) Cross section of SPM motor |

Figure 2.2 FSCW SPM motor for FreedomCAR 2020 traction applications [51]

The IPM motor seems to be more robust from the mechanical aspect and can have a higher airgap flux density. The IPM motor can be carefully designed to consider the contribution of magnet and reluctance torque. This capability gives IPM motor more flexibility in the designing and extending the constant power operation range. However, IPM motor normally involves a complicated rotor lamination geometry which requires more manufacturing effort. In addition, the ribs in the rotor may lead to high magnet flux leakage.

Figure 2.3 Rotor of different PM synchronous motors [24]-[27]
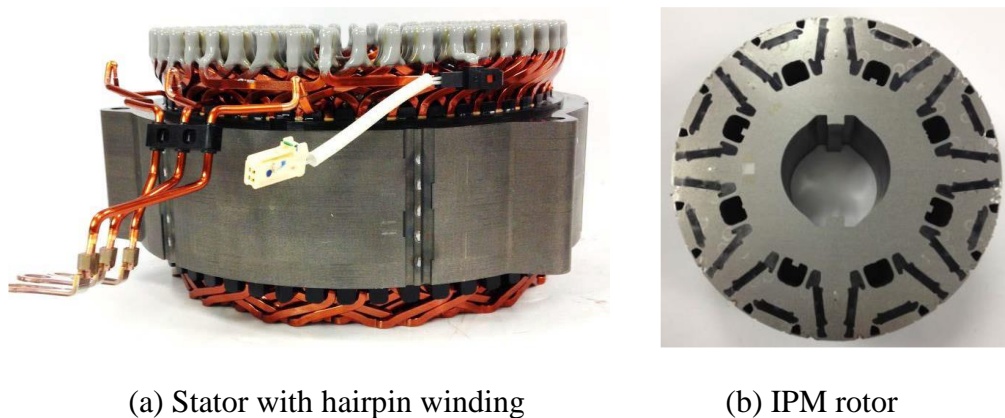
(a) Stator with hairpin winding   (b) IPM rotor

Figure 2.4 Toyota Prius gen 4 motor [27]

A number of IPM rotor topologies that are used in the EVs and HEVs have been summarized in Figure 2.3 [24]-[27]. The most famous example of using IPM motor for an electric car is likely the Toyota Prius HEV series, which normally adopts 48 slots stator and 8 poles IPM rotor. Their evolution of rotor structure can be observed from Figure 2.3 and Figure 2.4 [26][27]. It is reported that with the hairpin winding design, the motor has been made smaller and more compact, with considerable reduction in both the weight and losses [27].

While the Tesla Corporation originally used induction motors for all of its vehicles, they have recently used PM motors for the new Model 3, which is using a 54 slots 6 poles IPM motor with normal random winding, as in Figure 2.5 [28].

On the other hand, several Chinese automotive companies such as BYD and NIO also prefer permanent magnet synchronous motors. The NIO ES6/8 have used an electric powertrain system of a 160kW PM synchronous motor at the front axle and a 240kW induction motor at the rear [29].

Figure 2.5 Tesla model 3 motor

2.1.3 Switched reluctance motor (SRM)

The switched reluctance motor (SRM) is a motor without excitation in the ferromagnetic rotor, the torque is generated by magnetic reluctance effect. Due to the absence of magnet material and a simple double-salient structure, the SRM is cheap, robust and easy to manufacture. The SRM can offer a higher power density and overall comparable efficiency at a low cost compared to induction motor but a lower power/torque density compared to PMSM, making it a cost-effective candidate for EV and HEV applications, as in Figure 2.6 [30]-[32].

Without permanent magnet excitation in the rotor, the SRM can operate easily at high speed. Apart from that, the concentrated windings in the stator physically and electrically isolated from each other which provides high fault-tolerance. However, due to the reluctance torque effect and highly position-dependant inductance, the torque ripple is significant and may result in unacceptable noise and vibration, which is a critical drawback. Another disadvantage with SRM is the low power factor, which is caused by the discontinuous excitation current [33][34].

On the other hand, advanced control techniques are required for switched reluctance motor drives (SRD) compared to other AC and DC drives due to the non-sinusoidal drive waveform, limiting its applications [31].

Several investigations have been carried out to maximize average torque and minimize torque ripple [35]. These include implementing global optimization in the design of SRM and more advanced/optimal control strategy in the SRD. One of the successful business applications of SRM in the EV is Land Rover Defender powered by a 70kW SRM and a lithium-ion battery with capacity of 27kWh [36].
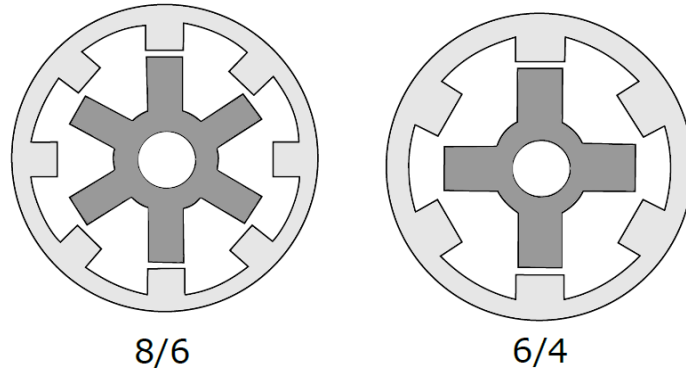
Figure 2.6 Most common SRM topologies [31]
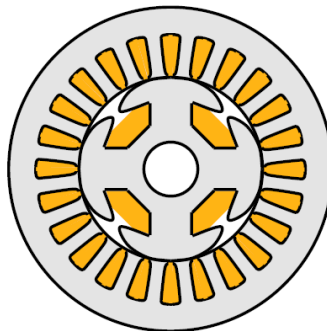
Figure 2.7 Wound field rotor synchronous motor [41]

2.1.4 Wound field synchronous motor (WFSM)

The wound field synchronous motor (WFSM) is a classic motor technology that is widely used in industry applications. Instead of using permanent magnets in the rotor for excitation, a rotor with wound coil excitation is adopted, as shown in Figure 2.7 [41]. Traditionally, the coil is connected to a stationary voltage source and both brush and slip ring are required. The rotor is only composed of coil and steel, making it more robust and less sensitive to temperature than the PMSM [13][37][38]. Renault has

implemented a wound field synchronous motor in the Kangoo/Fluence/Zoe, as in Table 1.1 [52].
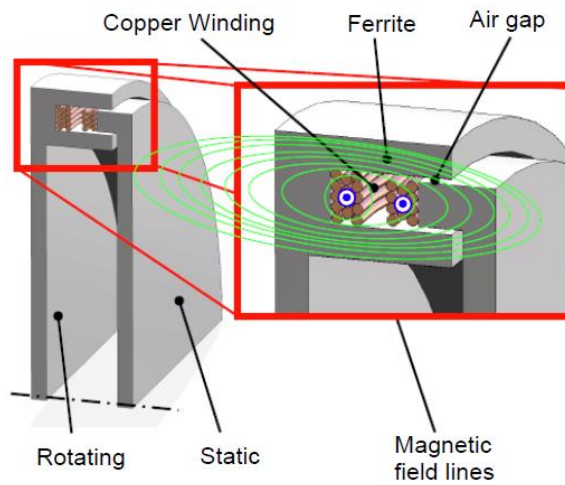
Figure 2.8 An example of inductive rotating transformer [41]

The flexible regulation of magnetic field given by the independent rotor excitation is the main advantage of this motor technology. In the constant power high speed region, a reduced flux linkage can be implemented to reduce the no-load back EMF and eliminate the flux-weakening control, which consequently decreases the stator copper losses and rotor losses and improves efficiency and constant power high speed operation range.

However, due to the copper losses in the rotor, the WFSM has a lower efficiency compared to the PMSM. The mechanical wear of brush in the conventional WFSM is also a challenge, which may impact motor's operation and maintenance. A self-excited WFSM [40], which uses a transformer to supply energy from stator coil to rotor coil without brush. By rectifying the induced current in the rotor coil with diodes, a DC current can be applied to the rotor field winding. The concept of rotating transformer has also been implemented in a brushless separately excited synchronous motor developed for electric vehicles; Figure 2.8 depicts the structure of a separately rotary transformer; a functional example has been built by ETH and BRUSA [41].

2.1.5 Synchronous reluctance motor (SynRM)

The synchronous reluctance motor (SynRM) is also a reluctance motor in which the rotor has flux barriers to provide a reluctance variation between the d- and q- axis. The generated torque depends on the saliency ratio of L_d/L_q. Extensive investigation indicates that the SynRM drive has advantages over IM in terms of cost, weight, cooling and efficiency [53]-[56]. The conclusion in [53] shows that the SynRM can give 10% to 25% of more torque depending on the motor size and higher efficiency over the corresponding induction motor. However, a drawback of SynRM is their poor power factor.
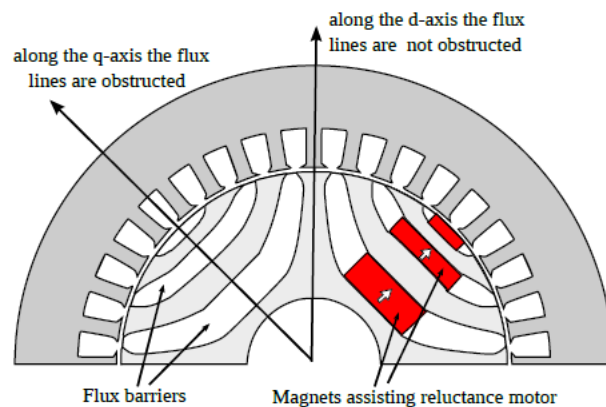
Figure 2.9 Scheme of a SynRM with magnet [57]

The pure SynRM does not feature comparable torque density as the PMSM. A typical way to address this issue is to add assisted magnet either NdFeB or Ferrite in the rotor flux barrier. In this case, the motor is termed as PM assisted SynRM (PMA-SynRM). A typical configuration of PMA-SynRM is shown in Figure 2.9 [57]. With this combination, a high saliency ratio of 3-5 or even more can be achieved, which is preferable for increasing the power/torque density [13]. It is reported that a PMA-SynRM with ferrite magnet can have a matched power density and 73% of torque density as the IPM motor used in Prius 2003 [14][58]. This topology provides a promising candidate to get rid of the expensive rare-earth magnet.

Compared to IPM motor, the PMA-SynRM features a lower power density and power factor due to the flux leakage coming from the multi-layer flux barriers in the rotor; however it gains the advantages of lower back EMF and higher inductance,

which are good for flux-weakening operation in the high speed region. The low short-circuit (SC) current due to the high inductance can also be beneficial to improving the fault-tolerant capability. Therefore, the PMA-SynRM represents a potential cost-effective solution in the EVs and HEVs.

2.1.6 Quantitative comparison of different motor technologies

Many researches and studies have been done on the comparison of different motor topologies for electric traction applications.

A comparison of IPM motor, IM, and SRM for a HEV traction applications has been undertaken in [59] and the geometry dimensions and weight breakdown are shown in Table 2.1. The performance figures at 1500 and 6000 rpm with maximum power are given in Table 2.2. The SRM tends to have a higher iron loss due to the increased frequency of the flux, and at 1500 rpm the copper losses are high. IPM motor features the highest efficiency, whereas more detailed design work can improve the generally lower efficiency for the IM and SRM.

Table 2.1 Comparison of geometry, weight and cost [59]

Parameter	IPM	IM	SRM
Outer stator diameter (mm)	269.0	269.0	269.0
Outer rotor diameter (mm)	160.5	180.0	170.0
Airgap length (mm)	0.73	1.5	0.3
Axial core length (mm)	84	84	84
Weight of stator core (kg)	18.65	11.86	14.11
Weight of stator copper (kg)	5.99	10.57	7.44
Weight of rotor core (kg)	5.22	6.15	5.16
Weight of rotor magnet/copper (kg)	1.30	7.67	--
Total weight (kg)	31.16	36.25	26.71
Laminated steel cost (US $)	31.03	23.41	25.05
Copper cost (US $)	39.53	120.38	49.10
NdFeB magnet (US $]	171.60	0	0
Total cost [US $]	242.17	143.80	74.16

Table 2.2 Comparison of performance at maximum power [59]

(a) 1500rpm

	Torque (Nm)	Copper loss (W)	Iron loss (W)	Efficiency (%)	Current density (A/mm^2)
IPM	303	4328	198	91.3	15.7
IM	297	8591	148	83.1	15.8/12.1
SRM	294	7653	404	85.2	20.1

(b) 6000rpm

	Torque (Nm)	Copper loss (W)	Iron loss (W)	Efficiency (%)	Current density (A/mm^2)
IPM	45.6	219	953	96.1	3.75
IM	50.8	730	439	95.2	4.51/3.72
SRM	52.1	306	4074	88.2	4.02

On the other hand, it is interesting to note that the material costs and manufacturing processes for high production volumes. For IPM motor, more cost is incurred because of the expensive magnet. The IM has much more copper than either IPM or the SRM, so SRM is relatively cheaper. In terms of manufacturing, the handling of magnetized magnet is a concern for IPM motor. The SRM prefers a much smaller airgap length, in order to realize a high reluctance ratio, so that more precision is needed. The IM requires a rotor with copper bars, which is expected to be relatively expensive to fabricate compared to aluminum bar [13] [60].

Based on the strict requirements to the key enabling technology of electric machine in the traction application, the figure of merit from 1 to 10, 10 being best and 1 being the worst, is used for qualitative comparison of different motor topologies, as in Table 2.3 [13][59][60]. As can be observed, the IPM, PMA-SynRM and IM are more competitive for EV traction applications compared to other motor topologies, with IPM and PMA-SynRM show the highest ranking due to their high efficiency, power density and controllability associated with relatively high magnet cost [13][59][60]. This can also be concluded from the current commercial applications of electric motors for EVs and HEVs where IM and IPM motor are dominant among the automobile companies as in Table 1.1.

Table 2.3 Qualitative comparison of different motor topologies

Performance	SPM	IPM	IM	SRM	PMA-SynRM	WFSM
Torque/power density	10	10	7	8	10	8
Torque ripple	8	8	9	6	8	8
Efficiency	10	10	8	8	10	8
Cost	6	7	10	9	7	8
NVH	10	9	8	6	9	8
High speed operability	6	7	8	10	8	6
Reliability/Fault tolerance	6	8	10	10	8	7
Manufacturability	6	8	9	10	7	8
Controllability	10	10	7	7	10	10
Sum	72	77	76	74	77	71
Ranking	5	1	3	4	1	6

Considering the sum of figures of merits, both IM and the SRM are promising candidates as magnet-less alternatives to IPM motor in HEVs and EVs. The IM is widely used and is characterized by low cost and high reliability; however, to improve the performance, the rotor with copper bar is needed which requires a high manufacturing effort [18].

The SRM features a relatively high performance with a crucial weakness of high torque ripple and relatively low power factor. More efforts to improving the torque ripple, power factor and noise are required [13].

To conclude, when designing an electric traction motor, the sizing and topology determination have to be integrated into a complete product cycle evaluation including performance, cost, and manufacturability [60].

2.2 Electric motor technologies in electromechanical actuator (EMA)

The electromechanical actuator can be classified as linear EMA and rotary EMA according to the motion form. A typical configuration of a linear EMA is a rotary

prime motor plus a reduction gearbox coupled with a mechanical screw, which converts the rotary motion to linear motion. A rotary EMA is normally a rotary prime motor with a multi-stage speed reducer like planetary gear or strain-wave gear, with features of low weight and no backlash. Compared to a hydraulic actuator, the EMA offers the advantages of lighter and more compact structure, less complexity than hydraulic actuation systems, easy installation and simple maintenance.

A major concern regarding the utilization of EMA is the mechanical jamming, which is critical and potentially disastrous for aircraft, but this is not a problem for hydraulic actuators as it will inherently be able to convert into damper mode after a failure, making it jamming-free and fail-safe. Therefore, it is crucial to assess the EMA jamming issue as this may results in catastrophic failure during flight if there is no suitable solution to handle the issue. The mechanical wear moreover is another important factor as this may results in free-play or other non-linearity. Hence the prediction of wear life of mechanical transmission part is also critical.

2.2.1 Linear EMA

The linear EMA, typically composed by high performance rotary prime motor plus a reduction gearbox coupled with a mechanical screw. It uses electromagnetic force/torque instead of hydraulic pressure to drive the ram [45] [50] [61]. There are two types of configurations for linear EMA, as shown in Figure 2.10 [62].

- Gear drive EMA: rotary prime motor coupled with a gearbox plus mechanical screw.
- Direct-drive EMA: Direct-drive rotary motor plus mechanical screw.

(a) Gear drive EMA   (b) Direct-drive EMA
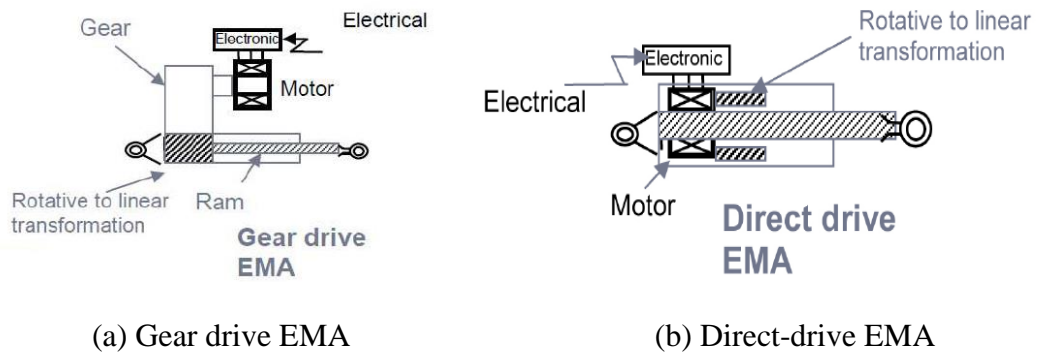
Figure 2.10 Two typical configurations of EMA [62]
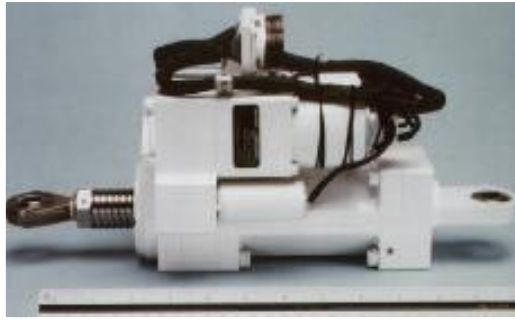
(a) EMA prototype   (b) EMA on iron-bird

Figure 2.11 F-18 Aileron test bench with linear EMA [65]

Linear EMA can also be realized by directly adopting a linear motor, removing the transmission screw that covert rotary motion to linear motion, which is inherently a direct-drive actuator and is jam-free [62]. However, the continuous force density of a linear motor is typically a few hundred newtons per active kilogram, making it too heavy to be used in aircraft actuators where the weight is one of the primary considerations [63][64]. Nonetheless, there are still some studies on the application of linear motor for aircraft actuation system, and it is obvious from these papers that the force per mass is too small [63][64], and this will also be proved in Chapter 6.

In the 1980s, a dual linear EMA has been built and tested to replace dual hydraulic actuator on the left Aileron in a C161, as in Figure 2.11 [62]. The Electrically Powered Actuation Design (EPAD) joint program between NASA, US Air Force, and Navy developed a Spoiler EMA (Max load: 222.411kN) based on a rotary five-phase SRM (peak power 40kW) coupled with mechanical screw. The Aileron EMA was developed for F-18 A/B Systems Research Aircraft. The performance in Iron-bird and on flight were tested, which shows the EMA matched that of the standard hydraulic actuator very well and is slightly better on the close-loop frequency response. However, the problems of thermal management, non-rotating shaft and mechanical stops still needs to be improved [65].

A. Garcia, *et al.*, discuss the general safety needs of EMA for aircraft applications, including suitability and reliability of actuator systems, electric motors, and power converters [66]. The mechanical jamming issue is highlighted. A solution through the monitoring and fault-tolerant systems is proposed for increasing reliability,

that is, using the scheme of direct-drive motor coupled with ball screw and improving the capability to detect, identify, and diagnose faults in their earlier states.

A 20 KW matrix converter driven EMA for an aircraft Rudder demonstrator is presented in [67][68]. Both induction motor and PMSM are evaluated, with the matrix converter providing good dynamic performance with a wide variation in static and non-static load. Testing results with a constant load of up to 55kN show the correct operation of the entire system with good power quality and drive performance.

(a) Stator with concentrated winding   (b) 20-pole rotor

Figure 2.12 PM motor designed for direct-drive Spoiler Actuator [11]

C. Gerada, *et al.*, present a direct-drive EMA without gearboxes designed for Spoiler actuation system for a large civil aircraft [11]. A low-speed 24 slots, 20 poles FSCW PM motor is developed as a potential solution to improve reliability, reduce weight and volume, with a high degree of fault tolerance, as in Figure 2.12. With roller screw (RS) as a rotary-linear gearing, a rated torque of 27Nm is needed for the rotary motor. The fault conditions of open-circuit (OC) phases and terminal short-circuit (SC) are investigated with a fault-tolerant drive topology of adopting individual controllers for each motor phase.

Airbus Group and SAFRAN Group collaboratively developed a linear EMA integrated with a direct-drive dual 3-phase PMSM and mechanical roller screw without reduction gearbox, as illustrated in Figure 2.13, which had been first tested for an Airbus A320 Aileron in Jan 2011, and 114 flight hours have been accumulated since then [62]. In the author's knowledge, this is the first project to work towards optimal solution of the EMA actuation system with integrated drive & control electronics, sensors and an electric motor to replace a conventional hydraulic actuation system in a commercial civil aircraft, aiming to achieve safety goals and aircraft

certification. System level, equipment level, and technology and methodology level have been studied. The results of both iron bird and flight test in A320 MSN1 (38 flights, 114 flight hours) show that the EMA is a promising technology for future flight control systems for MEA and AEA. Now, they are working to evaluate and extend the EMA life duration for product development [62][69].
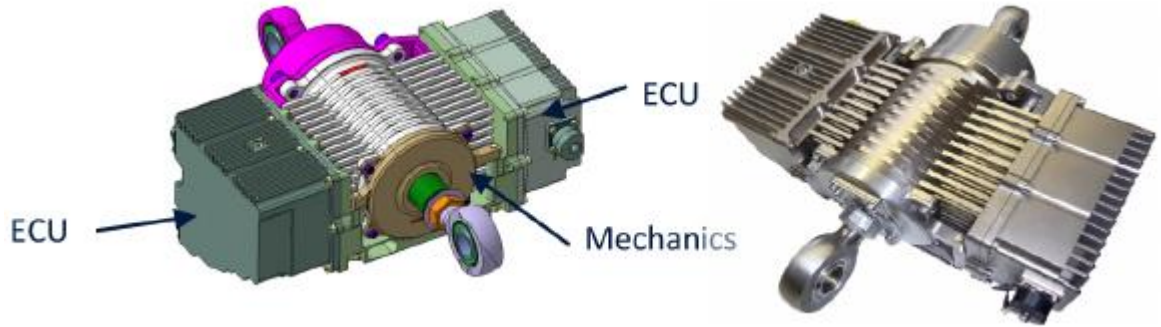
Figure 2.13 Aileron EMA developed by SAFRAN Group [62]

M. Villani, *et al.*, present an EMA designed for a helicopter rotor damper application to improve onboard comfort through balancing the typical vibration due to the main rotor [70]. The actuator system architecture is shown in Figure 2.14. Three types of PMSM with concentrated and distributed windings are analysed and compared, with a 12 slots, 10 poles FSCW PM motor selected due to its fault-tolerance, lower torque ripple and no unbalanced radial force. Preliminary test results confirm the achievement of the required specifications.
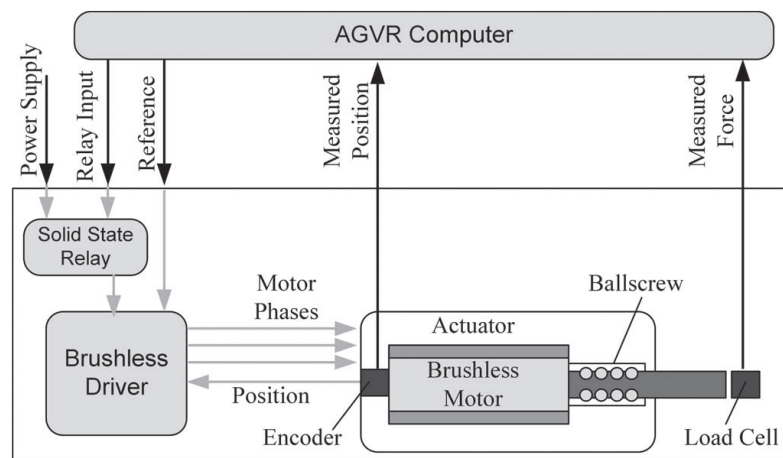
Figure 2.14 EMA scheme for helicopter active vibration reduction

(a) 5-phase PM BLDC motor   (b) Actuator prototypes
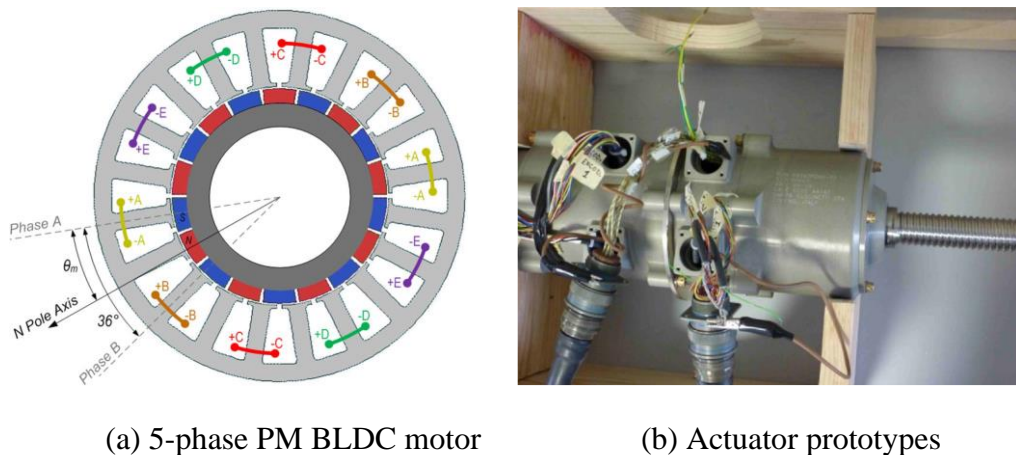
Figure 2.15 EMA motor and prototype [71]
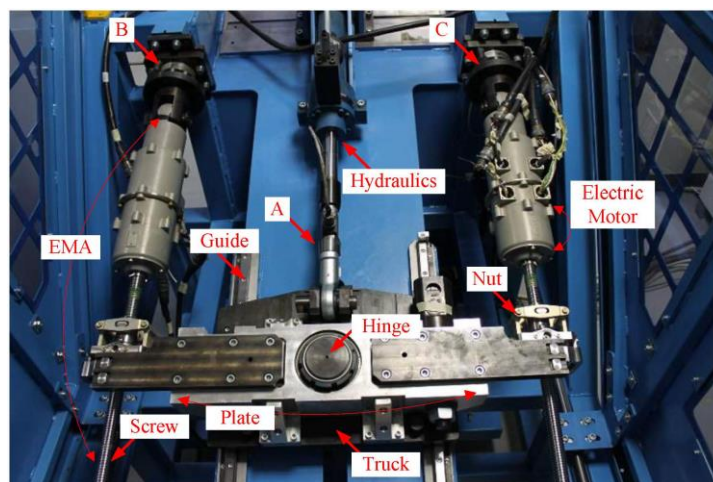
Figure 2.16 The twin EMAs' test bed [72]

M. Villani, *et al.*, also present a fault-tolerant EMA with 5-phase PMSM for a high lift Flap actuation system in Figure 2.15 [71][72]. The design philosophy, actuator configuration, and selection of motor to meet the dynamic loads, bearings, ball screw & sensor are discussed. The feasibility of keeping output rated torque with one or two phases open is confirmed which demonstrates the fault-tolerant requirements and the suitability for high reliability Flap application. The synchronization of two EMAs for simulating the synchronization of two Flaps actuation is implemented, as in Figure 2.16, which demonstrated good synchronization capability of the system with an adequate load sharing between the EMAs.
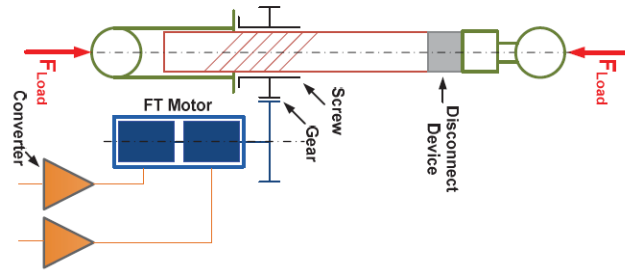
Figure 2.17 HEMAS EMA Scheme [73]
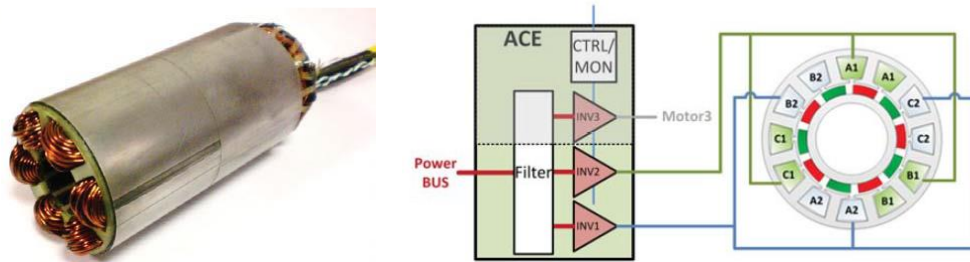
(a) Dual 3-phase stator   (b) Dual-Channel PMSM Drive

Figure 2.18 Dual 3-phase stator and drive system [73]
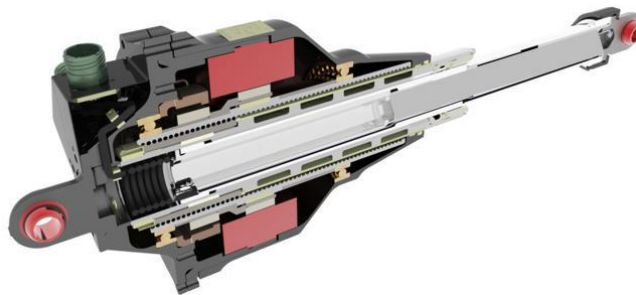
Figure 2.19 Jamming tolerant EMA [74][75]

M. Rottach, *et al.*, report a fault-tolerant PM motor drive helicopter electromechanical actuation system (HEMAS) [73]. To overcome the potential for mechanical jamming with EMAs, two EMAs are coupled with disconnect devices that provide fault tolerance against an individual EMA jamming or free-wheel failure, as in Figure 2.17, and each EMA is driven by a dual-channel fault-tolerant PMSM and dual 3-phase inverters with 270VDC supply, as in Figure 2.18. The experimental results of the integrated optimized prototype demonstrated the torque characteristics and fault-tolerant capability of limiting short-circuit current and braking torque.

More recently, a jamming tolerant flight control electromechanical actuator (EMA) is reported by CESA, a Spanish Aerospace System company, as in Figure 2.19 [74][75]. An anti-jamming system located inside the screw can disconnect the actuator from the control surface, avoiding possible jamming from mechanical single failure and assuring the manoeuvre of the flight control by means of a second actuator in parallel. A demonstrator with both EMA and electronic control unit (ECU) integrated has been developed. Three different control modes: Active, Damping and Anti-jamming mode, are tested and validated. It has demonstrated that the EMA with anti-jamming device can be adopted to perform safety-critical actuation systems such as Landing Gear or Primary Flight Control Surfaces [75].

2.2.2 Rotary EMA

Rotary EMA is a rotary actuation system composed of a rotary motor and a multi-stage speed reducer like planetary gear or strain-wave gear, with features of low weight and no backlash, as shown in Figure 2.20 [76].
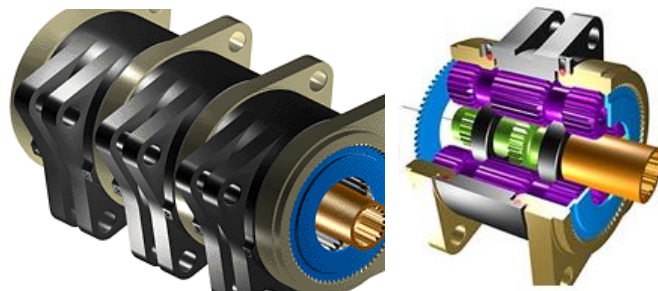
Figure 2.20 Compound Planetary Rotary Actuator [76]
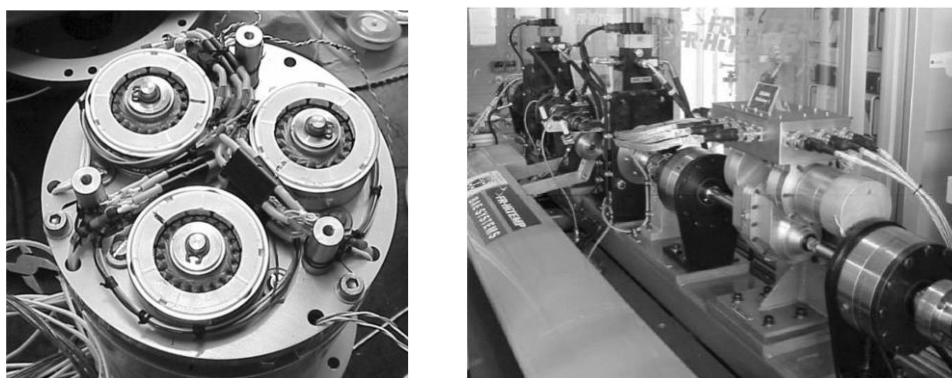
(a) One end of the actuator   (b) Full twin Flap test rig

Figure 2.21 Demonstration of EMA for a Flap actuation system [77]
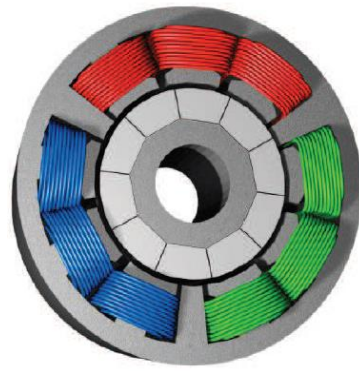
(a) Cross section of motor   (b) Prototype stator
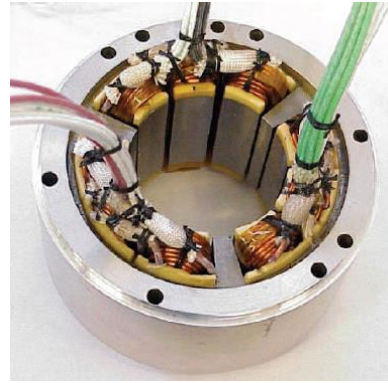
Figure 2.22 EMA motor with three independent phase windings [78]

Figure 2.21 shows a rotary EMA for Flaps and Slats for a civil aircraft developed by *J. Ben*nett and *B. Mecrow* from Newcastle University [77]. A '2+1' 9 slots, 10 poles FSCW PMSM with three independent phase windings is developed, with peak torque of 3.4Nm, operating speed of 10,000r/min, and peak power of 2kW, as in Figure 2.22. The mechanical separation between winding groups can mitigate the thermal coupling between winding groups. System architecture and a full-scale demonstrator have been presented, which meet the design specifications, including synchronisation of two Flaps and operation under short-circuit failure. In addition, the safety critical design requirement and fault-tolerant electric drives are fully discussed [61] [77].

Goodrich Actuation Systems and Newcastle University collaboratively developed a nose wheel steering actuator system, capable of load torque in excess of 7000Nm and an operating speed in excess of 18^0/s [78]. With a 595:1 gearbox, torque required from motor is taken to be 17Nm to allow a gearbox efficiency of 70% and provide some over-rating margin. A 24 slots, 20 poles FSCW PM motor with dual 3-phase winding is developed, as in Figure 2.23. Experimental results with the compensation strategies resulting from open-circuit and short-circuit failures of the motors show the dual 3-phase electric drives topology is simple to implement, with no requirement for current shifting or reshaping to maintain a smooth output torque at low speeds and a smooth SC braking torque.

Figure 2.23 Nose wheel actuator motor [78]
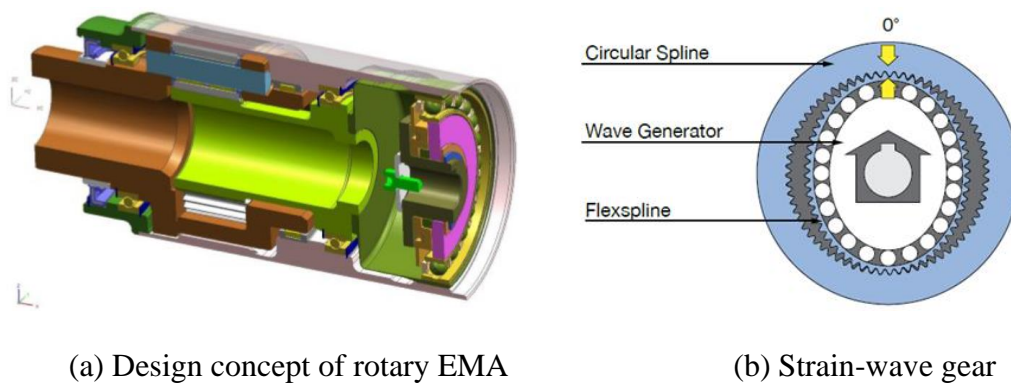
(a) Design concept of rotary EMA   (b) Strain-wave gear

Figure 2.24 Rotary EMA for landing gear system [79]

Another investigation on rotary EMAs is the EU Program-Actuation 2015: Modular EMAs for ACARE 2020 Aircraft and Helicopters, which includes both linear and rotary EMAs, and aims to validate a common set of standardised, modular and scalable EMA resources for all actuators (flight control, high lift, main landing gear applications) and all types of aircraft (civil, military, regional: aircraft and helicopter) [79]. A rotary actuator for retractable landing gear systems composed of motor with strain-wave gear is showed in Figure 2.24.

2.2.3 EMA design trends

The EMA system involves the safety and reliability of electrical motors, electronics control units, mechanical systems including bearing, mechanical screw and potentially gearbox in some cases. Some of the key design requirements on the EMA system components are summarized in Table 2.4 [66][80][81].

Table 2.4 EMA system design requirements [66][80][81]

Components	Characteristics and design requirements
Electric motor	- Low-speed high torque motor with direct-drive EMA. - High speed low torque motor with geared EMA. - High efficiency across the full operation range. - Magnetic, electrical, mechanical, and thermal isolation - SRM and PM motor are preferred in terms of high fault-tolerant capability under critical operation conditions. - PM motor is preferred than SRM due to high power dense and high efficiency required for aircraft applications. - Modular multi-phase motor design. - Large winding inductance to limit terminal short-circuit (SC) currents. - Maintain the normal output in the case of first fault. - Output degradation operation in the case of second fault.
Electronics control unit	- Fault-tolerant power converter topologies are required: - Independent H-Bridge converter for every phase if the motor phases are segregated. - Additional fourth leg in the classical three-phase inverter. - High reliability power switches and passive components. - Electromagnetic interference (EMI) with multiple electric actuators.
Monitor and diagnosis system	- Detect incipient faults at an early stage. - Online techniques for predictive maintenance, to check and evaluate performance conditions of both the rotating electrical motors and the whole electronics. - Certain redundancy level of sensors. - Crossing checking and comparison.
Mechanical components	- High reliability mechanical lead screw such as planetary roller screw. - High reliability bearing. - Model the wear down and life cycle and predict service life.
Mechanical system integration	Disconnected or decouple device to avoid mechanical jamming issue.

Different from the traction motor application, the design requirement is normally low-speed high torque motor for direct-drive EMA or high speed low torque motor for

geared EMA. Both high torque/power density and excellent fault-tolerant capability are extensively demanded.

From applications or research examples reviewed in the previous sections [66]-[73], [77][79], the use of FSCW PMSM motor which can provide the magnetic, electrical, mechanical, and thermal isolation is dominant. Considering fault tolerance, multiple winding groups supplied by independent power sources are necessary. Therefore, the multiple electric lanes FSCW PMSM with multiple electric drives is becoming a key enabling technology for aircraft EMA application [61][62].

2.3   Chapter summary

This chapter presents the electric motor technology advancements in traction motor applications for electric vehicles (EVs) and in electromechanical actuator (EMA) for more electric aircraft (MEA), respectively.

The comprehensive evaluation and comparison of typical electric motor topologies in the current EV market confirm that the IPM (including PMA-SynRM), IM and SRM are the most promising candidates for EV traction applications. To determine the most suitable topology, the sizing and topology determination must be integrated into a complete product cycle evaluation including performance, cost, and manufacturability. In addition, it is expected that the IPM motor (including PMA-SynRM) is anticipated to rule the market currently and possibly in the near future when pursuing a high-performance and high efficiency traction system.

The electric motor technologies applied in aircraft EMAs demonstrated a different design requirement from the traction motor, viz., low-speed high torque motor for a direct-drive EMA, or high speed low torque motor for a geared EMA. Both the high torque/power density and excellent fault-tolerant capability are required. Therefore, the FSCW PMSM with multiple electric lanes/drives capable of providing isolation in magnetic, electrical, mechanical, and thermal aspect and excellent fault-tolerant capability is the most promising technology for aircraft EMA applications.

Chapter 3

Fractional Slot Concentrated Winding (FSCW) Motors

This chapter deals with the operation principle and design aspects of the fractional slot concentrated winding (FSCW) motor. The stator MMF and winding inductance characteristics of ISDW and FSCW motor will be derived and compared using the winding function method. The stator MMF harmonic reduction techniques will be systematically reviewed and compared, which provides guidelines for developing new winding design methods.

3.1   Synchronous motor operation theory

3.1.1   Operation principle

The electric motor can be analyzed by using electromechanical energy conversion theory [82]. Figure 3.1 depicts an elementary rotational electric motor where the stator has a 3-phase winding and the rotor has two poles. The rotating magnetic fields, i.e., λ_s and λ_r, are produced in both the stator and rotor, respectively. One should note that the winding can be an arbitrary winding as long as it can generate a rotating magnetic field; the rotor magnetic field can be generated from either field windings or a permanent magnet.
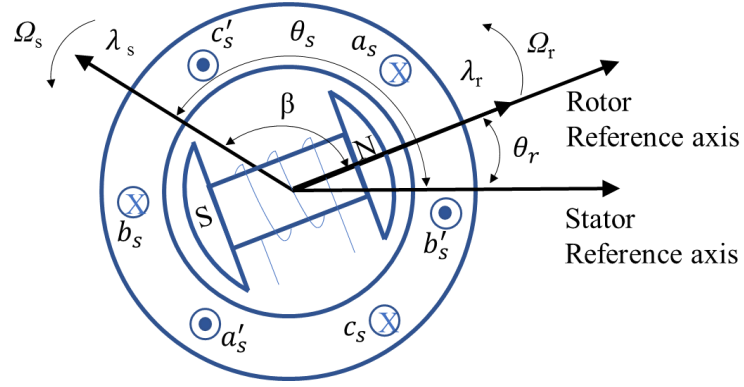
Figure 3.1 Schematic of an elementary rotational electric motor

The voltage equation in the stator and rotor winding can be written as

$$v_s = i_s R_s + \frac{d\lambda_s}{dt} \tag{3.1}$$

$$v_r = i_r R_r + \frac{d\lambda_r}{dt} \tag{3.2}$$

where i, R, and λ are the current, resistance, and flux linkage, respectively; the subscript of s and r means stator and rotor side, respectively.

To simplify the analysis, no magnetic saturation is considered, which means the system is linear. Thus, the flux linkages can be written as

$$\lambda_s = L_s i_s + M_{sr} i_r \tag{3.3}$$

$$\lambda_r = M_{rs} i_s + L_r i_r \tag{3.4}$$

where the self-inductance of L_s and L_r are constant; the mutual-inductance depends on the angle between stator and rotor magnetic field and can be expressed as

$$M_{sr} = M_{rs} = M cos\beta \tag{3.5}$$

Therefore, the energy in the system can be obtained.

$$dW_c(i_s, i_r, \delta) = (v_s i_s + v_r i_r) = i_s^2 R_s + i_r^2 R_r + i_s \frac{d\lambda_s}{dt} + i_r \frac{d\lambda_r}{dt} \tag{3.6}$$

$$W_c(i_s, i_r, \beta) = \int \frac{1}{2}(I_s^2 R_s + I_r^2 R_r)dt + \frac{1}{2}(L_s I_s^2 + L_r I_r^2)dt$$

$$+(2M_{sr} I_s I_r \sin \omega_s t \sin \omega_r t)dt \tag{3.7}$$

The first term to the right of the equal sign of (3.7) represents the ohmic losses, the second term represents stored field energy in the windings, and the last term is the coupling energy between stator and rotor which is responsible for generating electromagnetic torque. It can also be observed that only when $\omega_s=\omega_r$, namely, stator and rotor magnetic field have the same frequency, it may generate a smooth average electromagnetic torque. That is the operation principle of synchronous motor.

By applying the virtual work theory, the electromagnetic torque can be achieved

$$T_{em} = -\frac{\partial W_c(i_s, i_r, \beta)}{\partial t} = I_s I_r M sin\beta \tag{3.8}$$

Therefore, we can visualize the production of torque by the mutual interaction of the stator and rotor current. If the current amplitude is kept the same, the torque varies sinusoidally with the angle β.

3.1.2 Rotating magnetomotive force (MMF)

In the previous section, it has been confirmed that the stable operation of a synchronous motor requires two magnetic fields rotating at the same speed in the stator and rotor and interacting with one another. Normally, a permanent magnet synchronous motor (PMSM) consists of an armature winding in the stator and permanent magnet poles in the rotor.

In general, the armature winding that generates stator rotating magnetic field, can be classified according to the number of slots/pole/phase (SPP): Integral slot distributed winding (ISDW) for SPP≥1; otherwise, they are referred to as fractional slot concentrated winding (FSCW). This section introduces a comparison of these two winding types. In fact, there is another type of winding: fractional slot distributed winding (FSDW), which will be presented in Section 3.3.4.

The integral slot distributed winding normally has SPP≥1 and coil pitch of more than 1 slot. Figure 3.2 and Figure 3.3 depict a 30 slots, 10 poles (30S-10P) surface-mounted PMSM with double-layer (DL) ISDW and its winding distribution, respectively. A 12S-10P surface-mounted PMSM with double-layer (DL) ISDW and its winding distribution are shown in Figure 3.4 and Figure 3.5, respectively.
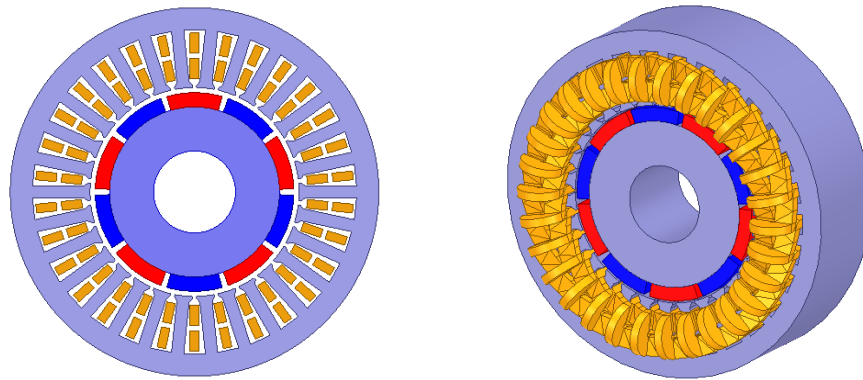
Figure 3.2 A 30S-10P surface-mounted PMSM with DL ISDW
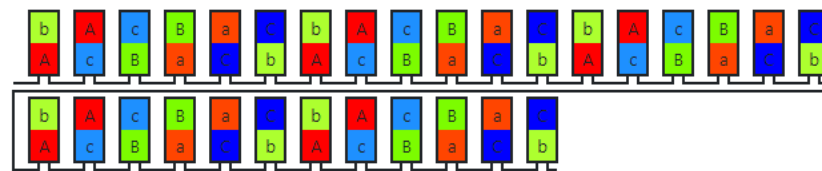
Figure 3.3 Winding distribution of a 30S-10P PMSM with DL ISDW
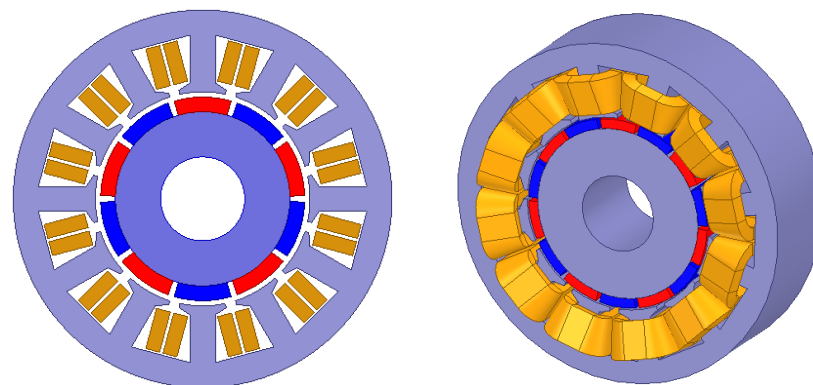
Figure 3.4 A 12S-10P surface-mounted PMSM with FSCW

Figure 3.5 Winding distribution of a 12S-10P PMSM with DL FSCW

Based on the winding distribution diagram, their stator winding rotating Magnetomotive Force (MMF) can be determined by using the winding function

method in Section 3.1.3. Its MMF waveform and corresponding Fast Fourier Transform (FFT) harmonic distribution are plotted in Figure 3.6. It should be noted that the stator MMF waveform are obtained without considering the stator slotting effect and rotor effect. It is apparent that the 30S-10P-DL has a more sinusoidal waveform while a concentrated winding exhibits more stator MMF harmonics such as 1st and 7th apart from the main working harmonic 5th harmonic. These MMF harmonics will increase airgap harmonic leakage inductance and can have other undesirable impacts, including high rotor/magnet losses and localized saturation.

(a) MMF waveform   (b) FFT spectrum
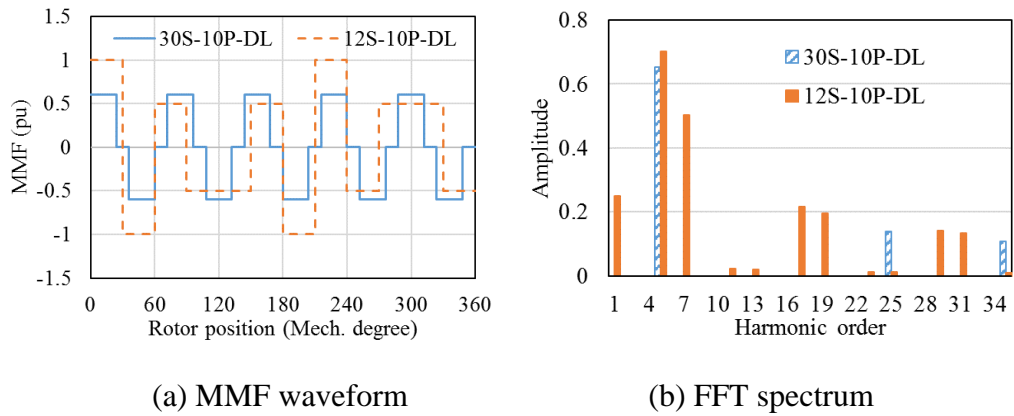
Figure 3.6 Stator MMF distribution of 30S-10P and 12S-10P PMSM

3.1.3 Winding function

Before calculating the motor inductances, we need to introduce the concept of the winding turn function to help in calculating flux linkage in a winding. The winding function is a description of how effectively a winding links flux density at any given position, in other words, the effective number of turns linked at different positions [82] [83]. It is apparent that winding turn is a function of rotor position. The winding function of an arbitrary winding can be expressed as [82]

$$N(\theta) = n(\theta) - < n(\theta) > \tag{3.9}$$

where $< n(\theta) >$ is the average value of the winding turns function, and it can be expressed as (3.10), and $g(\theta)$ is the airgap length function.

$$< n(\theta) >= \frac{\int_0^{2\pi} n(\theta) g^{-1}(\theta) d\theta}{\int_0^{2\pi} g^{-1}(\theta) d\theta} \tag{3.10}$$

Applying Fourier Transform to winding function, the harmonic components can easily be achieved; thereby, its general expression can be written as

$$N(\theta) = \sum_{v=1}^{\infty} N_v \cos(v\theta) \tag{3.11}$$

where N_v is the equivalent winding turns of vth harmonic.

Taking 30S-10P-DL ISDW and 12S-10P-DL FSCW PMSM as examples, Figure 3.7 illustrates their winding function waveform and corresponding FFT distribution. They can also be expressed in Fourier series, as in (3.12) and (3.13). It can be observed that the 12S-10P-DL FSCW have more harmonics including fractional harmonics whose orders are not integral multiple of rotor pole-pair numbers.

(a) Winding turn waveform   (b) FFT distribution
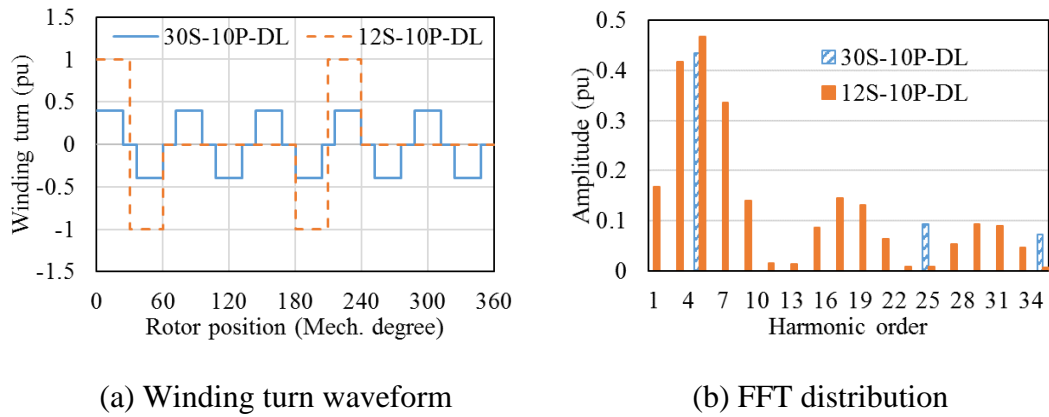
Figure 3.7 Phase winding function of 30S-10P-DL and 12S-10P-DL PMSM

$$N_{30S-10P-DL}(\theta) = \sum_{v=5,25,35}^{\infty} \frac{2N_{s1}}{v\pi} k_{wv} \cos(v\theta) \tag{3.12}$$

where N_{s1} is the number of turns per phase; $k_{wv} = \sin\frac{v\pi}{3}$ is the winding factor of vth harmonic order.

$$N_{12S-10P-DL}(\theta) = \sum_{v=1,3,5,7}^{\infty} \frac{2N_{s2}}{v\pi} k_{wv} \cos(v\theta) \tag{3.13}$$

where N_{s2} is the number of turns per phase; $k_{wv} = \sin\frac{v\pi}{12}\sin\frac{v\pi}{12}$ is the winding factor of vth harmonic order.

Comparing (3.12) to (3.13) we can see that they share the same formula of winding function. In fact, this formula, as in (3.14), is generally established if the distribution of the coils is uniform. In (3.14), N_s is the number of turns per phase, coefficient of 2 represents the relationship between conductors and coil numbers, and k_{wv} represents the effective turns coefficient for each harmonic, referring to the definition of winding turn function and properties of the Fourier Series [84] [85]. Otherwise, the more general formula of (3.11) can be used for any arbitrary winding, especially when the distribution of the coils is not uniform, and every coil has a different number of turns.

$$N(\theta) = \sum_{v=1}^{\infty} \frac{2N_s}{v\pi} k_{wv} \cos(v\theta) \qquad (3.14)$$

3.1.4 Winding inductance

In any real coupled inductance, the flux linking a winding will include both leakage flux linkage and magnetizing flux linkage. The inductance is associated with flux components of current. Thereby, the concept of leakage and magnetizing inductance are associated with the concept of leakage and magnetizing flux, respectively, where

1) *leakage flux*: flux links only a single stator or rotor winding and does not travel across the airgap and is not involved in energy conversion. It includes airgap harmonic leakage, slot leakage, tooth-tip leakage, and end-winding leakage. Due to the existence of the airgap in machines, it can form a significant portion of the total flux [82][84].

2) *magnetizing flux*: flux that travels across the airgap and links both a stator and a rotor winding, that is, mutual flux, can be considered as the useful component of flux [82][84].

$$\lambda = \lambda_l + \lambda_m \qquad (3.15)$$

$$L = L_l + L_m \qquad (3.16)$$

Recalled from Figure 3.1, the mutual-inductance between winding a_s and b_s is the sum of leakage and magnetizing inductance, hence

$$L_{ab} = L_{abl} + L_{abm} \qquad (3.17)$$

$$L_{abl} = \frac{\lambda_{al}}{i_b} \qquad (3.18)$$

$$L_{abm} = \frac{\lambda_{abm}}{i_b} \tag{3.19}$$

Then the self-inductance of a winding can be expressed as

$$L_{aa} = L_{aal} + L_{aam} \tag{3.20}$$

Since the leakage inductance, including slot leakage, tooth-tip leakage, end-winding leakage, and differential leakage component, is associated with leakage flux that does not travel across the airgap, the effective airgap variation due to the rotor topologies would normally not have a significant impact on it. In addition, it is not involved in the energy conversion within the machine. Hence, we can treat it as a constant value which depends mainly on the stator slot geometry, winding arrangement and end-winding shape, and detailed calculation for each leakage inductance components can be found in [82][86].

In this thesis, more focus will be on the calculation of airgap inductance which includes the magnetizing inductance and harmonic leakage inductance. According to [82][84], the general expression of total flux linkages in winding a_s due to current in b_s winding can be written as

$$\lambda_{ab} = \int_0^{2\pi} N_a(\theta_s)B(\theta_s)rl_{ef}d(\theta_s) = \mu_0 rl_{ef} \int_0^{2\pi} \frac{N_a(\theta_s)N_b(\theta_s)i_b}{g(\theta_s - \theta_r)}d(\theta_s) \tag{3.21}$$

where μ_0 is the permeability of free space; θ_s is the position measured relative to the stator reference axis; θ_r is the rotor position measured relative to the stator reference axis; r and l_{ef} are the airgap radius and active axial length, respectively; P is the rotor pole-pair numbers; $g(\theta_s - \theta_r)$ is the airgap length function.

Hence, the airgap mutual inductance between winding a_s and b_s can be expressed as

$$L_{abm} = \mu_0 rl_{ef} \int_0^{2\pi} \frac{N_a(\theta_s)N_b(\theta_s)}{g(\theta_s - \theta_r)}d(\theta_s) \tag{3.22}$$

It can be noted that the above equation will be equal to the magnetizing inductance if only the winding function of the main working harmonic is considered. In addition, one can note from Figure 3.7 that the harmonics of winding function for

FSCW are much more significant than that of ISDW, which is another inherent reason of high leakage inductance for FSCW motors.

From Figure 3.1, the rotor in consideration is an elementary salient-pole, or so-called synchronous reluctance rotor topology, where the effective airgap is a positive function in related to the rotor position θ_r. Applying Fourier transform to the effective airgap length function, we can get

$$g(\theta_s - \theta_r) = \frac{1}{g_0 + g_2 cos2P(\theta_s - \theta_r) + g_4 cos4P(\theta_s - \theta_r) + \cdots} \tag{3.23}$$

3.1.4.1 ISDW configuration

Recalled from (3.14) and only considering the first order harmonic, namely the main working harmonic which is associated with rotor pole-pair numbers P, the winding function of each phase for a ISDW motor can be written as

$$N_a(\theta_s) = \frac{2N_s}{P\pi} k_{wP} \cos(P\theta_s) \tag{3.24}$$

$$N_b(\theta_s) = \frac{2N_s}{P\pi} k_{wP} \cos\left(P\theta_s - \frac{2\pi}{m}\right) \tag{3.25}$$

$$N_c(\theta_s) = \frac{2N_s}{P\pi} k_{wP} \cos\left(P\theta_s - \frac{4\pi}{m}\right) \tag{3.26}$$

where m is phase numbers.

Substituting (3.23), (3.24), (3.25) and (3.26) into (3.22), and formalizing, we can get

$$L_{abm} = \frac{1}{\pi} \mu_0 r l_{ef} (\frac{2N_s k_{wP}}{P})^2 \left[g_0 \, cos\left(\frac{2\pi}{m}\right) + \frac{1}{2} g_2 cos\left(2P\theta_r - \frac{2\pi}{m}\right)\right] \tag{3.27}$$

Similarly, the magnetizing component of self-inductance can be expressed as

$$L_{aam} = \frac{1}{\pi} \mu_0 r l_{ef} (\frac{2N_s k_{wP}}{P})^2 \left[g_0 + \frac{1}{2} g_2 \, cos(2P\theta_r) \right] \tag{3.28}$$

Therefore, all the inductance components associated with a m-phase PMSM with symmetrical winding can be achieved. Below are all the inductance components associated with a three-phase PMSM.

$$L_{aa} = L_{ls} + L_{aam} = L_{ls} + L_A + L_B \, cos(2P\theta_r) \tag{3.29}$$

$$L_{bb} = L_{ls} + L_{bbm} = L_{ls} + L_A + L_B \cos 2\left(P\theta_r - \frac{2\pi}{3}\right) \qquad (3.30)$$

$$L_{cc} = L_{ls} + L_{ccm} = L_{ls} + L_A + L_B \cos 2\left(P\theta_r - \frac{4\pi}{3}\right) \qquad (3.31)$$

$$L_{ab} = L_{lm} + L_{abm} = L_{lm} - \frac{1}{2}L_A + L_B cos2\left(P\theta_r - \frac{\pi}{3}\right) \qquad (3.32)$$

$$L_{ac} = L_{lm} + L_{acm} = L_{lm} - \frac{1}{2}L_A + L_B cos2\left(P\theta_r - \frac{2\pi}{3}\right) \qquad (3.33)$$

$$L_{bc} = L_{lm} + L_{bcm} = L_{lm} - \frac{1}{2}L_A + L_B cos2(P\theta_r - \pi) \qquad (3.34)$$

where

$$L_A = \frac{1}{\pi}\mu_0 r l_{ef}(\frac{2N_s k_{wP}}{P})^2 g_0 \qquad (3.35)$$

$$L_B = \frac{1}{2}\frac{1}{\pi}\mu_0 r l_{ef}(\frac{2N_s k_{wP}}{P})^2 g_2 \qquad (3.36)$$

L_{ls} and L_{lm} represent a simpler notation for leakage component of self- and of mutual-inductance respectively, and they are common to all stator phases.

We can observe that both self- and mutual- inductance are position-dependent and the variation of them is a sinusoidal function of $2P\theta_r$ for a salient-pole PMSM or synchronous reluctance motor. For a PMSM with non-salient rotor structure, e.g. surface-mounted PMSM, the effective airgap length $g(\theta_r)$, ignoring the slotting effect on the effective airgap which can be considered by Carter's coefficient [82], is a constant and is independent of rotor position; in this case, both self- and mutual-inductance are a constant and are independent of rotor position theoretically. However, as the iron core saturation level varies with rotor position in a practical electric motor, a variation of sinusoidal function of $2P\theta_r$ may still exist.

3.1.4.2 FSCW configuration

Due to the concentrated winding characteristics, there may be no overlapping area between the flux path of different phase winding; thereby, the magnetizing component of mutual- inductance maybe zero or nearly negligible in some cases. In addition, there may be some FSCW winding topologies where the average value of winding turn function is not zero.

In [87], a modified winding function has been proposed to facilitate the slot/pole combinations with FSCW. The airgap inductance that includes the magnetizing inductance and harmonic leakage inductance of mutual-inductance can be expressed as (3.37). This expression is similar to (3.9).

$$M_{ab} = \mu_0 r l_{ef} \int_0^{2\pi} \frac{N_a(\theta_s) N_b(\theta_s)}{g(\theta_s - \theta_r)}$$

$$-\mu_0 r l_{ef} \frac{\int_0^{2\pi} \frac{N_a(\theta_s)}{g(\theta_s - \theta_r)} d(\theta_s) \cdot \int_0^{2\pi} \frac{N_b(\theta_s)}{g(\theta_s - \theta_r)} d(\theta_s)}{\int_0^{2\pi} \frac{1}{g(\theta_s - \theta_r)} d(\theta_s)} d(\theta_s) \quad (3.37)$$

Similarly, the airgap inductance that includes the magnetizing inductance and harmonic leakage inductance of self-inductance can be expressed as

$$L_{aa} = \mu_0 r l_{ef} \int_0^{2\pi} \frac{N_a(\theta_s)^2}{g(\theta_s - \theta_r)} - \mu_0 r l_{ef} \frac{(\int_0^{2\pi} \frac{N_a(\theta_s)}{g(\theta_s - \theta_r)} d(\theta_s))^2}{\int_0^{2\pi} \frac{1}{g(\theta_s - \theta_r)} d(\theta_s)} d(\theta_s) \quad (3.38)$$

With an evenly distributed airgap, the mutual-inductance can be simplified as

$$M = -2\pi \frac{\mu_0 r l_{ef}}{g} \langle N_a(\theta_s) \rangle^2 \quad (3.39)$$

where $\langle N_a(\theta_s) \rangle$ means the average value of winding function.

(a) SL   (b) DL
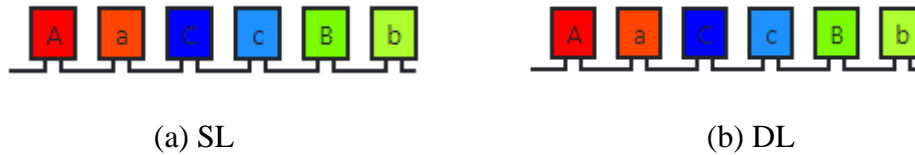
Figure 3.8 6S-4P FSCW configuration

In fact, this is reasonable as the flux generated by one coil must form a closed path. If the number of positive and negative coils are not equal like 6 slots, 4 poles (6S-4P) FSCW DL in Figure 3.8, some fluxes will couple with the coils of other phases. Therefore, it can be confirmed that for the slot/pole combinations in which the number of positive and negative coils are equal such as 12 slots, 10/14 poles (12S-10/14P) and 18 slots, 14 poles (18S-14P), the magnetizing component of mutual-inductance is nearly zero. The magnetizing component of mutual-inductance is determined by how

unbalanced the number of positive coils and negative coils for the slot/pole combinations where the number of positive and negative coils are not equal.

3.1.4.3 General expression of winding inductance

In general, if ignoring the high order winding inductances, the inductance of a three-phase winding can be expressed [87]

$$L_{xx} = L_0 + L_2 \cos 2P\theta_r \tag{3.40}$$

$$M_{xy} = M_0 + M_2 \cos\left(2P\theta_r - \frac{2\pi}{3}\right) \tag{3.41}$$

where L_0 and M_0 are the average value of respective inductance components; L_2 and M_2 are the amplitude of the 2nd order harmonic of the inductance, respectively; subscript x and y denote the winding phase name.

3.1.5 PMSM Mathematical model

From the previous sections, one can note that the flux linkage and current are vectors rotating in space at a certain speed, and the inductance is a position-dependent function. However, if we see the current and flux linkage from the rotor rotating frame, these components become constant, and constant value is more convenient for modeling and control. Therefore, it is beneficial to convert those items from static stator frame to rotating rotor frame. Figure 3.9 shows the phasor diagram of PMSM in the *d-q* rotating frame [86].
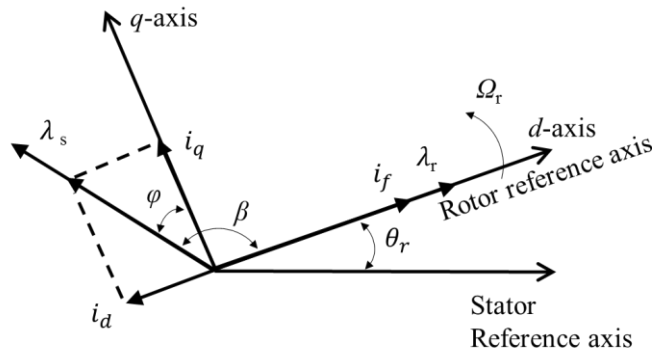
Figure 3.9 Phasor diagram of PMSM in *d-q* rotating frame

$$L_{dq} = PL_{abc}P^{-1} \tag{3.42}$$

$$G_{dq} = PG_{abc} \tag{3.43}$$

where G denotes flux linkage, current or voltage, and the d-q transformation matrix is

$$P = \frac{2}{3} \begin{bmatrix} cos(wt) & cos\left(wt - \frac{2\pi}{3}\right) & cos\left(wt + \frac{2\pi}{3}\right) \\ -sin(wt) & -sin\left(wt - \frac{2\pi}{3}\right) & -sin\left(wt + \frac{2\pi}{3}\right) \\ \frac{1}{2} & \frac{1}{2} & \frac{1}{2} \end{bmatrix} \tag{3.44}$$

Hence, the mathematical model of PMSM may be expressed as [86]

$$\begin{aligned} u_d &= \frac{d\lambda_d}{dt} - \omega\lambda_q + Ri_d \\ u_q &= \frac{d\lambda_q}{dt} + \omega\lambda_d + Ri_q \\ \lambda_d &= L_d i_d + \lambda_f \\ \lambda_q &= L_q i_q \\ T_{em} &= \frac{m}{2}P[\lambda_f i_q + (L_d - L_q)i_d i_q] \end{aligned} \tag{3.45}$$

where the expression of d- and q- inductance can be achieved from transforming the self- and mutual- inductance of (3.40) and (3.41) in the stator frame to the rotor rotating frame.

$$L_d = (L_0 - M_0) + (\frac{L_2}{2} + M_2) \tag{3.46}$$

$$L_q = (L_0 - M_0) - (\frac{L_2}{2} + M_2) \tag{3.47}$$

Therefore, the EM torque may also be expressed as

$$T_{em} = T_{pm} + T_r = \frac{m}{2}P[\lambda_f i_q + L_{diff} i_d i_q] \tag{3.48}$$

$$L_{diff} = L_2 + 2M_2 \tag{3.49}$$

One can note that the reluctance torque capability is technically determined by the amplitude of the 2nd order harmonic of self- and mutual- inductance.

For the ISDW topologies and DL FSCW with SPP=1/2 or 1/4 topologies, the amplitude of 2nd order harmonic of self- and mutual- inductance are equal, and the d- and q- inductance difference can be expressed as (3.50).

$$L_{diff} = 3L_2 \tag{3.50}$$

For FSCW configuration that the average value of phase winding turn function is zero such as SPP=2/5 and 2/7, the amplitude of 2nd order component of mutual-inductance is nearly zero or negligible, and the *d-* and *q-* inductance difference can be expressed as (3.51).

$$L_{diff} = L_2 \qquad\qquad (3.51)$$

Therefore, it can be observed that the reluctance torque capability of all the FSCW motor where average value of phase winding turn function is zero such as SPP=2/5 or 2/7 family are very limited, while SPP=1/2 or 1/4 family such as 6S-4P or 12 slots, 8 poles (12S-8P), or SPP=3/8 or 3/10 family such as 9S-8P and 9S-10P FSCW design are preferred in terms of giving more reluctance torque component due to their high mutual-inductance.

3.2 Fractional slot concentrated winding (FSCW) motor

As revealed before, the FSCW topology exhibits unique characteristics compared to the conventional ISDW topology. Depending on the number of layers, a fractional slot concentrated winding motor, i.e., single-layer (SL) and double-layer (DL) winding, can be seen in Figure 3.10. This section will present the design aspects of FSCW motor.

(a) Single-layer   (b) Double-layer
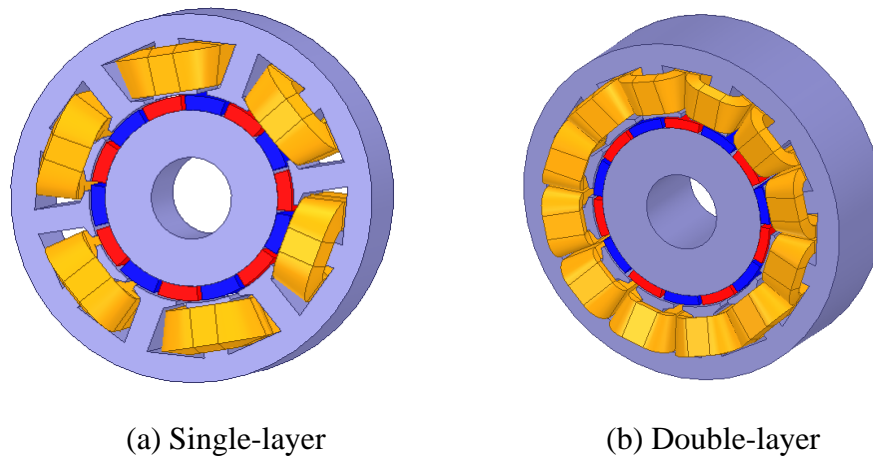
Figure 3.10 Example of a 12S-10P FSCW configurations

3.2.1 Slot/pole combinations

Due to the characteristics of concentrated winding or tooth wound winding, the pole numbers $2P$ and slot numbers Q must be close in order to have a high pitch factor and consequently high winding factor [88]. Normally, the selection criteria are $Q=2P\pm1$ or $Q=2P\pm2$. In some cases, it can be $Q=2P\pm4$. The star of slots theory which is based on a graphical representation and is useful to rapidly differentiate the harmonic orders in the winding distribution, back EMF and airgap MMF distribution, can be used in the analysis and the design of fractional slot windings [10][88].

The motor's electrical periodicity t_m is defined by the greatest common divisor (GCD) between the number of slots Q and pole pairs P. The unit motor being considered in this paper is when GCD equals to 1.

$$t_m = GCD(Q,P) \tag{3.52}$$

To have a balanced winding system, the value of Q/t_m must be a multiple of the phase numbers m. The electrical angle difference between the phasors of vth harmonic of two adjacent slots is $\alpha_v = v\alpha_s$, where $\alpha_s = 2\pi/Q$ is the mechanical slot angle. Hence, the design of the winding of a FSCW motor needs to differentiate the position of the coil phasors of each phase. To this aim, the phasor of each phase is obtained by summing those phasors of desired harmonic, that is the harmonic with rotor pole-pair order, with minimum angular displacement [10].

(a) Coils distribution   (b) Star of slots
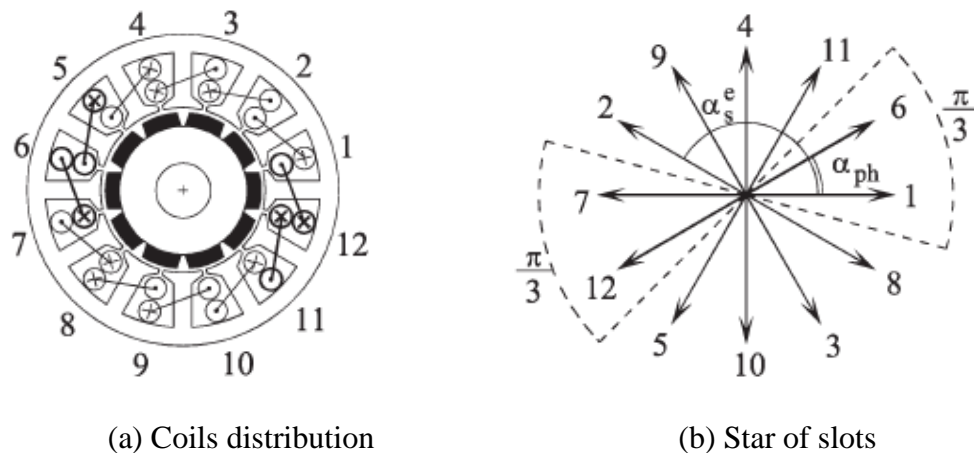
Figure 3.11 Star of slots of a three-phase 12S-10P DL motor [10]

An example is reported in Figure 3.11 showing the main harmonic of star of slots of a 12S-10P DL FSCW motor. The coil side connection is chosen with the aim

of maximizing the winding factor of the EMF main harmonic, i.e., $v = P = 5$. The phasors 1, 6, -7, and -12 are connected, obtaining the resultant phasor of the first phase. The distribution factor can also be determined in this way. Similarly, the distribution factor of other harmonics can also be determined. Some of the feasible slot/pole combinations can be found in [89][90]. The winding factor calculation method is systematically addressed in [91].

3.2.2 Cogging torque

Cogging torque is caused by variation of the magnetic energy of the field due to the interaction between PM rotor and stator slot. A concept of elementary torque may be defined as the interaction of a slot opening with a PM pole. For each revolution of the rotor, the number of periods N_p of the waveform depends on the least common multiple (LCM) of slots and poles [89] [92].

$$N_p = LCM(Q, 2P) \tag{3.53}$$

The value of N_p is an index that shows if the elementary cogging torque waveforms are in phase or not. The low N_p means the positive (and then negative) elementary torques occur at the same rotor position. In this case, the different addenda are superimposed, yielding a high cogging torque. Conversely, if N_p is high, different addenda are distributed along the slot pitch, namely some of them are counteracting from one another, yielding a low cogging torque. Since normally the FSCW features $Q=2P\pm1$ or $Q=2P\pm2$, N_p is a much higher number compared to the ISDW cases; hence, the FSCW motors inherently have a low cogging toque.

3.2.3 Design for winding isolation

Due to the tooth wound winding characteristic of the FSCW motor, there is a possibility to realize a maximum isolation between coils or phases. As can be seen in in Figure 3.10, the tooth wound winding makes it possible to physically and thermally isolate the phases from one another. With independent electric supply to different phase or coils, electrical isolation can also be achieved. In the case of SL FSCW, the coils are physically isolated by the alternate teeth and a fault in one phase will have minimum impact on the operation of other coils or phases.

(a) 12S-14P SL   (b) 12S-14P DL
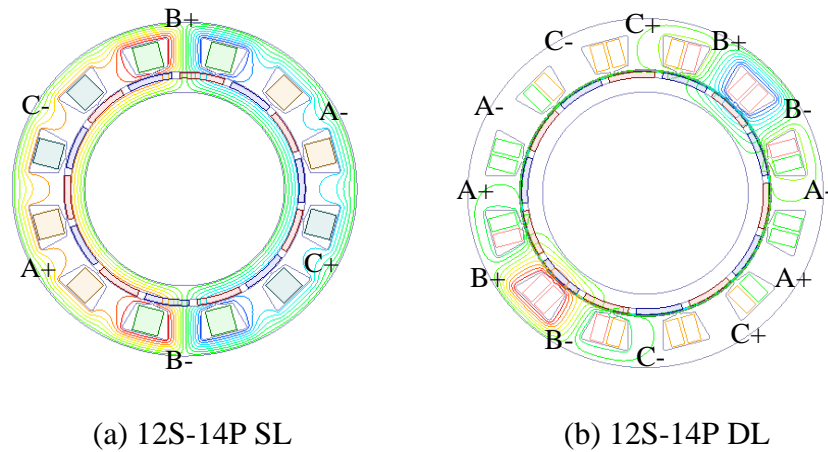
Figure 3.12 Flux distribution of a 12S-14P motor with phase B excitation

(a) 6S-4P SL   (b) 6S-4P DL
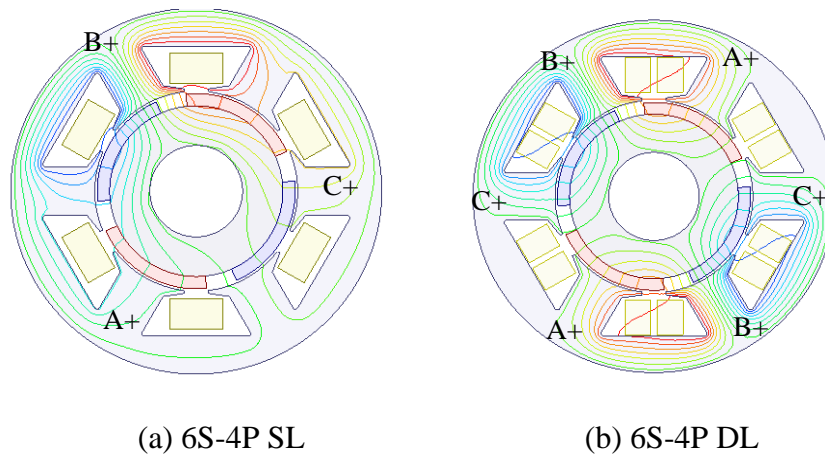
Figure 3.13 Flux distribution of a 6S-4P motor with phase B excitation

As for the magnetic isolation, it is not straightforward. Most of the FSCW topologies feature low mutual coupling between phases from the winding inductance analysis in Section 3.1. Specifically, the FSCWs where the average value of winding turn function is zero, feature no or negligible coupling between phases such as 12S-10/14P or 24S-22/26P, while for the FSCWs, such as with SPP=1/2 or 1/4, where the average value of phase winding turn function is not zero, will result in a strong coupling between phases.

For most of the SL FSCW, as in Figure 3.10 (a), the teeth are alternatively wound, where the flux generated by a positive coil will be closed by the corresponding negative coil without coupling with the flux path of other phases. Some leakage fluxes will also be closed with adjacent teeth. This can be observed from Figure 3.12(a)

showing the flux distribution of 12S-14P FSCW motor with only phase B excitation. For most of the DL FSCW configurations like the one in Figure 3.10(b), all the teeth are alternatively wound, the flux generated by a positive coil will be closed by the adjacent corresponding negative coil without coupling with the flux path of other phases. However, for FSCW with SPP=1/2 or 1/4, the coupling is strong, and this can be observed from the flux distribution in Figure 3.13.

A summary of normalized self- and mutual- inductance for both a 12S-14P and 6S-4P can be seen in Table 3.1. It should be noted that both SL and DL case have the same number of turns per phase. For a 12S-14P FSCW, the mutual-inductance is negligible for both SL and DL case, and the DL case tends to have a slightly higher mutual-inductance than the SL case. For a 6S-4P DL FSCW, the mutual-inductance is about half of the self-inductance, while for a 6S-4P SL FSCW, the mutual coupling is lower but still it is considerable.

Therefore, if a magnetic isolation between phases is required, it is better to choose the FSCW slot pole combinations have low mutual coupling where the average value of winding function is zero, and normally the SL case is preferred to the DL case in terms of giving maximum isolation. With FSCW design, the isolation physically, thermally, electrically, and magnetically can easily be implemented with appropriate slot-pole combination and winding arrangement.

Table 3.1 Normalized self- and mutual- inductances

	Self-inductance		Mutual-inductance	
	SL	DL	SL	DL
12S-14P	1	0.654	0.002	0.067
6S-4P	1	0.445	0.166	0.201

3.2.4 High phase inductance

The main components of inductance in a surface-mounted PMSM are attributed to the air-gap flux leakage due to the inherent stator space MMF harmonics and slot leakage flux due to high effective airgap length (physical airgap + magnet thickness), and the dominance of slot leakage flux might be weakening with effective airgap reduced

[87][93][94]. The airgap leakage inductance maybe comparable to the magnetizing inductance.

The inductance comparison between a SL FSCW, DL FSCW and ISDW motor, is reported in [93] with same SPM rotor configuration and the constraint of same flux-linkage for all the winding configurations. Regardless of end-winding leakage inductance, FSCW features much higher inductance than ISDW, and SL FSCW demonstrates higher inductance than DL FSCW due to higher air gap leakage and end-winding leakage components.

The characteristic current of an SPM motor is defined as:

$$I_{ch} = I_{sc} = \frac{\lambda_f}{L_d} \tag{3.54}$$

It is well-known that optimal flux-weakening, for both SPM and interior PM motors, occurs when the characteristic current I_{ch} equals the rated current [95]. The inductance of an SPM motor with ISDW configuration is, however, relatively low. As a result, the characteristic current tends to be significantly higher than the rated current, which severely limits the constant-power, flux-weakening operational range. However, thanks to the high slot leakage and airgap harmonic inductance, the SPM motor with FSCW configuration can achieve a high self-inductance reducing characteristic current and short-circuit current; these benefits give it a better constant-power and flux-weakening capability [96] [97].

With the high slot leakage inductance, a per-unit inductance can deliberately be designed; as a result, the symmetrical three-phase terminal short-circuit (SC) current will be equal to the rated current, which limits the per phase SC current to a safe value in the case of winding short-circuit fault, making the FSCW SPM motor a good candidate for fault-tolerant applications [98][99].

3.2.5 Modularity and manufacturability

One of the advantages of FSCW motors is the concentrated winding, where coils are wound around a single tooth, giving a highly modular winding [100]-[105]. This feature allows for a modular design of motor that can be segmented by teeth; both the tooth and coil can be separately manufactured and then assembled together. The segmented modular design makes manufacturing easy, more efficient, and is good for

automated processes. A high slot fill factor can also be achieved. With premade coils pressed, the slot fill factor can be further increased.

3.2.6 Summary of advantages and disadvantages

As has been detailed, a comprehensive comparison between FSCW and ISDW can be achieved in terms of EM performance, fault-tolerance, and manufacturability. The main advantages of FSCW are

- Short end-winding length due to the concentred winding characteristics, and hence shorter motor length and lower passive component cost associated with end-regions.
- High slot fill factor. With modular teeth design, the slot fill factor can be improved up to 85% [105].
- High power/torque density due to the reduction in copper loss associated with short end-winding and high slot fill factor. In addition, FSCW motor prefers high pole numbers which lead to a thin stator/rotor yoke and hence reduce the motor's weight and volume.
- Low cogging torque and torque ripple with appropriate slot-pole combinations where the GCD of slot and pole numbers is high.
- Due to the concentred winding characteristics, it is easier to manufacture with modular designs, offering advantageous cost-effective production solutions.
- Wide speed constant power region attributed to the high slot leakage, which can reduce the characteristic current. It is verified that an SPM motor equipped with FSCWs can achieve wide speed flux-weakening operation.
- Excellent fault-tolerant capability due to the feasibility of implementing the physical, electric, magnetic, and thermal isolation simultaneously.

Compared to ISDW topology, however, the main drawbacks are

- Significant stator space MMF harmonics can lead to localized magnetic saturation, and considerable iron losses, especially in the rotor core and magnet.
- Higher rotor losses attributed to asynchronous stator space MMF harmonics, resulting in a high risk of rotor thermal issues.
- Unbalanced magnetic force caused by the MMF harmonics which is more serious if the GCD between the slot and pole numbers is low [106]. This results

in higher stresses on the bearings and the risk of high vibration and acoustic noise [107].

3.3 FSCW stator MMF harmonics reduction techniques

As discussed in the Section 3.1, unlike the conventional ISDW configurations where their winding turn function and stator rotating MMF are more sinusoidal, the stator rotating MMF harmonic that is asynchronous to the main working harmonic in an FSCW motor is significant, which will result in high rotor/magnet losses, localized saturation, and unbalanced radial force [108].

This section will review four different stator MMF harmonics reduction techniques for FSCW motor, including multi-layer winding, multiple *m*-phase winding, two-slot pitch winding, and offset stator or stator shifting. Some other techniques such as unequal turn numbers and stator flux barriers are not discussed as they either are not easily implemented or feature low effectiveness [109] [110].

3.3.1 Stator MMF harmonics definition

Before presenting the MMF harmonic reduction techniques on the undesired stator MMF harmonics, the definition of different stator MMF harmonics will be required. There are four types of MMF harmonics in an FSCW motor, taking a 9 slots, 8 poles (9S-8P) DL winding as an example in Figure 3.14.

Working harmonic: This harmonic is the harmonic whose order is the same as the rotor pole-pair numbers. In a 9S-8P motor, it is the 4th, while for 9 slots, 10 poles (9S-10P) motor, it is the 5th.

Parasitic harmonic: This harmonic is the harmonic whose order is close to that of the working harmonic and normally having the same winding factor and comparable amplitude of the working harmonic. In a 9S-8P motor, it is typically the 5th; both 4th and 5th normally occur in a pair, making it difficult to reduce the parasitic harmonics, which will be seen in the next section.

Sub-harmonics: These harmonics are normally the harmonics whose order is lower than that of the working and parasitic harmonic. In a 9S-8P motor, they are the 1st and 2nd.

Slot harmonics: They are the harmonics characterized by the same winding factor as the main harmonics and each slot harmonic is correlated with a specific main harmonic [108]. In fact, these slot harmonics can be regarded as the modulated harmonics of the main harmonics due to the slot modulated effect. Their order may be expressed as

$$v_{sh} = kQ \pm v \tag{3.55}$$

where k=1, 2, 3…. In the example of a 9S-8P motor, 8th and 10th, and 7th and 11th may be regarded as the slot harmonics of the 1st and 2nd harmonic, respectively; 13th and 14th may be regarded as the slot harmonics of the 4th and 5th harmonic, respectively.
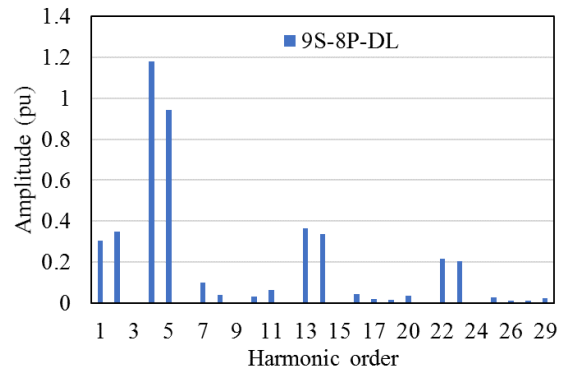
(a) Phase distribution (b) Stator MMF harmonics

Figure 3.14 9S-8P DL winding topology

3.3.2 Multi-layer winding

Winding layer number has played a critical role in reducing stator MMF harmonics in both ISDW and FSCW configuration. Normally, a *l*-layer winding configuration can be regarded as a combination of two *l*/2-layer combinations if the slot numbers is even, with shifting of certain slots between each other. For instance, a 6 slots, 2 poles (6S-2P) DL ISDW can be regarded as putting two 6S-2P SL ISDW configurations together, with shifting by 1 slot between them, as in Figure 3.15. Both the 5th and 7th harmonic have been slightly reduced to decrease torque ripple, while the main working 1st harmonic is negatively impacted. The critical winding shifting concept is involved which will be presented in the next section.

(a) Winding distribution (b) FFT spectrum
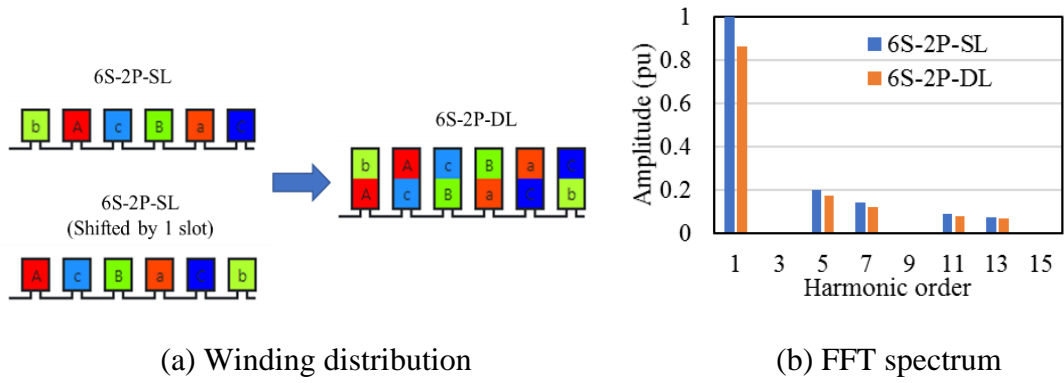
Figure 3.15 6S-2P ISDW configuration with SL and DL winding
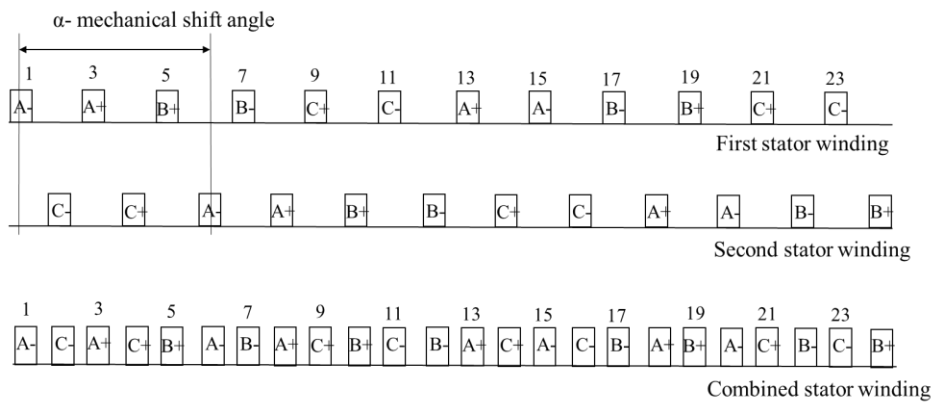
Figure 3.16 Concept of winding shifting

3.3.2.1 Concept of winding shifting

Generally, the concept of winding shifting is to use two of the same winding configuration to form a combined winding configuration having lower stator MMF harmonics, while maintaining or even improving the torque performance, with a certain mechanical shift angle α between these two stators/windings and the rotor unchanged [111] [112]. Figure 3.16 shows the principle of winding shifting. A second winding set, which is identical to the existing first winding set, is added to the existing motor, shifting by a specific mechanical angle over each other. The corresponding coils of each phase in these two winding sets can be connected either in series or in parallel. It should be noted that all the process is implemented in the stator winding side, the rotor is kept the same.

The winding shifting concept aims to reduce the undesirable stator MMF harmonics. By selecting an appropriate shift angle, some undesirable harmonics can be significantly reduced or even cancelled while the main working harmonic can be maintained or not significantly reduced.

The impact of winding shifting on each harmonic can be graphically expressed using the star of slots theory [10], as in Figure 3.17. Assuming A1 and A2 represents the resultant vector of phase A of first and second winding sets, respectively, and they are shifting by a mechanical angle of α from each other, the attenuation factor k_a due to the winding shifting and winding factor k_{wkc} of the resultant vector of phase A for the combined winding may be expressed as

$$k_a = \cos\left(\frac{k\alpha}{2}\right) \tag{3.56}$$

$$k_{wkc} = k_{wk}k_a = k_{wk}\cos\left(\frac{k\alpha}{2}\right) \tag{3.57}$$

where k_{wk} is the winding factor of corresponding $l/2$-layer winding configuration.
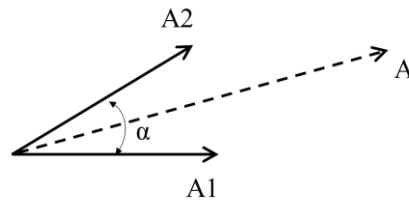
Figure 3.17 Impact of winding shift on winding factor of harmonics

It can be observed that an extra attenuation factor of cos ($k\alpha/2$) has been added to the winding factor of the combined winding. In fact, this factor can also be regarded as an additional distribution factor. Therefore, this equation can be used to find the shift angle for reducing undesired harmonics, and the negative impact on the desired working harmonic can also be evaluated.

3.3.2.2 Double-layer winding

From the concept of winding shifting, a DL winding can be regarded as a combination of two SL windings, with shifting by certain slots between each other.
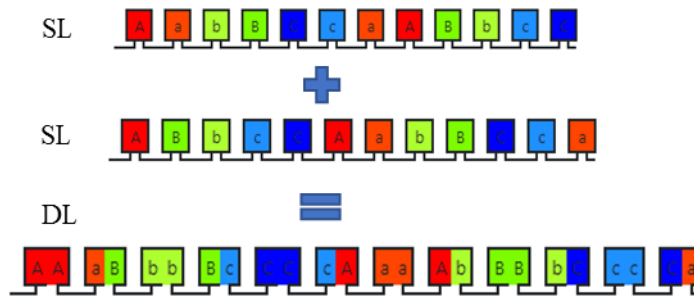
Figure 3.18 Illustration of a 12S-10P FSCW from SL to DL design
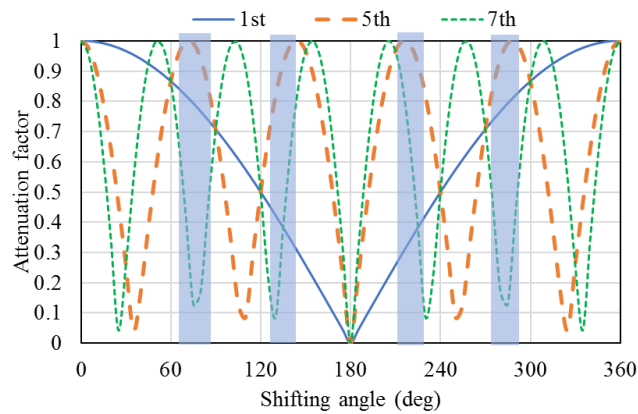
Figure 3.19 Attenuation factor for 12S-10/14P motor

A 12S-10P with DL winding can be regarded as a combination of two 12S-10P-SL winding configurations, as depicted in Figure 3.18. The attenuation factor of the harmonics can be calculated using (3.56) to identify the optimal shift angle, as in Figure 3.19, which has to be $k*30^0$ as it can only be shifted by a whole number of slots. It can be observed that shifting 150 or 210^0, viz., 5 or 7 slots, gives the better impact in reducing the 1st sub-harmonic while having a slightly negative effect on the working 5th harmonic. The attenuation factor for the 1st, 5th and 7th harmonic are 74.15%, 3.4%, and 3.4%, respectively and they agree well with MMF spectrum and winding factor comparison in the Figure 3.20.

One should note that for some FSCW motors with odd slot numbers, it is not possible to have a balanced single-layer winding configuration; thereby the minimum layer number is 2. Figure 3.21 depicts the winding layout of 9S-10P DL configuration, which can easily be obtained from star of slots theory [10].
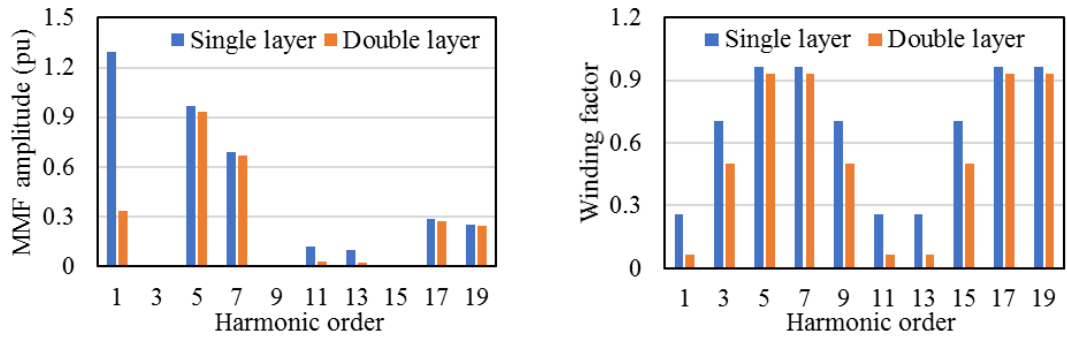
(a) MMF harmonic spectrum

(b) Winding factor

Figure 3.20 Comparison of single and double layer 12S-10P motor
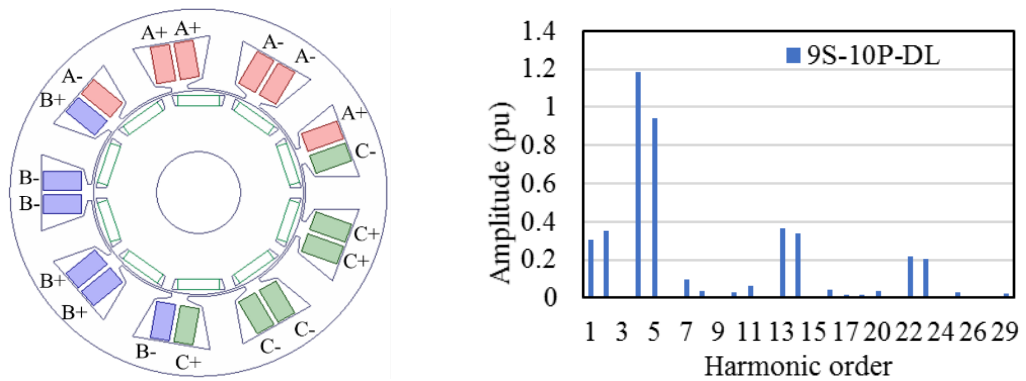
(a) Winding configuration

(b) MMF harmonic spectrum

Figure 3.21 9S-10P FSCW motor

3.3.2.3 Quadruple layer winding

To further reduce or cancel the sub-harmonics, a higher layer of triple or quadruple layer windings are proposed, which can be derived from double-layer or single-layer winding configuration by the concept of winding shifting [113]-[116].

Figure 3.22 illustrates the process of a 12S-10P FSCW motor from DL to quadruple layer winding configuration. The top and bottom layer winding distribution in Figure 3.22 (b) is exactly the same as a normal 12S-10P -DL winding in the Figure 3.22 (a), shifting by a certain angle between each other. The optimal shift angle can be identified by calculating the attenuation factor of the concerned harmonics, as in Figure 3.19. Again, shifting 5 or 7 slots can reduce 1st sub-harmonics considerably while having slightly negative effect on the working 5th harmonic. The Figure 3.22 (b)

depicts the resultant 12S-10P FSCW with quadruple layer winding with shifting by 5 slots between each other, and the comparison of MMF harmonic spectrum and winding factor are plotted in Figure 3.23. A similar concept can be applied to a 9S-8/10P FSCW motor [117];

(a) Double-layer   (b) Quadruple layer (shifting by 5 slots)
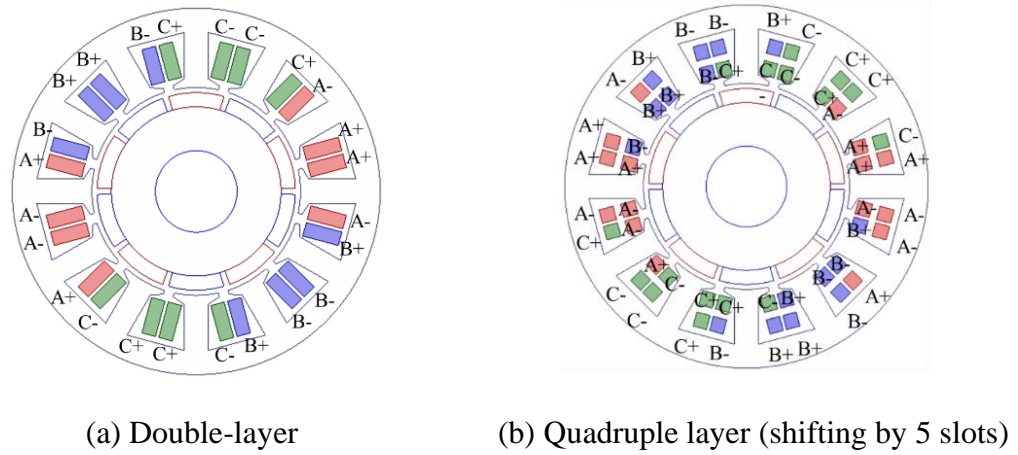
Figure 3.22 12S-10P FSCW motor [115]

(a) MMF spectrum   (b) Winding factor
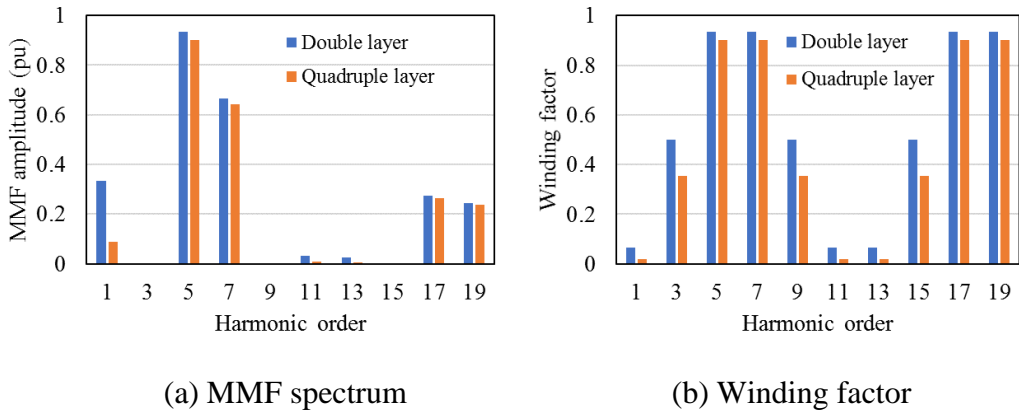
Figure 3.23 Comparison of double and quadruple layer 12S-10P motor [115]

3.3.3 Multiple m-phase winding

Multi-layer winding configuration can reduce stator MMF sub-harmonics, but it cannot cancel the sub-harmonics in most of cases. This section introduces the method of using multiple m-phase winding configuration to cancel all the sub-harmonics.

Based on the star of slots theory [10], the coils can be regarded as a phasor in different position. In the cases of SPP≠1/2 or 1/4 family with DL winding, e.g., 12S-

10/14P and 9S-8/10P, each phase has more than 1 phasor in each sector and the phasors belong to each phase are in different position, which means there is an angle offset between them. This provides an opportunity to use multiple *m*-phase windings with shifting from each other in time to cancel the sub-harmonics.

(a) Star of slots   (b) Winding layout of phase A
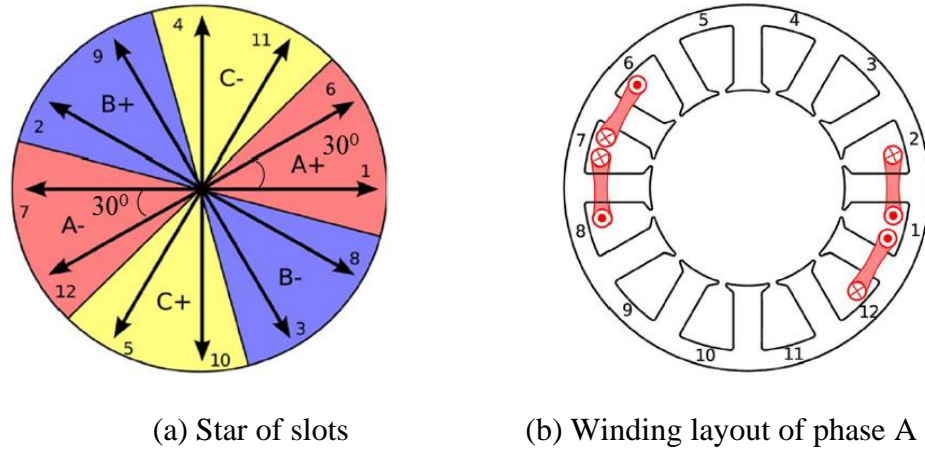
Figure 3.24 12S-10P FSCW DL motor [117]

(a) MMF spectrum   (b) Winding factor
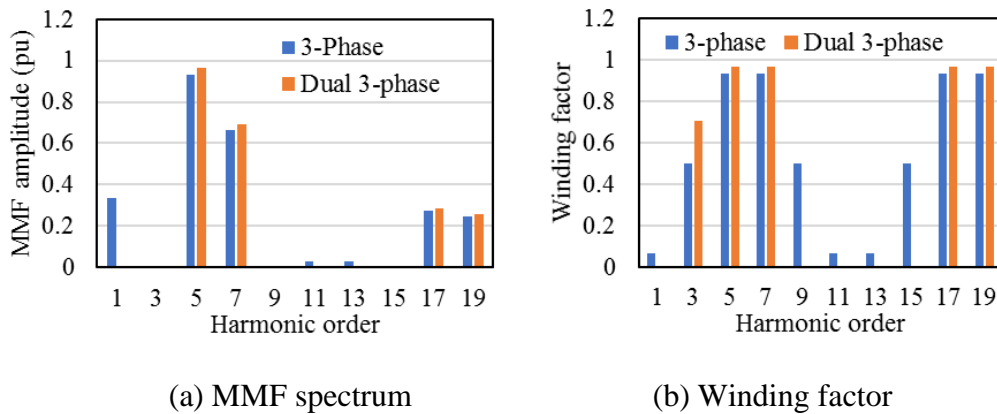
Figure 3.25 Comparison of 3-phase and dual 3-phase 12S-10P motor

Figure 3.24 shows the star of slots of a 12S-10P motor, which is an example of SPP=2/5 family [117]. It can be seen that there is 30 electric degree shift between phasor 1 and 6, and between phasor 7 and 12. To make the excitation current in line with the corresponding coil phasor, a dual 3-phase winding with 30^0 shifting in time from each other can be applied [118]. In this case, the 1st sub-harmonic is cancelled, and both the 5th and 7th harmonics are slightly increased by 3.5%, as in Figure 3.25(a).

In fact, the dual 3-phase concept can be extended to any *m*-phase winding, e.g. 5-phase 20S-18P FSCW motor [118]. For a split-phase motor, the phase belt of a conventional *m*-phase winding is split into two halves with an electrical space phase separation of π/2*m* between the two *m*-phase winding sets. This entails that the angle between two successive slots should be π/2*m*, which corresponds to a number of slots equal to 4*m* or its multiples.

The implementation of a dual 3-phase winding can also be realized by the Star-Delta connection as the angle difference between Star and Delta connection is exactly 30 degrees, as shown in Figure 3.26 (a) [118]. In this case, only 3 terminals come out simplifying the cable connection; in addition, the electric motor can be controlled as a 3-phase winding system as the dual 3-phase current with shifting 30 deg in time is realized by the physical internal connection. However, there is a current ratio of $\sqrt{3}$ between the Star and Delta connected winding. Hence, the number of turns of the Delta connected winding should be $\sqrt{3}$ times of turn numbers of the Star connected winding. It is worth noting that if the winding topology contains the $(3*i)^{\text{th}}$ EMF harmonics it will create circulating current within Delta connection.

One should note that the method of multiple *m*-phase winding eliminating sub-harmonics can be extended to any FSCW configurations and ISDW configurations where there is an angle difference between the coil phasors belong to the same phase, such as 18S-14/22P and 24S-22/26P [119] [120] and 24S-2P ISDW motor [121].
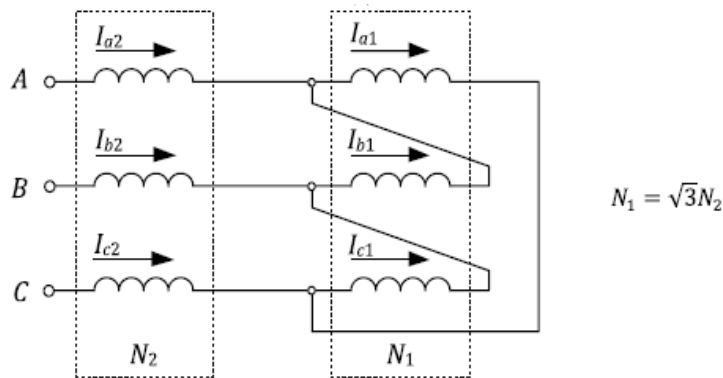
Figure 3.26 Implementation of dual 3-phase winding [118]

3.3.4 Two-slot pitch winding

Those methods introduced in previous sections are only effective in reducing or cancelling the sub-harmonics while having negligible effect on reducing the parasitic harmonic which normally has a high amplitude and is more detrimental due to its very high asynchronous frequency seen from the rotor, e.g. 7th and 5th in the 12S-10/14P motor and 5th and 4th in the 9S-8/10P motor. This section will review the two-slot pitch winding which provides more shift angle options to reduce or cancel the more detrimental parasitic harmonics by winding shifting.

If we recall the attenuation factor of winding shifting in Figure 3.19 for 12S-10P motor, there is a shift angle of 75^0 which can significantly reduce the 7th harmonic, while having no considerably negative impact on the 5th harmonic. However, shifting 75^0 is not possible for 12S-10P motor as the angle should be an integer times of slot angle, that is $k*30^0$. When doubling the slot numbers e.g. changing from 12S-10P to 24S-10P, and splitting the concentrated winding into a two-slot pitch winding, more shift angles are possible, which provides more flexibility in cancelling the undesired space MMF harmonics [112][122][123].

Dajaku, et al., proposed a 24 slots, 10 poles (24S-10P) motor with two-slot pitch DL winding, which is obtained by doubling the slot numbers of a conventional 12S-10P-DL motor and then adding another set of windings into the stator[112]. The attenuation factor of harmonics with shift angle can be seen in Figure 3.19, where the optimal shift angles are in the angular ranges shaded grey areas. As the shift angle can only be $k*15^0$, shifting 75^0 or 107^0, viz., 5 or 7 slots, are the best options. The process of achieving a 24S-10P motor with two-slot pitch winding is depicted in Figure 3.16, where shifting 5 slots between two winding sets is illustrated. The more detrimental 7th harmonic is reduced by 87% while only sacrificing 0.8% of 5th (working) harmonic, as in Figure 3.27. In fact, this winding topology is a fractional slot distributed winding (FSDW) where SPP is not an integer.

However, the 1st sub-harmonic still exists, which can be eliminated by using multiple *m*-phase windings, as presented in previous sections [123]. In addition, the two-slot pitch winding method can be applied to other FSCW motors in reducing the more detrimental parasitic harmonic, e.g. the 4th and 5th in the 9S-10/8P motor.
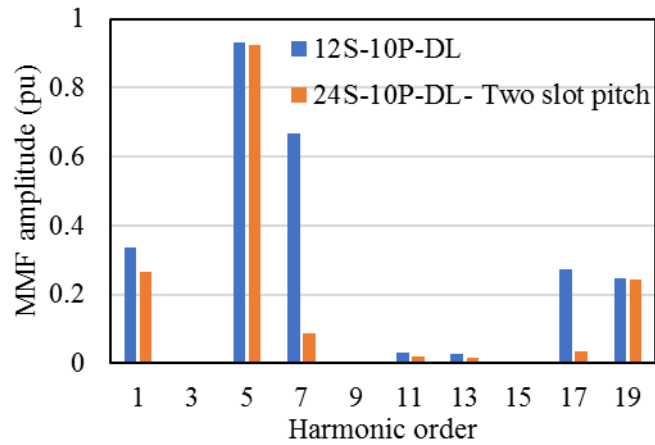
Figure 3.27 Stator MMF spectrum of 12S-10P-DL and 24S-10P-DL-2-slot
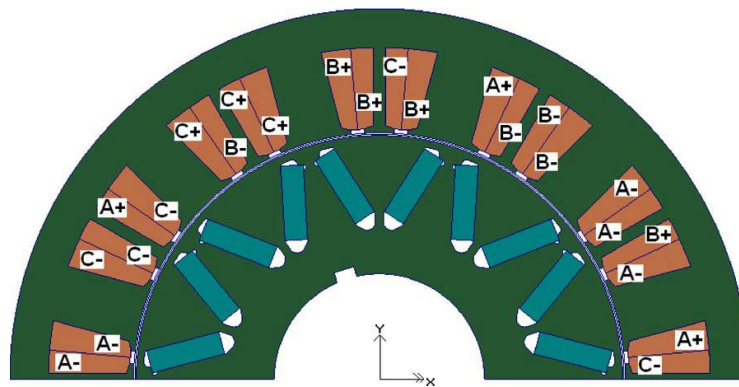
Figure 3.28 24S-10P-DL motor with shift angle of 700^0 [124]

One can note that the winding shifting method can only be applied by shifting by a whole number of slots, which limited the available shift angles. To further extend the two-slot pitch winding method, *B. Reddy, et al.,* propose a generalized approach of stator shifting in interior permanent-magnet motors equipped with unequal slot/tooth [124]. In this case, any shift angle is possible and consequently can achieve the optimal effect of reducing undesirable harmonics while keeping the working harmonic unaffected. The disadvantage, however, is the resultant unequal slot/tooth, as in Figure 3.28, which complicates the stator core manufacturing.

3.3.5 Offset stator

As has been depicted, the winding shifting is a good method in reducing MMF harmonics. Using two stators offset from each other was proposed to cancel out the negative harmonics in the MMF waveform leaving only the positive working harmonics in [125] and [126]. Figure 3.29 depicts the 2 and 4 pole flux waveform components in a double-sided 3 coil section of a concentrated winding linear motor; with 180^0 offset or shifting, the 2 pole flux is cancelled. The same concept can be applied to other FSCW configurations such as 9S-8/10P and 12S-10/14P.

This offset stator method offers the most flexible options in reducing stator MMF harmonics. The disadvantage is two stators are required, which is complex in a radial-flux rotating motor; However, this can be easily implemented and beneficial in linear motors and axial-flux motors.
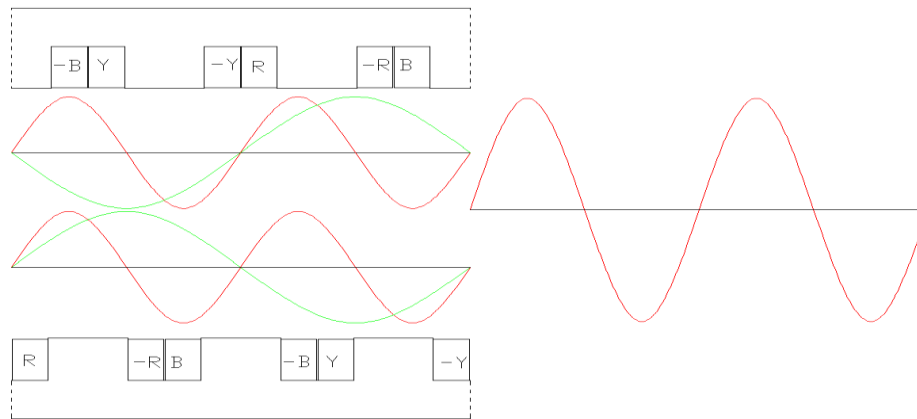
Figure 3.29 Description of offset double-sided concentrated winding [125]

3.3.6 Summary of stator MMF harmonics reduction techniques

Different techniques were proposed to reduce the stator space MMF harmonics. The advantages and disadvantages are summarized in Table 3.2. Depends on the requirements such as losses, speed and fault tolerance, a careful design consideration should be involved.

Table 3.2 Comparion of different MMF harmonic reduction techniques

Techniques	Harmonics concerned	Advantages	Disadvantages
Unequal turn numbers [109]	Sub-harmonics	- Stator core kept the same - No sacrifice on the working harmonic for optimum turn ratio	- Limited turn numbers available for optimum turns - Difficult in winding coils with unequal turns coil side
Stator flux barriers [110]	Sub-harmonics	- Easy implementation - Additional space for weight saves or cooling channel - Modular tooth design	- Reduced magnetic loading - Penalized performance at heavy load condition;
Multi-layer winding [113]-[116]	Sub-harmonics	- Easy implementation	- Higher layer numbers - Mutual phase coupling - Insulation issue - Low slot fill
Multiple m-phase winding [117][118]	Sub-harmonics	- Slightly improved working harmonic - Fault tolerance	- Higher power switch numbers in some cases - Control complexity
Two-slot pitch winding [112][122]	Sub-harmonics & parasitic harmonics	- Reduce most of harmonics - No or tiny sacrifice on the working harmonic	- Literally short pitch distributed winding - Mutual phase coupling - Low slot fill
Offset stators [125][126]	Sub-harmonics & parasitic harmonics	- Most flexible design in reducing any harmonics - Possible fault tolerance - Easy implementation in linear motor or axial-flux motor	- Complex structure of two stators for radial-flux rotating motor

3.4 Selection of motor topologies for traction motor and EMA motor

Based on the comprehensive analysis and literature review on the current state-of-the-art technologies, the following motor topologies have been selected to assess in this thesis.

3.4.1 IPM motor with proposed FSCW for traction application

For traction application in HEVs or EVs, the wide speed constant power operation and fault-tolerant capability are required apart from the high power/torque density. The IPM motor with FSCW configuration can meet these requirements and is also characterized by high reliability and easy manufacturability attributing from concentrated winding features. These features make a modular stator structure possible and so it is good for automated production.

One of the challenges with FSCW IPM motor is the significant stator MMF harmonics which result in considerable rotor losses in the high speed operation range [97], which may be comparable or even higher than the copper loss.

Therefore, this thesis will investigate the significant stator MMF harmonics issue of the IPM motor with conventional FSCW configuration used for traction application and propose a novel generalized FSCW topology with reduced stator MMF harmonics while keeping the concentrated winding characteristics.

3.4.2 SPM motor with conventional FSCW for EMA application

For the direct-drive EMA motor, the key demands are the high torque density and excellent fault-tolerant capability. The SPM motor with FSCW configuration is expected to be the best candidate due to its high torque density and high inductance limiting short-circuit (SC) current [96] [97]. Due to the low speed characteristics attributing from direct-drive EMA motor, the iron loss and magnet eddy current loss coming from the significant stator MMF harmonics associated with conventional FSCW configuration are negligible compared to the copper loss [127]. The isolation design in the physical, electrical, magnetic, and thermal aspect can also easily be implemented with a single-layer FSCW topology. However, more attention must be paid to the unbalanced magnetic pull with FSCW configurations, especially under fault conditions.

Hence, this thesis will focus on the SPM motor with conventional FSCW topology, aiming to develop a high torque density and compact modular EMA motor with excellent fault-tolerant capability.

3.5 Chapter Summary

This chapter introduces the principle and design aspects of the FSCW motor by using the synchronous motor operation theory. The stator MMF and winding inductance characteristics of ISDW and FSCW motor are derived and compared using the winding function method.

Secondly, the design aspects of the FSCW motor are comprehensively analysed. The method to give a low cogging torque, low mutual coupling, and high winding inductance is reviewed. The highest isolation in electric, magnetic, physical, and thermal aspect that can be realized in FSCW motors have been highlighted.

Then, the issue of the significant stator MMF harmonics in FSCW motors is specifically dealt with. Several stator space MMF harmonic reduction techniques are discussed and compared, including multi-layer winding, multiple *m*-phase winding, two-slot pitch winding, and offset stator method. The methods such as multi-layer winding and multiple *m*-phase winding that can reduce or cancel sub-harmonics and keep the concentrated winding characteristics cannot restrain the parasitic harmonics. The two-slot pitch winding method can reduce or cancel all unwanted harmonics but moves away from the simple concentrated winding. The offset stator method can eliminate any selected harmonics but requires two stators and so is normally only easy to be implemented in linear motors and axial-flux motors. All this confirms that new methods to reduce the stator MMF harmonics without sacrificing the concentrated winding and structure characteristics for FSCW motors are needed.

Finally, the motor topologies for different applications concerned in this thesis are identified. First, the IPM motor with novel FSCW configuration featuring reduced stator MMF harmonic is identified for traction motor application. Second, the SPM motor with conventional FSCW configuration is identified for direct-drive EMA motor application.

Chapter 4

Generalized FSCW Design Method to Reduce Stator MMF Harmonics

This chapter deals with the significant stator space MMF harmonics issue in the FSCW topologies. A generalized FSCW design method with reduced stator space MMF harmonics will be proposed using a winding shifting concept. This will be based on a novel single-layer FSCW topology in which the two opposite coils of each phase are distributed adjacently. It is worth noting that unlike the existing winding shifting method in Section 3.3.4 which requires a two-slot pitch winding, non-overlapping or concentrated winding characteristics can be kept in the proposed method.

4.1   Stator space MMF harmonics issue

Figure 4.1 depicts the phase distribution and flux contours (with only phase C fed with current) of a 12S-14P FSCW motor with both SL and DL winding. The flux path in the motor with a SL winding must be closed through a long flux path across the half of the circumference since the two opposite coils per phase are on each side of the circumference. This is the inherent reason for the significant 1st harmonic in the conventional SL winding motor. For the DL configuration, the flux path can be closed by the adjacent coils owing to the two adjacent opposite coils of each phase. This can also be observed from their normalized MMF harmonic distributions in Figure 4.2.

The 7th harmonic is the main working or synchronous harmonic, and the rest are unwanted or asynchronous harmonics.

(a) SL winding   (b) DL winding
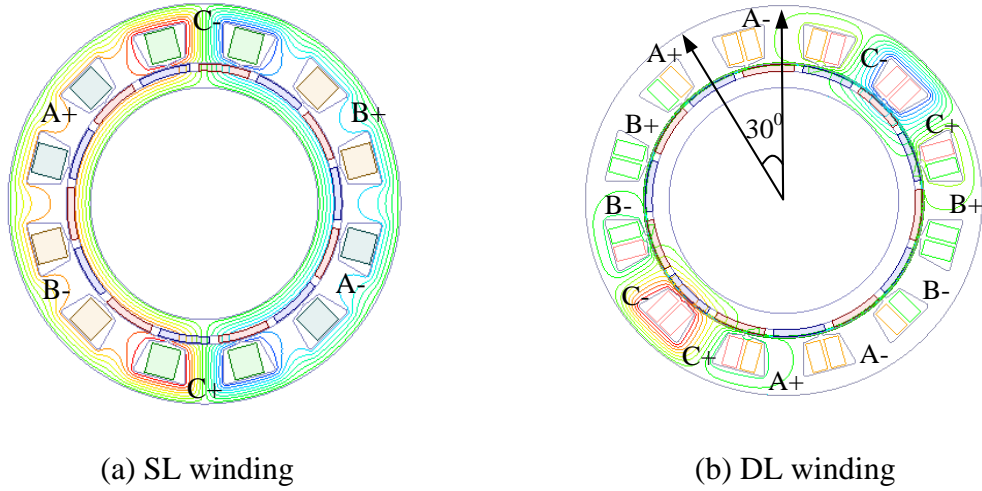
Figure 4.1 Conventional 12S-14P FSCW motor
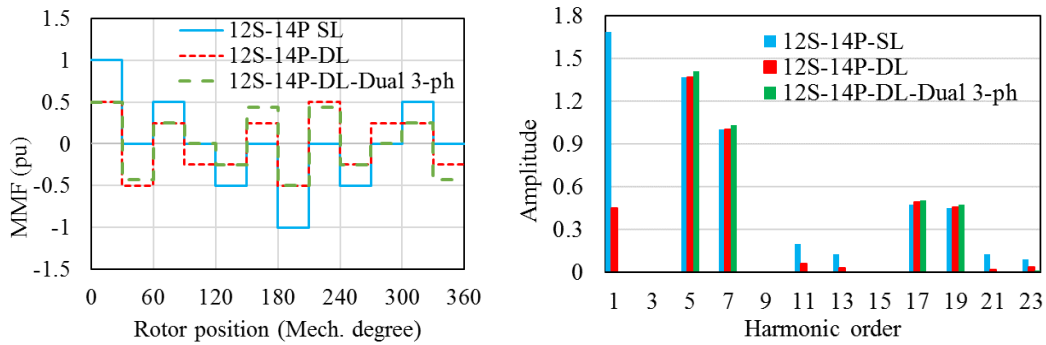
Figure 4.2 Stator MMF characteristics of 12S-14P FSCW motor

The MMF distribution of the 12S-14P FSCW motors with conventional SL and DL winding can also be expressed as Fourier series by using winding function method.

For a 12S-14P FSCW SL motor,

$$F(\theta, t) = \sum_{v=1,-5,7}^{\infty} \frac{6NI}{v\pi} \sin\left(\frac{v\pi}{12}\right) \sin(v\theta - \omega t) \qquad (4.1)$$

For a 12S-14P FSCW DL motor,

$$F(\theta, t) = \sum_{v=1,-5,7}^{\infty} \frac{6NI}{v\pi} \sin\left(\frac{v\pi}{12}\right) \sin\left(\frac{v\pi}{12}\right) \sin\left(v\theta - \omega t - \frac{v\pi}{12}\right) \qquad (4.2)$$

where v is the harmonic order, N is the number of conductors per slot, I is the current amplitude, θ is the space angle, and ω is the angular speed.

A dual 3-phase winding can be used to cancel out the 1st harmonic for the DL configuration [118]. Except for 1st sub-harmonic, the parasitic harmonic which occurs along with the working harmonic 7th, e.g., the 5th harmonic, is also undesirable and its amplitude is comparable to the main working harmonic.

These undesirable stator MMF harmonics may result in high iron losses, localized saturation, and unbalanced magnetic force. Therefore, it is necessary to develop a solution to deal with this issue, which will be presented in the next sections.

4.2 Proposed FSCW design method to reduce stator MMF harmonics

This section presents a FSCW design method to reduce stator MMF harmonics for FSCW motors based on the winding shifting concept. As discussed in Section 3.3.2.1, an appropriate shift angle is required for elimination or significantly reduction of some undesirable stator MMF harmonics using winding shifting concept.

In order to provide an appropriate shift angle, a FSCW motor with novel SL winding topology is used [12][128]. Based on this, a FSCW topology with DL winding featuring reduced stator MMF harmonics can be achieved using winding shifting concept. This will be illustrated in the following sections.
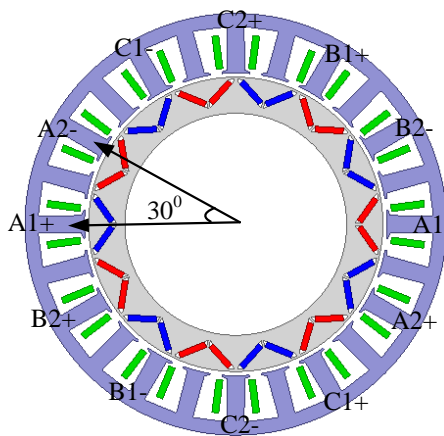
Figure 4.3 24S-14P motor with SL winding topology

4.2.1 Novel SL FSCW topology

Similar to the conventional DL winding configuration, a novel SL FSCW topology of 24 slots, 14 poles (24S-14P) was proposed [12][128], in which the two opposite coils per phase are adjacently distributed, as in Figure 4.3(a). The magnetic flux generated by one coil can be closed by the adjacent opposite coil that belongs to same phase and the significant 1st sub-harmonic can then be avoided, as shown in Figure 4.4.

(a) Stator MMF waveform   (b) FFT spectrum
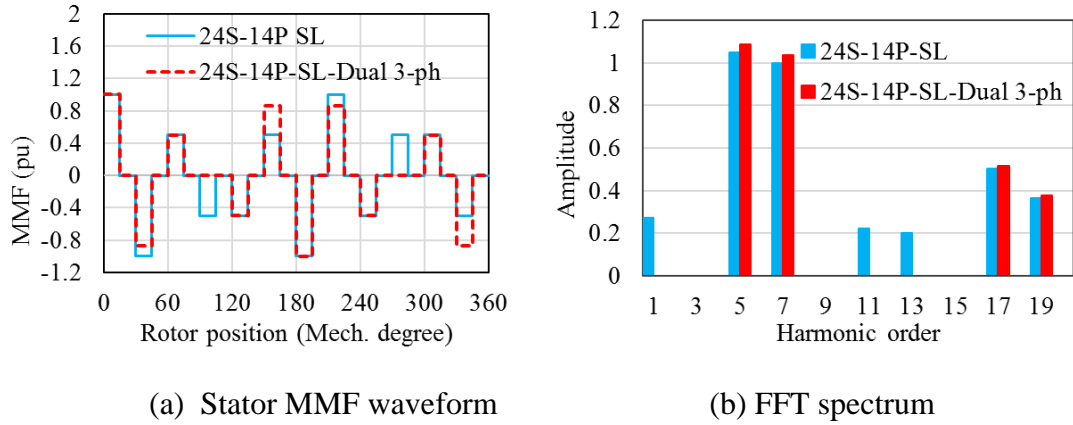
Figure 4.4 Stator MMF characteristics of a 24S-14P motor with SL winding

The MMF distribution of the 24S-14P motor with SL winding configuration may be expressed as Fourier series by using the winding function method.

$$F(\theta,t) = \sum_{v=1,-5,7}^{\infty} \frac{12NI}{v\pi} \sin\left(\frac{v\pi}{24}\right) \sin\left(\frac{v\pi}{12}\right) \sin\left(v\theta - \omega t - \frac{v\pi}{12}\right) \qquad (4.3)$$

The corresponding stator MMF harmonic distribution is illustrated in Figure 4.3 (b). This harmonic distribution is similar to that of a conventional 12S-14P motor with DL winding, but the amplitude of the 1st sub-harmonic is significantly reduced from 1.7 pu to 0.31 pu compared to a 12S-14P motor with conventional SL FSCW design.

Since the slot mechanical angle is 15^{0} (360^{0}/24), the electric angle difference between the vectors of the two opposite coils in each phase, e.g. A1+ and A2- in Figure 4.3, is 30^{0} (2*7*15^{0}-180^{0}). A dual 3-phase winding set (A1B1C1& A2B2C2) may be adopted with phase shifting to each other in time by 30^{0}, as depicted in Figure 4.5. Thus, the resulting MMF can be written as

$$F_d(\theta, t) = \sum_{v=1,-5,7}^{\infty} v_{dv} \sin\left(v\theta - \omega t - \frac{v-1}{12}\pi\right) \tag{4.4}$$

$$v_{dv} = \frac{12NI}{v\pi} \sin\left(\frac{v\pi}{24}\right) \sin\left(\frac{v-1}{12}\pi\right) \tag{4.5}$$

where v_{dv} is the amplitude of kth space harmonic for the motor with dual 3-phase winding configuration.
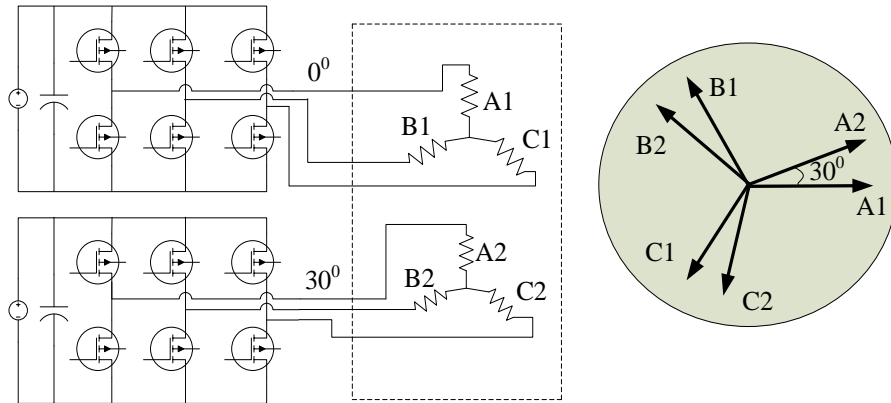
Figure 4.5 Dual 3-phase with two converters

In this case, compared to equation (4.3), it can be observed that the factor of sin $(k\pi/12)$ in (4.3) is replaced by sin $((v\text{-}1)\pi/12)$. When v equals to 1, that is, the 1st sub-harmonic, the corresponding amplitude v_{d1} is zero, which implies the 1st sub-harmonic has been eliminated. Moreover, all the harmonics with orders of $(12v\pm1)$ have been eliminated as they are the slot harmonics corresponding to the 1st sub-harmonic.

On the other hand, both the 5th and 7th harmonic have been slightly increased due to this additional factor. This increase also applies to the slot harmonics corresponding to these two harmonics such as 17th and 19th, etc. All of this agrees well with the observations from their MMF harmonic distributions in Figure 4.3. However, the parasitic harmonic of 5th still exists; a method using winding shifting will be proposed to reduce it in the next section.

4.2.2 Proposed DL FSCW winding design method

There are parasitic harmonics in the FSCW motors, e.g., 5th and 7th harmonic for a 12 slots 10/14 poles motor. They usually occur in pairs, and their winding factor is normally the same, making it very difficult to reduce only one of them.

In this thesis, by applying the winding shifting method into the 24S-14P motor with the novel SL FSCW design presented in the previous section, the parasitic harmonic can be significantly reduced or eliminated without using an overlapping winding. The process of the method is as below.

(a) 24S-14P-SL
(b) 24S-14P-SL (shifting by 105^0)
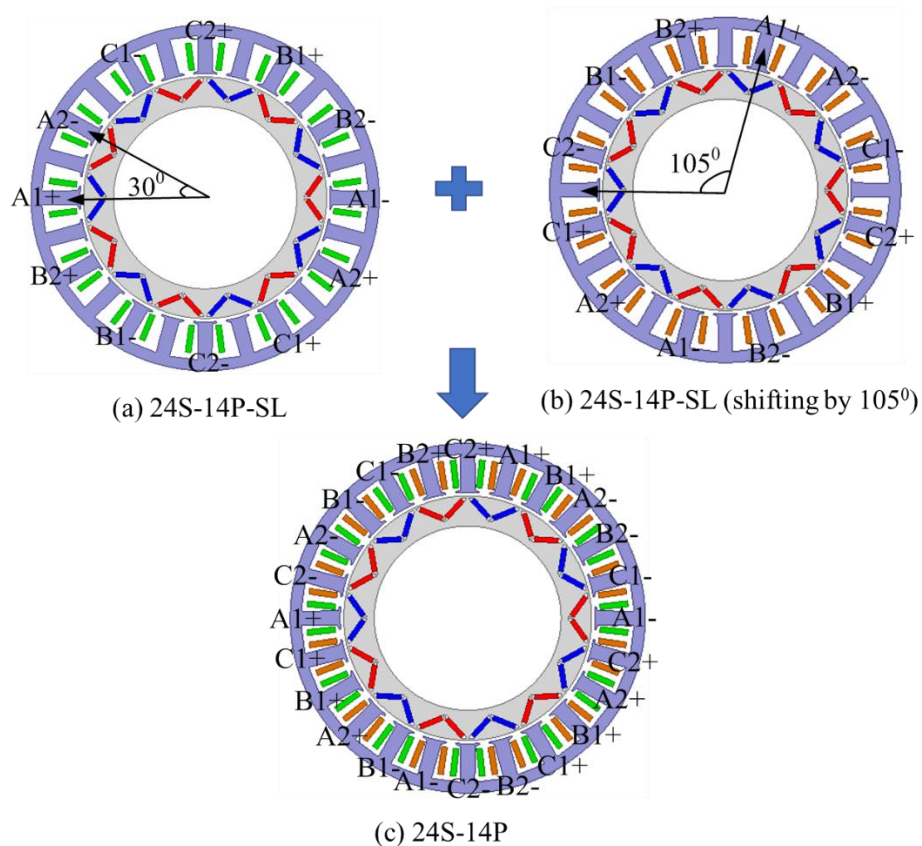
(c) 24S-14P

Figure 4.6 New configuration of 24S-14P with double-layer winding

- Doubling the slot numbers of a conventional 12S-14P FSCW motor, viz., going from 12S-14P to 24S-14P motor.

- A novel SL FSCW design configuration with two opposite coils of each phase distributed adjacently is applied to the new 24S-14P FSCW motor, as in Figure 4.6 (a).

- Another 24S-14P motor with the same SL FSCW design topology but with a mechanical shift angle over the previous 24S-14P motor can be achieved, as in Figure 4.6 (b).

- Combing these two motors, a novel 24S-14P motor with DL FSCW design is achieved, as in Figure 4.6 (c). Both the stator and rotor maintain the same while the coils of each phase in the two winding sets can be connected either in series or in parallel, e.g. A1 and A3 or A2 and A4, depending on the requirement.

One should note that different mechanical shift angles will lead to different winding configurations and consequently a different MMF harmonic contents. From (4.4), the resulting MMF for the combined 24S-14P motor with the proposed DL winding with a single 3-phase winding configuration can be expressed as

$$F(\theta, t) = \sum_{v=1,-5,7}^{\infty} k_{av} \frac{12NI}{v\pi} \sin\left(\frac{v\pi}{24}\right) \sin\left(\frac{v\pi}{12}\right) \sin\left(v\theta - \omega t - \frac{v\pi}{12} + \frac{v\alpha}{2}\right) \quad (4.6)$$

Similarly, if a dual 3-phase with 30^0 shift is used, the resulting MMF can be expressed as

$$F(\theta, t) = \sum_{v=1,-5,7}^{\infty} k_{av} \frac{12NI}{v\pi} \sin\left(\frac{v\pi}{24}\right) \sin\left(\frac{v-1}{12}\pi\right) \sin\left(v\theta - \omega t - \frac{v-1}{12}\pi + \frac{v\alpha}{2}\right)$$

$$(4.7)$$

where

$$k_{av} = \cos\left(\frac{v\alpha}{2}\right) \quad (4.8)$$

Compared to (4.5), one can find that an additional factor of k_{av} has been added to the amplitude of each MMF harmonic. This factor is the '*attenuation factor*', as defined in Section 3.3.2.1, which is added to each harmonic to be used as an index of the effect of harmonic reduction by winding shifting. It also essentially determines the distribution factor of each harmonic.

For a 24S-14P motor, the slot angle is 15^0, so the available shift angle is $j*15^0$. The attenuation factor for each harmonic versus the mechanical shift angle can be calculated using (4.7), and the variation of the attenuation factor of 1st, 5th, and 7th harmonics with respect to the mechanical shift angle α is plotted in Figure 4.7. It can

be observed that the best results, in terms of reducing unwanted stator MMF harmonics, can be achieved in the angular ranges shaded grey areas.
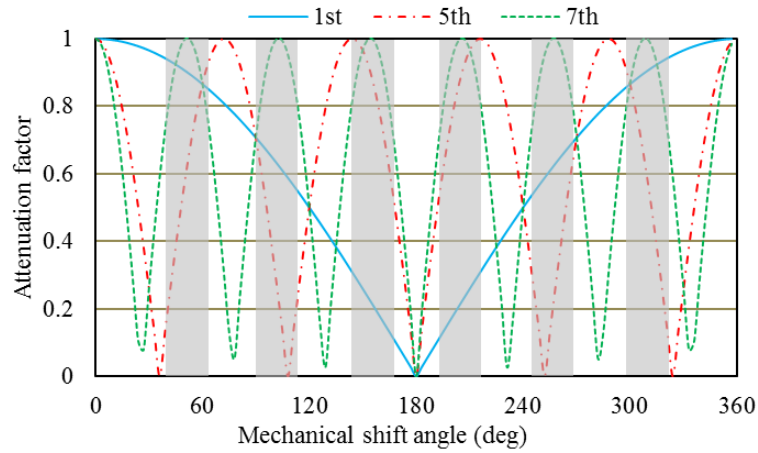
Figure 4.7 Attenuation factor of 1st, 5th, and 7th harmonic
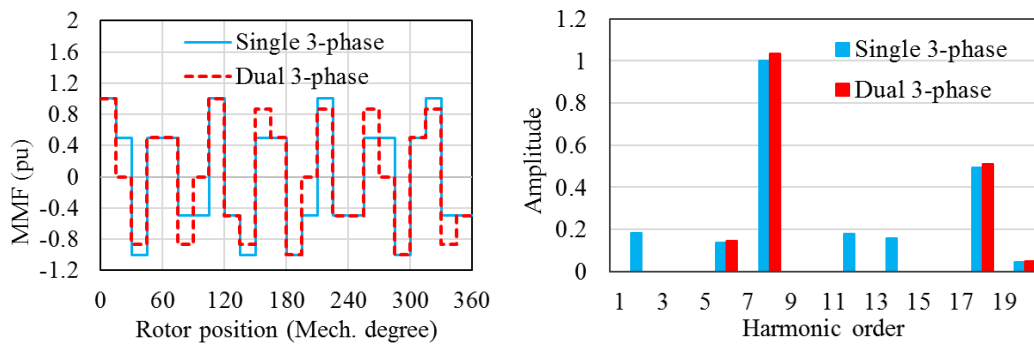
(a) Stator MMF waveform

(b) FFT spectrum

Figure 4.8 Stator MMF characteristics of the proposed 24S-14P DL motor

With a shift angle of 105^0, that is, 7 slots, the winding distribution and resulting MMF harmonic distribution are shown in Figure 4.8. One can find that the parasitic harmonic of 5th as well as $24k\pm5$ order harmonics are significantly reduced for the proposed 24S-14P motor with a single 3-phase DL winding configuration, while the 1st sub-harmonic is reduced to 0.19 pu. With the configuration of dual 3-phase DL winding with 30^0 shift, both the 1st and its corresponding slot harmonics are eliminated. All this is in accordance with the results from winding function method analysis.

Both the 1st and 5th harmonics principally impact the rotor losses. Therefore, the rotor losses can be significantly reduced with the proposed 24S-14P motor with DL

winding. Reducing the MMF harmonics will also decrease unbalanced magnetic saturation and may improve the overload capability.

This winding layout uses the concept of winding shifting while keeping the concentrated or non-overlapping winding characteristics which is different from the existing winding shifting method in Section 3.3.4 that normally adopts two-slot pitch overlapping winding [112][122]. This method avoids physical contact between different coils and the high mutual-inductance, and so is preferable for ease of manufacturing and fault-tolerant electric drive systems.

However, the winding factor is lower due to the lower pitch factor compared to the conventional FSCW motors. For instance, the pitch factor for a 24S-14P motors is 0.793, while it is 0.975 for a 12S-14P motor. To achieve equivalent ampere turns, more coil turns should be used in the 24S-14P motor under the same current which will result in more copper loss. Due to the doubling of slot numbers, the end-winding length of the proposed 24S-14P motor is reduced. Moreover, the magnetic core is less saturated due to the reduced stator space MMF harmonics improving the overload torque capability. A larger reluctance torque could be produced if the proposed DL FSCW design is applied to an IPM or synchronous reluctance (SynRM) motor. These advantages would compensate the sacrifice attributing to its low winding factor.

4.2.3 Cancellation of parasitic harmonic

As can be seen from Figure 4.8, the 5th harmonic is not completely cancelled with either single 3-phase DL winding or dual 3-phase DL winding with 30^0 shift configuration, and this can also be observed by calculating the harmonic amplitude from expression (4.7). In fact, there is an electric phase shift between coil phasors of each phase in the first and second winding sets due to the mechanical shift angle α, as illustrated in Figure 4.9. If the shift angle α equals to 105^0 (7*15^0), both the phase shift between A1 and A3 and between A2 and A4 are 15^0. Thus, a possible winding solution for the combined 24S-14P with DL winding is using quadruple 3-phase winding sets, with phase shifting to each other by 15^0(π/24), viz. 0^0, 15^0, 30^0, and 45^0, as depicted in Figure 4.10. Therefore, the resulting MMF for the combined 24S-14P motor with quadruple 3-phase DL windings can be achieved as

$$F_d(\theta, t) = \sum_{v=1,-5,7}^{\infty} 2v_{dv}k_{av1} \sin\left(v\theta - \omega t - \frac{v-1}{12}\pi + \left(\frac{v\alpha}{2} + \frac{\pi}{24}\right)\right) \quad (4.9)$$

$$k'_{av} = \cos\left(\frac{v\alpha}{2} - \frac{\pi}{24}\right) \quad (4.10)$$
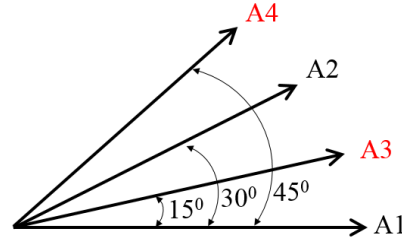
Figure 4.9 Coil phasors of phase A for the proposed 24S-14P DL motor
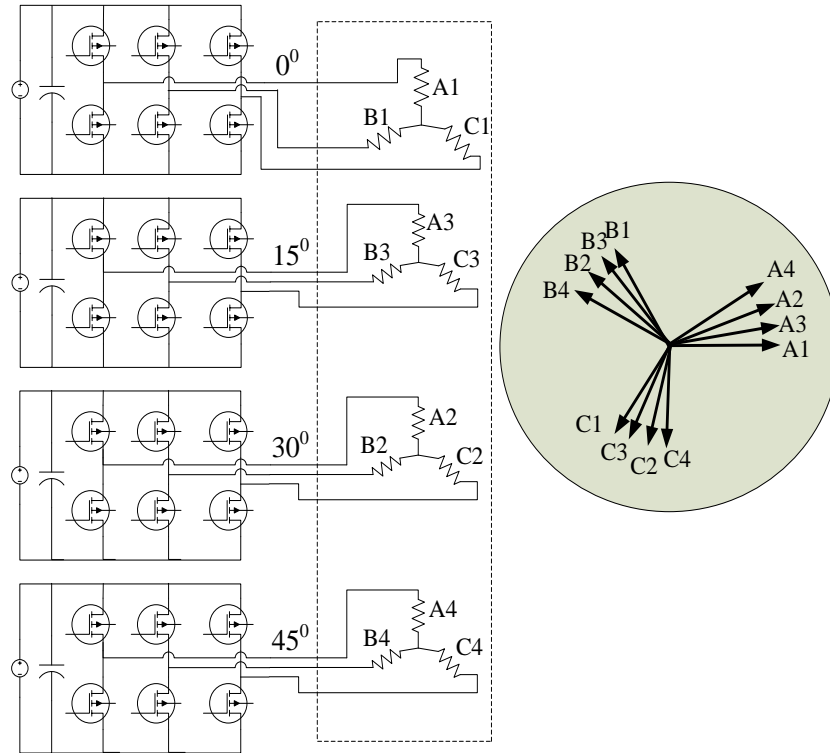
Figure 4.10 Quadruple 3-phase winding system

The attenuation factor is now $\cos\left(\frac{k\alpha}{2} - \frac{\pi}{24}\right)$, with an additional phase shifting of $\pi/24$ (15^0) in it. When v is 5, the attenuation factor of the 5th harmonic is zero, which can easily be calculated using (4.10). It is also the case for all the $24k\pm5$ order harmonics. This can also be observed from the MMF harmonic distribution in Figure

4.11, where both the 1st and 5th harmonic that mainly determine the rotor losses are eliminated. Only the working harmonic of 7th and its corresponding slot harmonics remain at significant level.
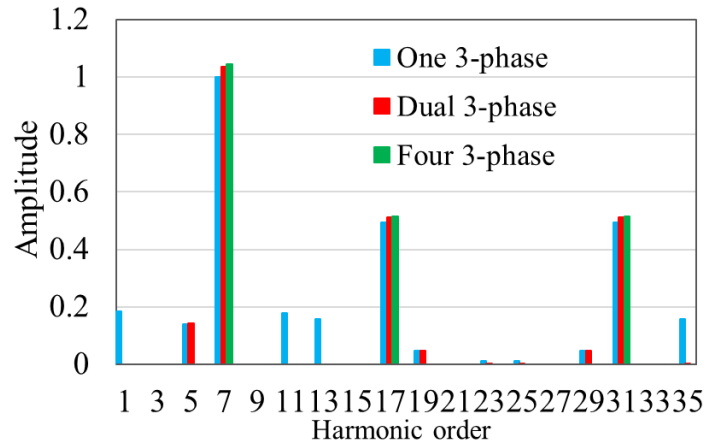
Figure 4.11 MMF spectrum of a 24S-14P DL motor with different windings
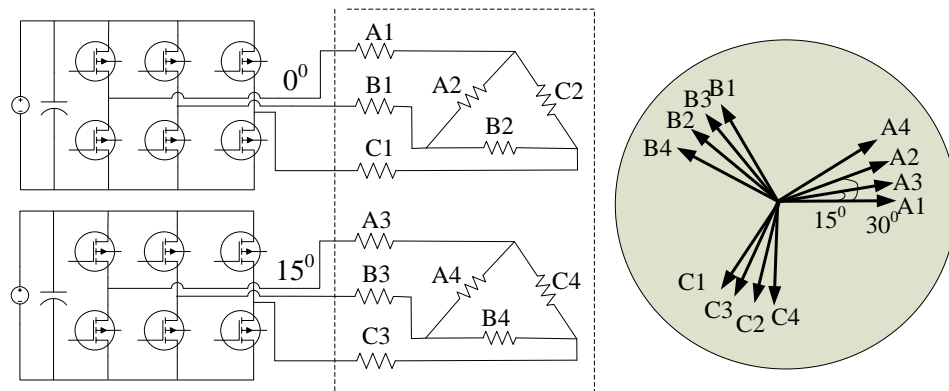
Figure 4.12 Proposed quadruple 3-phase winding system

With the quadruple 3-phase winding system in Figure 4.10, there are 12 terminals coming out, which adds complication and increases the number of power switches to 24, and thus is unlikely to be a good solution from the point of view of both cost and reliability. This thesis proposes a novel winding connection solution to implement the quadruple 3-phase winding system through Star-Delta winding connection to realize the 30^{0} shifting within electric machine. The proposed winding connection is shown in Figure 4.12, which has only 6 terminal connections, and requires only 12 power switches (dual 3-phase converters) to control the electric motor

with a quadruple 3-phase winding system (literally 12 phases). One should note that there is a ratio of $\sqrt{3}$ between current in the Star and in the Delta connected winding. Hence, the number of turns of the Delta connected winding should be $\sqrt{3}$ times of the turn numbers of the Star connected winding to offer a balanced electrical loading.

The same concept can be applied to other FSCW or ISDW motor with similar quadruple 3-phase winding topologies like 24 slots, 22 poles (24S-22P) and 24 slots, 2 poles (24S-2P) or quadruple 5-phase winding topologies. It should be noted that the ratio between turn numbers of stator and pentagon connected winding for 5-phase winding is 1.1756.

4.3 Performance study of proposed 24S-14P FSCW motor

4.3.1 Inductance and torque capability

After getting the phase distribution of the proposed 24S-14P FSCW motor, their winding function with SL and DL winding configurations can be obtained, as shown in Figure 4.13.

(a) 24S-14P-SL   (b) 24S-14P-DL
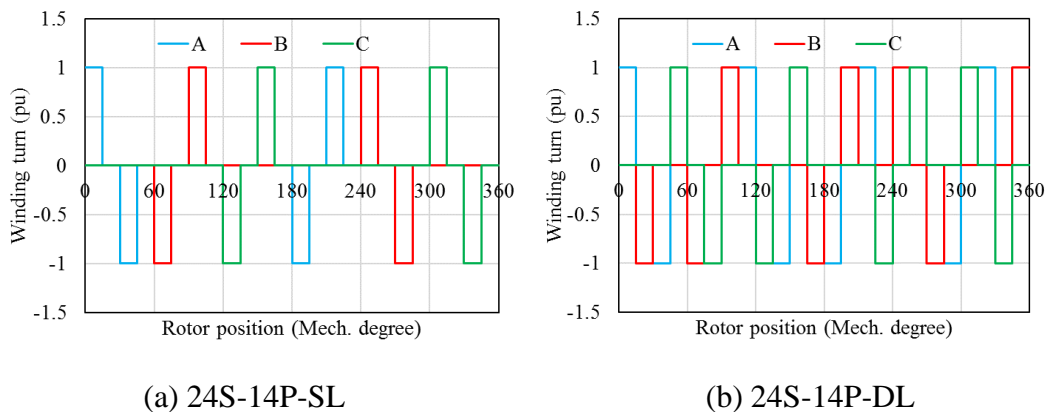
Figure 4.13 Winding function of proposed 3-phase 24S-14P motor

It can be observed from Figure 4.13(a) there is no overlap between different phase winding functions. Thus, no mutual coupling exists. It is expected that even with a salient rotor structure such as IPM or SynRM rotor, the mutual-inductance is negligible or nearly zero, which means the second harmonic component M_2 is zero as

well. Therefore, the reluctance torque capability is expected to be very limited, referring to the torque equation (4.11) that was derived in Section 3.1.5.

$$T_{em} = \frac{m}{2} P \left[\psi_f i_q + (L_2 + 2M_2) i_d i_q \right] = T_{pm} + T_r \qquad (4.11)$$

The flux distribution of the 24S-14P-SL motor with either SPM or IPM rotor under only phase A excitation is plotted in Figure 4.14. It is apparent that in both cases the main magnetic flux generated by phase A is not linked to other phase windings and it is only some leakage flux that may link with other phase windings, confirming the conclusion of no mutual coupling between phases obtained from the winding function method.

(a) SPM rotor   (b) IPM rotor
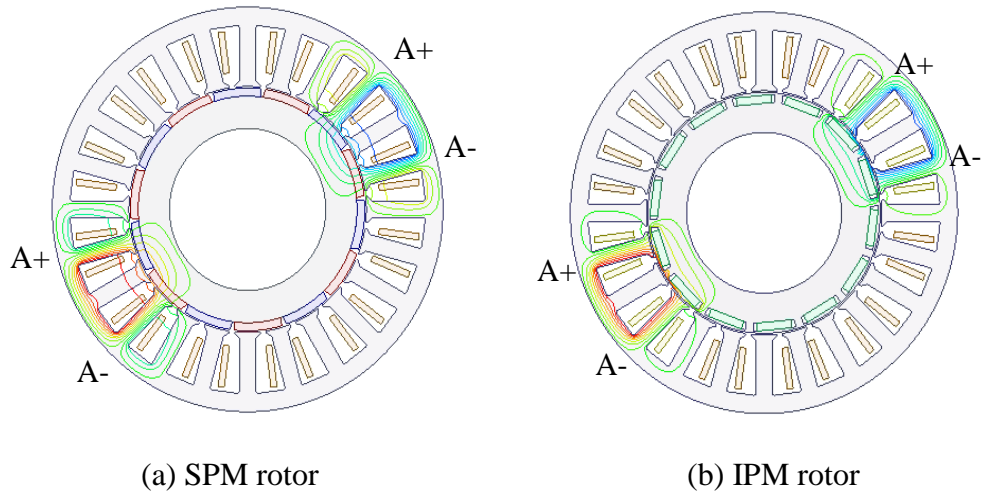
Figure 4.14 Flux distribution of 24S-14P-SL winding with Phase A excitation

(a) SPM rotor   (b) IPM rotor
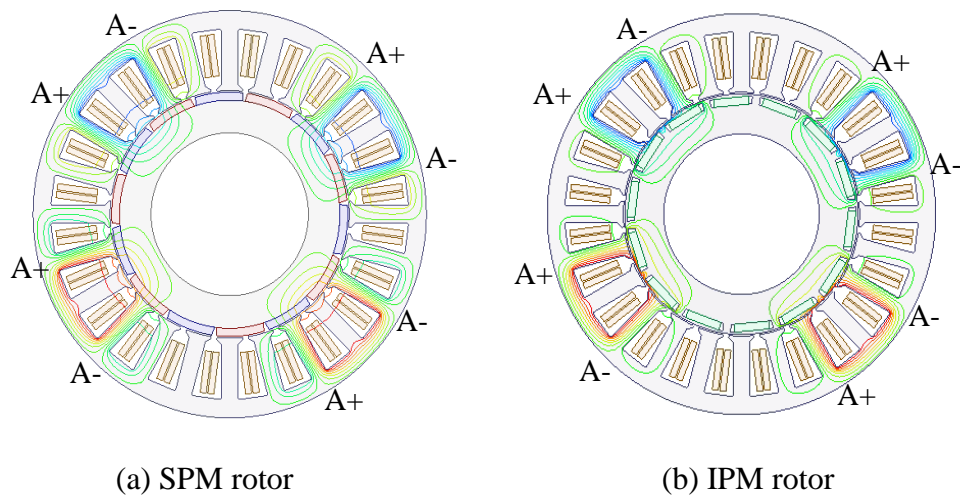
Figure 4.15 Flux distribution of 24S-14P-DL winding with Phase A excitation

In the case of the 24S-14P motor with DL winding, as in Figure 4.13 (b), there is also no overlap area between different phase windings. However, as the flux will follow a path with lowest magnetic reluctance, it is expected that there will be some flux components linking with adjacent coils of other phases, which is similar to the case of conventional FSCW with DL winding configuration like 12S-10/14P. This can also be observed from the flux distribution of 24S-14P-DL motor with SPM and IPM rotor under only phase A excitation in Figure 4.15. Most of the flux generated by one coil is closed by the corresponding opposite coil of the same phase, but a small portion of magnetic flux is linked to the adjacent coils of other phase windings. Thus, a considerable mutual-inductance is expected in the proposed 24S-14P-DL motor.

Table 4.1 summarizes the self- and mutual- inductance components for the proposed 24S-14P IPM motor with different layer windings calculated from FEM software. To have a fair comparison, the stator and rotor geometry, and turn numbers per phase are kept the same. It is worth noting that the airgap length is relatively low to mitigate the impact of slot leakage inductance. As expected, the mutual-inductance is zero for the 24S-14P motor with SL winding. In the case of 24S-14P-DL motor, the ratio between M_0 and L_0 is about 10%, while the ratio between M_2 and L_2 is 48.9%.

To compare the mutual-inductance of different FSCW configurations, the self- and mutual- inductance components of a conventional 12S-14P IPM motor and a 24S-14P IPM motor with 2-slot pitch winding (which is a FSDW topology) with phase distribution shown in Figure 4.16 [129], are calculated and summarized in Table 4.2 and Table 4.3, respectively. It can be observed that there is no significant mutual coupling between phases in the conventional 12S-14P motor with either SL or DL winding. For the 24S-14P IPM motor with 2-slot pitch winding, however, a significant mutual coupling can be seen by calculating the ratio between M_0 and L_0, which is 18.7 % and 12.7% for SL and DL winding, respectively. It should be noted that the M_2 is even higher than L_2 in the 24S-14P IPM motor with 2-slot pitch winding which is preferable in improving reluctance torque capability. In fact, these phenomena can also be observed from the winding function of these three winding design topologies in Figure 4.13, Figure 4.17(a), and Figure 4.17(b). No overlap in winding function between phases reprents no or negligible mutual coupling between phases, and the overlap area literally determines the mutual coupling level between phases.
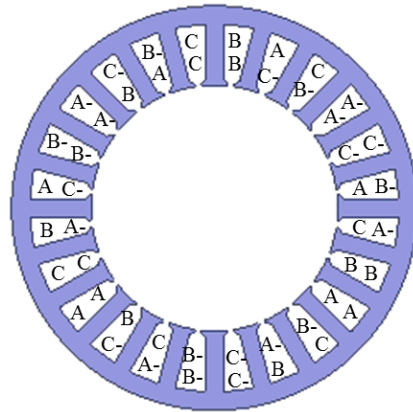
Figure 4.16 Phase distribution of 24S-14P-DL with 2-slot pitch winding [129]
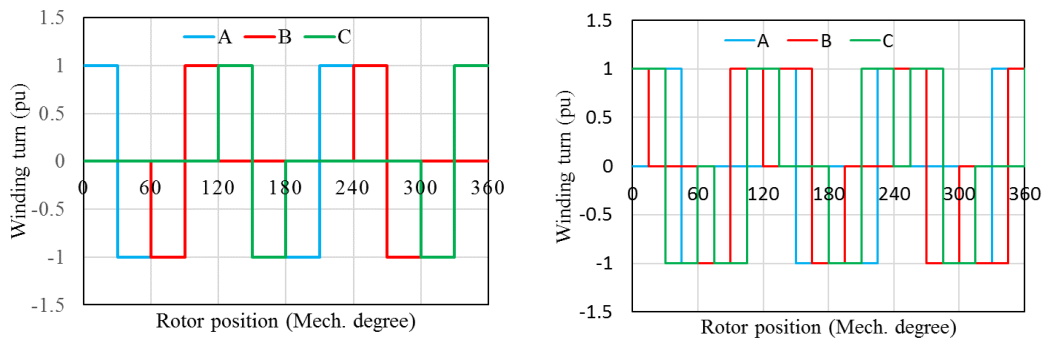
(a) 12S-14P-DL

(b) 24S-14P-2slot-DL

Figure 4.17 Winding function of 12S-14P and 24S-14P-2slot motor

Table 4.1 Inductance of proposed 24S-14P IPM motor

Winding topology	Self-inductance		Mutual-inductance	
	L_0 (mH)	L_2 (mH)	M_0 (mH)	M_2 (mH)
24S-14P-SL	7.286	1.619	0.004	0.014
24S-14P-DL	3.637	1.559	0.374	0.762

Table 4.2 Inductance of conventional 12S-14P IPM motor

Winding topology	Self-inductance		Mutual-inductance	
	L_0 (mH)	L_2 (mH)	M_0 (mH)	M_2 (mH)
12S-14P-SL	19.664	1.258	0.161	0.175
12S-14P-DL	10.793	2.088	0.401	0.526

Table 4.3 Inductance of 24S-14P IPM motor with 2-slot pitch winding

Winding topology	Self-inductance		Mutual-inductance	
	L_0 (mH)	L_2 (mH)	M_0	M_2 (mH)
24S-14P-2slot-SL	10.633	0.484	1.986	0.611
24S-14P-2slot-DL	5.622	1.139	0.714	1.488

Table 4.4 Comparison of *d-q* inductance difference

	12S-14P-DL	24S-14P-DL	24S-14P-DL with 2-slot pitch
L_2+2*M_2	3.140	3.083	4.115

(a) Average torque (b) Ripple torque
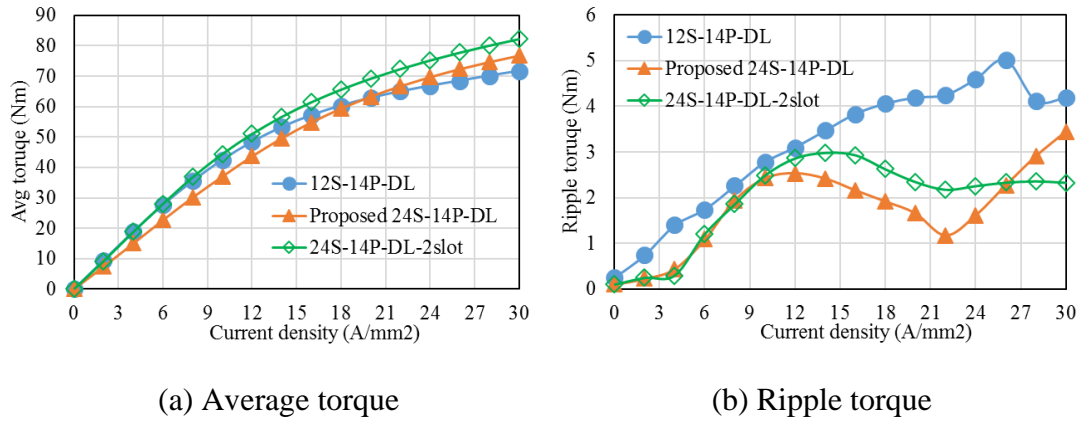
Figure 4.18 Torque comparison of three IPM motors

A comparison of the difference between *d*- and *q*- inductance, viz., (L_2+2*M_2), of these three designs with DL winding has been summarized in Table 4.4, which can be used to quantitively compare their reluctance torque capability. Clearly, the proposed 24S-14P-DL winding may have the same level of reluctance torque as the conventional 12S-14P-DL winding, while the 24S-14P-DL with 2-slot pitch winding is expected to exhibit a much higher reluctance torque.

The average torque and ripple torque under different current densities of the three IPM motors is depicted in Figure 4.18. It should be noted that a maximum torque per ampere (MTPA) control strategy is applied, which means the current phase advance angle is varied under different current densities. One can note that, the 12S-14P IPM motor features a higher average torque than the proposed 24S-14P-DL IPM

motor when current density increases until 20 A/mm^2, after which the proposed 24S-14P IPM motor has seen a higher average torque in spite of its lower winding factor; this is mainly because of the lower saturation effect and the higher reluctance torque due to the reduced stator MMF harmonics of the proposed 24S-14P IPM motor. The 24S-14P-DL-2 slot has the highest torque capability because of its reduced stator MMF harmonics and relatively high winding factor. A lower ripple torque can be seen in both the proposed 24S-14P-DL and 24S-14P-DL-2 slot IPM motor.
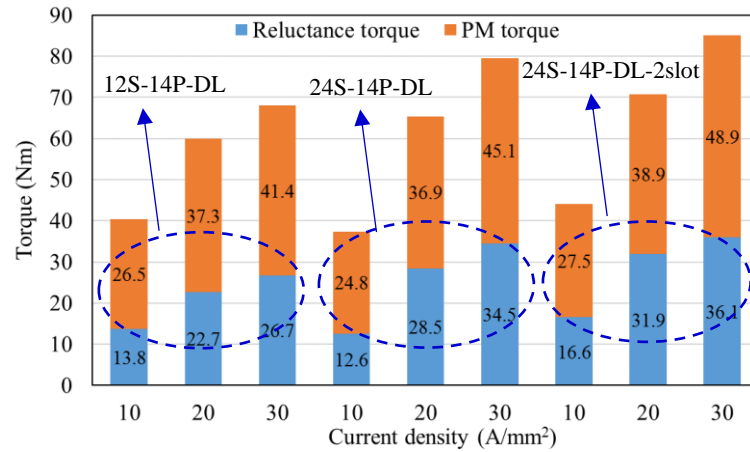
Figure 4.19 Torque breakdown of three IPM motors

Table 4.5 Comparison of average toque and reluctance torque capability

	Conventional 12S-14P-DL			Proposed 24S-14P-DL			24S-14P-DL with 2-slot pitch		
J (A/mm^2)	10	20	30	10	20	30	10	20	30
Total torque (Nm)	40.3	60.0	68.1	37.4	65.4	79.6	44.0	70.8	85.0
Reluctance torque (Nm)	13.8	22.7	26.7	12.6	28.5	34.5	16.6	31.9	36.1
Reluctance torque ratio (%)	34.3	37.8	39.3	33.7	43.6	43.4	37.6	45.0	42.4

Table 4.5 and Figure 4.19 summarize the output torque and reluctance torque capability of the IPM motor with different winding designs at maximum torque per ampere (MTPA) operating point. One can note that at a low current density of 10A/mm^2, the conventional 12S-14P and proposed 24S-14P-DL IPM motor have a similar level of reluctance torque capability; the 24S-14P-DL with 2-slot pitch

winding motor have the highest reluctance capability. Under the high current density of 20 or even 30 A/mm^2, the reluctance torque of the conventional 12S-14P IPM motor is very limited due to the magnetic saturation coming from the significant stator MMF harmonics; while both the proposed 24S-14P-DL and 24S-14P-DL with 2-slot pitch winding IPM motor have a higher reluctance torque capability due to the less saturated magnetic circuit attributing to the reduced stator MMF harmonics.
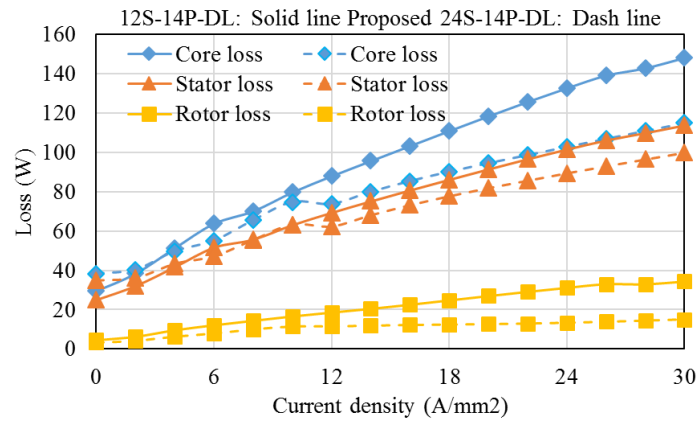
(a) Iron loss
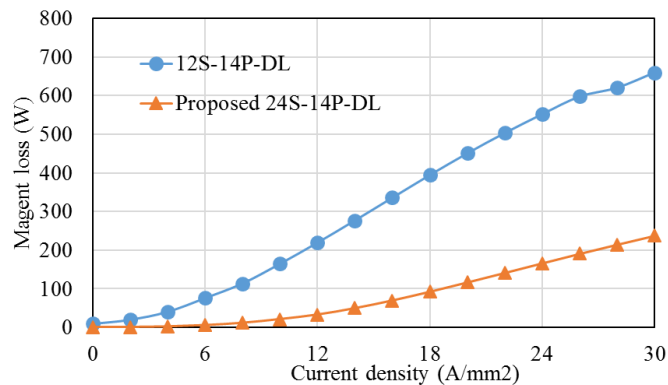
(b) Magnet loss

Figure 4.20 Losses comparison of two IPM motors

4.3.2 Loss characteristics

Figure 4.20 shows the iron loss and magnet loss at the speed of 1910rpm under different current densities. The core loss is the sum of stator and rotor iron loss. No segmentation is applied to the magnet. The stator iron loss is significant compared to rotor iron loss. The 12S-14P-DL IPM motor has a slightly lower stator iron loss and

core loss than the proposed 24S-14P-DL IPM motor when current density is lower than 10A/mm^2, after which the later one shows a lower stator iron loss. This can be explained by the fact that the IPM motor design exhibits a lower magnetic reluctance, which intensifies the effect of stator MMF harmonics on the stator iron losses. A much lower rotor core loss and magnet eddy current loss can be seen in the proposed 24S-14P-DL IPM motor under the heavy load conditions due to the reduced stator MMF harmonics. The magnet loss in the 12S-14P-DL IPM motor can be seen to be 8 times higher at a current density of 10 A/mm^2, and 4 times higher at 20 A/mm^2, respectively. One should note that the loss in the rotor is particularly difficult to dissipate.
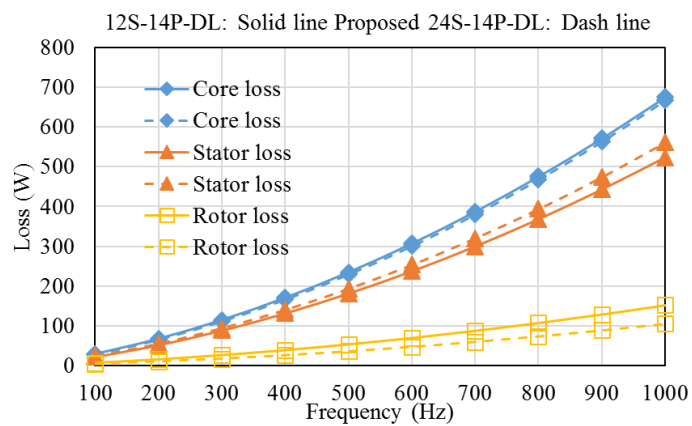
(a) 10A/mm^2
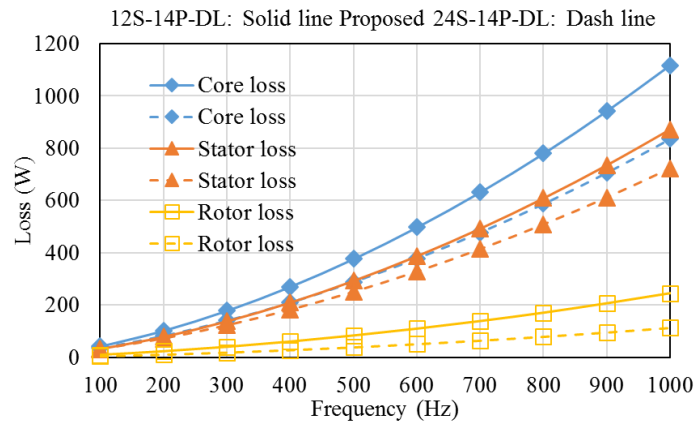
(b) 20A/mm^2

Figure 4.21 Iron losses characteristics of two IPM motors

The loss characteristics of both motors at 10 and 20 A/mm2 under different fundamental frequencies are plotted in the Figure 4.21 and Figure 4.22. Obviously, the

losses are proportional to the fundamental frequency. The proposed 24S-14P-DL IPM motor exhibits a higher stator iron loss under 10 A/mm^2. However, under heavy load of 20A/mm^2, it features a lower value both in core loss and magnet loss.

In all, the proposed 24S-14P IPM motor is competitive in output torque capability under heavy load conditions. Apart from this, it is effective in reducing torque ripple, saturation effect and rotor losses especially in the high speed heavy load conditions where the iron loss and magnet eddy current loss are significant concern.
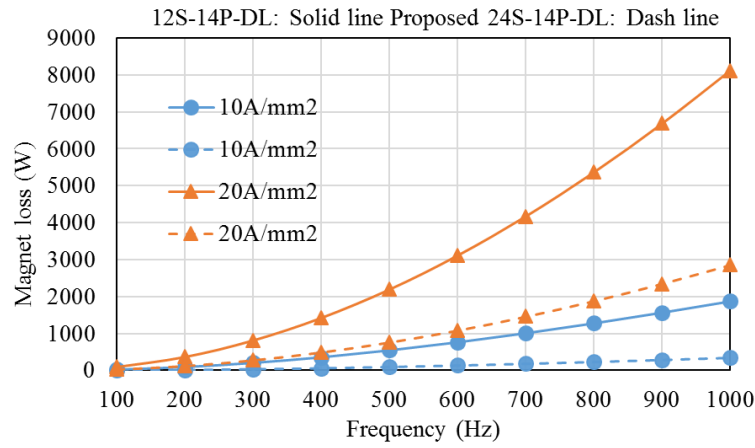
Figure 4.22 Magnet losses characteristics of two IPM motors

4.3.3 Radial magnetic force characteristics

The radial magnetic force density can be determined according to the Maxwell's stress method [130], as expressed in (4.12).

$$f_r = f_{rr} - f_{rt} = \frac{B_r^2}{2\mu_0} - \frac{B_t^2}{2\mu_0}$$ (4.12)

where B_r and B_t represents the radial and tangential airgap flux density, respectively.

Generally, the airgap flux density can be expressed as

$$B_h = \sum_v^\infty B_{h,v}\cos{(v\theta - \omega_{h,v}t - \varphi_{h,v})}$$ (4.13)

where h denotes r or t.

By substituting (4.13) into (4.12), the expression of radial force density contributing from radial flux density B_r can be deduced as

$$f_{rr}(\theta, t) = \frac{1}{2\mu_0} \sum_{v}^{\infty} B_{r,v}{}^2 \cos^2(v\theta - \omega_{r,v}t - \varphi_{r,v})$$

$$+ \frac{1}{2\mu_0} \sum_{v}^{\infty} \sum_{v'}^{\infty} B_{r,v}B_{r,v'}\cos(v\theta - \omega_{r,v}t - \varphi_{r,v})\cos(v'\theta - \omega_{r,v'}t - \varphi_{r,v'}) \quad (4.14)$$

then it can be written as

$$f_{rr}(\theta, t) = \frac{1}{4\mu_0} \sum_{v}^{\infty} B_{r,v}{}^2 \left[1 + \cos(2v\theta - 2\omega_{r,v}t - 2\varphi_{r,v})\right]$$

$$+ \frac{1}{4\mu_0} \sum_{v}^{\infty} \sum_{v'}^{\infty} B_{r,v}B_{r,v'} \left[\cos\left((v + v')\theta - (\omega_{r,v} + \omega_{r,v'})t - (\varphi_{r,v} + \varphi_{r,v'})\right)\right]$$

$$+ \frac{1}{4\mu_0} \sum_{v}^{\infty} \sum_{v'}^{\infty} B_{r,v}B_{r,v'} \left[\cos\left((v - v')\theta - (\omega_{r,v} - \omega_{r,v'})t - (\varphi_{r,v} - \varphi_{r,v'})\right)\right] \quad (4.15)$$

The expression of radial force density contributing from tangential flux density B_t is in similar form to (4.15).

(4.15) shows two kinds of harmonic force components. The frequencies of the first ones are two times higher than the frequencies of the corresponding airgap magnetic flux components; the frequencies of the second ones are sum and difference of the frequencies of the airgap magnetic flux components.

The general form of the radial magnetic force density in the airgap can be written as

$$f_r(\theta, t) = \sum_{\eth}^{\infty} f_{r,\eth}\cos(\eth\theta - \omega_{\eth}t - \varphi_{\eth}) \quad (4.16)$$

where $\eth$ is the model number; $f_{r,\eth}$ is the force component amplitude; $\omega_{\eth}$ represents the angular velocity and $\varphi_{\eth}$ represents the corresponding spatial angle.

The comparisons of airgap flux density including radial (B_r) and tangential (B_t) components for the two IPM motors, i.e., 12S-14P-DL and proposed 24S-14P-DL, under both no-load and load condition (MPTA @10A/mm^2) are plotted in Figure 4.23. Under no-load condition, the conventional 12S-14P-DL IPM motor has 5th and 19th harmonics which are the slot harmonics of the 7th harmonic in the rotor MMF harmonics, but these two harmonics do not exist in the proposed 24S-14P-DL motor.

Under load condition, the stator MMF harmonics are generated; as expected, the 5th and 19th harmonic are significantly lower in the proposed 24S-14P-DL motor.

(a) B_r under no-load

(b) B_r under load

(c) B_t under no-load

(d) B_t under load

(e) FFT spectrum of B_r

(f) FFT spectrum of B_t
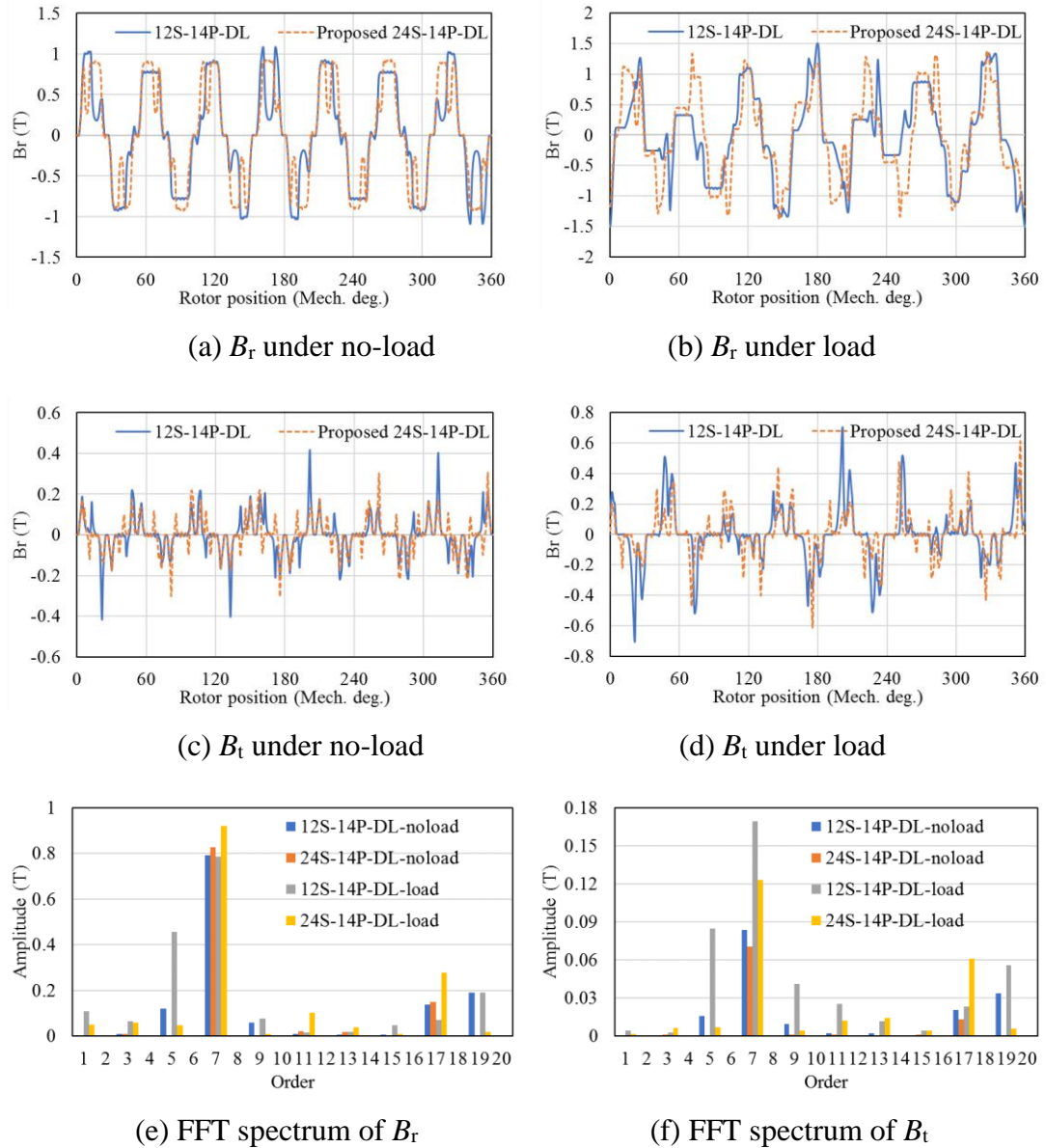
Figure 4.23 Comparison of flux density of two IPM motors

Figure 4.24 shows the radial magnetic force density in the airgap under both no-load and load condition (MPTA @10A/mm²). The radial magnetic force density contains only harmonics with even orders. This is due to the interaction of the odd order harmonics in the airgap magnetic field. Under no-load condition, the 12th and 16th order radial force density harmonics are almost cancelled in the proposed 24S-14P-DL motor due to elimination of 5th and 19th harmonic in no-load airgap flux

density, compared to the 12S-14P-DL IPM motor. Under load condition, it can be observed that for the proposed 24S-14P-DL motor the 2nd and 12th order radial force density harmonics are significantly reduced by 92% and 90%, respectively, compared to the 12S-14P-DL IPM motor; this is due to the significant reduction of 5th and 19th harmonic in stator MMF harmonics. However, the 4th and 10th of airgap radial force density are slightly increased.

The radial force essentially acts on the stator core and causes deformation and vibration. Normally, the deformation amplitude is inversely proportional to δ^4 [131]. Thus, the lower order radial force is more detrimental. Having less lower order harmonics helps reduce vibration. Therefore, it can be confirmed that the proposed 24S-14P-DL IPM motor would have comparatively reduced vibration and noise.

(a) Waveform at no-load   (b) Waveform at load

(c) FFT spectrum at no-load   (d) FFT spectrum at load
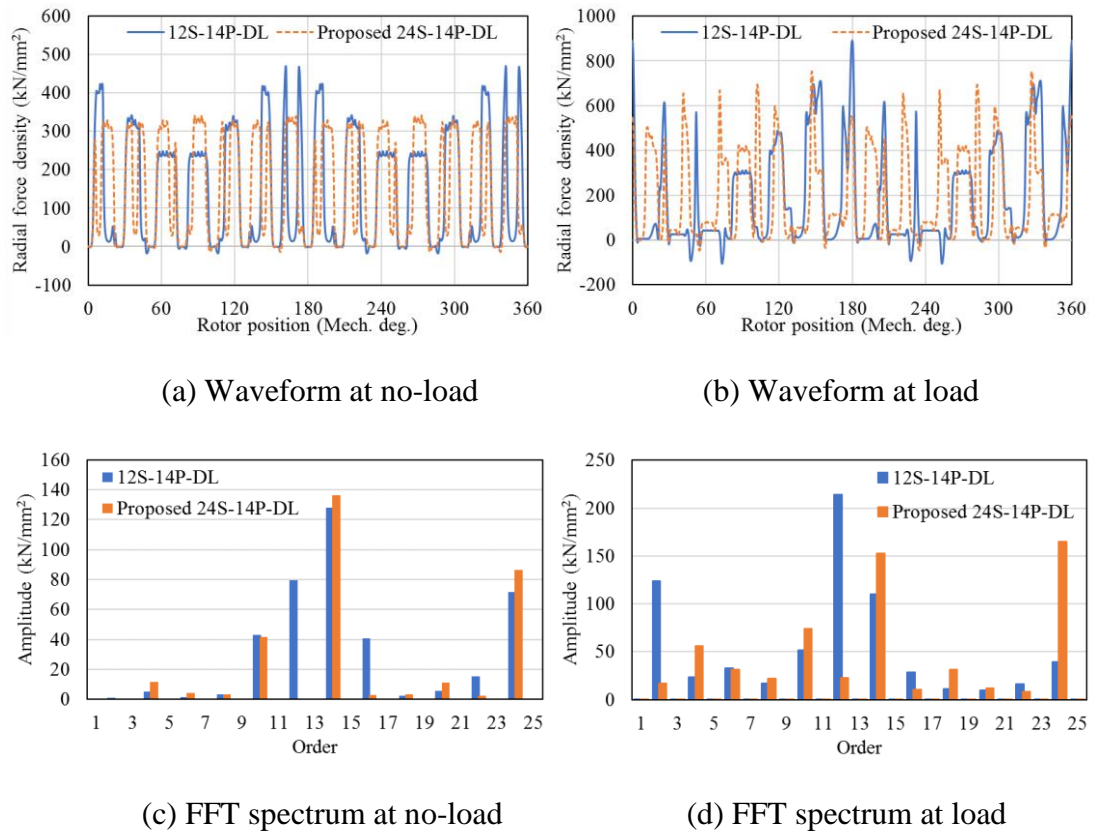
Figure 4.24 Comparison of radial force density of two IPM motors

4.4 Generalization of proposed FSCW design method

With the concept of winding shifting based on the novel SL winding topology in Section 4.2, a more general FSCW design method of significantly reducing or

cancelling the 1st and parasitic harmonic component for multi-phase FSCW motors with different slot/pole combinations can be achieved.

The proposed winding topology is based on doubling the slot numbers of the conventional FSCW motors. Therefore, all the slot-pole combinations that can use the proposed FSCW design method to reduce the stator MMF harmonics can be obtained by doubling the slot numbers of conventional FSCW motors while maintaining the pole numbers.

4.4.1 Three-phase FSCW Motors

The concept proposed in Section 4.2 can be applied to a conventional 9S-8/10P motor. Its coil distribution and FFT spectrum can be recalled from Figure 3.21, where the parasitic harmonics of 4th and 5th have a comparable amplitude. By doubling the slot numbers and making the three opposite coils per phase adjacently distributed, a single-layer 18S-8/10P can be achieved, as shown in Figure 4.25 (a).

By putting two 18S-10P SL winding motors together, with a specific mechanical shift angle over each other, a combined 18S-10P motor with DL winding can be achieved. Referring to Section 3.3.2.3, it is worth noting that there are two types of winding configurations due to the unequal numbers of positive and negative coils per phase [12]. For Type 1, both the first and second winding set are the same, while for Type 2, the phase distribution in the second winding set is opposite to the phase distribution of the first winding set.

(a) 18S-10P-SL   (b) 18S-10P-DL
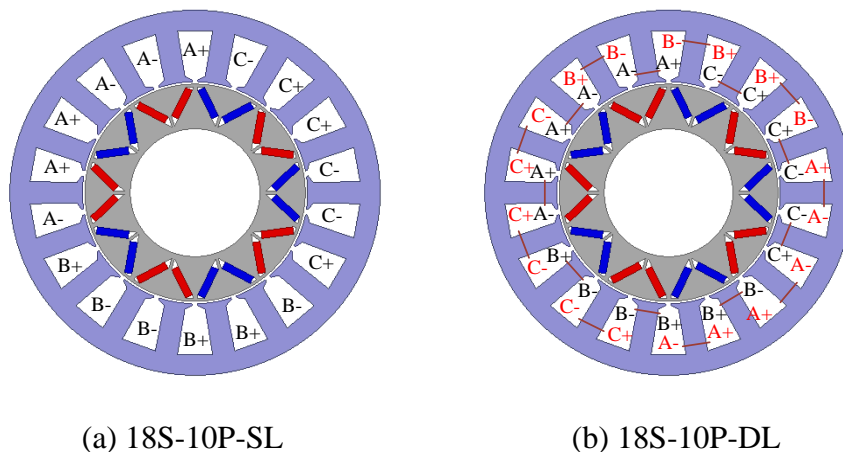
Figure 4.25 Proposed 18S-10P FSCW topology

(a) Type 1   (b) Type 2
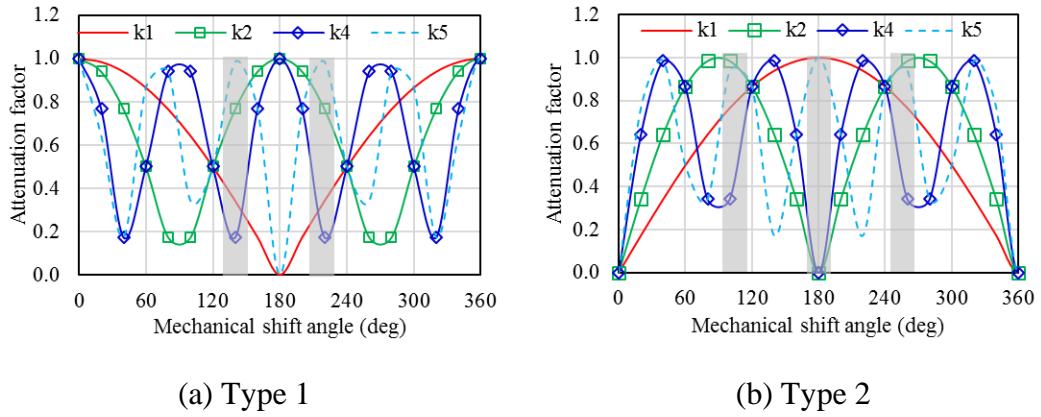
Figure 4.26 Attenuation factor of 1st, 2nd, 4th and 5th harmonic

Table 4.6 Attenuation factor of better shift angles for a 18S-8/10P motor

Type	α (degree)	slots	k_1	k_2	k_4	k_5
1	140	7	0.34	0.77	0.17	0.98
	220	11	0.34	0.77	0.17	0.98
2	100	5	0.77	0.98	0.34	0.94
	180	9	1	0	0	1
	260	13	0.77	0.98	0.34	0.94

Similarly, different shift angles result in different effects on the reduction of unwanted harmonics, and the attenuation factor of each harmonic can be calculated by using (4.7), as in Figure 4.26. Since the unwanted harmonics are 1st, 2nd, and 4th, in this case, the best shift angles in terms of reducing these harmonics while not having a considerably negative impact on the 5th harmonic are in the shaded areas in Figure 4.26. As the coils can only be shifted by a whole number of, all the applicable shift angles with their corresponding attenuation factor that give better results are summarized in Table 4.6. It is evident that the configuration of Type 1 with a shift angle of 180^0 is the best, eliminating 2nd and 4th harmonic and having no impact to the 1st and 5th; the corresponding phase distribution is depicted in Figure 4.25(b).

The MMF waveform and FFT spectrum of the 18S-10P with SL and DL windings are plotted in Figure 4.27. It can be observed that both the 2nd and 4th harmonic are eliminated and the 1st is not affected, which agrees well with the analysis.

The concept of multiple 3-phase winding configuration [117] can be used to cancel out the 1st sub-harmonic. As can be seen from their coil phasors in Figure 4.28, there are 6 coil phasors for each phase, and there is an angular difference between coil phasors per phase; thereby a triple 3-phase winding with 20^0 shift can be used in Figure 4.29 (b). With this triple 3-phase configuration, the corresponding MMF waveform and FFT spectrum are plotted in Figure 4.27 (b) and (c). Both 1st and 2nd sub-harmonics can be eliminated in either SL or DL case. Finally, the 18S-10P-DL motor with triple 3-phase features only 5th, 13th and 23rd harmonic, where the 13th and 23rd are the slot harmonics corresponding to working harmonic of 5th.

(a) 3-phase   (b) Triple 3-phase

(c) FFT spectrum
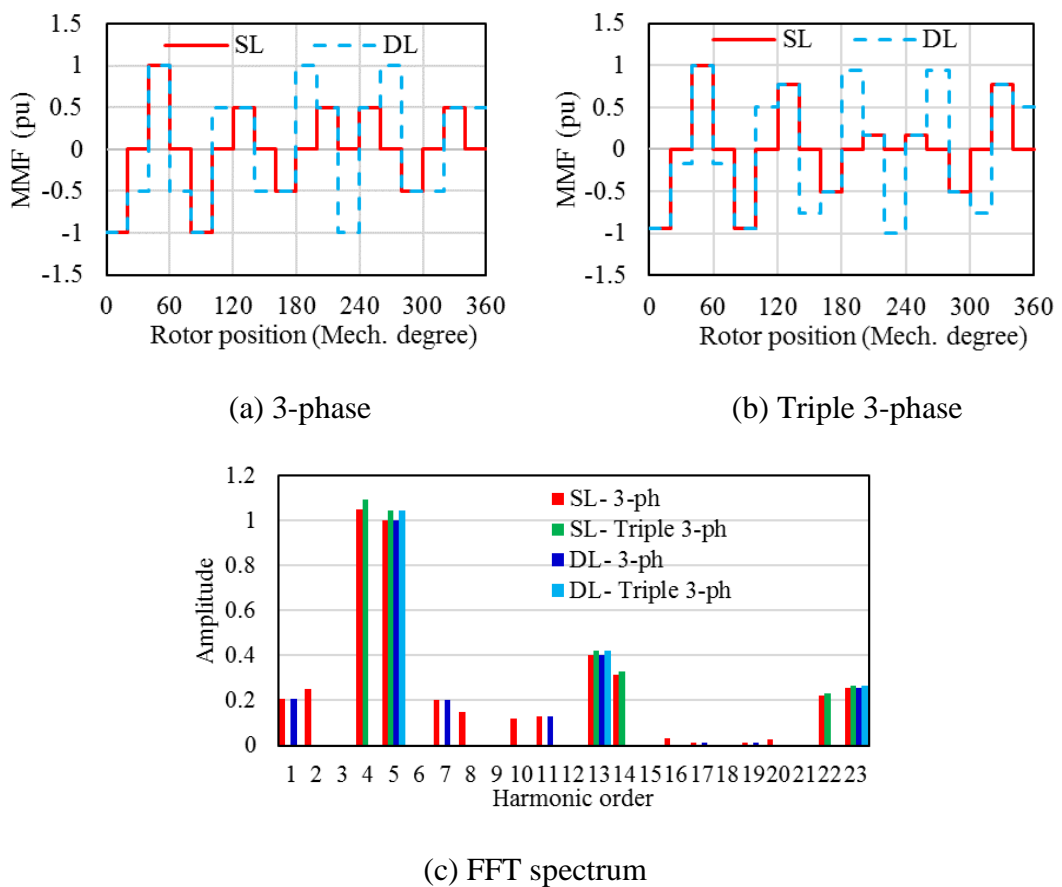
Figure 4.27 MMF comparison of a 18S-10P motor with SL and DL winding

Similarly, all the possible slot-pole combinations for three-phase motors which can adopt the proposed FSCW design method are summarized in Table 4.7. The maximum achievable winding factor is utilized to characterize the performance of each slot-pole combination. The winding factor is determined by the pitch factor and distribution factor, while pitch factor is determined by the slot numbers and pole

numbers, which means a close slot and pole numbers results in a higher winding factor. Thus, a higher pole number is preferred (underlined in Table 4.7) in terms of achieving a higher winding factor. It is worth noting that these proposed winding designs can also be applied to linear motors and induction motors, where harmonic cancellation is more important as they tend to generate parasitic torque from harmonics.
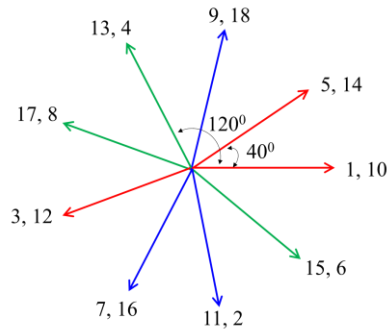
Figure 4.28 Coil phasors diagram of proposed 18S-10P-DL winding topology

(a) 3-phase   (b) Triple 3-phase with 20^0 shift
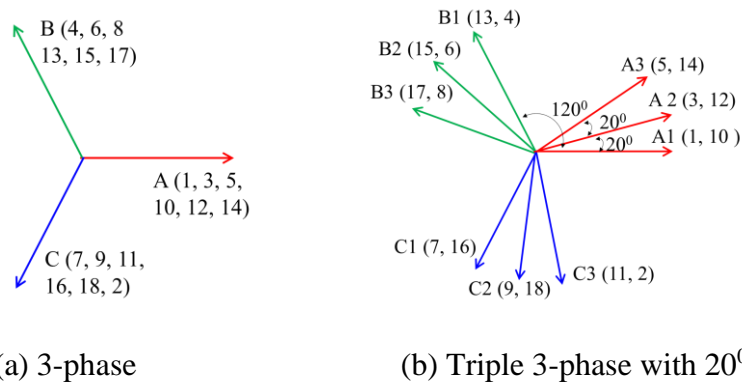
Figure 4.29 Multiple 3-phase configurations of proposed 18S-10P-DL winding

Table 4.7 Possible slot-pole combinations for three-phase FSCW Motor

Conventional slot-pole combinations	Proposed slot-pole combinations	Maximum winding factor
6S-4/8P	12S-4/8P	0.5/0.866
9S-8/10P	18S-8/10P	0.643/0.766
12S-10/14P	24S-10/14P	0.609/0.793
15S-14/16P	30S-14/16P	0.669/0.743
18S-16/20P	36S-16/20P	0.643/0.766

4.4.2 Multi-phase FSCW Motors

Following the same principle, all the applicable slot-pole combinations for the multi-phase FSCW motors such as four- and five- phase motors that use the proposed FSCW design method can be achieved, as summarized in Table 4.8 and Table 4.9, with preferable slot-pole combinations underlined. The slot-pole combinations in the tables can easily be extended to higher slot/pole numbers. The examples of a four-phase 16 slots, 10 poles (16S-10P) and a five-phase 20 slots, 12 poles (20S-12P) FSCW motor are described in Appendix A.1 and A.2.

Table 4.8 Possible slot-pole combinations for four-phase FSCW Motor

Conventional slot-pole combinations	Proposed slot-pole combinations	Maximum winding factor
8S-6/10P	16S-6/<u>10P</u>	0.556/<u>0.831</u>
16S-14/18P	32S-14/<u>18P</u>	0.634/<u>0.773</u>
24S-22/26P	48S-22/<u>26P</u>	0.659/<u>0.752</u>
32S-30/34P	64S-30/<u>34P</u>	0.672/<u>0.741</u>

Table 4.9 Possible slot-pole combinations for five-phase FSCW Motor

Conventional slot-pole combinations	Proposed slot-pole combinations	Maximum winding factor
5S-4/6P	10S-4/6P	0.556/<u>0.809</u>
10S-8/12P	20S-8/12P	0.634/<u>0.809</u>
15S-12/18P	30S-12/18P	0.588/<u>0.809</u>
20S-16/24P	40S-16/24P	0.588/<u>0.809</u>

4.5 Chapter Summary

This chapter proposed a generalized FSCW design method with reduced stator space MMF harmonics for electric motors using a winding shifting concept. This is based on a novel single-layer FSCW topology in which the two opposite coils of each phase are distributed adjacently. The method is illustrated by going from a 12S-14P to a 24S-14P motor. It does not require the overlapping two-slot pitch winding that normally used in the existing winding shifting method. In addition, when applied with multiple

m-phase windings, it can cancel out all unwanted harmonics except for the working harmonic and its slot harmonics.

The performance characteristics of the proposed 24S-14P FSCW IPM motor in terms of torque capability, losses, and radial magnetic force, are investigated and compared to the conventional 12S-14P FSCW motor. The comparison shows that with reduced stator MMF harmonics, the proposed 24S-14P FSCW IPM motor is less saturated and features higher reluctance torque capability and better over-load capability while keeping the non-overlapping or concentrated winding characteristics, despite of its low winding factor. A much lower rotor loss and magnet loss are also observed. On top of this, the proposed 24S-14P FSCW IPM motor would have comparatively less vibration and noise.

Generalized double-layer FSCW topologies with reduced stator MMF harmonics for different slot/pole combinations and different phase numbers have been summarized. The winding factors are calculated, and the preferable slot/pole combinations are given.

Although the proposed winding design topologies can reduce stator space MMF harmonics and thereby reduce rotor losses and improve overload capability, it is worth noting that their winding factors are generally lower compared to their conventional FSCW counterparts. Therefore, a trade-off must be made depending on the design requirements of the power, speed, electrical loading, thermal management, and overload capability, etc. In addition, these proposed winding design methods can be applied to other machine types, including linear motors and induction motors.

Chapter 5

Design and Analysis of a 24 Slots, 14 Poles FSCW IPM Motor

In the previous chapter, several fractional slot concentrated winding (FSCW) designs based on the proposed stator MMF harmonic reduction method have been presented. To evaluate the effect of the proposed winding designs with reduced stator MMF harmonics on the motor's performance, an IPM motor with the proposed 24 slots, 14 poles (24S-14P) FSCW topology will be designed and evaluated for an EV traction motor application, with focus on the torque capability and efficiency. Apart from this, the fault-tolerant capability of the proposed 24S-14P IPM motor with different configurations of dual 3-phase winding system will also be analysed under both healthy and fault conditions.

5.1   Design specification

This section defines the design specifications of the traction motor, as summarized in Table 5.1. Based on this, the torque-speed and power-speed characteristics of the IPM motor are shown in Figure 5.1.

An IPM motor with the proposed 24S-14P winding topology is designed, with the main geometry data summarized in Table 5.2. The B-H curve of the magnetic steel-DW270-35 is shown in Figure 5.2. The designed copper slot fill factor is 39.2%. Due

to the motor's short axial length, 3-D FEM is used to evaluate the EM performance and the FEA model is shown in Figure 5.3.

Table 5.1 Motor design specifications

Parameter	Data	Parameter	Data
Peak power (kW)	10	DC link voltage (V)	400
Rated power (kW)	7	Peak current (Arms)	60
Base speed (rpm)	1910	Peak current density (A/mm^2)	18
Peak speed (rpm)	6000	Rated current density (A/mm^2)	8.5
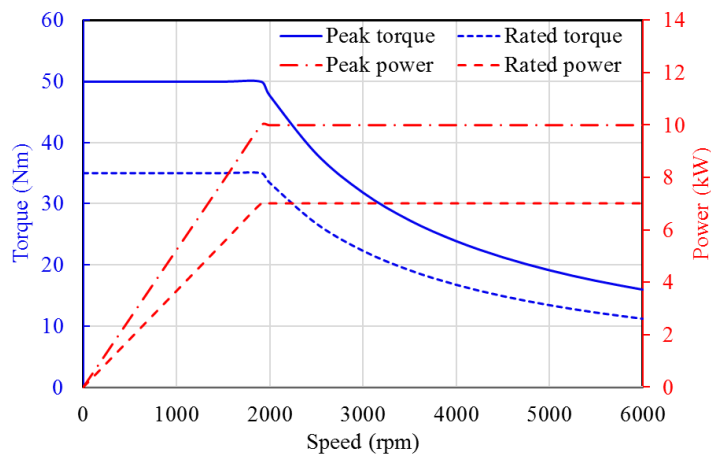
Figure 5.1 Torque-speed and power-speed envelopes against speed

Table 5.2 Main geometry data and specifictaion of IPM motor

Parameter	Data	Parameter	Data
Stator outer diameter (mm)	200	Stator core material	DW270-35
Stator inner diameter (mm)	121.6	Rotor core material	DW270-35
Stack length (mm)	40	Magnet material	N38SH
Airgap length (mm)	0.8	Peak current (Arms)	50
Magnet thickness (mm)	4	Rated current (Arms)	27
Magnet width (mm)	13.5	Peak torque (Nm)	50
Turns per coil	24	Rated torque (Nm)	35
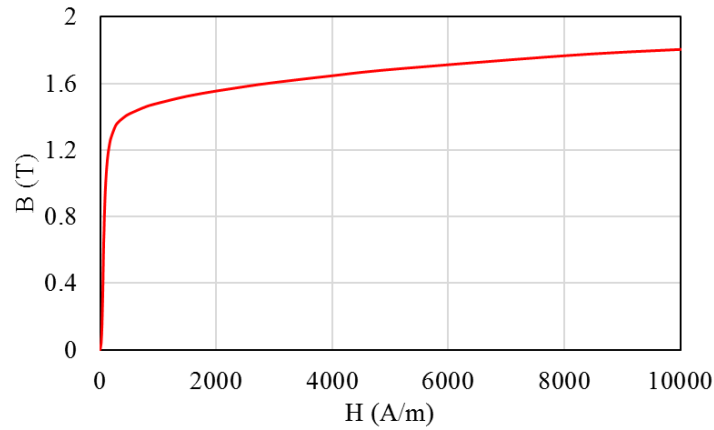
Figure 5.2 B-H curve of DW270-35
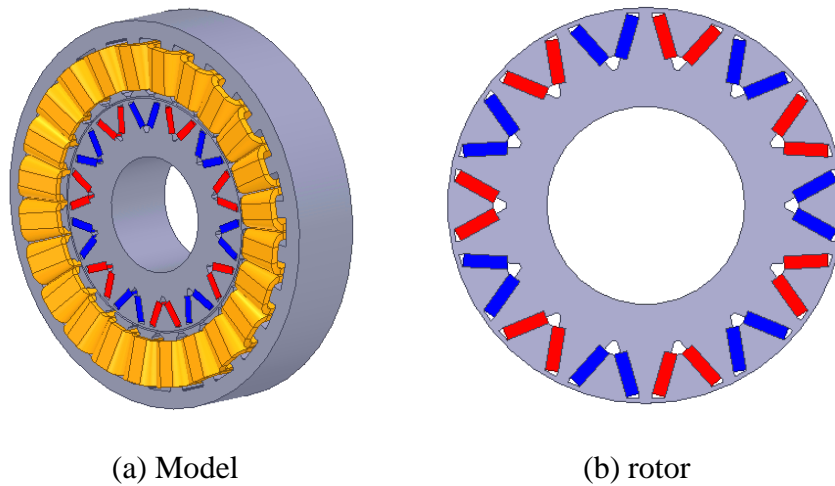
(a) Model   (b) rotor

Figure 5.3 FEM model of the proposed 24S-14P IPM motor

5.2   EM performance of proposed 24 slots, 14 poles IPM motor with single three-phase winding system

This section reports the general performance of the proposed 24S-14P IPM motor designed for an electric vehicle traction application. The EM performance with respect to the torque capability, saliency, as well as fault operation are analysed. A magnet temperature of 85ºC is assumed. This work will be used as a baseline for comparison with dual 3-phase winding configuration developed using the methods previously outlined.

5.2.1 No-load Performance

Figure 5.4 shows the back electromagnetic force (EMF) under no-load condition at a base speed of 1910rpm. A small 3rd harmonic exists, which provides an opportunity for improving output torque by injecting high-order (3rd) current harmonic [132]. Both 5th and 7th harmonics, which are the main contributor of torque ripple, are nearly negligible, thereby a low torque ripple can be expected in the proposed 24S-14P IPM motor.

The calculated cogging torque is plotted in Figure 5.5. It is obvious that the cogging torque is very small, with peak to peak value of 57mNm, which is negligible compared to the rated and peak torque.

(a)Waveform   (b) FFT distribution
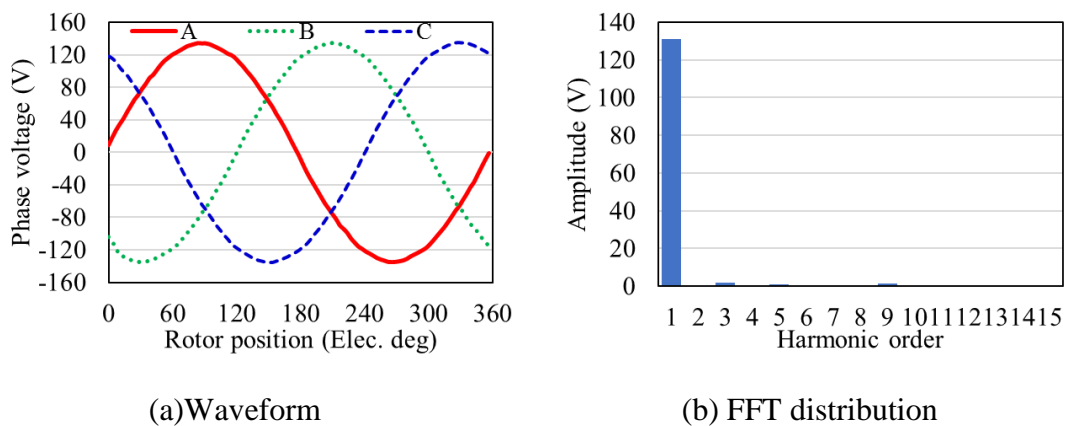
Figure 5.4 No-load back EMF at 1910 rpm
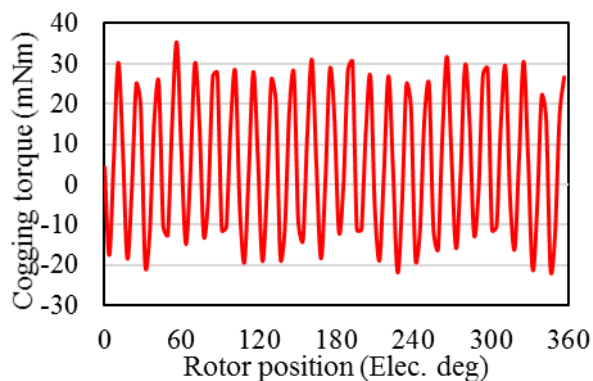
Figure 5.5 Cogging torque waveform

5.2.2 Torque capability

By imposing a balanced three-phase fundamental current into the armature winding, a steady-state EM torque can be generated. Figure 5.6 shows the calculated instantaneous EM torque waveform of the proposed 24S-14P IPM motor in both the rated and peak load condition at base speed. As can be seen, the motor can generate 35 Nm of rated torque and 50 Nm of peak torque, where the corresponding torque ripple is 3.3% and 5.9%, respectively. It should be noted that no additional mechanical methods such as stator and rotor skewing are used to reduce the torque ripple. The slightly higher torque ripple in the peak load condition is due to the saturation effect. However, the torque ripple may be reduced in the dual 3-phase winding configurations with different shift angles.
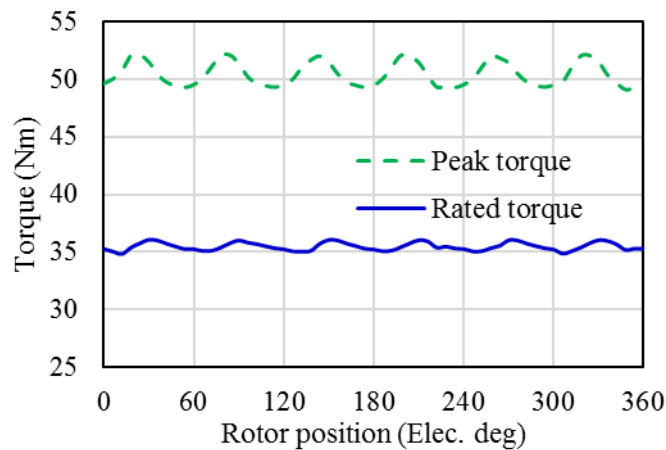
Figure 5.6 Output torque calculated at rated and peak load

Stator MMF space harmonics have a considerable impact on the saliency of the motor as the magnetic flux path depends on them, and significant stator MMF harmonics may reduce the rotor saliency. The average torque at different current phase advance angle in the rated and peak load condition are plotted in Figure 5.7. The proposed 24S-14P IPM motor generates a maximum torque of 50Nm at maximum torque per ample (MTPA) angle of 35^0, while at rated load condition, the MTPA angle is 30^0. Therefore, it can be concluded that the proposed 24S-14P IPM motor features some reluctance torque capability and a non-negligible saliency ratio.
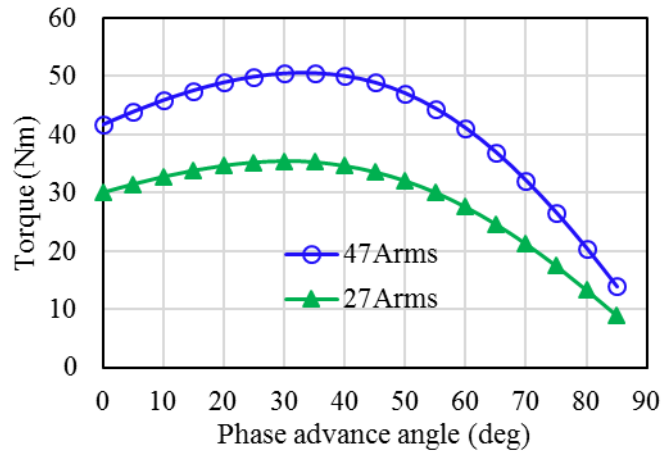
Figure 5.7 Average torque versus current phase advance angle

5.2.3 Efficiency map

The efficiency map of the proposed 24S-14P IPM motor is calculated using the 3-D FEM analysis method with the MTPA control strategy applied [133], as shown in Figure 5.8. High efficiency can be observed in most of the operation area. Efficiency of higher than 94% can be kept at high speed range which can be attributed to lower iron losses due to the reduced stator MMF harmonics. It should be noted that the iron loss calculation is based on the loss coefficient data of lamination steel provided by supplier. No additional build factor is considered.
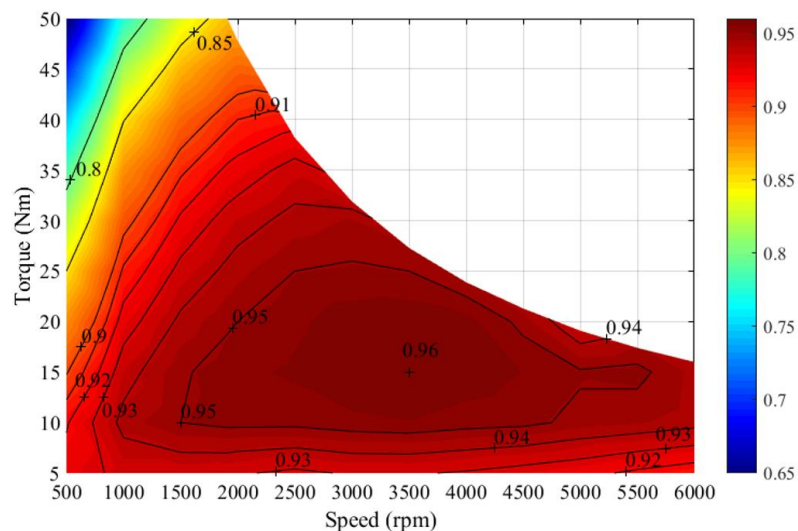
Figure 5.8 Calculated efficiency map of the proposed 24S-14P IPM motor

It is well known that continuous power operation across the speed range is significantly constrained by both DC bus voltage limits and by high iron losses especially the high rotor losses at peak speed. Higher rotor loss may result in unacceptably high rotor temperature, which can deteriorate the magnet performance and possibly lead to irreversible demagnetization. Therefore, it is expected that the proposed 24S-14P IPM motor with reduced stator MMF harmonics can maintain a higher continuous power output at high speed than at the base speed while keeping a high efficiency.

5.2.4 Short-circuit (SC) fault performance

The benefit of using FSCW topology and the IPM rotor is their reduced steady-state SC current under terminal SC fault which is critical for safety-critical applications. A lower SC current can maintain the motor within thermal limit in fault conditions.

(a) SC current   (b) SC braking torque
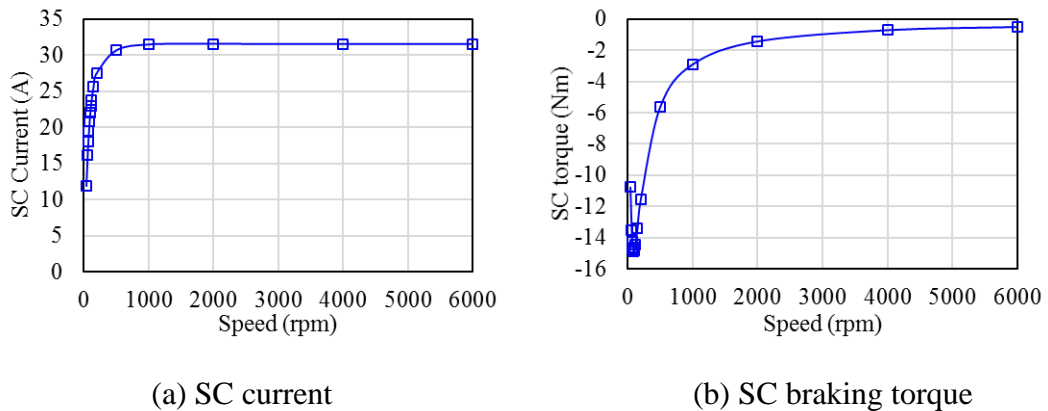
Figure 5.9 Steady-state SC characteristic of single 3-phase 24S-14P IPM motor

The steady-state SC current and braking torque against speed for the single 3-phase 24S-14P IPM motor are calculated and plotted in Figure 5.9. As expected, the steady-state SC current increases when the speed goes up, and remains almost constant after 2000rpm, which can be explained by the analytical SC current expression (5.1) derived from steady-state mathematical model in the synchronous *d-q* reference frame [134]. At high speed, the impact of resistance on the SC current becomes negligible, thus the SC current may be expressed as (5.2), which is independent from speed.

$$I_{sc} = \frac{\sqrt{(\omega^2 L_q \lambda_f)^2 + (\omega R \lambda_f)^2}}{R^2 + \omega^2 L_d L_q}$$

(5.1)

$$I_{sc} = \frac{\lambda_f}{L_d} \tag{5.2}$$

The highest SC current is about 31.5A that corresponds to 22.3Arms, which is smaller than rated current of 27Arms. It is worth noting that the motor was designed with the highest SC current to be qual to rated current of 27Arms; however, due to the end-winding leakage effect, the 3-D FEM calculated SC current is less than that of 2-D FEM calculation.

The steady-state SC braking torque may be expressed as [134]

$$T_{sc} = -\frac{3}{2} PR\lambda_f^2 \omega \frac{R^2 + \omega^2 L_q^2}{(R^2 + \omega^2 L_d L_q)^2} \tag{5.3}$$

The critical speed where the maximum braking torque occurs can easily be achieved by equating the derivative of (5.3) with respect to the speed ω to zero; and normally the critical speed is at low speed.

The variation of the steady-state SC braking torque in Figure 5.9(b) is as expected, with the highest SC braking torque of -14.8Nm occurring at the critical speed of 110rpm. After that, the steady-state SC braking torque decreases as the speed increases. At peak speed of 6000rpm, the steady-state SC braking torque is very small, about -0.5Nm.

5.3   EM performance of proposed 24 slots, 14 poles IPM motor with dual 3-phase winding system

5.3.1 Different dual 3-phase winding configurations

As has been depicted in Section 4.2, there are different multiple 3-phase configurations for the proposed 24S-14P motor offering fault-tolerant capability. Based on the star of slots theory [88], the coil phasor distribution for the 24S-14P motor is plotted in Figure 5.10. There are eight phasors available each phase for a three-phase winding system. By arranging the coil phasors of one phase into different phases, several dual 3-phase winding configurations can be achieved. Three kinds of dual 3-phase winding configurations with different shift angle, viz., 0^0, 15^0, and 30^0, are summarized in Figure 5.11, Figure 5.12, and Figure 5.13, respectively.
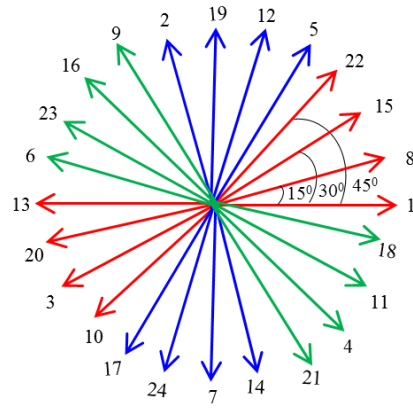
Figure 5.10 Coil phasors diagram of the proposed 24S-14P-DL winding
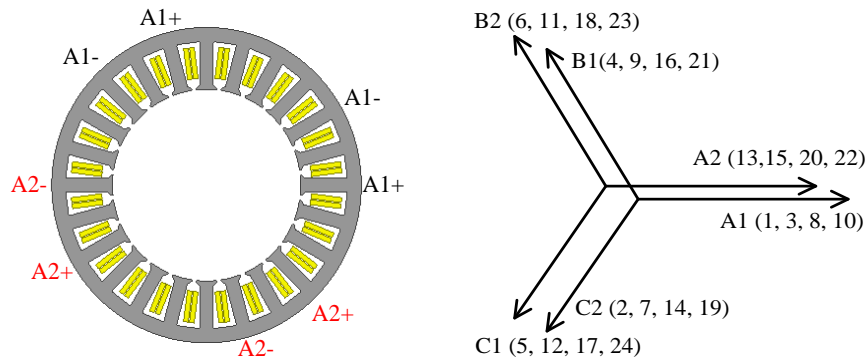
(a) Phase A1&A2 distribution   (b) Coil phasor diagram

Figure 5.11 Dual 3-phase 24S-14P-DL winding with 0^0 shift
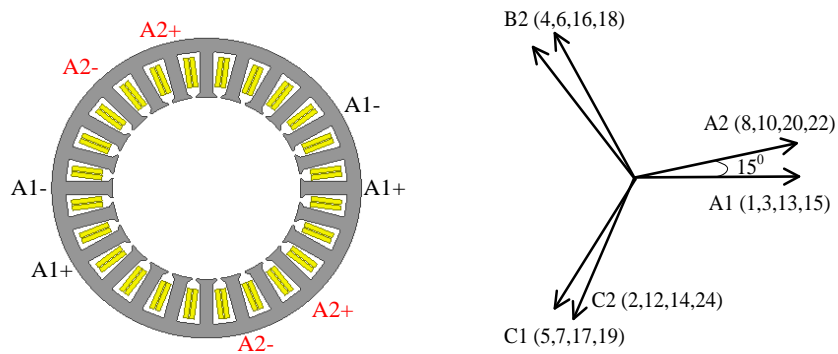
(a) Phase A1&A2 distribution   (b) Coil phasor diagram

Figure 5.12 Dual 3-phase 24S-14P-DL winding with 15^0 shift

(a) Phase A1&A2 distribution   (b) Coil phasor diagram
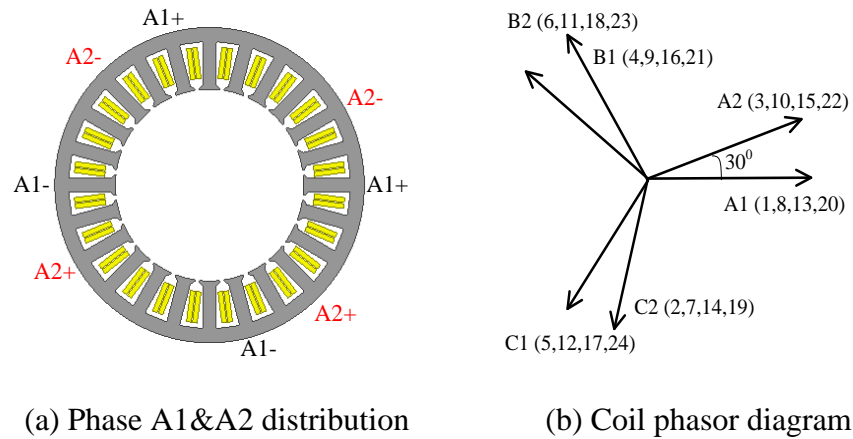
Figure 5.13 Dual 3-phase 24S-14P-DL winding with 30^0 shift

Table 5.3 Winding factor of dual 3-phase 24S-14P motor

Shift angle	0^0	15^0	30^0
Winding factor	0.760	0.766	0.787

It is evident that different shift angles between dual 3-phase windings lead to different winding factors and electromagnetic performance, especially the performance under fault conditions. The corresponding winding factors are calculated and summarized in Table 5.3. A higher winding factor can be achieved by using a higher shift angle configuration.

5.3.2 No-load EMF

The no-load EMF of the dual 3-phase 24S-14P IPM motor with different shift angles is calculated using 3-D FEM analysis, as shown in Figure 5.14. Only 15^0 and 30^0 configurations are plotted as the 0^0 configuration can easily be obtained from no-load EMF of the single 3-phase configuration in Figure 5.4.

FFT spectrum comparison of their phase and line EMF are depicted in Figure 5.15. Due to different winding factors attributing from different shift angles between dual 3-phase windings, their EMF amplitude with corresponding harmonic orders are different. The 30^0 configuration has the highest fundamental EMF amplitude, as well as 5th and 7th harmonic. A lower EMF amplitude is seen in 15^0 configuration, but the lowest EMF amplitude is in the case of 0^0 configuration.

(a) 15^0 (b) 30^0
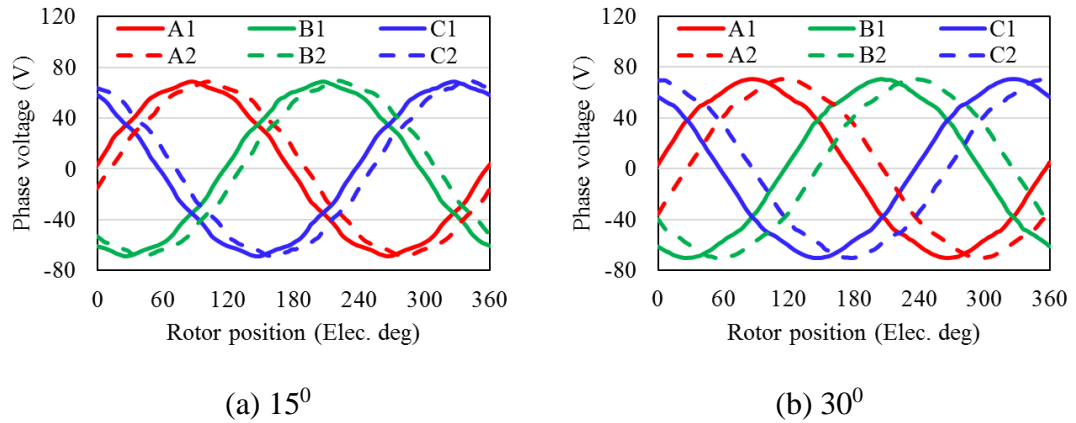
Figure 5.14 No-load EMF of dual 3-phase 24S-14P IPM motor with different shift angles

(a) Phase voltage   (b) Line voltage
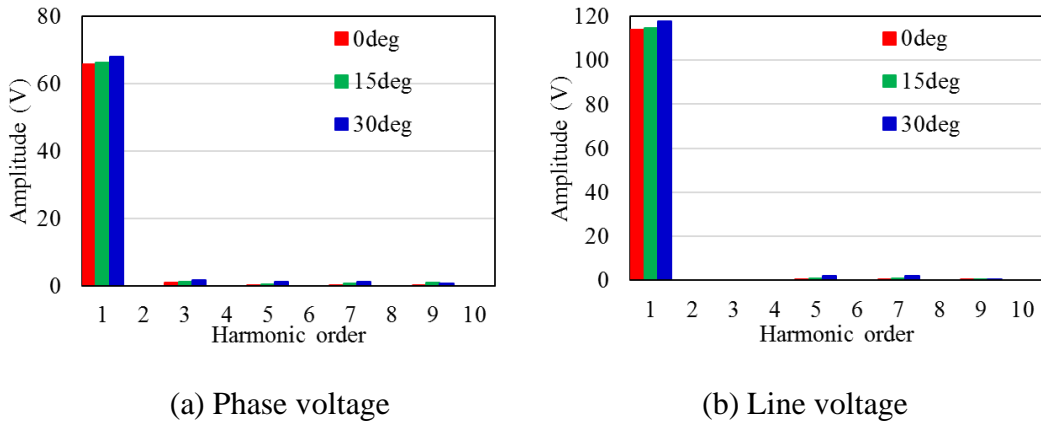
Figure 5.15 FFT spectrum comparison of no-load EMF of dual 3-phase 24S-14P IPM motor with different shift angles

5.3.3 EM performance under healthy condition

In this section, the peak and rated torque capability of the 24S-14P IPM motor are evaluated and compared under healthy conditions, where the dual 3-phase windings are fed with corresponding appropriate current excitations. The EM torque characteristics of the dual 3-phase 24S-14P IPM motor with different shift angles are calculated and plotted in Figure 5.16. The torque ripple is defined as the ratio between peak to peak value and average value of EM torque. The higher the back EMF the higher the output torque; thereby, it is evident that the highest average torque of 53.3Nm is generated in the 30^0 configuration, which is 7% higher than average torque

of 50Nm of 0^0 configuration; 15^0 configuration can generate 51.3 Nm, which is 3% higher than that of 0^0 configuration. A general torque improvement is observed for both 15^0 and 30^0 configurations.

Both 15^0 and 30^0 configurations have less torque ripple than the 0^0 configuration, as some of the ripple torque components are eliminated or cancelled by the shift angle between two 3-phase windings, which can be explained by the EM torque expression. From the power conversion theory, the EM torque mainly includes 6th and 12th order ripple torque components; Thus, the EM torque generating from one set of 3-phase winding ignoring harmonics with orders higher than 12 can be expressed as

$$T_{em1} = T_1 + T_6 \sin(6\omega t) + T_{12} \sin(12\omega t) \tag{5.4}$$

The EM torque of dual 3-phase 24S-14P IPM motor with 0^0 configuration can be written as

$$T_{em-0^0} = 2T_1 + 2T_6 \sin(6\omega t) + 2T_{12} \sin(12\omega t) \tag{5.5}$$

The EM torque of dual 3-phase 24S-14P IPM motor with 15^0 configuration can be written as

$$T_{em2-15^0} = T_1 + T_6 \sin\left(6\omega t - \frac{\pi}{2}\right) + 2T_{12} \sin(12\omega t - \pi) \tag{5.6}$$

$$T_{em-15^0} = T_{em1} + T_{em2-15^0} = 2T_1 + \sqrt{2}T_6 \sin\left(6\omega t - \frac{\pi}{4}\right) \tag{5.7}$$

The EM torque of dual 3-phase 24S-14P IPM motor with 30^0 configuration can be written as

$$T_{em2-30^0} = T_1 + T_6 \sin(6\omega t - \pi) + T_{12} \sin(12\omega t - 2\pi) \tag{5.8}$$

$$T_{em-30^0} = T_{em1} + T_{em2-30^0} = 2T_1 + 2T_{12} \sin(12\omega t) \tag{5.9}$$

It can be seen from above torque equations that the 15^0 and 30^0 configurations can cancel out the 12th and 6th order harmonic torque component, respectively, which explains their characteristics giving less torque ripple.
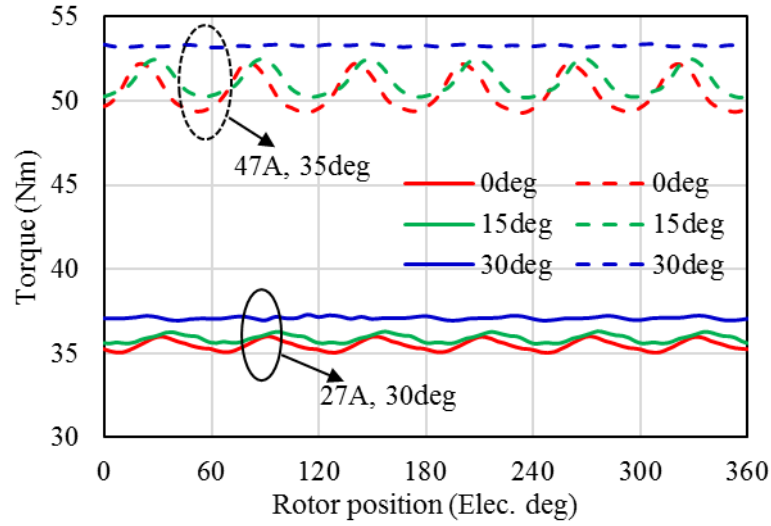
(a) Torque waveform
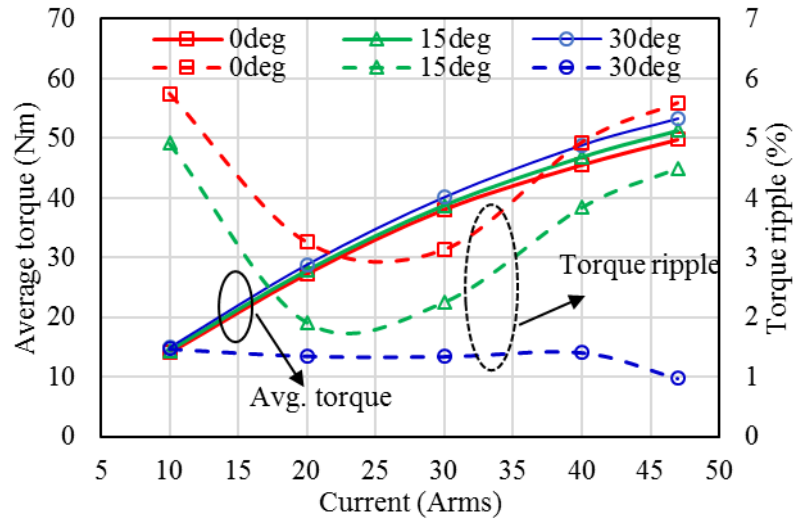
(b) Torque characteristics against current

Figure 5.16 Torque capability of dual 3-phase 24S-14P IPM motor with different shift angles

In fact, the torque ripple characteristic can also be explained by the reduced stator MMF harmonics. Based on the Lorentz force law, the instantaneous torque can be expressed as [136]

$$T_{em1} = T_{avg} + T_{ripple} \tag{5.10}$$

$$T_{avg} = \frac{\mu_0}{g} r l_{ef} \pi P f_{s,P} f_{r,P} \sin\gamma_d \tag{5.11}$$

$$T_{ripple} = -\frac{\mu_0}{g} r l_{ef} \pi P \sum_{\substack{v=(6m\mp1)P \\ m=1,2,3\ldots}} v f_{s,v} f_{r,v} \sin\big((v \pm P)\omega_r t \pm \gamma_d\big) \qquad (5.12)$$

where $f_{s,v}$ and $f_{r,v}$ are the amplitude of vth order harmonic of stator and rotor MMF harmonics, respectively; γ_d is the current phase advance angle measured from d-axis.

It can be observed that harmonic orders of the ripple torque are in multiples of six and only stator and rotor MMF harmonics with orders of $(6m\pm1)P$ can contribute to the ripple torque [136] [137]. Since only the winding configurations are different and the rotor MMF harmonics are the same, the comparison of ripple torque is only related to their stator MMF harmonic components with orders of $(6m\pm1)P$.

Therefore, the amplitude of corresponding ripple-torque-producing harmonics can be used to evaluate the ripple torque. For instance, both 35$^{\text{th}}$ and 49$^{\text{th}}$ of stator space MMF harmonics are contributing to 6$^{\text{th}}$ order of ripple torque, while for the 12$^{\text{th}}$ order of ripple torque, the contributing stator MMF harmonics are 77$^{\text{th}}$ and 91$^{\text{st}}$ harmonic.

The MMF waveforms and their FFT spectrum under healthy conditions for the dual 3-phase 24S-14P IPM motor with different shift angles are plotted in Figure 5.17. The main ripple-torque-producing stator MMF harmonics amplitude are summarized in Table 5.4. Both 35$^{\text{th}}$ and 49$^{\text{th}}$ harmonics corresponding to 6$^{\text{th}}$ order of ripple torque are eliminated in the 30^0 configuration which explains its lowest ripple torque. The lower ripple torque of 15^0 configuration compared to 0^0 configuration can be attributed to the lower 35$^{\text{th}}$ harmonic and the cancellation of both 77$^{\text{th}}$ and 91$^{\text{st}}$ which contribute to 12$^{\text{th}}$ order torque ripple.
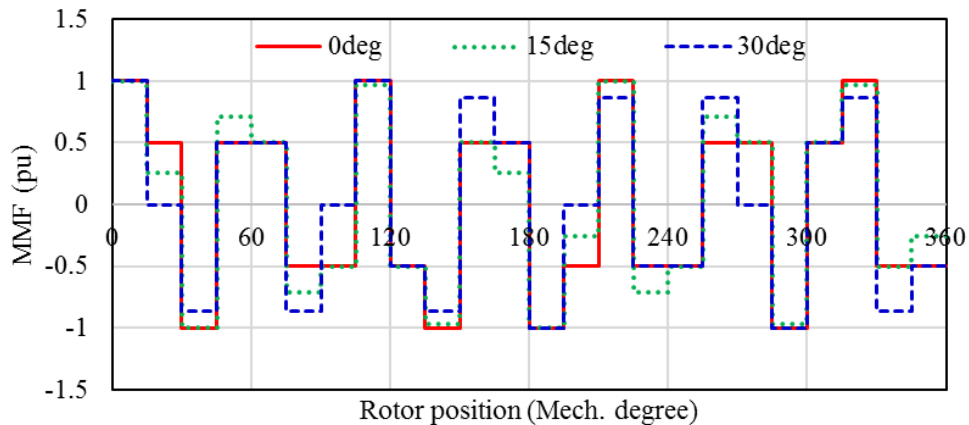
(a) Stator MMF waveform
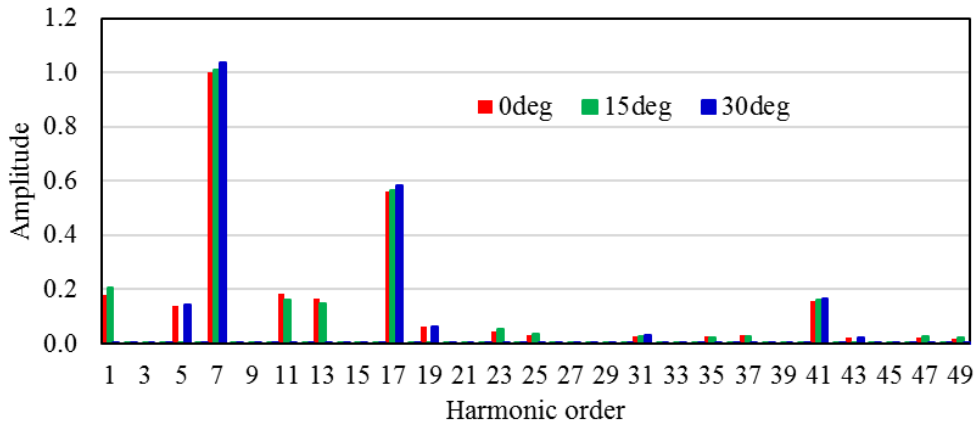
(b) FFT spectrum

Figure 5.17 Stator MMF waveform under healthy condition of dual 3-phase 24S-14P IPM motor with different shift angles

Table 5.4 Ripple-torque-producing stator MMF harmonics amplitude of dual 3-phase 24S-14P IPM motor under healthy condition

Torque ripple order	Corresponding Stator MMF harmonics	0^0	15^0	30^0
6th	35th	0.0240	0.0212	0.0001
	49th	0.0186	0.0218	0.0012
12th	77th	0.0049	0.0007	0.0051
	91st	0.0015	0.0001	0.0017

5.3.4 EM performance under open-circuit (OC) fault condition

As has been discussed, the dual 3-phase motor supplied by two independent power inverters can offer a certain level of redundancy. It can maintain torque output while losing one of the 3-phase winding sets, and the fault-tolerant control strategy is simple in that the current on the remaining 3-phase winding set is only required to be scaled by the appropriate factor (assuming this is possible from the point of view of drive and thermal constraints).

Under the open-circuit fault condition of losing one 3-phase winding set, the EM torque characteristics of the dual 3-phase 24S-14P IPM motor with different shift angle are calculated and plotted in Figure 5.18. In contrary to the healthy condition,

the 30^0 configuration tends to have the highest torque ripple while the 0^0 configuration exhibits the lowest torque ripple. The 15^0 configuration has a slightly higher average torque and much lower torque ripple than the 30^0 configuration.
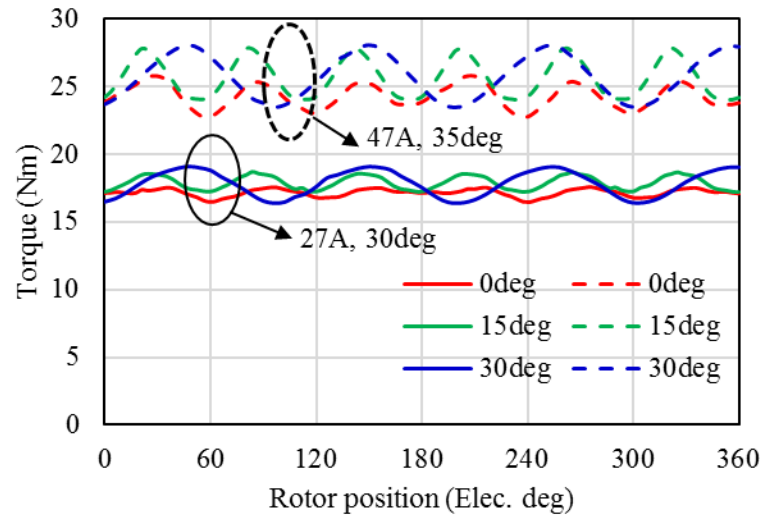
(a) Torque waveform
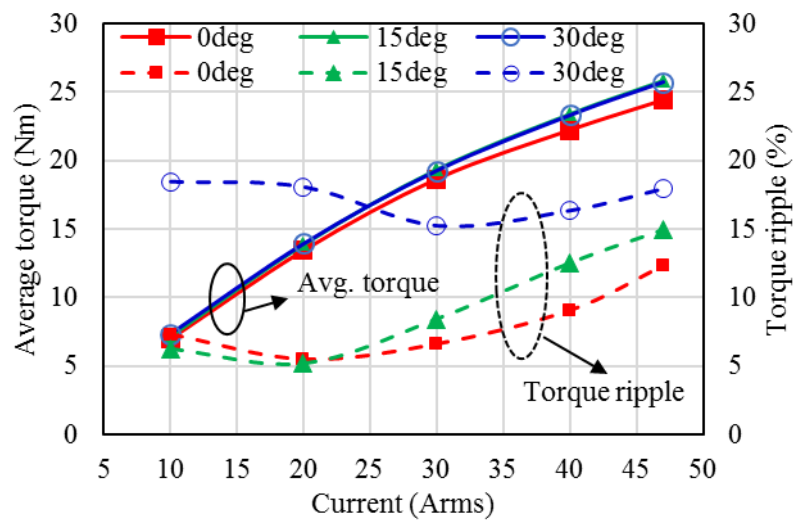
(b) Torque characteristics against current

Figure 5.18 Torque capability under one 3-phase winding OC fault of dual 3-phase 24S-14P IPM motor with different shift angles

These phenomena can be explained by their stator space MMF harmonics distribution under one 3-phase OC fault condition, as shown in Figure 5.19 and Table 5.5. Compared to 0^0 and 15^0configuration, both 35th and 49th harmonics with much

higher amplitude contributing to 6th ripple torque are observed in the 30^0 configuration which generates a much higher torque ripple under one 3-phase OC fault condition.
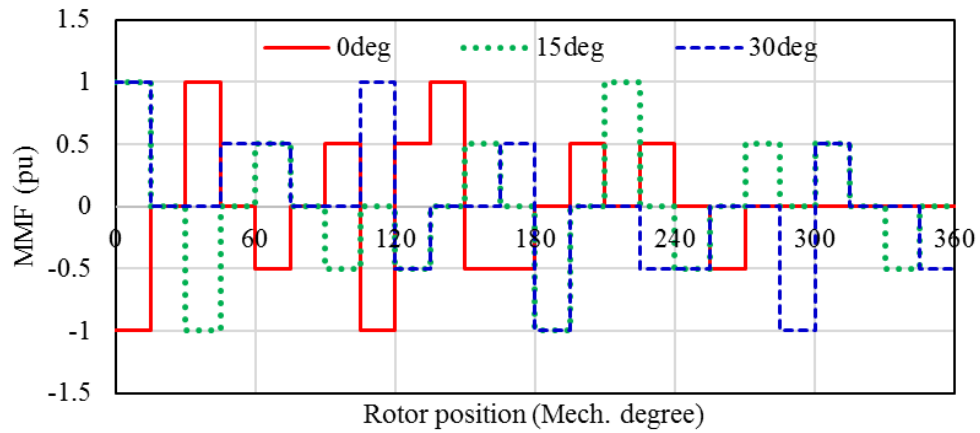
(a) Stator MMF waveform
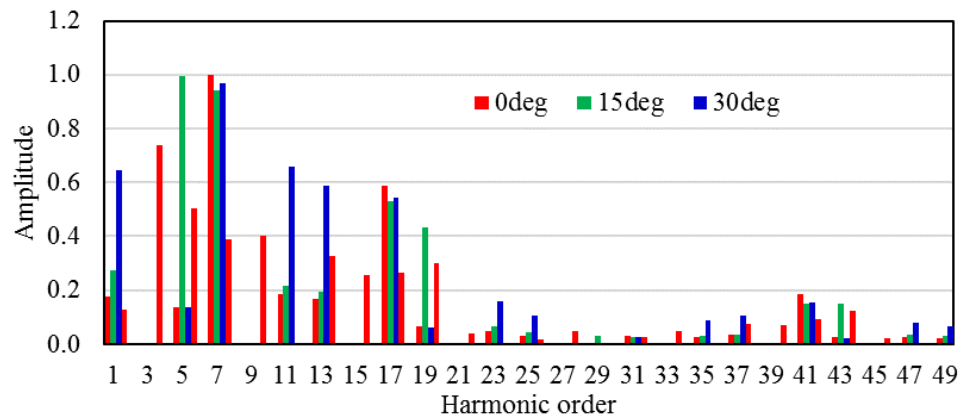
(b) FFT distribution

Figure 5.19 Stator MMF waveform under one 3-phase OC fault condition of dual 3-phase winding 24S-14P IPM motor with different shift angles

Table 5.5 Ripple-torque-producing stator MMF harmonics amplitude of dual 3-phase 24S-14P IPM motor under OC fault condition

Torque ripple order	Corresponding Stator MMF harmonics	0^0	15^0	30^0
6th	35th	0.0270	0.0284	0.0865
	49th	0.0224	0.0296	0.0668
12th	77th	0.0073	0.0344	0.0038
	91st	0.0005	0.0118	0.0021

(a) 0^0 (b) 15^0 (c) 30^0
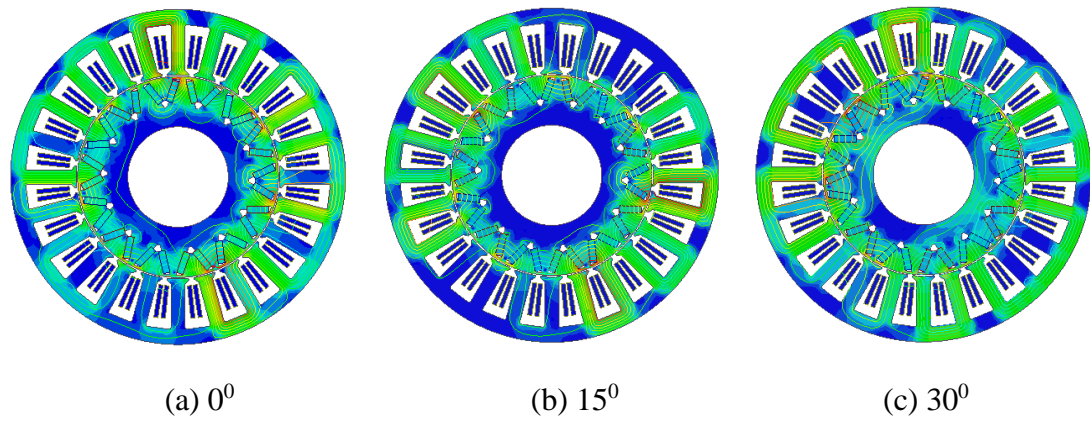
Figure 5.20 Magnetic field distribution under OC fault condition of dual 3-phase winding 24S-14P IPM motor with different shift angles
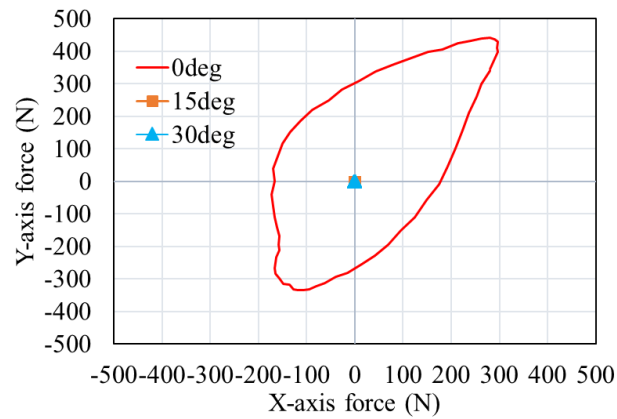
Figure 5.21 UMP under OC fault condition of dual 3-phase winding 24S-14P IPM motor with different shift angles

On the other hand, the unbalanced magnetic pull (UMP) characteristics have changed under the OC fault condition as the magnetic field might not be diametrically symmetrical [138]. Figure 5.20 shows the magnetic field distribution comparison when the operational 3-phase winding set is fed with peak current of 47Arms, 35^0. Although the magnetic fields of all configurations are not balanced along the circumference, only the 0^0 configuration exhibits a diametrically unsymmetrical magnetic field, which yields a significant radial UMP, as shown in Figure 5.21; both 15^0 and 30^0 configuration have no radial UMP under OC fault condition. In fact, the UMP is considerably related to the stator MMF; a diametrically symmetrical stator MMF leads to no UMP while a diametrically unsymmetrical stator MMF results in

significant UMP and the UMP increases significantly with the phase current. Thus, the UMP characteristics can also be explained by the diametrically symmetry characteristics of the stator MMF waveforms in Figure 5.17 and Figure 5.19.

5.3.5 Mutual-coupling between dual 3-phase windings

This section deals with the mutual-coupling for dual 3-phase windings with different shift angles. The self- and mutual- inductance between phases is calculated, as shown in Figure 5.22, Figure 5.23, and Figure 5.24. All the inductance average values are summarized in Table 5.6.

All self-inductances of different winding configurations have about the same average value of ~2mH. The ratio between self-inductance L_{A1A1} and mutual-inductance L_{A1B1}, L_{A1C1} provides the level of coupling within one 3-phase winding. It shows that the mutual coupling ratio within one 3-phase winding is low for all configurations; 15^0 configuration shows almost no coupling, while 0.038 and 0.075 mutual coupling ratio are seen for 0^0 and 30^0 configuration, respectively.

On the other hand, the ratio between self-inductance L_{A1A1} and mutual-inductance between phases in different 3-phase windings such as L_{A1A2}, L_{A1B2}, gives the level of mutual-coupling between two 3-phase windings. The average mutual coupling ratios are calculated as an indication to compare the mutual coupling between two 3-phase windings for different winding configurations, as shown in Table 5.6. Overall, the mutual coupling between two 3-phase windings are extremely low, although there is a slight difference for different winding configurations. The 30^0 configuration has a ratio of 0.008, featuring almost no mutual coupling between two 3-phase windings. The 15^0 and 0^0 configuration give a ratio of 0.052 and 0.027, respectively, showing slightly higher mutual coupling but still extremely low. It is worth noting that an extreme low mutual-coupling is advantageous for fault-tolerant operation as it mitigates the negative impact of fault windings on the operational healthy windings, especially in the SC fault conditions which will be comprehensively examined in the next section.

(a) Within one 3-phase winding   (b) Between two 3-phase windings
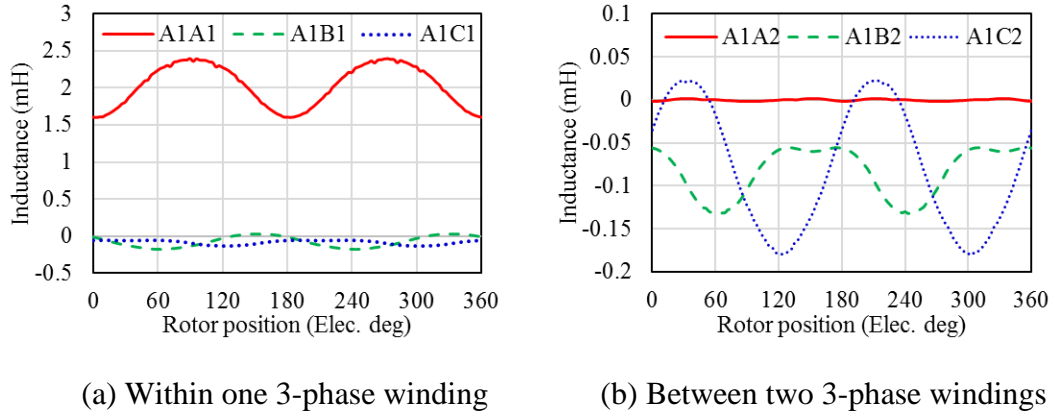
Figure 5.22 Inductance of dual 3-phase 24S-14P IPM motor with 0^0 shift

(a) Within one 3-phase winding   (b) Between two 3-phase windings
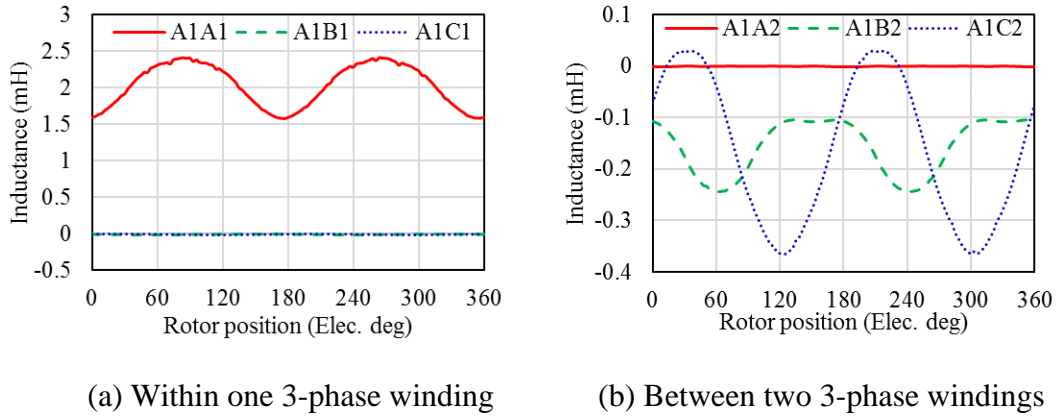
Figure 5.23 Inductance of dual 3-phase 24S-14P IPM motor with 15^0 shift

(a) Within one 3-phase winding   (b) Between two 3-phase windings
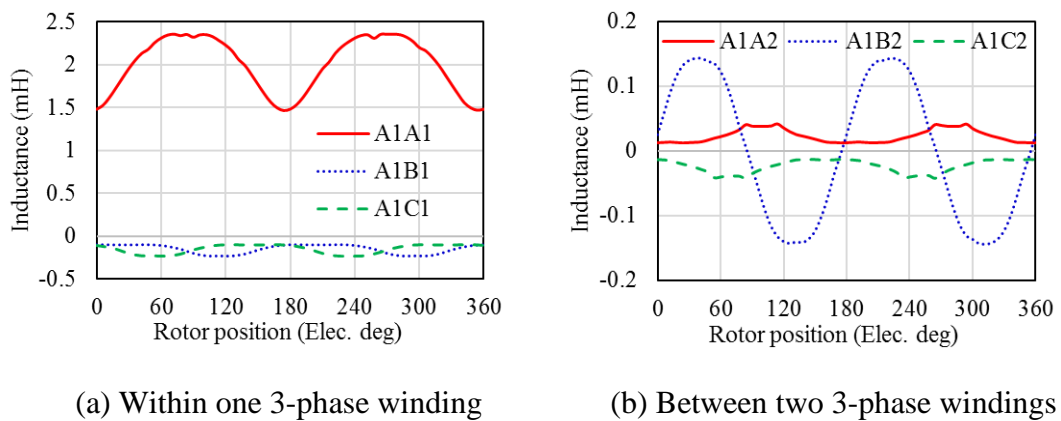
Figure 5.24 Inductance of dual 3-phase 24S-14P IPM motor with 30^0 shift

Table 5.6 Comaprison of average value of inductance components of dual 3-phase winding 24S-14P IPM motor with different shift angles

	L_{A1A1} (mH)	L_{A1B1} (mH)	L_{A1C1} (mH)	L_{A1A2} (mH)	L_{A1B2} (mH)	L_{A1C2} (mH)	Average mutual coupling ratio between dual 3-phase windings
0^0	2.030	-0.077	-0.083	0.000	-0.083	-0.078	0.027
15^0	2.031	-0.003	-0.003	0.000	-0.155	-0.161	0.052
30^0	2.006	-0.150	-0.150	0.023	-0.023	0.000	0.008

5.3.6 EM performance under short-circuit (SC) fault condition

As discussed above, the mutual-coupling between the dual 3-phase windings is low enough to be negligible, which is advantageous for the post SC fault operation as this offers a magnetically independent dual 3-phase system in the 24S-14P IPM motor; the SC current in one 3-phase would not significantly negatively affect the EM performance in the remaining healthy 3-phase winding set ensuring the outstanding power/torque output capability during SC fault condition.

Like the single 3-phase winding configuration, the SC current increases when the speed goes up, and remain almost constant after 800 rpm, as shown in Figure 5.25. It can be observed that due to the almost same self-inductances and the negligible mutual-coupling in the dual 3-phase winding configuration with different shift angles, their steady-state SC current are almost the same. The SC braking torque for both the 0^0 and 15^0 configuration reach the highest level of -8.1Nm at around 110rpm, but for the 30^0 configuration, the maximum SC braking torque reach -8.5Nm at 90rpm.

The average and peak to peak value of the steady-state output torque after one 3-phase winding SC fault with the remaining healthy 3-phase winding fed with peak current of 47Arms, 35^0 are calculated and plotted in Figure 5.26. In terms of output torque after one 3-phase SC fault, the 30^0 configuration exhibits a higher average torque output compared to 0^0 and 15^0 configuration due to its higher winding factor and relatively less mutual-coupling between the two 3-phase windings. The lowest output torque happens at around 110rpm, where the braking torque generated by the SC 3-phase winding reaches the highest level.

The variation of steady-state SC ripple torque, on the other hand, is quite similar to the OC fault condition. The 30^0 configuration gives the highest torque ripple, while the 15^0 configuration has a lower torque ripple, with the lowest torque ripple in the 0^0 configuration. This can be explained by the fact that some of the ripple-torque-producing stator MMF harmonics components such as 35th and 49th that are cancelled or reduced in the healthy condition appeared again in the SC fault condition where the currents in remaining healthy and SC 3-phase winding are different. Similarly, it is evident that only significant UMP can be expected in the 0^0 configuration under one 3-phase SC fault condition.
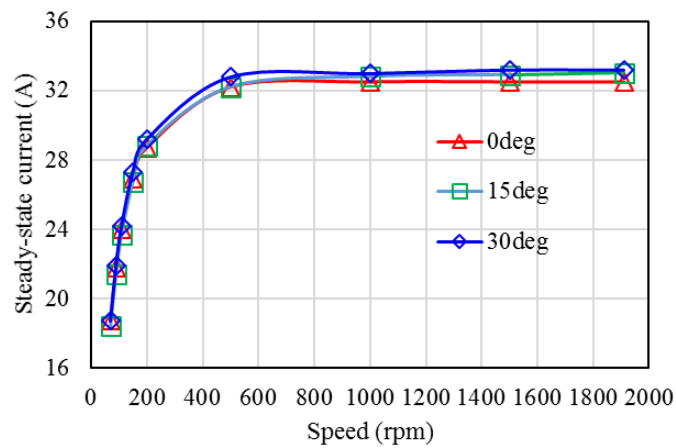
(a) Steady-state SC current
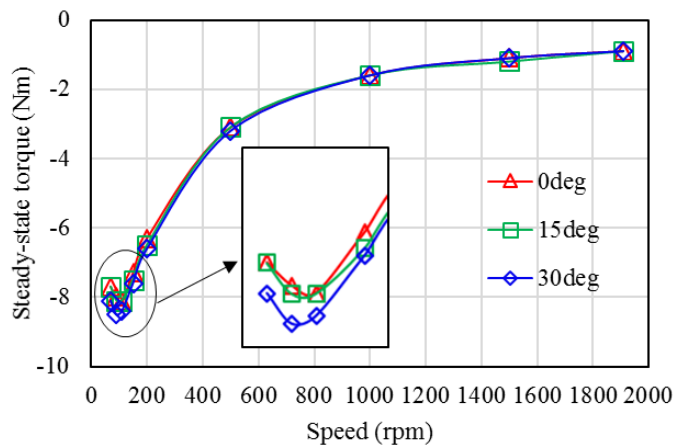
(b) Steady-state SC braking torque

Figure 5.25 Steady-state SC characteristics of dual 3-phase winding 24S-14P IPM motor with different shift angles
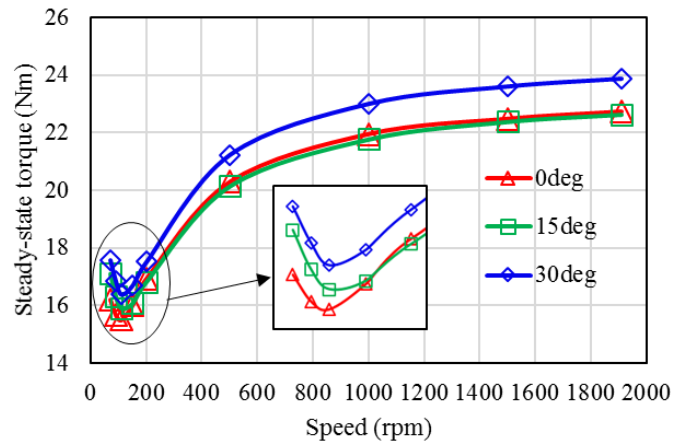
(a) Average output torque
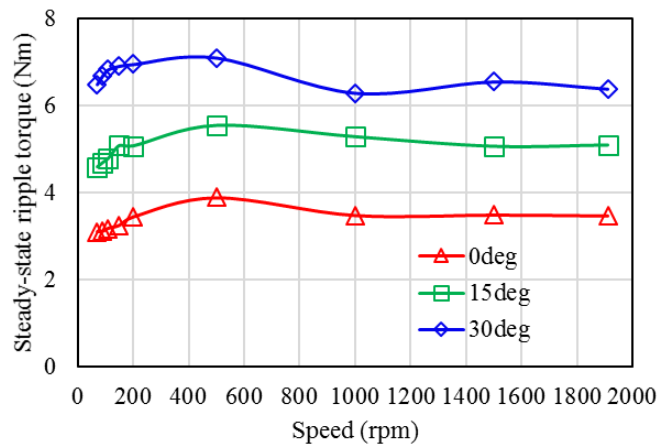
(b) Peak to peak output torque

Figure 5.26 Steady-state output torque capability of dual 3-phase winding 24S-14P
IPM motor with different shift angles when one 3-phase SC fault while other one
loaded with peak current

5.3.7 Comparison of different dual 3-phase winding configurations

This section provides a comprehensive comparison of dual 3-phase 24S-14P IPM
motor with different shift angles in terms of torque capability, UMP, and mutual-
coupling under both healthy and fault conditions, as summarized in Table 5.7.

The 30^0 configuration exhibits the highest output torque under both healthy and
fault conditions including OC and SC fault, but only under healthy condition, it has
the lowest ripple torque, otherwise highest torque ripple is observed. The 0^0

configuration, on the other hand, shows the lowest output torque under all conditions but it offers the lowest ripple torque under fault conditions with the concern of significant UMP. A trade-off design between the 0^0 and 30^0 configuration is the 15^0 configuration, which under all operation conditions exhibits a slightly higher average torque compared to the 0^0 configuration and a lower ripple torque compared to the 30^0 configuration.

As the fault-tolerant operation only operates at emergency conditions, the performance under normal operation would be more of interest. The 30^0 configuration has been finally selected for prototype validation which can provide the highest output torque and lowest ripple torque under normal operation condition; and in fact, the output under healthy condition is almost constant, which means no extra measures is required for reducing torque ripple that may induce additional cost and negative impact on average torque.

Table 5.7 Comparison of dual 3-phase 24S-14P IPM motor with different shift angles

Item		0^0	15^0	30^0
Mutual-coupling		Low	Low	Low
	Average torque	Low	Middle	High
Healthy condition	Torque ripple	High	Middle	Low
	UMP	No	No	No
	Average torque	Low	Middle	High
OC fault	Torque ripple	Low	Middle	High
	UMP	High	No	No
	Average torque	Low	Middle	High
SC fault	Torque ripple	Low	Middle	High
	UMP	High	No	No

5.4   Chapter summary

In this chapter, an IPM motor with the proposed 24S-14P winding topology is designed and evaluated based on an EV traction application. The EM performance such as torque capability and efficiency has been evaluated across the speed range. High efficiency can be observed in most of the operation area and it can maintain an

efficiency higher than 94% in the high speed zone. The torque ripple is very low which means no extra measures like rotor skewing, that may induce additional cost and negative impact on average torque, are required.

The fault-tolerant capability of the proposed 24S-14P winding design is demonstrated with the dual 3-phase winding topology equipped with different shift angles in time, viz., 0^0, 15^0, and 30^0. The comparison of different dual 3-phase winding configurations have been analyzed in both healthy and fault conditions including OC and SC fault conditions, with focus on the torque capability and UMP. The 15^0 configuration maybe a good trade-off solution which exhibits a slightly higher average torque compared to the 0^0 configuration under all operation conditions and a lower ripple torque compared to the 30^0 configuration under fault conditions. It is confirmed that the 30^0 configuration exhibits the best torque performance in the healthy condition, while maintaining a higher output torque with higher torque ripple, and no significant UMP in both healthy and fault conditions.

In addition, the concentrated winding of the proposed 24S-14P IPM motor features less manufacturing effort and a higher slot fill. A segmented modular tooth structure may be implemented to further facilitate the manufacturing and reduce cost.

Therefore, this chapter has demonstrated the practicability and good prospects of the proposed 24S-14P winding design in fault-tolerant traction motor applications.

Chapter 6

Electromechanical Actuator: Architecture and Design Considerations

The more electric aircraft (MEA) has become a general trend in future aircraft technology in terms of systematically improving efficiency and cost, weight reduction and decarbonisation. Actuation systems such as flight control actuation systems and landing gear systems are a key part in aircraft. Moving towards electromechanical actuator (EMA) systems can offer the advantages of lighter and more compact structure, less complexity than hydraulic actuation systems, easy installation and simple maintenance [45].

On the other hand, aircraft typically use many control surface actuators with varying requirements of size, power and duty. Having as few components as possible is a huge benefit for design, certification, construction and maintenance. Therefore, a distributed actuation system using integrated modular actuators is preferable.

In the following two chapters, the actuation system architecture and actuator configurations are studied in terms of weight, reliability, and cost, and specifications are determined for modular electrical actuators capable of meeting a diverse range of actuation requirements. A modular fault-tolerant FSCW PM rotary motor will be developed to meet these strict requirements. Both electromagnetic and thermal performance will be evaluated.

6.1 Actuation system architecture

6.1.1 Conventional concentrated actuation architecture

Conventional concentrated actuation system architecture such as in the A320 and Boeing 777, adopts the centralized hydraulic system or centralized electrically powered actuation system. For centralized hydraulic system, the centralized redundant hydraulic systems supply the required pressure to hydraulic actuators of control surfaces. Figure 6.1 depicts a typical high-lift actuation system for a small commercial aircraft with mechanical shaft [72], in which Slat/Flap movement is driven by the central motor through mechanical transmission. This configuration ensures the synchronization of Flaps or other control surfaces like Slats but prohibit the functionalities and flexibilities of implementation. The aerodynamic loads on the inboard and outboard Flaps or Slats are different, which means complete synchronization of deployment of these devices cannot maximize efficiency and is required to be improved. In addition, the mechanical transmission shaft is composed of high numbers of components with many parts which requires high installation and design-engineering efforts and so is not preferable for manufacturing and certification [139].
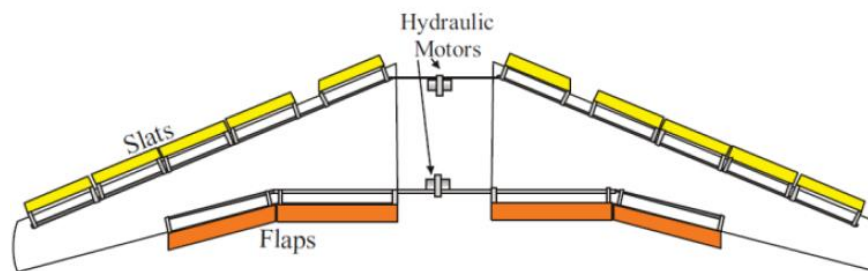
Figure 6.1 A typical high lift system for a small commercial aircraft [72]

6.1.2 Advanced distributed actuation architecture

Recent development programs at Airbus and Boeing have extended the functional flexibilities of wing surface by introducing advanced distributed actuation architecture. In this configuration, each control surface is deployed independently from each other. An advanced distributed Flap actuation system architecture is shown in Figure 6.2 [72].

Each control surface like Flaps and Slats is a self-contained actuation system, which includes actuators and power electronics. Thus, a power on demand flight control system is realized [50].

This distributed system architecture offers the capability for implementation of additional functionalities, such as improved function flexibility via differential actuators setting, weight reduction, improved manufacturability and reduced installation efforts due to the highly integrated actuator component design. In addition, the distributed configuration offers further redundancy both on mission and control surface level. Thus, in this thesis, the distributed actuation architecture is to be studied.
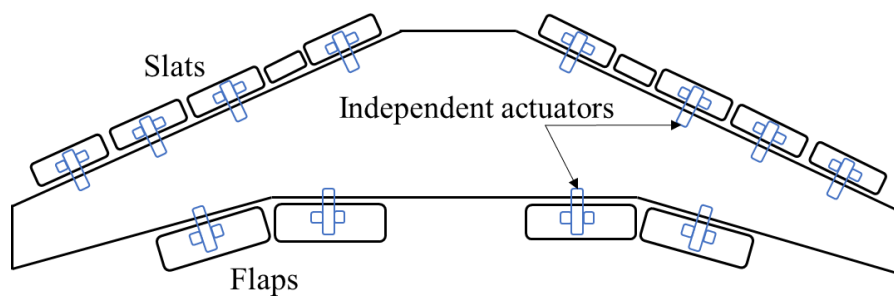
Figure 6.2 Advanced distributed high lift actuation system architecture [72]

6.2 Actuation system architecture

In an aircraft distributed actuation system, each control surface can be deployed independently from each other. Furthermore, a control surface can be controlled by independently integrated actuators, and different number of actuators and power electronics drives allow for different redundancy capability at the control surface level.

For considerations of the feasibility and deployment of aircraft actuation systems, the evaluation criteria include reliability, weight, efficiency, complexity and cost, etc. Among these, the level of failure probability is a critical factor. There are many configurations available for an individual control surface of the actuation system due to different combinations of flight control computers (FCCs), power supplies, actuators. This indicates the necessity to evaluate the failure rate of each configuration to determinate the feasibility of deployment in the aircraft actuation system.

A typical flight control actuation system is illustrated in Figure 6.3. In general, three to four FCCs and two or three independent electrical power systems are available

for a commercial aircraft to provide the necessary level of redundancy for safety. The configuration of control surfaces and actuators depends on the function, safety criticality, and aircraft size.

Three typical actuator configurations for an individual control surface are illustrated in Figure 6.4. According to the failure probability of each component, the overall failure probability can be evaluated by using the method of either fault tree analysis or a fault dependency diagram.
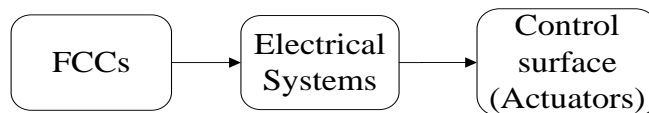
Figure 6.3 Typical flight control actuation system
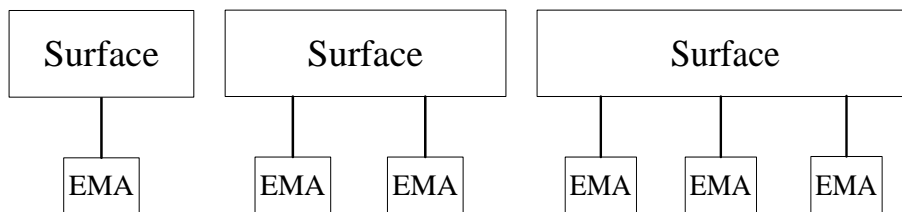
Figure 6.4 Different actuator system configurations

6.3 Modular EMA design requirements

6.3.1 Actuator requirements

The single-aisle type airplane such as A320 or B737 is the most in demand aircraft for the future [140]. The replacement for the A320/B737 will be enormously important for the major aircraft manufacturers and airlines alike based on the number of these aircraft currently in service and on order, coupled with the rapid growth in air transport predicted for the foreseeable future [140]. Therefore, the single-aisle aircraft of A320 is selected as a baseline aircraft for investigation of advanced distributed actuation system architecture and for the EMA design evaluation.

Table 6.1 shows a summary of primary flight control surfaces design requirements from hydraulic actuators on-board the Airbus A320 [141]. On the other hand, the stall load on the secondary flight control surfaces like Flaps and Slats is

difficult to estimate, and engineers usually use wind tunnel experiments to measure this data [142]. Unfortunately, there is no accessible information about the secondary control surface requirements for the A320. However, the loads on the secondary flight control surfaces are expected to be lower than primary control surfaces. Thus, it is expected that an actuator system designed for primary control surfaces could be suitably adapted to the less demanding secondary control surfaces. Thus, this project will focus on designing actuators for the primary control surfaces.

It should be noted that the data in Table 6.1 is not design requirements for actuators of each control surface due to the control surfaces' redundancy configuration improving failure-safe capabilities. Table 6.2 shows the redundancy configuration of each primary flight control surfaces. For instance, the Rudder has three active actuators, and all of these are active at the same time, so it's one third of Rudder's load on each actuator if the torque/force summing configuration (speed synchronization) is adopted. For the Aileron surface, there are two actuators with only one active, so the load on each actuator is the load on each Aileron. Therefore, the actuator requirement for each primary control surface can be figured out and summarized in Table 6.3

Table 6.1 Primary control surfaces requirements for A320

	Aileron	Spoiler	Elevator	Rudder
Stroke (mm)	44	84	60	110
No Load Speed (mm/s)	90	100	60	110
Max. Extend Force (kN)	48.0	44.9	27.7	44.3
Max. Retract Force (kN)	48.0	36.6	27.7	44.3

Table 6.2 Redundancy configuration of primary control surfaces for A320

Control surface	NO. of surfaces	Actuators per surface	Active per surface	Active actuators	Total actuators
Ailerons	2	2	1	2	4
Primary Spoilers	8	1	1	8	8
Elevators	2	2	1	2	4
Rudders	1	3	3	3	3

Table 6.3 Actuator requirements of each primary control surface for A320

	Aileron	Spoiler	Elevator	Rudder
Stroke (mm)	44	84	60	110
No-load speed (mm/s)	90	100	60	110
Peak extend force (kN)	48.0	44.9	27.7	14.8
Peak retract force (kN)	48.0	36.6	27.7	14.8

Table 6.4 Unit actuator for primary control surfaces for A320

	Stroke (mm)	Peak speed (mm/s)	Peak force (kN)
Unit Actuator	110	110	16

Table 6.5 Modular actuator specification of primary control surface

	Aileron	Spoiler	Elevator	Rudder
No. of units	3	3	2	1
Peak speed (mm/s)	110	110	110	110
Peak force (kN)	48	48	32	48

6.3.2 Modular EMA design requirements

Aircraft typically use many control surface actuators with varying requirements of size, velocity, thrust, power and duty, as shown in Table 6.1. Having as few components as possible is a huge benefit for design, certification, construction and maintenance. This research will develop modular linear electrical actuators capable of meeting a diverse range of actuation requirements for aircraft by using modular components.

First, it is necessary to modularize the design requirement for each actuator so that a generic unit actuator can be found. The size of an actuator is primarily determined by the force requirement, which means a modular design scheme could be achieved based only on the required force of each control surface. According to Table 6.3, the design requirement of a unit actuator for primary control surfaces in A320 can be figured out and is summarized in Table 6.4. It can be observed that 16kN has been chosen as the maximum force of the unit modular actuator. Then, how many units of

modular actuators for each primary control surface can be calculated, as summarized in Table 6.5. In comparison to Table 6.3, it is obvious that combined with different numbers of modular unit actuators, all the design specifications like force and speed meet the requirements of the corresponding control surface.

6.4 Electromechanical actuator (EMA) scheme

Before evaluating the control surface architecture, the linear EMA scheme must be determined. Since our project focuses on direct-drive actuators, the configuration of geared motor drive plus linear screw (either magnetic lead screw or mechanical screw) is not considered. In this case, there are three typical linear EMA configurations, as shown in below.

- Direct-drive linear motor.
- Direct-drive rotary motor + mechanical screw.
- Direct-drive rotary motor + magnetic lead screw (MLS).

Another thing that should be noted is that an actuator system includes actuator and drive & control electronics. The actuator not only includes electric motor and transmission mechanism but also protection components, such as brakes, stroke limits, sensors, and healthy monitoring, etc. However, these parts are beyond the profile of this thesis. Hence this thesis will only focus on electric motor part and drive & control electronics.

To compare these three EMA schemes, the primary control surface Aileron in Table 6.5 has been chosen as a benchmark. Since we are trying to build a modular EMA, the modularization of the EMA will be considered in the process of designing and comparison.

6.4.1 Direct-drive linear motor

The first scheme composed of only a linear motor, which is authentically a direct-drive actuator without any transmission part like mechanical screw and is normally characterised by excellent dynamic characteristic, high acceleration, and easy maintenance [143][144].

The modulization of a linear motor is simply done by dividing a short stator (primary) into three parts, each of which is a unit. The motor is modularized as three units, so the peak force of each unit is 16kN. Assuming an overload coefficient of 2, the rated force of each unit is 8kN. On the other hand, the maximum force will not occur at maximum speed. Hence the turning point of maximum force can be chosen at rated speed, which is half of the peak speed. The force-speed curve of the unit linear motor is shown in Figure 6.5.
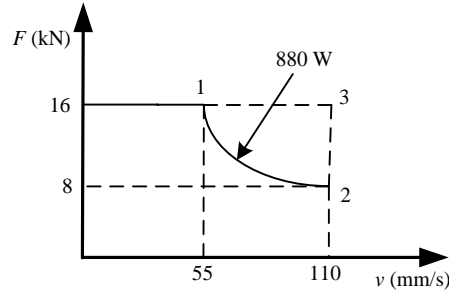
Figure 6.5 Force-speed curve of unit TPMLM
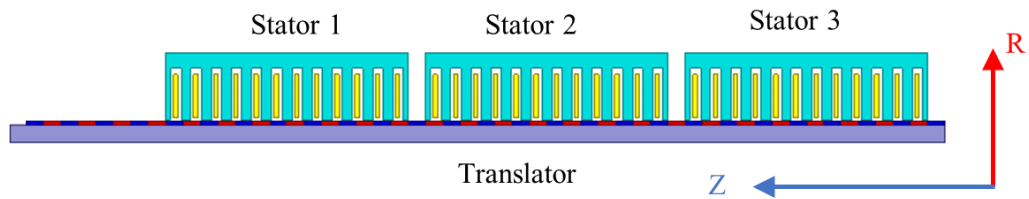
Figure 6.6 R-Z Model of a unit TPMLM

A 12 slots, 14 poles tubular PM linear motor (TPMLM) with FSCW, as in Figure 6.6, has been chosen due to its relatively high force density and no end-winding.

Referring to a rotary motor, the main dimensions equation of TPMLM can be written as

$$F = \frac{\sqrt{2}}{4}\pi K_w K_\Phi A B_{\delta av} D l_{ef} \qquad (6.1)$$

where K_Φ, K_w are winding factor and waveform factor, respectively; A, $B_{\delta av}$ are electric and magnetic loading, respectively; D, l_{ef} are airgap diameter and active axial length, respectively.

Table 6.6 Main design dimensions of a unit TPMLM

Parameters	Data	Parameters	Data
Stator outer diameter (mm)	420	Pole pitch (mm)	30 mm
Stator inner diameter (mm)	264	Air-gap length (mm)	0.8 mm
Active axial length (mm)	280	Stator slot numbers	12
PM magnetization length (mm)	5	Pole pair numbers	14
Width of PM (mm)	20	Peak frequency (Hz)	1.83

Table 6.7 Output characteristics of a unit TPMLM

	Point 1 (55mm/s, 16kN)	Point 2 (110mm/s, 8kN)	Point 3 (110mm/s, 16kN)
R (Ω)	0.216	0.216	0.216
Speed	0.055	0.11	0.11
Current (Arms)	94	37	94
J (A/mm^2)	9.8	3.9	9.8
Force (kN)	16	8	16
Copper loss (W)	5733	888	5733
Output power (W)	880	880	1760
Input power (W)	6614	1779	7494
Efficiency (η)	13.3%	50.1%	23.5%

From (6.1), the main design dimensions of a unit TPMLM can be obtained in Table 6.6. Their output performances on each operational point can be calculated using ANSYS Maxwell software and are summarized in Table 6.7. Iron losses are ignored due to the low speed characteristic.

The mass of each part of the motor is calculated in Table 6.8. Since the unique characteristics of short stator and long mover of TPMLM, the active mass of three modular TPMLM can also be achieved. It should be noted that the auxiliary components such as housing and support part are not considered, and this will be kept the same for the other two schemes. One can note that the net weight of a unit TPMLM is about 177 kg, and it would be 531 kg for three modular TPMLMs. The massive weight of linear motor topology seems to be not acceptable for aircraft actuation system applications.

Table 6.8 Mass distribution of the TPMLM

	Unit TPMLM (Active part)	Total TPMLM (Active part)
Armature copper weight (kg)	27	81.1
Magnet weight (kg)	9.7	29.2
Armature core steel weight (kg)	109.8	329.3
Translator core steel weight (kg)	30.6	91.8
Total net weight (kg)	177.1	531.4
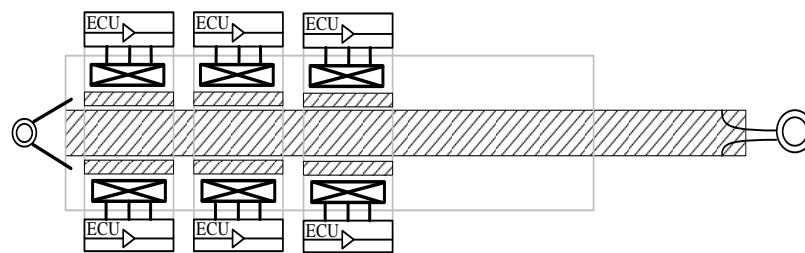
Figure 6.7 Modular EMA: direct-drive rotary motor with mechanical screw

6.4.2 Direct-drive rotary motor + mechanical screw (MS)

This configuration, as shown in Figure 6.7, adopts a direct-drive rotary motor integrated with a mechanical screw, which essentially serve as a force amplifier like a gear set, to convert rotary motion to linear motion. The simple modular design concept is also presented. The design requirements are the same as the linear motor.

The first thing is to determinate the characteristic of mechanical screw, specifically the lead of the screw, which will decide the gear ratio, and thereby the requirements for the rotary motor can be obtained.

Three primary factors are considered when selecting and sizing the roller screw: lead, nominal diameter, and dynamic load carrying capability. The lead of the screw determinates the gear ratio. The smaller the lead of the screw, the higher the gear ratio between torque and force conversion, whereas smaller lead means smaller load capabilities. Thus, there is a trade-off in selecting lead length. On the other hand, the

nominal diameter is a significant factor of impacting the mass of assembly and dynamic load carrying capability.

Table 6.9 shows the characteristics of the selected planetary roller screw from SKF [145]. Based on the force requirement, a lead of screw P_h of 5mm and normal diameter of 25mm is selected. The dynamic load carrying capability is 68.4 kN, which gives 40% of margin in terms of the required force; and the theoretical efficiency is 0.85.

Table 6.9 Selected planetary roller screw from SKF

Normal diameter (mm)	P_h (mm)	Dynamic load capacity (kN)	Efficiency
25	5	68.4	85%

Then, the gear ratio of roller screw can be calculated.

$$G_{rs} = 2\pi/P_h = 1256 \tag{6.2}$$

Maximum rotation speed n_{screw} and output torque T_{max} for prime rotary motor can be determined.

$$n_{screw} = 0.11/0.005*60 = 1320 \text{ rpm} \tag{6.3}$$

$$T_{max} = F_{max}/G_{rs}/\eta_{screw} = 45 \text{Nm} \tag{6.4}$$

Similar to linear motor scheme, the peak load will not appear at maximum velocity. Therefore, the torque-speed curve can easily be achieved, as shown in Figure 6.8.
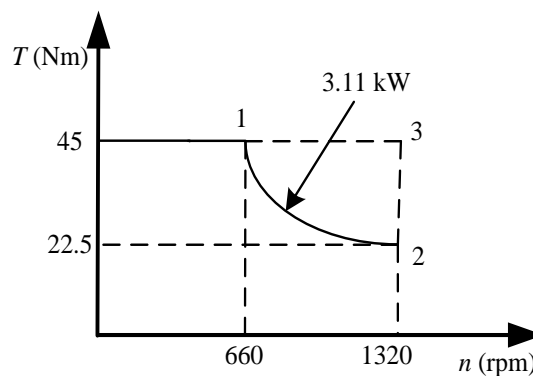
Figure 6.8 Torque-speed curve of 24S-22P PMSM

Table 6.10 Main design dimensions of 24S-22P PMSM

Parameters	Value	Parameters	Value
Stator outer diameter (mm)	136	Slot numbers	24
Airgap length (mm)	0.8	Number of turns/coil	48
Rotor outer diameter (mm)	82	Pole numbers	22
Rotor inner diameter (mm)	52	Pole-arc coefficient of magnet	0.85
Axial length (mm)	96	Thickness of magnet (mm)	5

Table 6.11 Characteristics of the 24S-22P PMSM

	Point 1 (660rpm, 45Nm)	Point 2 (1320rpm, 22.5Nm)	Point 3 (1320rpm, 45Nm)
R (Ω)	0.617	0.617	0.617
Current (Arms)	15	7	15
J (A/mm^2)	10.37	4.84	10.37
Iron loss (W)	40.7	76.5	119.5
Copper loss (W)	416.5	90.7	416.5
Output power (W)	3109.9	3109.9	6219.9
Total loss (W)	457.2	167.2	536.0
Input power (W)	3567.1	3277.1	6755.9
Efficiency (η)	87.2%	94.9%	92.1%
Torque (Nm)	45	22.5	45

A FSCW PMSM is selected as the prime rotary motor due to its higher torque density and fault-tolerant capability. Based on the main dimension formula of electric motor as below:

$$\frac{D^2 l_{ef}}{9.55T} = \frac{6.1}{K_\Phi K_w A B_{\delta av}} \qquad (6.5)$$

Considering the requirement of low speed and high torque density, a 24-Slots 22-Poles single-layer FSCW surface-mounted PMSM has been selected. The main design dimensions of this motor are summarized in Table 6.10.

The output characteristics such as EM torque and efficiency and mass distribution of the motor are summarized in Table 6.11 and Table 6.12, respectively.

An efficiency of higher than 90 % is observed in the rotary motor, and the scheme features a low weight of 13.1kg. Associated with the mechanical screw, the resulting efficency is higher than 76.5%. One should note that only the weight of active part is considered. In fact, the dimensions of the scheme are much smaller than the linear motor scheme; the difference in terms of auxililary parts like the housing and mounting components between the two schemes is also significant.

Table 6.12 Active mass distribution of EMA composed of rotary motor + MS

	Value (kg)
Copper weight	2.5
Permanent magnet weight	0.73
Stator core steel weight	3.74
Rotor core steel weight	1.35
Motor net weight	7.39
Roller screw weight	1.5
EMA total net weight	8.89

6.4.3 Direct-drive rotary motor + magnetic lead screw (MLS)

Like the second scheme, this configuration, as shown in Figure 6.9, adopts a direct-drive rotary motor integrated with a magnetic lead screw (MLS) instead of a mechanical screw. The modular design concept would be similar to scheme 2.

The MLS is similar to mechanical screw but without mechanical contact and works based on interacting magnetic force between two sets of helical magnets, making the gear system free from wear and friction losses. Without physical contact between rotary part and linear part, this provides the advantage of being free from jamming when compared to their mechanical counterpart, which is a critical factor for EMAs used in an aircraft actuation system. Moreover, the MLS has a built-in overload protection capability as it would slip if the load force is larger than the pull-out force (maximum magnetic force between rotary part and linear part), preventing it from permanent damage in the case of over-load. However, manufacturing complexity and demagnetization risk are concerns [146][147].

The first thing is to find out the design requiremnt of the MLS, such as the lead of the screw which determines the gear ratio, and pull-out force (force capability), and consequently the design requirement for the rotary motor can be achieved. To this end, the design of the MLS and rotary motor are presented accordingly.
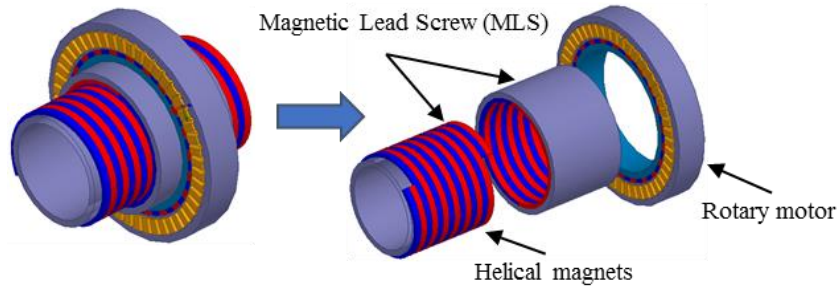
Figure 6.9 Rotary motor integrated with MLS

6.4.3.1 Magnetic Lead Screw (MLS)

As shown in Figure 6.9, the short outer part of the MLS is taken as the rotary part and the long inner part is taken as the translator (linear motion). It should be noted that the rotary part and linear part can be exchanged with each other. As with the mechanical screw, the gear ratio is inversely proportional to the lead length, and the lead also has a significant influence on pull-out force; the higher the lead, the higher the pull-out force [146].

The maximum load force should not exceed the pull-out force of an MLS to ensure the safe operation (without slipping). Therefore, the pull-out force is set to be 40% higher than that of maximum force requirement, namely 68.4 kN, which is the same as the mechanical screw in the scheme 2.

A pole pitch of 10mm and the numbers of poles of 2 is selected, then the resulted gear ratio can be calculated

$$G_{mls}=2\pi/(2*10*0.001)=314 \tag{6.6}$$

From the data in [146] and [147] and the preliminary study, the shear stress δ_g (force per surface airgap area) of MLS of 350 kN/m^2 can be achieved, under which the air-gap surface area $S=F/\delta_g=0.195m^2$ can be determined ($S=\pi D*L_{ef}$, D is the outer diameter of tranlsator, L_{ef} is the effective rotor length). It is apparent that the D will change with different L_{ef}.

Figure 6.10 summarized the variation of effective axial length and mass distribution versus different outer diameter D of MLS. It can be observed that the L_{ef} of MLS is decreasing when outer diamenter D increases. A decreasing trend exists for the rotor mass part when increasing D, but the translator mass and total mass considering the stroke part is increasing. To have a higher force density and reasonable dimensions, a translator outer diameter of 150 mm and active axial length of 414.7 mm are selected. By using 3-D FEM alaysis, the parameters such as magnet dimensions and translator diameter D are optimized. Finally, the main dimensions of the MLS are summarized in Table 6.13.

(a) Active axial length   (b) Mass
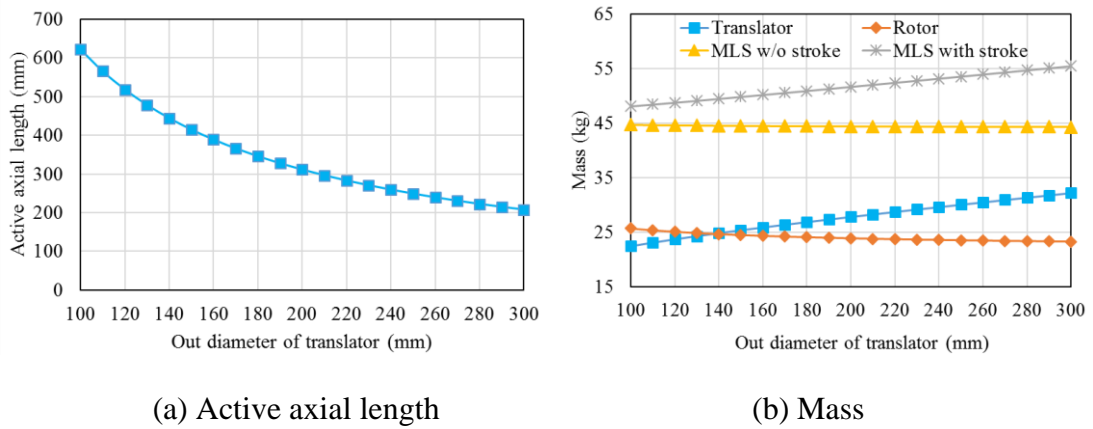
Figure 6.10 Active axial length and mass as a function of outer diameter of translator

Table 6.13 Main design dimensions of MLS

Parameters	Value	Parameters	Value
Pole numbers	2	Thickness of magnet (mm)	7
Pole pitch τ (mm)	10	Embrace of magnet (mm)	10
Active axial length (mm)	414.7	Translator mass (kg)	17.9
Translator outer diameter (mm)	150	Rotor mass (kg)	21.7
Rotor outer diameter (mm)	180	Total mass w/o stroke (kg)	39.6
Airgap length g (mm)	1	Total mass w/ stroke (kg)	44.9

6.4.3.2 Direct-drive rotary motor design

A conservative conversion efficiency of 80% is assumed for the designed MLS from the data in [146] and [148]. With the gear ratio of 314, the torque and speed requirement to the rotary motor can be achieved.

- Maximum toque: T= 48000 / (0.8*314) = 192 Nm
- Maximum rotation speed: n=314*0.11*60/(2π) = 330 rpm

The same design process as for the previous 24S-22P motor can be used for this rotary motor. A 48 slots 44 poles single-layer FSCW surface-mounted PMSM is designed. The main dimensions and output performances are summarized in Table 6.14 and Table 6.15, respectively. Therefore, the total weight distibution can be summarzied in Table 6.16 and Table 6.17.

Table 6.14 Main design dimensions of the 48S-44P PMSM

Parameters	Value	Parameters	Value
Stator outer diameter (mm)	285	Conductor numbers per slot	37
Airgap length (mm)	0.8	Pole-arc coefficient of magnet	0.85
Rotor outer diameter (mm)	214	Thickness of magnet (mm)	5
Rotor inner diameter (mm)	185	Slot numbers	48
Axial length (mm)	54	Pole numbers	44

Table 6.15 Output characteristics of the 48S-44P PMSM

	Point 1 (165rpm, 192Nm)	Point 2 (330rpm, 96Nm)	Point 3 (330rpm, 192Nm)
R (Ω)	0.296	0.296	0.296
Current (Arms)	27	12	27
J (A/mm^2)	9.27	4.12	9.27
Iron loss (W)	36.5	65.0	98.8
Copper loss (W)	647.2	127.8	647.2
Output power (W)	3317.3	3317.3	6634.6
Total loss (W)	683.7	192.8	746.0
Input power (W)	4001.0	3510.1	7380.5
Efficiency (η)	82.9%	94.5%	89.9%

Table 6.16 Mass distribution of 48S-44P PMSM

	Value (kg)
Armature copper weight	3.1
Permanent magnet weight	1.1
Armature core steel weight	6.9
Rotor core steel weight	2.3
Total net weight	13.4

Table 6.17 Mass distribution of EMA composed of rotary motor plus MLS

	Weight (kg)
MLS w/o stroke	39.6
Drive rotary motor	13.4
Total w/o stroke	53

6.4.4   Scheme comparison

Now that we have three designs for a possible actuator, the characteristics of different EMA design schemes are compared in terms of weight (thrust density), fail-safe capability, cost, efficiency, life duration, and stiffness.

Performance comparison of these three schemes has been summarized in Table 6.18, and Figure 6.11 plotted their thrust density comparison. The first EMA scheme composed of linear motor seems a good option for its direct-drive characteristic, jamming free capability, and aptness for modular design, but its thrust density, which is a critical factor for aircraft actuator, is too low (only about 0.1kN/kg), making it unacceptable. In fact, this is reasonable as linear motor is a direct-drive without conversion from rotary to liner motion (which act as force amplifiers), compared to the other two schemes. In addition, the efficiency is a very low.

The second EMA scheme that used a 24S-22P FSCW PMSM integrated with a planetary roller screw is a great option in terms of high thrust density (5.4 kN/kg) and high efficiency; the prime rotary motor is fault-tolerant. In addition, the efficiency is the highest among the three schemes. However, the roller screw may bring in the risk of mechanical jamming, which is a crucial factor for aircraft actuators as this may

result in a catastrophic accident. An additional disconnect device should be included for the actuator which makes the actuator system more complicated. Another concern is mechanical wearing, which is hard to predict, bringing in the risk of backlash.

Table 6.18 Performance comparison of three EMA schemes

	Tubular PM linear motor (18S-20P FSCW)			Rotary motor (24S-22P PMSM)+ RS			Rotary motor (48S-44P PMSM) +MLS		
Maxiumum thrust (N)	48000			48000			48000		
Component mass (kg)	NA			24S-22P PMSM		RS	48S-44P PMSM		MLS
				7.4		1.5	13.4		39.6
Actuator net mass (kg)	531.4			8.9			53		
Thrust density (N/kg)	90.3			5393.3			905.7		
Motor Efficiency (η)	P1	P2	P 3	P1	P 2	P 3	P 1	P 2	P 3
	0.13	0.50	0.24	0.87	0.95	0.92	0.83	0.95	0.90
J (A/mm2)	9.8	3.8	9.8	10.4	4.8	10.4	9.3	4.1	9.3
Converter efficiency	N/A			0.85			0.80		
Actuator efficiency	0.13	0.50	0.24	0.74	0.81	0.78	0.66	0.76	0.72
Active size (mm)	Outer diamater		Length	Outer Diamater		Length	Outer Diamater		Length
	420		860	136		96	285		370
Power factor	Vey low			Average			Average		
Dynamic capability	Low (high inertia, large mover mass)			Average			Large rotor moment inertia (Large diameter, large rotor mass)		
Positioning accuracy	High			Average			Average		
Manufacturing	Average			Average			Complex, helical magnet		
Stiffness & Reliability	Free from jamming; Easy for modular design.			Mechanical jamming; wearing; High maintenance cost.			No physical contact; Free from jamming.		

The third scheme consists of a 48S-44P FSCW PMSM coupled with a magnetic lead screw (MLS). The thrust density is about 0.9 kN/kg, which is 6 times smaller than the second scheme and nine times higher than that of linear motor scheme. On the other hand, the rotation-to-linear converter is a magnetic lead screw (MLS) working based on the interacting magnetic force between two sets of helical magnets, giving it no physical contact between rotor and translator and therefore free from jamming. Moreover, the prime rotary motor is also fault-tolerant.

It can be concluded that the first scheme of linear motor, at least so far, is not acceptable due to its poor thrust density; Both second and third scheme are promising, which are integrated with a torque-to-force amplifier making them light. The second scheme is not possible unless used in conjunction with a disconnect device to deal with the critical jamming problem. The third scheme is free from jamming which is critical to the aircraft, however, the relatively low thrust density and the manufacturing complexity of helical magnet and the high risk of demagnetization in the magnetic lead screw (MLS) are significant concerns, resulting in weak stiffness and a low life cycle. Therefore, the second EMA scheme of rotary motor integrated with roller screw is selected in this thesis for further investigation.
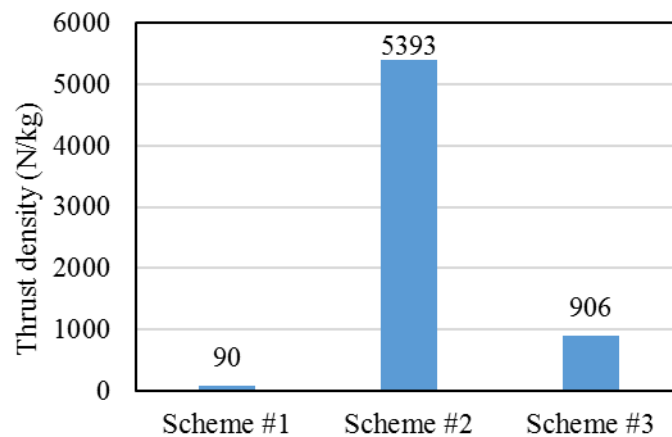
Figure 6.11 Comparison of thrust density of the three EMA schemes

6.5   Reliability of actuation system architecture

Reliability is the critical factor in the deployment of aircraft subsystems as safety is the highest priority. The exploration of deploying electromechanical actuator (EMA) system in aircraft raises concerns on their reliability and failure probability. The large

number of components of the prime electric motor, mechanical screw, power converter, and control electronics included in the EMA system brings a big challenge. Therefore, it is necessary to evaluate the overall reliability and performance of EMA system at aircraft application-level, e.g. control surface level.

Risk of mechanical jamming acts as a crucial limit on the deployment of EMAs for safety-critical systems. However, jamming might be allowed for some non-safety-critical systems such as secondary control surface and cabin actuation systems. Therefore, the EMA reliability should be evaluated in the circumstances of both allowing and avoiding jamming.

6.5.1 Failure probability analysis without considering jamming

The method of a fault dependency diagram offers a rapid evaluation of overall failure rate for a given control surface actuation system configuration. In a A320, two Elevator Aileron Computers (ELAC) and two Spoiler Elevator Computers (SEC) are utilized for the Elevator surface, and each Elevator has two actuators. Figure 6.12 depicts the fault dependency diagram of a control surface with two EMAs connected in parallel without considering mechanical jamming.
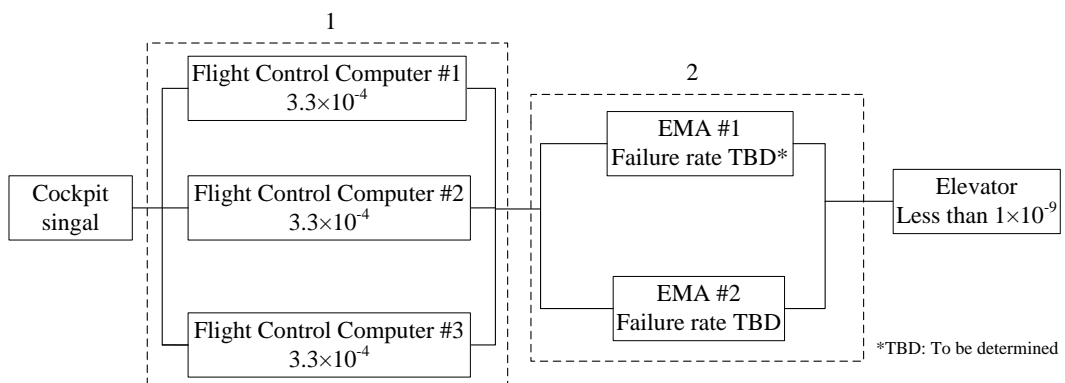
Figure 6.12 Fault dependency diagram of Elevator with two EMAs in parallel

The Flight Control Computer (FCC) is at the core of any modern civil or military aircraft and is subject to strict compliance to safety standards for software and hardware such as DO-178C and DO-254, with a failure probability in a level of 10^{-4} [149][150]. Considering the criticality of FCC, it is often used with dual or triple redundancy.

According to the specification regulation for development of civil aircrafts and systems from ARP4754 [151], the probability of loss of control (PLOC), which is the worst case, should be less than 1.0×10^{-9} per flight hour. The failure probability demands on the actuator or EMA could then be obtained from Figure 6.12, and it can be expressed as below

$$P(1) + P(2) - P(1)*P(2) \leq 1.0 \times 10^{-9} \qquad (6.7)$$

$$P(1) = (3.3 \times 10^{-4})^{\wedge}3 \qquad (6.8)$$

$$P(2) = (P(EMA))^{\wedge}a \qquad (6.9)$$

where $P(1)$ and $P(2)$ is the equivalent failure probability of first part and of second part, respectively; $P(EMA)$ is the failure probability of each EMA in the second part; a is the number of EMAs connected in parallel.

Therefore, the equivalent failure probability of second part $P(2)$ can be calculated, which value is 1.0×10^{-9}. As for the example showing in the Figure 6.12, two EMAs are used for the control surface, so the failure probability of each EMA should be lower than 3.2×10^{-5}. Based on a similar idea, if a control surface e.g. Rudder, is deployed with three EMAs connected in parallel, the failure probability of an EMA should be less than 1.0×10^{-3}. If only one EMA #1 is used for a control surface, e.g. a Spoiler, the failure probability of EMA should be less than 1.0×10^{-9}. In all, the failure probability demands on EMAs for control surface with different levels of redundancy are summarized in Table 6.19.

The failure probability of an EMA is determined by its components. An EMA normally consists of a direct-drive rotating motor or of a high speed motor plus a gearbox under some circumstances, a mechanical screw such as roller screw or ball screw converting rotary to linear movement, and a controller & power inverter. A fault tree analysis (FTA) can be utilized for determining the failure probability of an EMA [61] and the simplified fault tree of a single-lane EMA is shown in Figure 6.13.

Table 6.19 EMA failure probability demand for different levels of redundancy

	One EMA only	Two EMAs in parallel	Three EMAs in parallel
Failure probability limit	1.0×10^{-9}	3.2×10^{-5}	1.0×10^{-3}
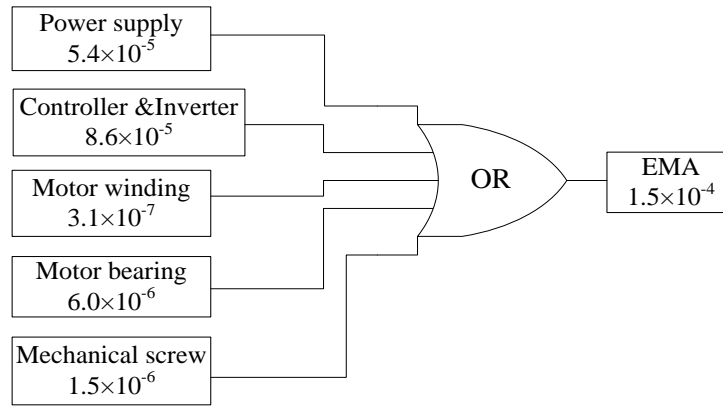
Figure 6.13 Fault tree of a single-lane EMA

The failure probability of a power supply is not direct as it may include both AC and DC power bus for current civil aircrafts with 115-120V/400HZ AC power system, in which a AC/DC converter has to be used although a matrix converter could possibly be adopted to avoid the AC/DC converter [67]. A probability of 7.0×10^{-4} for loss of one channel AC power was suggested in [152] in 2008. In 2011, John and Glynn [61] suggest that the probability of loss of power bus is around 5.4×10^{-5}, and a figure of 4.8×10^{-5} was assumed in [149]. With the increasing demanding for on-board generation system, a higher voltage DC electrical system such as ±270V DC system is to be considered to reduce current rating, improve efficiency and reduce system weight, which will also improve the reliability of aircraft electrical power system [153]. Thus, a figure of 5.4×10^{-5} for the loss of power supply is used.

The mechanical part involves mechanical screw, e.g., planetary roller screw and bearings. A failure probability of 1.5×10^{-6} for a roller screw could be identified from their MTBF in [154]. According to [155], the bearings are to be responsible for the 95% of AC motor failure in the worst case, from which a failure probability of 6.0×10^{-6} could be achieved by the MTBF of 159021 hours obtained by an IEEE industrial Survey.

Similarly, the winding failure probability of 3.1×10^{-7} can be calculated by assuming winding failure responsible for the remaining 5% of total failures in the AC motor [155]. A conservative figure of 8.6×10^{-5} can be assigned to the Controller & Inverter failure [156]. Apparently, the mechanical components are more reliable than the electronic components.

Each component failure will lead to the loss of control of EMA, and the resultant probability of loss of control of the EMA is around 1.5×10^{-4} per flight hour from Figure 6.13, which clearly is not less than 1.0×10^{-9} per flight hour; this data however is reasonable compared to the merged failure rate of 50.2 failures per million operating hours for military quality linear EMAs stated by NPRD-2011[157].

In fact, all components of the EMA have a failure probability that is many orders of magnitude higher than the target requirement. For a control surface with two EMAs connected in parallel, the single-lane EMA is still unable to provide the required reliability, but it works for a control surface with three EMAs in parallel, as compared to the data in Table 6.19. Hence, one EMA configuration may be used for non-safety-critical surfaces like Spoilers, while the safety-critical control surfaces such as Aileron and Rudder necessarily require a higher level of redundancy of three EMAs in parallel.

To make an EMA feasible for the safety-critical control surfaces such as Elevators and Ailerons with two EMAs connected in parallel, the failure probability of EMA must be improved. A scheme of EMAs with multi-lane fault-tolerant electric drive is proposed. Figure 6.14 shows the basic fault tree of an EMA with dual-lane electric drives, which also refers to a dual-lane fault-tolerant EMA.
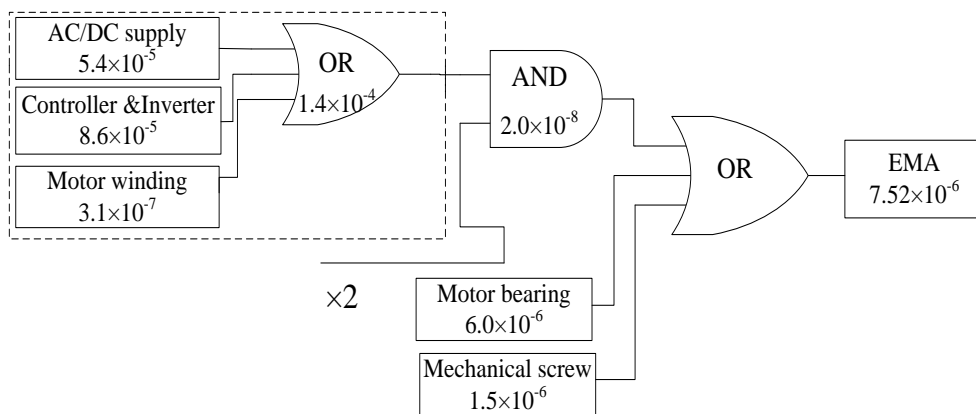
Figure 6.14 Fault tree of a dual-lane EMA

The resulting failure probability of the dual-lane EMA is 7.52×10^{-6}, which is significantly reduced compared to its single-lane counterpart and apparently meets the demands of less than 3.2×10^{-5} stated in Table 6.19. Similarly, if a third lane electric drive is incorporated into the EMA, the failure probability of the electric part can be further reduced to 2.7×10^{-12}, under which the resulting reliability of the EMA is now

restricted by the mechanical failure probability of 1.5×10^{-6}. Therefore, an EMA with dual-lane electric drives could deliver the best failure probability requirement for the safety-critical control surfaces without considering mechanical jamming.

6.5.2 Failure probability analysis considering jamming

For conventional hydraulic actuators (HA) or electro-hydrostatic actuators (EHAs), fluid pressure will be removed when a fault occurs, and the actuator will be converted to damping mode automatically, under which the parallel connected redundant actuators can still drive the control surface according to commands from the Cockpit without any serious issues. However, this is not the case for an EMA, as the jamming of EMA, e.g. mechanical screw failure, could make the control surface freeze even if another parallel connected EMA works. Therefore, the problem of mechanical jamming is a critical concern, and must be carefully considered, as this may otherwise result in a disastrous event even in a surface with multiple redundant EMA units.

In the aspect of reliability, fault tree analysis can also be used, but the failure probability and the logic connection of the jamming problem should be carefully dealt with. The jamming of an EMA will result in the loss of control of the surface even with redundant EMAs connected in parallel without breakdown. The methods of using an anti-jamming system, a dual load path, or disconnect devices have been proposed [61][75], ensuring the free movement of control surfaces governed by the redundant actuators after the jamming of one actuator. These methods inevitably increase the system complexity, but it is necessary if we want to advance the EMA for safety-critical flight control surfaces in MEA.

In order to analyse the reliability, taking a control surface with two EMAs as an example, the fault dependency diagram of the control surface and revised fault tree of an EMA can be redrawn, as shown in Figure 6.15 and Figure 6.16. One can observe that both mechanical screw and anti-jamming part have been taken out from the EMA and are being put on the last part of the fault dependency diagram to represent fault logic conditions, under which the EMA is divided into electric and mechanical subsystems. The exact type of anti-jamming system is not specified, but it is reasonable to regard it as an electromagnetic actuation system including control, monitoring, and actuation component. Thus, a failure probability of 1.5×10^{-4}, which equals to the failure probability of a single-lane EMA, could be assigned to it [158].
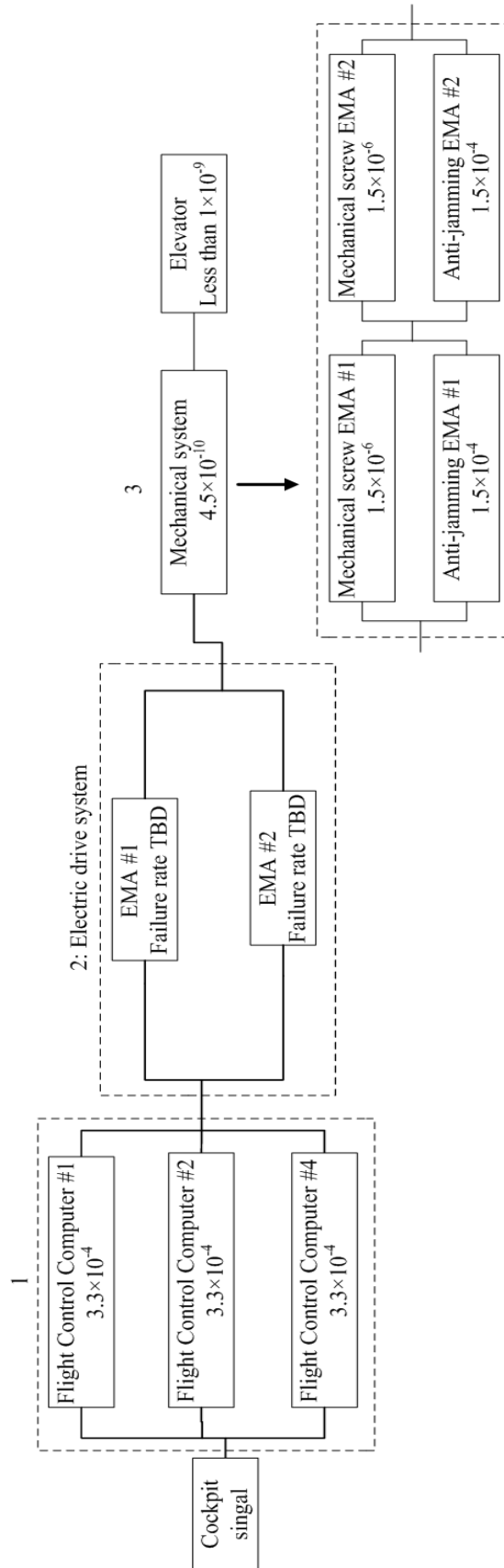
Figure 6.15 Fault dependency diagram of a control surface with two anti-jamming EMAs in parallel connection
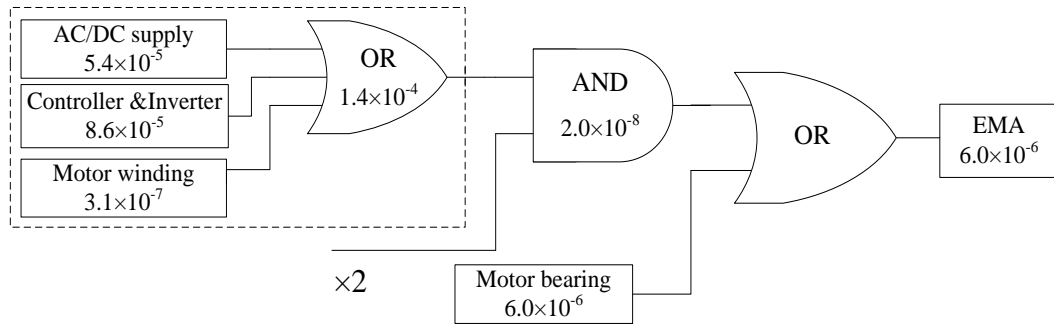
Figure 6.16 Revised fault tree of anti-jamming EMA with dual electric drives

Table 6.20 Failure probability demands on EMA for different levels of redundancy considering jamming

	One EMA	Two EMAs	Three EMAs
Failure probability limit	7.4×10^{-10}	2.3×10^{-5}	7.3×10^{-4}

Table 6.21 Failure probability of revised EMA with different levels of electric drives

	Single-lane Electric drive	Dual-lane Electric drives	Triple-lane Electric drives
Failure probability	1.5×10^{-4}	6.0×10^{-6}	6.0×10^{-6}

The overall failure probability of the safety-critical control surfaces must meet the requirement of 1.0×10^{-9}. This means the constraints on the failure probability of the EMA can be expressed as

$$P(1)+P(2)+P(3)-P(1)*P(2)-P(1)*P(3)-P(2)*P(3)+P(1)*P(2)*P(3) \leq 1.0 \times 10^{-9} \quad (6.10)$$

where $P(3)$ is the equivalent failure probability of the mechanical system part.

From Figure 6.15, the requirement of failure probability limit on the second part $P(2)$ can be calculated, which is 5.2×10^{-10}. For different levels of EMA redundancy, the corresponding failure probability limit on each EMA can be calculated from (5.10) and they are being summarized in Table 6.20.

An example of the revised fault tree of EMA with dual-lane electric drive is shown in Figure 6.16, without considering the mechanical subsystem failure, in which the resulting failure probability is 6.0×10^{-6}. Similarly, the failure probability of the

revised EMA with different redundancy levels of electric drives can be calculated as well, and their values are summarized in Table 6.21. One can note that the failure probability will not be less than 6.0×10^{-6}; this is because of the restriction from motor bearing failure.

For a control surface with only one EMA, the EMA cannot meet the safety failure probability limit irrespective of the redundancy level of electric drive. Thus, a control surface with one EMA can only be used for non-safety-critical actuation systems.

For a control surface with two parallel EMAs, the EMA equipped with dual electric drives with a failure probability of 6.0×10^{-6} could meet the corresponding requirement of less than 2.3×10^{-5} in Table 6.20. It is also the case for EMA driven by triple electric drives. Therefore, it is demonstrated for the surface with two parallel EMAs, the EMA with more than one electric drive is necessary to achieve a reliability of less than 1.0×10^{-9} for safety-critical actuation systems.

The reliability demands on each EMA will be reduced when the control surface has three or more EMAs in parallel. In the case of three EMAs, e.g. Rudder, the failure probability demand on a single EMA is less than 7.3×10^{-4}, suggesting that an EMA could meet the reliability requirement irrespective of the redundancy level of the electric drive, according to the data in Table 6.21.

In all, it is confirmed that a level of redundancy of two anti-jamming EMAs in parallel is necessary for the deployment of EMA in the aircraft safety-critical actuation control surface such as Elevator and Rudder. A single EMA configuration could only be considered for a less critical control surface, for example a Flap or Slat.

6.6   Fault-tolerant rotary motor design considerations

After demonstrating the topology and redundancy levels of EMA for safety-critical control surfaces in the MEA, the design of primary motor has come to the focus. Both the electromagnetic and thermal performance must be considered and evaluated in the whole design cycle. This section deals with the considerations for designing a fault-tolerant motor.

6.6.1 Design aspects of rotary motor for EMA

It has been proved that a prime rotary motor with dual-lane electric drive is required for safety-critical applications in the MEA. On top of this, both high torque density and good fault-tolerant capability are also compulsory requirements. An advantageous motor topology of permanent magnet synchronous motor (PMSM) is preferred; When equipped with fractional slot concentrated winding (FSCW), a low-speed high-torque density with excellent fault-tolerance can be achieved. The duty cycle and thermal behaviour of the actuators must be fully considered to determine the peak electric loading/current density of the motor within the given temperature limits.

The fault-tolerant motor typically involves multi-lane electric drives with either multiple single-phase or multiple three-phase windings to provide levels of redundancy, ensuring normal operation or reduced output after faults occur. The motor's thermal behaviour under normal and especially fault conditions required to be studied as the motor will be fed with overload current under single-lane fault in order to overcome the loss of and even negative dragging torque of the faulty lane. In addition, the isolation between different lanes in the electrical, thermal, magnetic, and physical aspect must be carefully considered to mitigate the propagation of faults. Unbalanced magnetic pull (UMP) under normal and fault conditions is also critical as this may present a crucial impact on the stiffness and life cycle of the mechanical system.

Table 6.22 Comparison of different motor topologies in the EMA application

	PMSM		IM	SR
	FSCW	ISDW		
High torque density	*	+	-	-
Low speed	+	-	-	*
Electrical isolation	+	-	-	+
Magnetic isolation	+	-	-	+
Physical (thermal) isolation	+	-	-	+
Suppress the short-circuit current	+	-	-	+
No UMP under normal and faults	+	+	*	*
Stiffness	*	-	+	+

+: superior; *: average; -: inferior.

A comparison of different motor topologies such as PMSM and IM, are summarized in the Table 6.22. Due to the extreme requirements of high torque density and operation capability under fault or fail-safe conditions for EMA, the FSCW PMSM topology arises due to their high torque density and achievable isolations between lanes in the EM, thermal and physical aspect. Moreover, this topology could provide the possibility of limiting the terminal short-circuit (SC) current to 1 pu of rated/peak current because of their large per-phase inductance.

6.6.2 Thermal behavior over the mission profile

The thermal requirements on the EMA are represented by the demands over the whole mission profile. In order to meet the safety regulations, the most serious conditions (such as critical flight phases of serious turbulence and faults) must be considered, and this determines the sizing of an EMA. The actuation system is usually without any additional cooling system, making the thermal design quite a challenge. Moreover, the thermal behaviour of motor itself is not only determined by the thermal limitations from the materials but also limited by the requirements from aircraft level. For example, the maximum temperature at EMA skin should be around 100°C for qualitative safety requirement at wing level [69], which is obviously much lower than the thermal limit of the housing material (aluminium).

Another critical challenge is the extreme working environments of high altitudes and high temperature variation ranges. For instance, the air temperature could be higher than 40 °C on the ground when taxing or in the low attitude during take-off while a negative 50 °C could be expected in a height of 35,000 feet during cruise phase.

Thermal performance under fault conditions must be involved during the whole design cycle as this determines the fail-safe capability of an EMA which is critical for aircraft actuation system. For example, in the case of losing one lane for a dual-lane EMA system, the remaining healthy lane has to offer the full load demands, which might double the electrical loading and consequently results in a higher thermal load/stress in the healthy lane.

In addition, the duty cycle is an important criterion in sizing the actuator. Actuator force and rate demands vary at different flight phases. A generic aircraft mission profile includes taxi, take-off, climb, cruise, descend, and landing. Apparently,

the mission profile would be the start point in specifying the actuator design requirement.

Figure 6.17 depicts a worst duty cycle scenario of two minutes of peak torque and peak speed demand and one minute off repeating 3 times, which is reasonable as the extreme demands occurs at serious turbulence which is usually less than one or two minutes. This torque profile will be used for the EMA design and thermal performance evaluation in the next section.

In all, the thermal management of an EMA should be studied with regards to the torque/speed demands, fault conditions, material properties and the duty cycle requirement in the aircraft mission level.
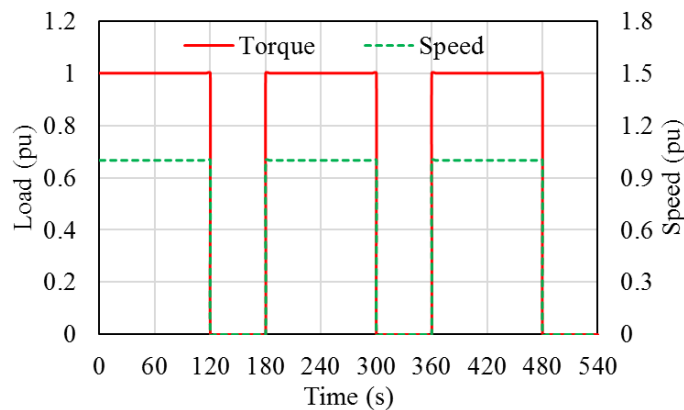
Figure 6.17 Duty cycle for EMA design evaluation

6.6.3 Fault-tolerant motor design, control strategy and comparison

The redundancy and fault management requirements applied to the rotary motor for an aircraft actuator can be defined as below [156]. It should be noted that the output is based on the flight control surface level regarding the load demand.

- No output degradation after the first fault (e.g. open-circuit (OC) & terminal short-circuit (SC)).
- Acceptable output degradation, e.g. 50%, after the second fault.

The design requirements for a fault-tolerant motor are directly related to the redundancy level of the control surface, and the configuration with at least two anti-jamming EMAs connected in parallel has been confirmed as necessary in the

deployment of EMA for safety-critical aircraft actuation applications, which is regarded as a basis to give an insight on the issues in the designing of a fault-tolerant motor. Two alternative multiple lane fault-tolerant drives, viz. multiple single-phase and multiple three-phase as in Figure 6.18, are considered.

(a) Triple-lane single-phase   (b) Dual 3-phase
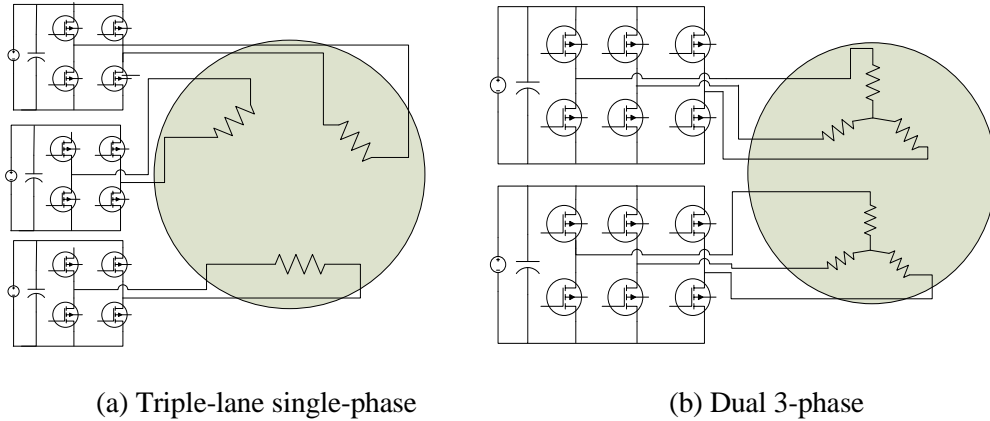
Figure 6.18 Electric motor with multiple drive systems

Table 6.23 Comparison of fault-tolerant electric drive topologies

Configuration of motor	Multiple single-phase		Multiple three-phase		
	Dual-lane	Triple-lane	One-lane	Dual-lane	Triple-lane
Total number of lanes	4	6	2	4	6
Number of phases	4	6	6	12	18
Number of switches	16	24	12	24	36
SF* after first OC	0.67	0.75	1	0.67	0.75
SF after second OC	0.5	0.75	N/A	0.5	0.75
SF after first SC	0.8	0.67	2	0.8	0.67
SF after second SC	1	0.5	N/A	1	0.5
Overall SF of Motor	1	0.75	N/A	1	0.75
SF for mechanical failure	1	1	1	1	1
Overall SF of Surface	2	2	N/A	2	2

Table 6.23 summarized a comparison of different multiple lane topologies for the actuation architecture with two anti-jamming EMAs connected in parallel in terms of sizing factor, number of total lanes, and power switches, etc. One should note that a suitable motor design has been assumed so that the motor can continuously operate

to provide the required torque under both open-circuit (OC) and terminal short-circuit (SC) conditions, and the same peak current limit is applied. In addition, three or four independent power supplies are available for a modern commercial aircraft, implying non-isolated lanes exist for EMA with up to three lanes electric drives.

It is clear that for either multiple single-phase electric or multiple three-phase drives, each EMA is required to be driven by at least two independent or isolated lanes to provide the necessary fault-tolerance at control surface level; with the same number of lanes, the multiple 3-phase drives generally require a higher amount of power switches.

In addition, it indicates that the higher the number of lanes, the lower the overall sizing factor (SF) of the motor, suggesting an EMA with a higher number of lanes is preferred. However, the independent power supply is limited with usually three or four lanes for modern commercial aircraft. On the other hand, this view only accounted for electric faults, but the control surface must survive or keep working after the mechanical failure such as failure of the mechanical screw and bearing. Thus, a minimum size factor of 1 is necessary in case of one EMA faults, while the parallel connected EMA can still provide required output load requirement. Therefore, the motor with dual-lane electric drives is selected, under which the resultant overall SF of surface level is 2.

For a motor with dual-lane configuration, the number of switches for multiple 3-phase drives is 24, which is higher than that for a multiple single-phase drive. However, the influence of remedial strategy under fault has also to be considered. For a multiple single-phase motor, a large torque ripple is expected after remedial strategy employed to overcome the influence of the faulty lane, and the current in each individual phase must be reshaped or re-scaled to overcome that, implying a higher harmonic current and consequently a higher PWM implementation complexity. However, for multiple 3-phase motors, the motor is divided into multiple independent 3-phase motor lanes, which means the current on each lane only requires to be scaled by the required factor, reducing the control complexity and PWM implementation cost [61].

On the other hand, the motor is driven by a power converter. This implies another requirement to the DC input filter to minimize the distortion of power supply.

The multiple single-phase motor operated from an independent DC power requires significant input filter efforts, increasing the power converter volume and weight. In contrast, the demands on the input filter for a three-phase inverter is much less due to less harmonics. Therefore, the motor with dual three-phase drive is identified as the final candidate for our EMA application.

6.7   Chapter summary

In this chapter, the concerns of the electromechanical actuator (EMA) including actuation system architecture and actuator topologies have been evaluated, in terms of weight, reliability, size, efficiency and cost. A fault-tolerant rotary motor plus mechanical screw has been identified as the final EMA candidate.

The reliability of the actuation system architecture and the failure probability of different actuation configurations have been evaluated. Specifically, the feasibility of deployment of EMAs with anti-jamming system in a safety-critical actuation system was confirmed.

The considerations including electromagnetic and thermal aspects in the design of a fault-tolerant rotary motor are presented, and the best configuration of two anti-jamming EMAs in parallel connected, with each EMA equipped with a dual three-phase drive, has been identified, which meets the requirements of the safety-critical actuation applications. All of this provides a significant step advance towards the deployment of pure electric actuation systems in the MEA.

Chapter 7

Electromechanical Actuator: Fault-Tolerant Rotary Motor Design

In the previous chapter, the EMA configuration composed of rotary motor with mechanical screw is identified as a promising solution to develop a modular electromechanical actuator (EMA) featuring high force density and high efficiency. The design considerations of the EMA with a fault-tolerant rotary PMSM motor equipped with dual 3-phase electric drives (defined as a dual 3-phase EMA motor) have been evaluated. In this chapter, the modular structure design, electromagnetic design, and thermal management of the dual 3-phase EMA motor will be investigated.

7.1 Modular EMA envelope

As has been depicted in Section 6.3, the EMA design requirement was evaluated for the primary control surface such as Aileron or Rudder for a single-aisle aircraft. Different control surfaces have different levels of force/power requirement. To meet a diverse range of actuation requirements, a modular EMA design concept is desired; thus, for different force/power requirements, several modular EMAs can be assembled to deliver the desired requirement. Therefore, the modular EMA envelope must be established first.

Taking three EMA units as an example, the basic envelope of the originally designed actuator (not a modular configuration) is shown in Figure 7.1(a). Based on this, a semi-modular and full-modular envelope are presented, as in Figure 7.1 (b) and (c).

With the full-modular design, each modular unit is completely independent and has its own prime electric motor, rolling bearings, and endcap. It is obvious that this scheme will result in larger mass and space wasted. There are only two bearings and two endcaps in the semi-modular scheme, which can reduce the total mass by elimination of additional bearings and induced shorter housing axial length, but this is just a modularization of the rotary motor. Taking the factors of weight, space limitation and modular concept into account, an improved full-modular design is proposed, as in Figure 7.1 (d), which can remove the two sets of bearing and endcap between the modular units, saving weight and space without losing the modularization. In addition, the single set of bearings between units can improve the mechanical stiffness.

(a) Original

(b) Semi-modular

(c) Full-modular

(d) Improved full-modular
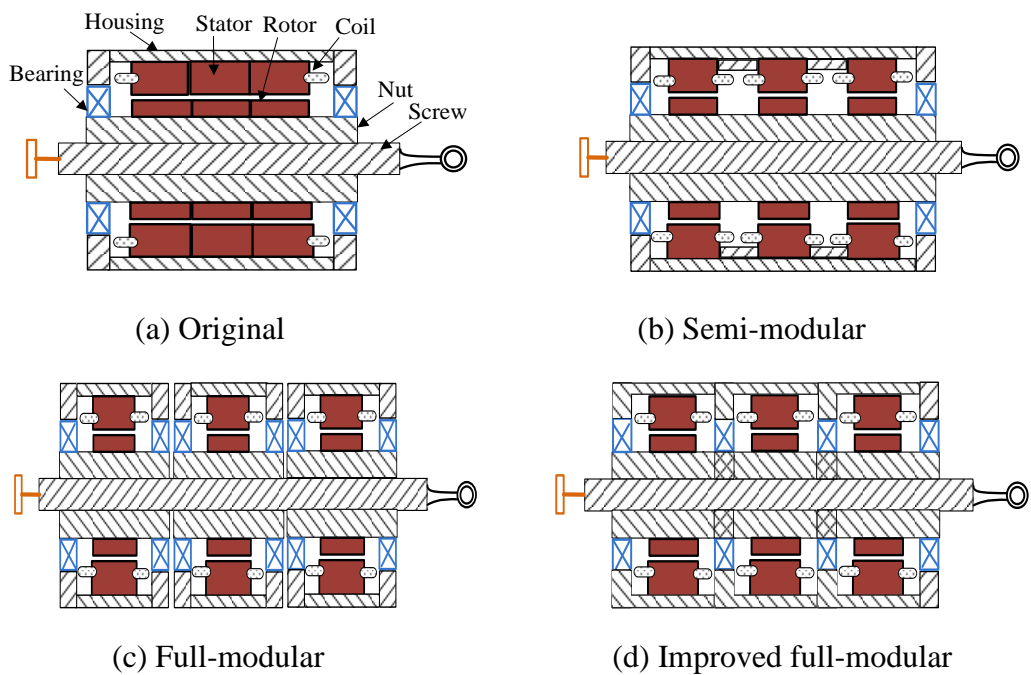
Figure 7.1 Comparison of different modular design envelopes

However, with the configuration of short nut and long screw, the linear movement of the long screw demands space on both sides of the housing, which may create additional space claim and increase total volume; In addition, there is a potential risk of screw rotating, which poses a torsional torque to the load. Thus, another

configuration with long rotating screw and short nut linearly moving is proposed, as in Figure 7.2(a). In this case, the long screw is connected to the rotating rotor, while the short nut is coupled with the rod connected to load. An anti-rotating slider is coupled with the nut imbedding into the long housing channel. The modular concept can still be implemented from the primary rotary motor side, as shown in Figure 7.2(b). Single set of bearing and end plate between the two units can be eliminated, as can be seen from the cross section view in Figure 7.3; and if there are three units, two sets of bearings and end plates between the three units can also be eliminated. Therefore, this EMA configuration is adopted.
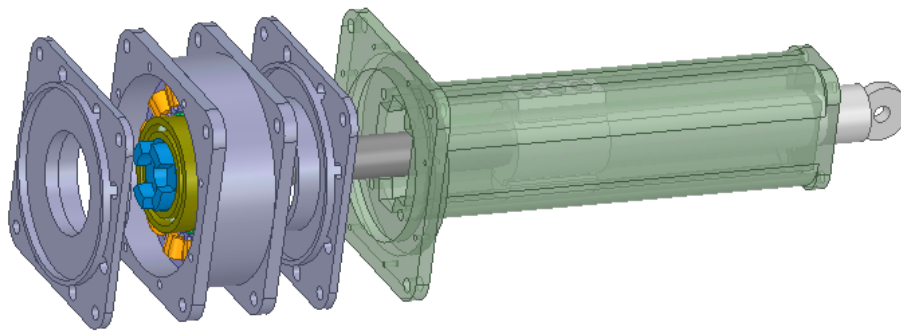
(a) One unit
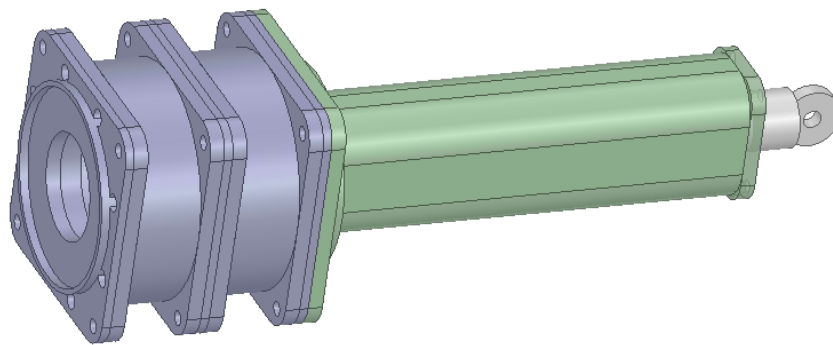
(b) Two units

Figure 7.2 Configuration of proposed modular EMA concept

(a) One unit   (b) Two units
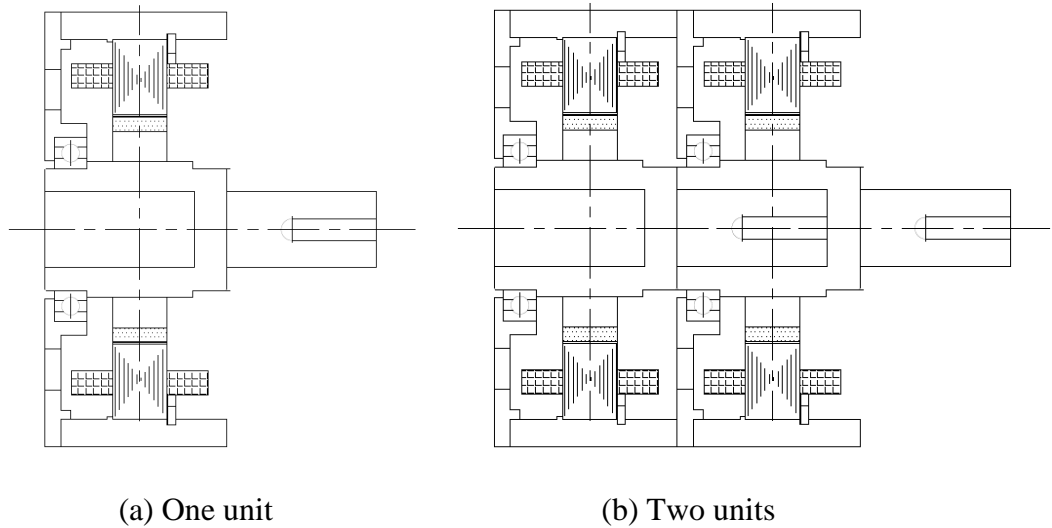
Figure 7.3 Cross section of proposed modular EMA motor

7.2 Initial design specifications

As mentioned in the Section 6.1, the EMA demands a primary rotary motor with high torque density, compact structure, and high reliability and excellent fault-tolerant capability.

The SPM motor with FSCW configuration is expected to be the best candidate due to its high torque density and high leakage inductance capable of limiting short-circuit current [80][81][96][97]. In addition, the concentrated winding is easily to manufacture with high reliability avoiding physical contact between coils. Due to the low speed characteristics attributing from the direct-drive EMA motor, the iron loss and magnet eddy current loss coming from the significant stator space MMF harmonics associated with conventional FSCW configuration are negligible compared to the copper loss [127]. Isolated design in the physical, electrical, magnetic, and thermal aspects can be easily implemented with a single-layer FSCW topology. However, more attention should be paid to the potentially high torque ripple and unbalanced magnetic pull for some FSCW configurations.

According to Section 6.4.3.2, the design specifications of the primary rotary motor for a unit EMA can be summarized in Table 7.1. It is evident that the EMA motor features low power and low speed characteristics.

Table 7.1 Design specifications of the EMA motor

Parameters	Values	Parameters	Values
Peak power	2.1 kW	Rated speed	660 rpm
Peak torque	15 Nm	Peak speed	1320 rpm
Rated power	1.0 kW	DC voltage	270V
Rated torque	7.5 Nm	Max current	20 Arms

7.3   Initial studies of the EMA motor

After determining the design specifications, initial studies are required to achieve a preliminary design solution of EMA motor. The SPM motor with FSCW configuration is identified as a potential motor topology offering high torque density, reliability and excellent fault-tolerant capability.

7.3.1 Winding layers

The winding layer number is the first to be determined. Compared to a double-layer (DL) winding configuration, the single-layer (SL) winding configuration features an increased phase inductance, improved slot fill factor as well as an increase of the synchronous or working harmonic winding factor which is directly related to the torque capability if the magnetic saturation is not considered. Moreover, the highest isolation in terms of physical, electric, magnetic, and thermal aspect can be achieved. On the other hand, the SL configuration is disadvantageous in terms of having significant stator space MMF harmonics and thereby reduced overload capability. In addition, the higher torque ripple and noise of the SL configuration is expected to be a concern if the motor is not well designed.

In this thesis, the electric motor is being designed for an aircraft actuator, which is a safety-critical application. The SL configuration can provide the strictly required highest level of physical isolation between windings and magnetic isolation between different phases. The issues of significant stator MMF harmonics in the SL configuration inducing rotor losses and limiting overload capability are not the critical concerns as the electric motor is of low power and low speed, and the peak electrical loading is limited by the available cooling options. And more importantly, SL

configuration features higher leakage and airgap harmonic inductance which helps to restrain the short-circuit current in the SC fault conditions. Thus, the SL configuration is preferable for the EMA motor.

7.3.2 Slot-pole combinations

The typical slot/pole combinations with SL configuration are when pole numbers are equal to $Q \pm 2j$ or $Q \pm j$, where Q is slot numbers and j is an integer. All the possible slot/pole combinations for the EMA motor are summarized in Table 7.2, considering achieving reasonable winding factor and mechanical dimension limitations.

Table 7.2 Characteristics of various slot-pole combinations

Slots/ poles	SPP	t_m	LCM	Mutual index ratio [87]	Multi three-phase		k_w
					UMP (Healthy)	UMP (Fault)	
6S-4P	1/2	2	12	-0.2	Yes	Yes	0.866
6S-8P	1/4	2	24	-0.2	Yes	Yes	0.866
12S-8P	1/2	2	24	-0.2	No	Yes	0.866
12S-10P	2/5	1	60	0	No	Yes	0.966
12S-14P	2/7	1	84	0	No	Yes	0.966
18S-12P	1/2	6	36	-0.2	No	Yes	0.866
18S-14P	3/7	1	126	-0.02	Yes	Yes	0.902
18S-16P	3/8	1	144	-0.02	Yes	Yes	0.945
18S-20P	3/10	1	180	-0.02	Yes	Yes	0.945
18S-22P	3/11	1	198	-0.02	Yes	Yes	0.902
18S-24P	1/4	6	72	-0.2	No	Yes	0.866
24S-16P	1/2	4	48	-0.2	No	No	0.866
24S-20P	2/5	2	120	0	No	No	0.966
24S-22P	4/11	1	264	0	No	No	0.958
24S-26P	4/13	1	312	0	No	No	0.958
24S-28P	2/7	2	168	0	No	No	0.966
24S-32P	1/4	4	96	-0.2	No	No	0.866

Normally, for a FSCW motor, there is no mutual coupling between phases if the average value of winding turn function of each phase is zero due to the concentrated

winding characteristics and non-overlapping area between phases. For the SPP family of 1/2 or 1/4 motor, however, there is significant mutual coupling between phases because the average value of turn function of each phase is not zero, which creates significant overlapping area between the flux paths of different phases, leading to a high mutual-inductance ratio [87]. This is also the case for SPP family such 3/7 or 4/8, where the average value of turn function of each phase is not zero. The mutual-inductance ratio is proportionally related to the ratio between the average value and total surrounding area of per phase turn function [87]. Low and no mutual-inductance is preferable for fault-tolerant applications. Thus, these slot/pole combinations with high mutual-inductance such as 6 slots 4 poles are excluded.

On the other hand, the UMP is a critical factor in determining the feasibility of slot/pole combinations as significant UMP may result in noise and vibration and damage to the bearing and rotor shaft. Both healthy and fault conditions must be considered as post-fault operation is required for the EMA motor. Under healthy operation conditions, the UMP normally exists for SPP family of 3/7 or 3/10 if their modular unit number is an odd number. However, under fault conditions, with one set of a 3-phase winding open-circuit (OC), the UMP characteristics for those slot/pole combinations that do not feature significant UMP under healthy conditions may change. For instance, in the case of dual 3-phase winding configuration there are 6 coils in the motor and only one coil per phase in the SPP family of 2/5 or 2/7 with 12 slots; an unsymmetrical magnetic field may be generated if losing one set of 3-phase winding and thereby results in a significant UMP. However, for the SPP family of 2/5 or 2/7 with 24 slots, there are two coils per phase and a symmetrical magnetic field can still be maintained when losing one set of 3-phase winding. Hence, the configurations that have an even number of coils per phase are preferred. It is evident from Table 7.2 that only configurations with 24 slots can meet the requirement of no significant UMP under OC fault condition; in fact, it is similar for a 3-phase SC fault condition where the electric loading in different 3-phase is different but their magnetic field is symmetrical on its own, and thereby no significant UMP is generated under a 3-phase SC fault condition.

The winding factor is directly related to the output torque for permanent magnet synchronous motor with surface-mounted magnets as there is no additional reluctance torque. Thus, the slot/pole combinations with high winding factor are advantageous.

Considering all the above, four slot/pole combinations with 24 slots, viz., 24S-20P, 24S-22P, 24S-26P, 24S-28P, are selected to be further investigated.

7.3.3 Comparison

After selecting the possible slot/pole combinations, the FEM models of each combination are built. The preliminary design study is done with a target torque of 15 Nm. A fixed peak current density of 12 A/mm^2 as well as the same diameter and axial length are applied. The four studied models are plotted in Figure 7.4.

(a) 24S-20P   (b) 24S-22P

(c) 24S-26P   (d) 24S-28P
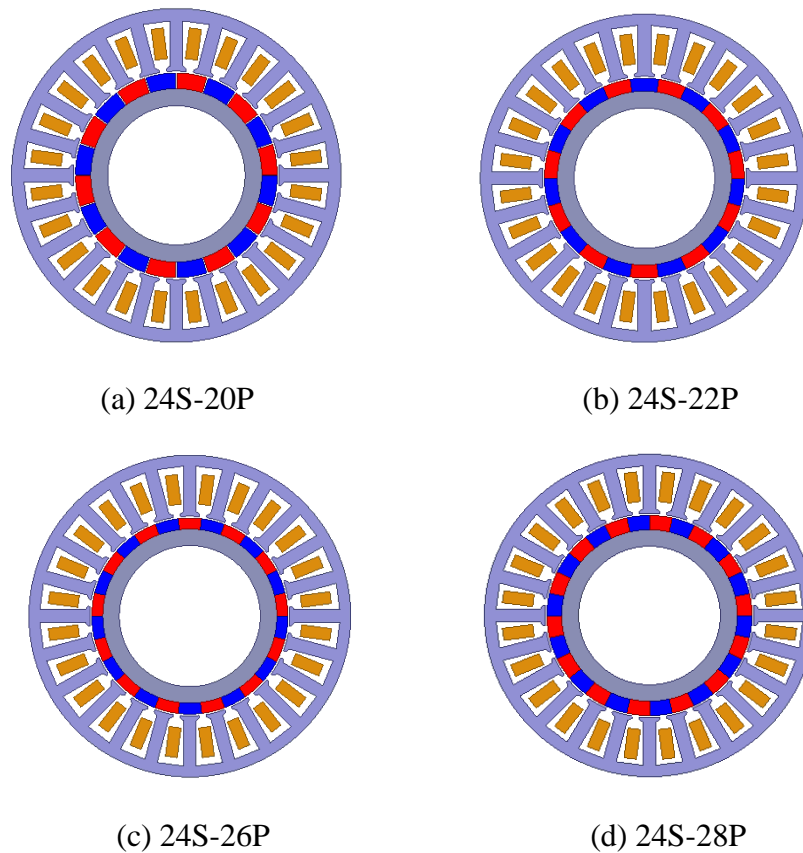
Figure 7.4 2-D FEM models of the four considered slot-pole combinations

Table 7.3 summarized the comparison results of these four slot-pole combinations. The average torque and torque density are plotted in Figure 7.5. The 24S-28P tends to have a slightly higher torque than 24S-22P and 24S-26P, but the pole number is too high. On the other hand, if a dual 3-phase winding configuration is applied, the 24S-22P and 24S-26P may have a higher winding factor, as indicated in Table 7.4, and thereby a higher torque output due to the configuration of dual 3-phase

winding with 30^0 shift, which is also effective in cancelling out the ripple torque component with orders of 6th and 18th and thus a smooth torque waveform can be achieved. More details on the winding configurations will be explained in the next section. Higher pole numbers result in thinner stator tooth thickness and much smaller PM spans which increase the slot leakage and inter-pole leakage and may reduce the overload capability. Considering all the above, the SPM motor with 24S-22P slot-pole combination is selected for further investigation.

(a) Average torque   (b) Torque density
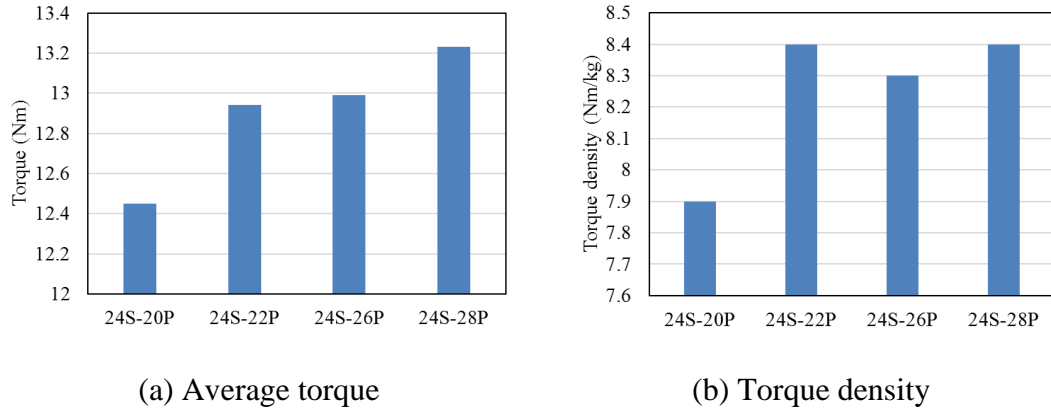
Figure 7.5 Average torque and torque density of the four motors

Table 7.3 Performance comparison of the four motors

	24S-20P	24S-22P	24S-26P	24S-28P
D_o (mm)	136	136	136	136
l_{ef} (mm)	20	20	20	20
g (mm)	0.8	0.8	0.8	0.8
D (mm)	83.3	82.8	84	84.4
h_m(mm)	6.3	5.3	5	6
PM arc coefficient a_{pm}	0.95	1	1	1
w_t (mm)	5.4	5.4	5.4	5.4
Turns per coil, N	52	54	55	52
J (A/mm^2)	12	12	12	12
T (Nm)	13.0	13.4	13.4	13.6
Active mass (kg)	1.57	1.52	1.54	1.57
Shear stress δ_g (kN/m^2)	28.7	29.7	28.9	29.5

Table 7.4 Winding factors of the four considered motors

	24S-20P	24S-22P	24S-26P	24S-28P
One 3-phase	0.966	0.958	0.958	0.966
Dual 3-phase*	0.966	0.991	0.991	0.966

*: Maximum achievable winding factor of dual 3-phase winding configuration

7.4 Performance improvement

After confirming the slot-pole combination, further performance improvement is required. This section deals with performance improvement by investigating different magnetization patterns, steel materials, and winding configurations.

7.4.1 The use of parallel magnetization

There are two main magnetization patterns for a surface-mounted magnet, viz., radial and parallel direction, as in Figure 7.6. Halbach array may be possible but the manufacturing and assembly is complicated and so it is not considered here [102]. Previous studies have suggested that the adoption of radial magnetization does not necessarily give advantages compared to parallel pattern in regards to magnetic flux and torque capability [159][160] [161]. This provides an opportunity to explore the effect of different magnetization pattern in terms of performance improvement.

The no-load and load performance under the same current density of 12 A/mm^2 are calculated using 2-D FEM, as shown in Figure 7.7. It can be noted that the EMA motor with parallel magnetization pattern features a 3.5% higher no-load back EMF and thereby a higher output torque. Radial magnetization patterns tend to have a higher 3rd harmonic making it more suitable for brushless DC motor operation, whilst the parallel patterns have a negligibly higher 5th harmonic and lower 7th harmonic, implying a negligible torque ripple difference between both patterns. The impact of magnetization pattern on the cogging torque is significant, with a lower cogging torque for the radial pattern; however, the cogging torque amplitude for both patterns are extremely low compared to the peak output torque. On the other hand, the radial magnetization pattern normally requires more effort to implement and is more

expensive. Therefore, the parallel magnetization pattern which features higher torque output and less magnetization effort is selected for further investigation.
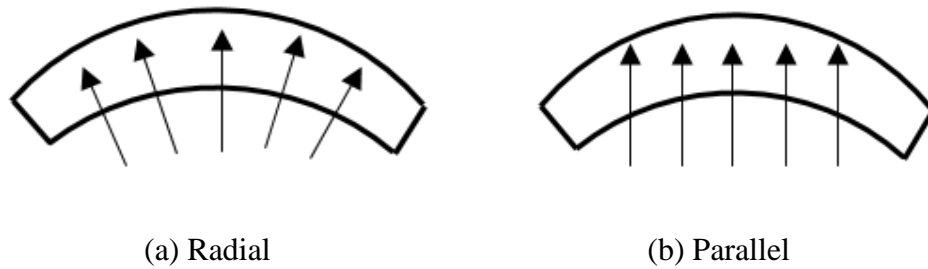
(a) Radial   (b) Parallel

Figure 7.6 Radial and parallel magnetization pattern

(a) Back EMF   (b) FFT Spectrum of back EMF

(c) Output torque   (d) Cogging torque
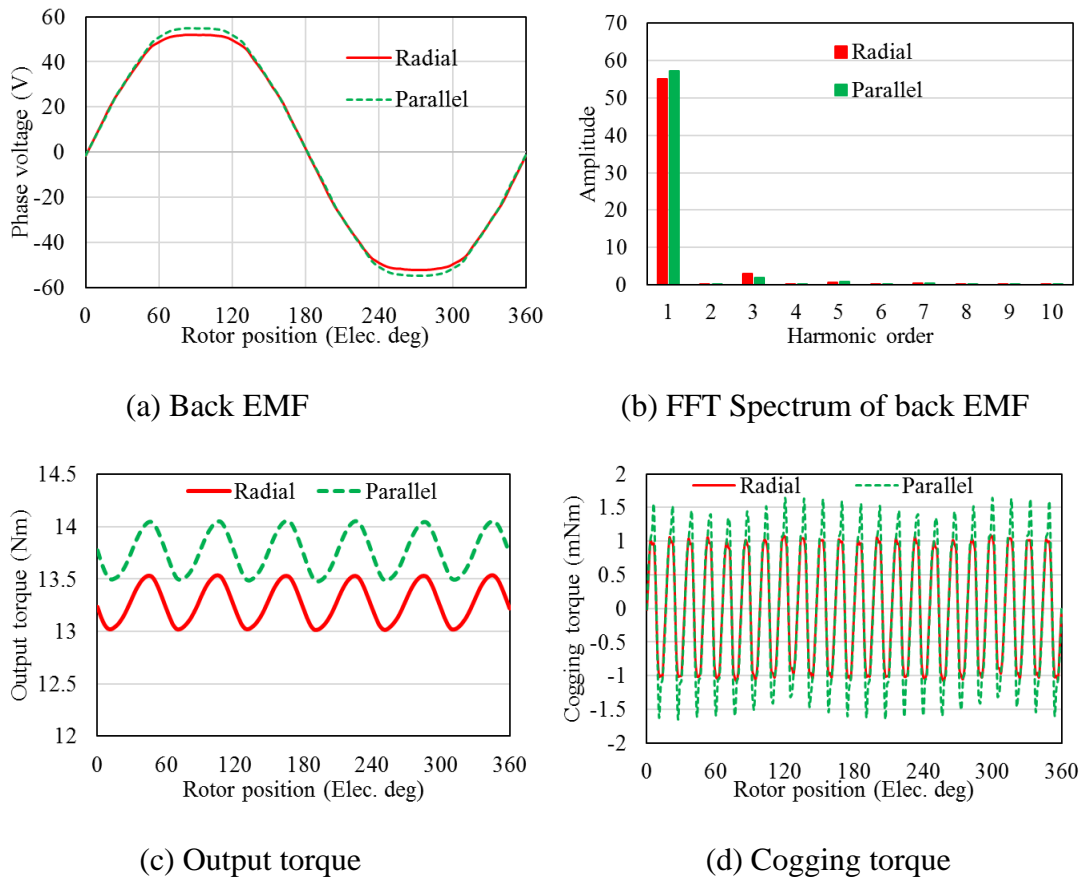
Figure 7.7 24S-22P motor with different magnetization patterns

7.4.2 The use of cobalt iron steel

For the electrical motor, different lamination steel material will lead to different EM performance. Previously the lamination material for stator and rotor used for design

and simulation is DW270-35, which is a typical silicon steel, and it is obvious that there are many high-performance steels available in the market. Among all of them, the cobalt iron alloys have the highest saturation magnetic flux density by far, about 2.35T, as in Figure 7.8. The drawback with this high-performance steel is the cost, which may not a big concern for aircraft applications if it can offer considerable torque improvement. Another concern is the weight as their mass density is normally higher. For example, the mass density of Vacoflux-50 is about $8120 \, kg/m^3$ whilst for DW270-35, it is $7600 \, kg/m^3$. Therefore, it is necessary to undertake quantitatively comparative study to evaluate the gains of adopting high performance iron steel. Three kinds of material combinations, viz., both stator and rotor with DW270-50, both stator and rotor with Vacoflux-50, and combination of stator with Vacoflux-50 and rotor with DW270-35, have been studied in this section to evaluate their impact on output performance.
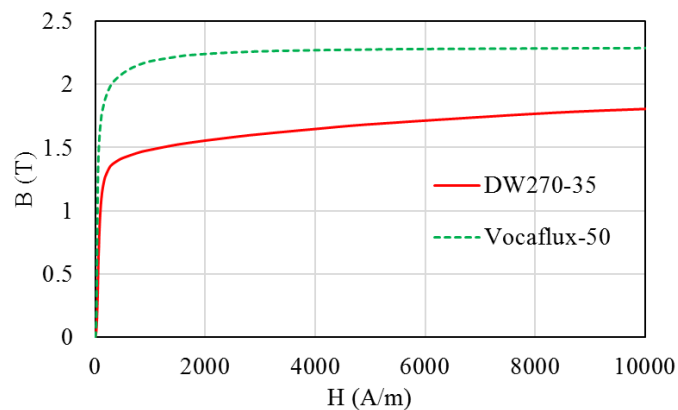
Figure 7.8 B-H curve of the two considered lamination steels

The torque performance with different material combinations is calculated using 2-D FEM, as summarized in Figure 7.9 and Table 7.5. Using Vacoflux-50 to replace the DW270-35 steel can considerably improve the peak torque of an EMA motor by about 11.6%. On the other hand, if only replacing the stator lamination material with Vacoflux-50, it can deliver almost the same torque as the motor with both stator and rotor equipped with Vacoflux-50. This is because the stator tooth is more easily saturated than the rotor yoke and the peak torque capability is mostly limited by stator tooth saturation level. In addition, the added weight due to the Vacoflux-50 is negligible, and 6.7% higher torque density can be achieved by adopting Vacoflux-50

and DW270-35 as stator and rotor steel, respectively. Considering all the above, the combination of stator with Vacoflux-50 and rotor with DW270-35 is selected.

(a) Peak torque   (b) Torque vs current
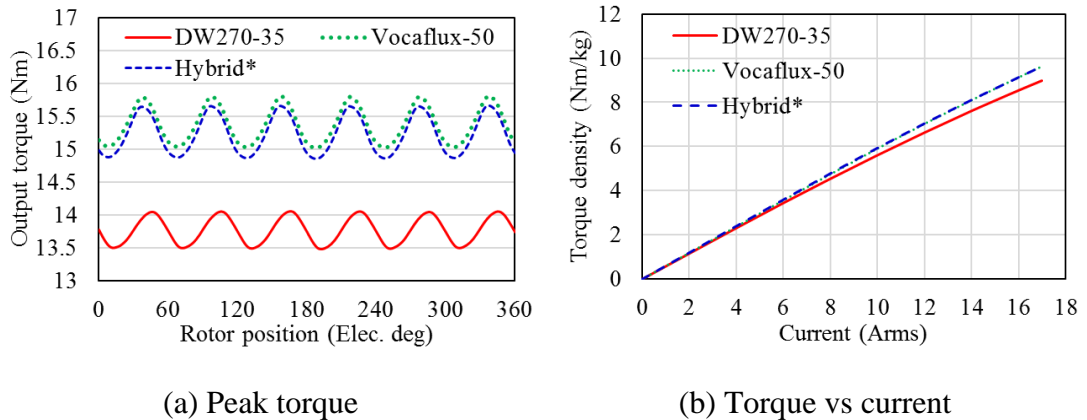
Figure 7.9 Performance comparison of 24S-22P EMA motor with three different steel combinations (*Hybrid: stator with Vacoflux-50 and rotor with DW270-35)

Table 7.5 Performance comparison of 24S-22P EMA motor with three different lamination steel combinations

	DW270-50 (stator & rotor)	Vocaflux50 (stator & rotor)	Hybrid Combination
J (A/mm^2)	12	12	12
Active mass (kg)	1.535	1.595	1.582
Average torque (Nm)	13.8	15.4	15.2
Ripple torque (Nm)	0.6	0.8	0.8
Torque ripple	4.3%	5.2%	5.3%
Torque density (Nm/kg)	9.0	9.6	9.6

7.4.3 The use of dual 3-phase winding with 30^0 shift

As has been identified, the EMA motor should be designed with dual 3-phase electric drives to meet the fault-tolerance requirement and give fail-safe capability. According to star of slots theory [88], there are four coil phasors per phase for a three-phase winding configuration, as shown in Figure 7.10.

For a dual 3-phase winding topology, three different configurations can be achieved by dividing the four coil phasors into two groups and then arranging them to two phases, respectively, as shown in Figure 7.11 and Figure 7.12. There is no shift in

time between the two 3-phase windings for the Type 1 and 2 configurations, while for the Type 3 configuration, there is a 30^0 shift between the two 3-phase windings.
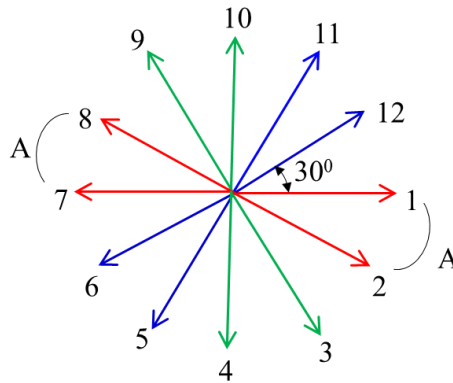
Figure 7.10 Coil phasor diagram of a single 3-phase 24S-22P motor
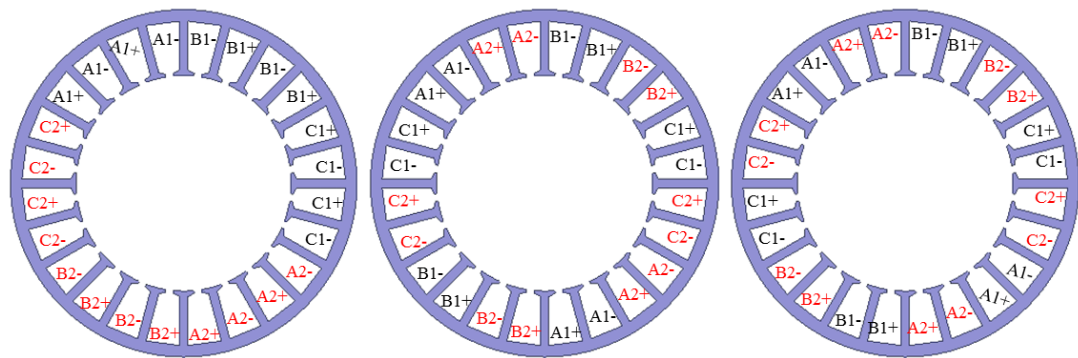
(a) Type 1 (0^0 shift)   (b) Type 2 (0^0 shift)   (c) Type 3 (30^0 shift)

Figure 7.11 Phase distribution of three dual 3-phase winding configurations

A comparison of winding factors, torque behaviors and UMP characteristics of different dual 3-phase configurations is summarized in Table 7.6. One can note that both Type 1 and Type 2 feature the same synchronous winding factor. The Type 3 configuration has a 3.5% higher winding factor due to the improved distribution factor. The higher the winding factor, the higher the back EMF; this can be seen from the EMF waveform and FFT spectrum comparison in Figure 7.13. Type 1 and Type 2 exhibit the same no-load back EMF and there is no shift in time between the two 3-phase windings. Higher no-load back EMF and 30^0 shift in time between the two 3-phase windings are observed in the Type 3 configuration; both 5th and 7th harmonic increase, which is the source of ripple torque component with order of 6th and a higher

torque ripple is expected in the condition of only one 3-phase winding operating; however the 6th ripple torque can be cancelled out in the dual 3-phase winding with 30^0 shift configuration due to the elimination of those stator MMF harmonics corresponding to 6th order of ripple torque such as 55th and 77th, the explanation of which can be recalled in Section 5.3 [136] and will also be presented afterwards.

(a) Type 1 (0^0 shift)   (b) Type 2 (0^0 shift)   (c) Type 3 (30^0 shift)
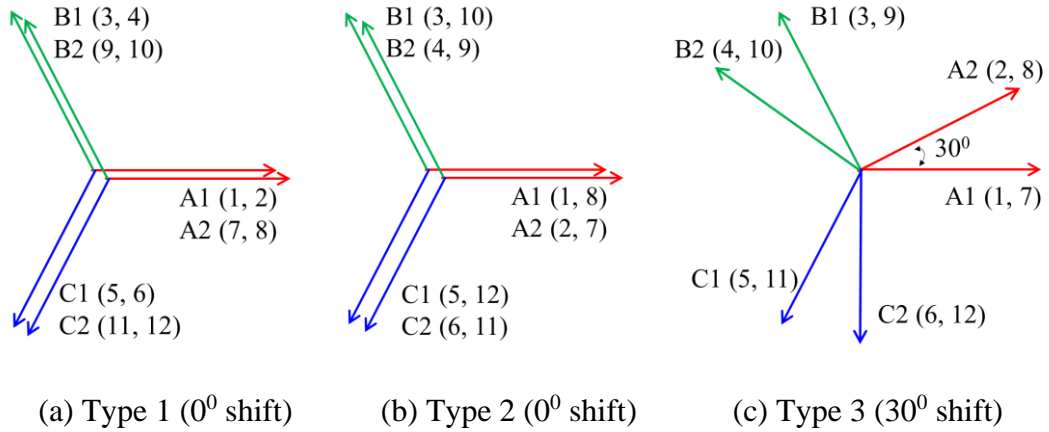
Figure 7.12 Coil phasor arrangement of three dual 3-phase winding configurations of 24S-22P motor

Table 7.6 Comparison of 24S-22P motor with different dual 3-phase winding configurations

		Type 1	Type 2	Type 3
Winding factor k_w		0.945	0.945	0.991
Healthy condition	Average torque (Nm)	15.2	15.2	16.0
	Ripple torque (Nm)	0.6	0.6	0.2
	UMP	Low	Low	Zero
One 3-phase OC fault	Average torque (Nm)	7.6	7.6	8
	Ripple torque (Nm)	0.4	0.3	0.5
	UMP	High	Low	Zero

(a) Back EMF of Type 1

(b) Back EMF of Type 2

(c) Back EMF of Type 3

(d) FFT Spectrum comparison
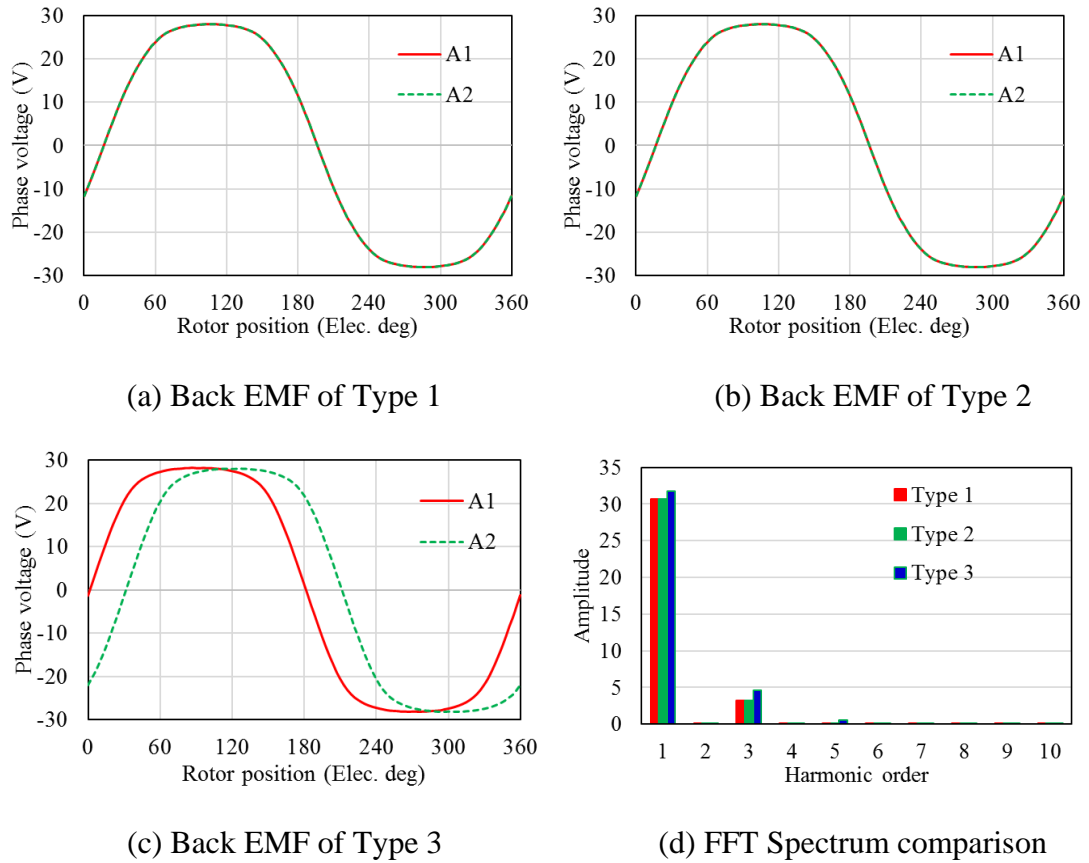
Figure 7.13 No-load back EMF comparison of 24S-22P EMA motor with different dual 3-phase winding configurations

The torque behavior comparison under healthy and fault condition is depicted in Figure 7.14 and Table 7.6. The same torque performance for Type 1 and Type 2 under healthy condition is observed, with a lower average torque and much higher torque ripple in the healthy condition compared to Type 3 configuration. Type 3 configuration under healthy condition features only 12th and 18th ripple toque components and the 6th ripple torque is eliminated. This is due to the elimination of those stator MMF harmonics corresponding to 6th and 18th order of ripple torque, which can be observed in Figure 7.14 (b) and Table 7.7; a higher 12th ripple torque is observed as the increased amplitude of those stator MMF harmonics corresponding to 12th ripple torque such 121st and 143rd. In addition, the Type 3 winding configuration is characterized by the reduced stator MMF harmonics such as elimination of 5th and 7th in healthy condition, and their corresponding slot harmonics, which can reduce the magnetic saturation and improve the overload capability.

(a) Torque @Healthy

(b) FFT spectrum of torque @Healthy

(c) Torque @OC fault

(d) FFT spectrum of torque @OC fault
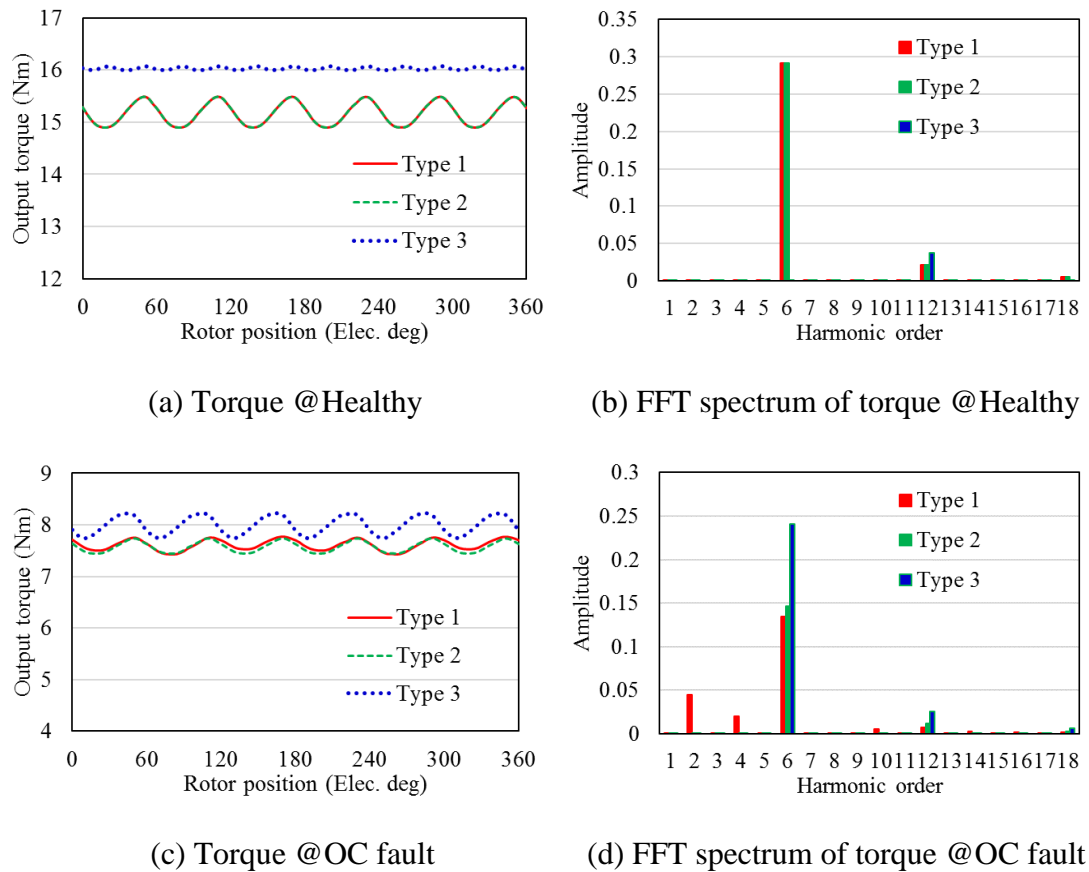
Figure 7.14 Comparison of 24S-22P EMA motor with different dual 3-phase winding configurations

In the OC fault condition, a similar torque ripple is seen in Type 1 and Type 2 configuration, and it is worth noting that Type 1 configuration includes 2nd and 4th harmonic torque which is mainly due to the diametrically asymmetrical magnetic field distribution attributing to the diametrically symmetric stator MMF waveform, as in Figure 7.15 (c) and (d). Those stator MMF harmonics corresponding to 6th order of ripple torque such 55th and 77th in the Type 3 configuration are higher than those in the Type1 and Typ2 configuration, as shown in Table 7.7; this is the same for 18th ripple torque; thus, a higher ripple torque with order of 6th and 18th is seen in Type 3 configuration, Figure 7.14 (d); The 12th order MMF harmonic is the same as it is in the healthy condition.

(a) MMF waveform @ Healthy

(b) MMF spectrum @ Healthy

(c) MMF waveform @ OC fault

(d) MMF spectrum @ OC fault
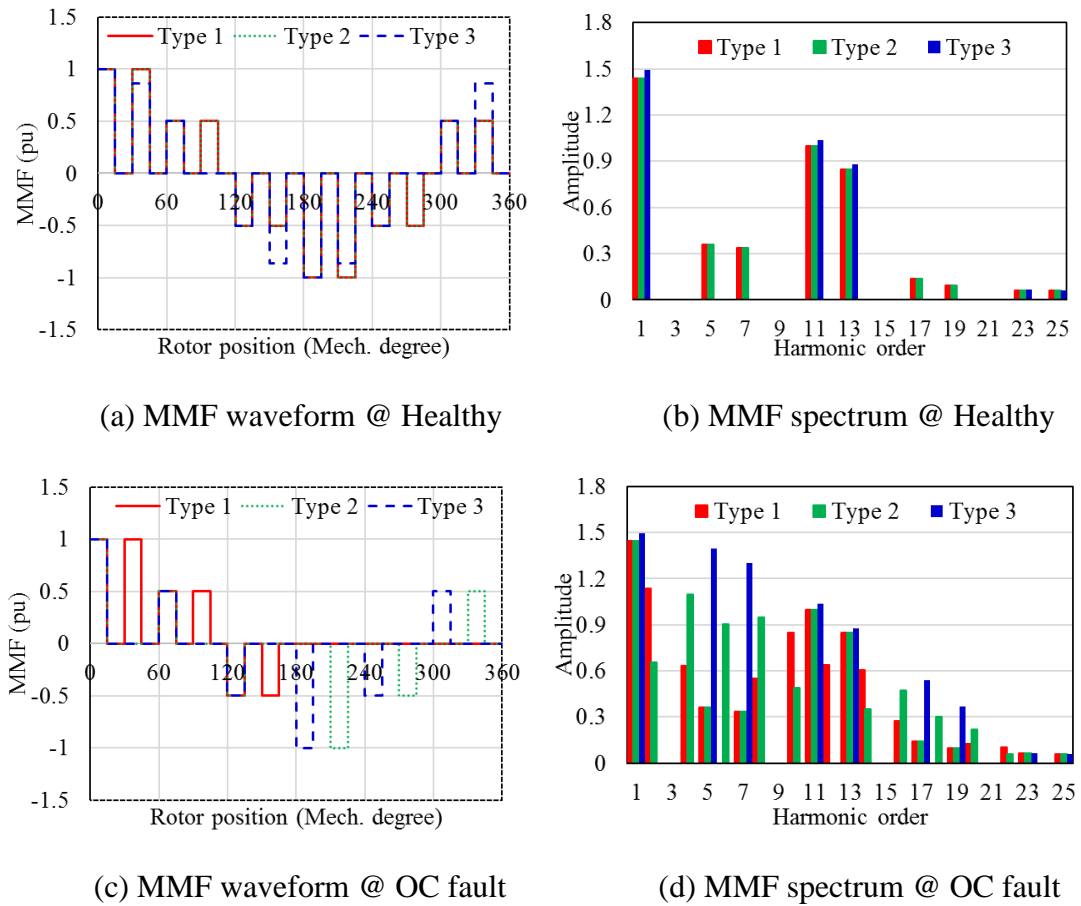
Figure 7.15 MMF waveform and FFT spectrum comparison of 24S-22P EMA motor with different dual 3-phase winding configurations

Table 7.7 Amplitude of ripple-torque-producing stator MMF harmonics of 24S-22P EMA motor with different dual 3-phase winding configurations

Operation condition	Torque ripple order	Corresponding Stator harmonics	Type 1	Type 2	Type 3
Healthy	6th	55th	0.0443	0.0443	0
		77th	0.0251	0.0251	0
	12th	121st	0.0142	0.0142	0.0146
		143rd	0.0129	0.0129	0.0132
OC fault	6th	55th	0.0443	0.0443	0.1712
		77th	0.0251	0.0251	0.0970
	12th	121st	0.0142	0.0142	0.0147
		143rd	0.0129	0.0129	0.0133

Figure 7.16 (a) plots the UMP characteristics of the 24S-22P EMA motor with different winding configurations. As can be seen, no significant UMP occurs for all three configurations under the healthy condition due to the diametrically symmetric magnetic field distribution attributing to the diametrically symmetric stator MMF waveform in Figure 7.15 (a) [138]. However, under the one 3-phase OC fault condition, a significant UMP occurs in Type 1 configuration and a considerable UMP occurs in Type 2 configuration due to the resulting diametrically unsymmetrical stator MMF waveform, as in Figure 7.15 (c). For Type 3 configuration, the stator MMF is displaying the highest level of symmetry under either healthy or OC fault conditions as in Figure 7.15 (a) and Figure 7.15 (c), and thereby no significant UMP exists under both conditions.

Considering all the above, the Type 3, that is, the dual 3-phase winding with 30^0 shift is selected due to its improved average torque and torque ripple in the healthy condition and no UMP in both healthy and fault conditions. Although a higher torque ripple is expected in the OC fault condition, it is a condition that can be tackled with certain control techniques if needed [162].

(a) Healthy   (b) One 3-phase OC fault
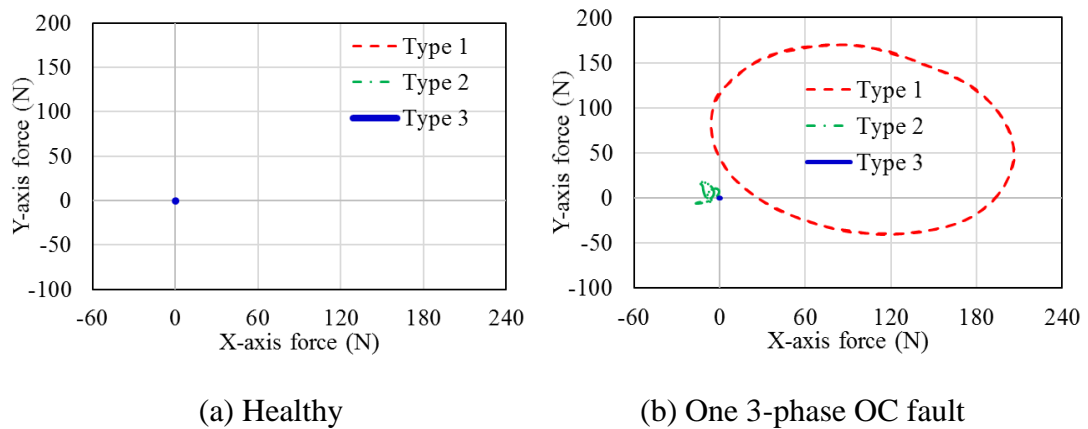
Figure 7.16 UMP comparison under one 3-phase OC fault of 24S-22P EMA motor with different dual 3-phase winding configurations

7.5 Analysis of 3-phase short-circuit (SC) fault

The fault-tolerant capability is a crucial characteristic for the EMA motor. The OC fault performance has been addressed in the previous section, whilst the short-circuit (SC) performance is the focus of this section. To maintain operation of the EMA motor

under 3-phase terminal SC fault, the terminal SC current must be kept to an acceptable level. Generally, one per-unit phase inductance is required to limit the terminal SC current under rated or peak speed [163][164]. For the SPM motor with concentrated winding configuration, the key method to achieve this is by increasing slot leakage inductance by controlling the slot opening and slot depth, as the slot leakage inductance is the dominant component due to its inherently large effective airgap length [93] [163][165]. It is worth noting that the variation of slot opening dimension will inevitably change the main magnetic flux generated by the permanent magnets linking the coils.

7.5.1 Single 3-phase SC current and braking torque

In the case of a 3-phase terminal SC fault condition, the $I_{d,sc}$ and $I_{q,sc}$ can be computed from (3.45) by making $u_d=u_q=0$ in the synchronous d-q reference frame [134].

$$I_{d,sc} = -\frac{\omega_e^2 L_d \lambda_f}{R^2 + (\omega_e L_d)^2} \tag{7.1}$$

$$I_{q,sc} = -\frac{\omega_e R \lambda_f}{R^2 + (\omega_e L_d)^2} \tag{7.2}$$

and the amplitude of SC current is

$$I_{sc} = \frac{E_o}{\sqrt{R^2 + (\omega_e L_d)^2}} = \frac{\omega_e \lambda_f}{\sqrt{R^2 + (\omega_e L_d)^2}} \tag{7.3}$$

It is evident that the SC current always increases with the speed, approaching to a constant value of ψ_m/L_d, that is defined as the characteristic current, at high speed.

$$I_{scmax} = \lambda_f/L_d \tag{7.4}$$

Since this is a SPM motor, no significant reluctance torque exists. The steady-state SC braking torque may be expressed as [135]

$$T_{sc} = -\frac{3P}{2} \frac{\lambda_f^2 \omega_e R}{R^2 + (\omega_e L_d)^2} \tag{7.5}$$

It can be noticed that the maximum SC braking torque can be calculated by equating the derivative of (7.5) with respect to the speed ω_e to zero; the maximum SC braking torque can be written as [134]

$$T_{scmax} = -\frac{3P\lambda_f{}^2}{4L_d} = -\frac{1}{2}\frac{3P}{2}\lambda_f\frac{\lambda_f}{L_d} \tag{7.6}$$

and it occurs at critical speed of

$$\omega_m^* = \frac{R}{L_d} \tag{7.7}$$

By substituting (7.4) into (7.6), the maximum SC braking torque can be written as

$$T_{scmax} = -\frac{1}{2}\frac{3P}{2}\lambda_f I_{scmax} = -\frac{1}{2}T(I_{scmax}) \tag{7.8}$$

which is half of the EM torque of the motor generated by imposing $I_q = I_{scmax}$ into the motor.

Therefore, it can be concluded that for a dual 3-phase SPM motor, the maximum resulting output torque under one 3-phase SC fault can be expressed as

$$T_{out} = \frac{1}{2}T(I_{max}) - \frac{1}{4}T(I_{scmax}) \tag{7.9}$$

If the max SC current I_{scmax} is normalized with respect to I_{max}, the minimum resulting output torque of the dual 3-phase EMA motor under one 3-phase SC fault can be expressed as

$$I_{scmax} = a * I_{max} \tag{7.10}$$

$$T_{outmin} = \left(\frac{1}{2} - \frac{1}{4}a\right)T(I_{max}) \tag{7.11}$$

According to Section 6.6.3, for the aircraft actuation system with two EMA motors, each of which is a dual 3-phase SPM motor, it must maintain half of peak torque under SC faults of two 3-phase windings. Thus, without considering the saturation effect, the following relationship must be met.

$$T_{outmin} = 2 * \left(\frac{1}{2} - \frac{1}{4}a\right)T(I_{max}) \geq \frac{1}{2}T(I_{max}) \tag{7.12}$$

namely,

$$a \leq 1 \quad \text{or} \quad I_{scmax} \leq I_{max} \tag{7.13}$$

If $I_{scmax} = I_{max}$, this is a one per-unit phase inductance design and the key to achieve this is by adjusting the armature leakage inductance which will be studied in the following section.

According to the EMA motor design specification in Table 7.1, the peak target torque is 15Nm, so the maximum braking torque of the dual 3-phase EMA motor under one 3-phase SC fault should be less than 1/4*15Nm, viz., 3.75Nm, and thereby the minimum output torque of the EMA motor under one 3-phase SC fault condition is higher than 1/4*15Nm, viz., 3.75Nm. In this case, the actuation system with two EMA motors, each of which is a dual 3-phase SPM motor, can still generate half of peak target torque, viz., 7.5Nm when two 3-phase windings are short-circuit.

Finally, associated with the design requirement specified in the Section 6.6.3, the fault tolerant capability design requirement for the EMA motor can be summarized in Table 7.8.

Table 7.8 Fault tolerant capability design requirement of the EMA motor

Performances	Specifications
Output torque under one 3-phase OC fault	>1/2*Tmax
Braking torque under one 3-phase SC fault	<1/4*Tmax
Braking torque under two 3-phase SC faults	<1/2*Tmax
Output torque under one 3-phase SC fault	>1/4*Tmax

7.5.2 Armature inductance calculation method

As has been depicted, the inductance is essential in calculating the steady-state SC current and SC braking torque. The armature phase inductance L_s that consists of magnetizing inductance L_m and leakage inductance L_l can be analytically calculated as in (7.14), which provides reference for initial design considerations [166][167].

$$L_s = L_m + L_l = L_m + L_{h\sigma} + L_{s\sigma} + L_{tt} + L_{ew} \qquad (7.14)$$

where the leakage inductance L_σ consists of airgap harmonic leakage inductance $L_{h\sigma}$, slot leakage inductance $L_{s\sigma}$, tooth-tip leakage inductance L_{tt}, and end-winding leakage inductance L_{ew}. The analytical calculation of each inductance component will be discussed in the following sections. For simplicity, the end-winding leakage

inductance is not considered for comparison with 2-D FEM results as the end-winding leakage inductance is a 3-D phenomenon and many developed empirical and analytical models give quite different results [166][168].

7.5.2.1 Magnetizing inductance

The magnetizing inductance L_m is related to the magnetic flux travel across the airgap and links both stator and rotor. The derived formula of (3.22) using winding function method in the Section 3.1.4 is adopted to calculate L_m.

$$L_m = \frac{\mu_0 r l_{ef}}{g'} \int_0^{2\pi} \left(\frac{2N_s}{P\pi} k_{wP} \cos(P\theta) \right)^2 d(\theta_s) \qquad (7.15)$$

where $g' = g + h_m/\mu_r$ is the effective airgap length considering the thickness of magnet; N_s is the turn numbers in series per phase; k_{wP} is the synchronous winding factor and P is pole-pair numbers.

7.5.2.2 Airgap harmonic leakage inductance

Unlike the ISDW configuration, the winding function waveform of FSCW motor is far from sinusoidal. It is evident for FSCW motor that there are significant spatial harmonics in the stator winding function except for the synchronous or working harmonic with order of P [166] which is interacting with the rotor harmonic; these harmonics travel across airgap but do not participate the energy conversion and generate EM torque, consequently only contributing to the leakage inductance. The airgap harmonic leakage inductance can be expressed as [167]

$$L_{h\sigma} = \frac{\mu_0 r l_{ef}}{g'} \int_0^{2\pi} \sum_{\substack{v=1 \\ v \neq P}}^{\infty} \left(\frac{2N_{s2}}{v\pi} k_{wv} \cos(v\theta) \right)^2 d(\theta_s) \qquad (7.16)$$

This can also be written as

$$L_{h\sigma} = \sigma_\delta L_m \qquad (7.17)$$

where σ_δ is the harmonic airgap leakage factor [167][168].

$$\sigma_\delta = \sum_{\substack{v=1 \\ v \neq P}}^{\infty} \left(\frac{P \cdot k_{wv}}{v \cdot k_{wP}} \right)^2 \qquad (7.18)$$

Clearly, FSCW motors generally has a much higher harmonic airgap leakage factor compared to ISDW motors. In addition, the single-layer FSCW configuration is expected to have a much higher harmonic airgap leakage factor than that of double-layer counterpart.

7.5.2.3 Slot leakage inductance

Due to the existence of the airgap, part of the flux generated by the armature current will travel from one tooth to another by crossing the slot, contributing to slot leakage inductance. For a SPM motor, the effective airgap length is high, making slot leakage inductance a dominant component in the armature inductance and accounting for more than 50% of total inductance in some cases [93].

The analytical expression of slot leakage inductance can be written as

$$L_{s\sigma} = 2N_c l_{ef} N_1^2 \lambda_{s\sigma} \tag{7.19}$$

where $\lambda_{s\sigma}$ is the slot leakage permeance factor [167][168]; N_c is the coil numbers per phase and N_1 is the turn numbers per coil.
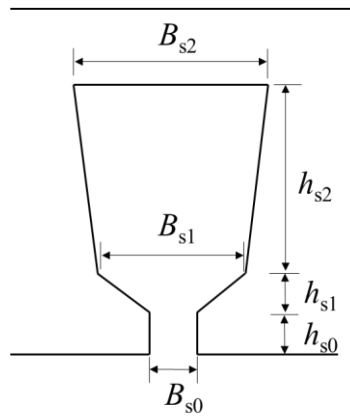
Figure 7.17 Slot geometry

A simplified 1-D permeance model can be used to calculate the slot leakage inductance, as in Figure 7.17, assuming the leakage flux passes straight from one side of the slot to the other side crossing the centre line of the slot in the orthogonal direction. The slot leakage permeance factor can be calculated as [86][166]

$$L_{s\sigma} = \mu_0 \frac{h_{s0}}{B_{s0}} + \mu_0 \frac{h_{s1}}{B_{s1} - B_{s0}} ln \frac{h_{s1}}{B_{s1}} + \mu_0 \frac{h_{s2}}{B_{s2}} \left[\frac{\left(\frac{B_{s1}}{B_{s2}}\right)^2 - \frac{1}{4}\left(\frac{B_{s1}}{B_{s2}}\right)^4 - ln\frac{B_{s1}}{B_{s2}} - \frac{3}{4}}{\left(1 - \frac{B_{s1}}{B_{s2}}\right)\left(1 - \left(\frac{B_{s1}}{B_{s2}}\right)^2\right)^2} \right]$$

(7.20)

where the first, second, and third item to the right of the equal sign of (7.20) represents slot leakage permeance factor corresponding to slot opening, slot wedge and slot body area, respectively.

7.5.2.4 Tooth-tip leakage inductance

Similar to slot leakage flux, there is some flux travel from one tooth to another by crossing tooth-tip area, which does not travel across the airgap and thereby corresponds to tooth-tip leakage inductance.

The analytical expression of the tooth-tip leakage inductance can be determined by applying a permeance factor [168].

$$L_{\mathrm{tt}} = 2N_c l_{ef} N_1^2 \lambda_{tt}$$

(7.21)

$$\lambda_{tt} = u_0 \frac{5(\frac{g'}{B_{s0}})}{5 + 4(\frac{g'}{B_{s0}})}$$

(7.22)

7.5.3 Analysis of armature inductance variation

The impact of slot opening dimension on the phase inductance of dual 3-phase 24S-22P EMA motor is evaluated and compared with 2-D FEM in this section.

Figure 7.18 plotted the comparison of phase inductance against slot opening B_{s0} for different slot opening depth calculated by analytical expression and 2-D FEM. The inductance is sensitive to the variation of slot opening B_{s0}. The smaller the B_{s0}, the higher the inductance. Generally, the calculated value difference between the two methods is within 5%, with some of them between 5 to 10% when B_{s0} is higher than 2mm.
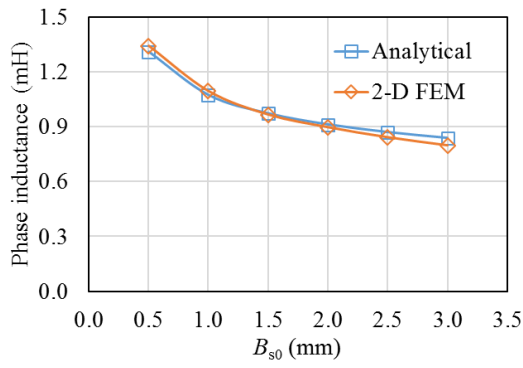
(a) h_{s0}=0.5mm, h_{s1}=1mm
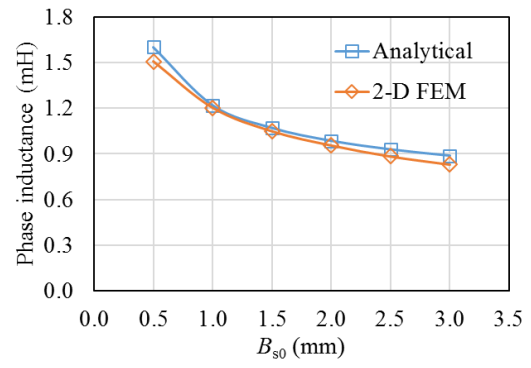
(b) h_{s0}=1mm, h_{s1}=1mm
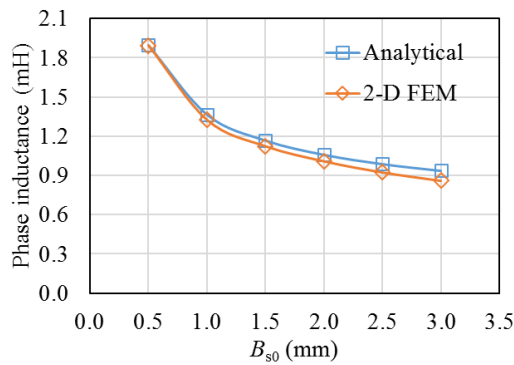
(c) h_{s0}=1.5mm, h_{s1}=1mm
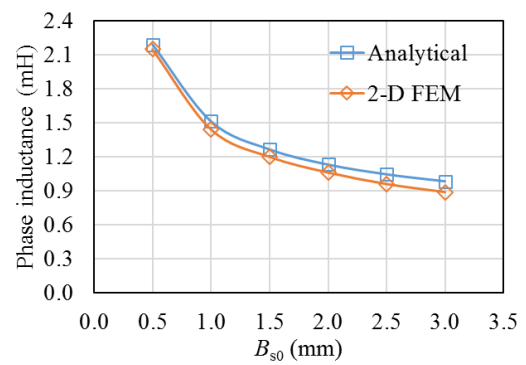
(d) h_{s0}=2mm, h_{s1}=1mm

Figure 7.18 Inductance comparison against B_{s0} with different h_{s0} and h_{s1}

The impact of h_{s0} on the phase inductance for different B_{s0} and h_{s1} is plotted in Figure 7.19. The inductance is proportional to the h_{s0}. For a smaller h_{s0}, the analytically calculated value agrees well with the value calculated by 2-D FEM; however, when h_{s0} becomes higher, the calculated value difference between the two methods is getting bigger, with up to 12% higher value seen in analytical calculation.
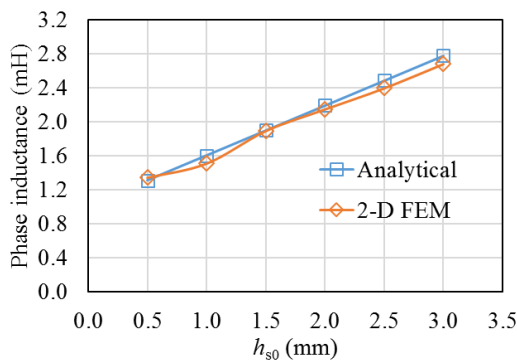
(a) B_{s0}=0.5mm, h_{s1}=1mm
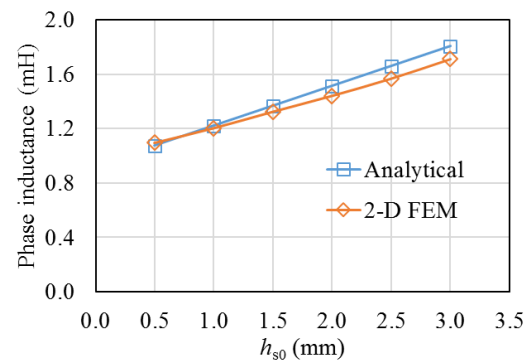
(b) B_{s0}=1mm, h_{s1}=1mm
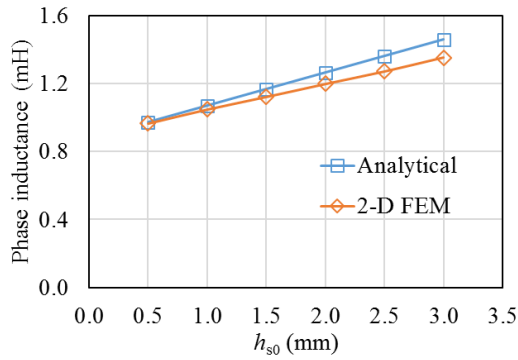
(c) B_{s0}=1.5mm, h_{s1}=1mm
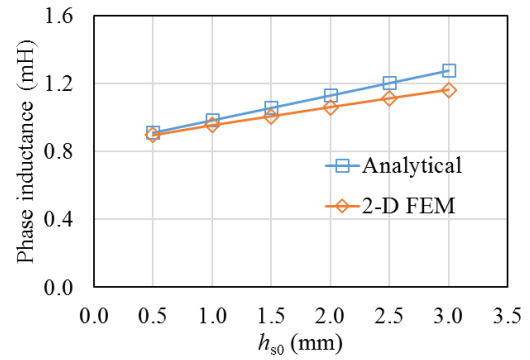
(d) B_{s0}=2mm, h_{s1}=1mm

Figure 7.19 Inductance comparison against h_{s0} with different B_{s0} and h_{s1}
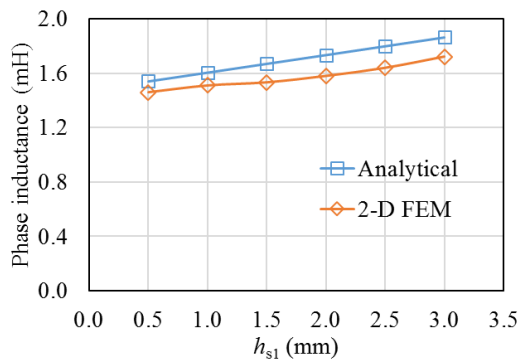
(a) B_{s0}=0.5mm, h_{s0}=1mm
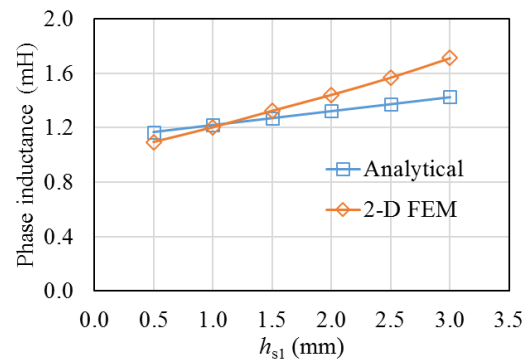
(b) B_{s0}=1mm, h_{s0}=1mm
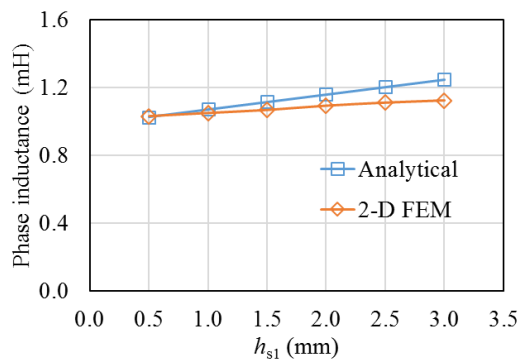
(c) B_{s0}=1.5mm, h_{s0}=1mm
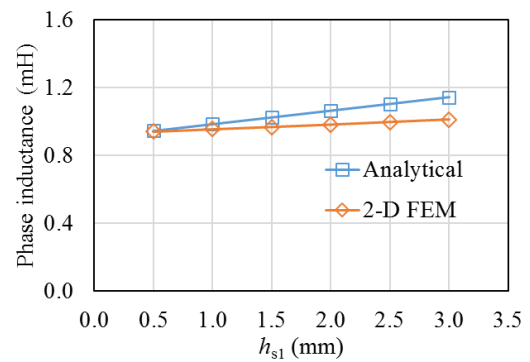
(d) B_{s0}=2mm, h_{s0}=1mm

Figure 7.20 Inductance comparison against h_{s1} with different B_{s0} and h_{s0}

Figure 7.20 depicts the impact of h_{s1} on the phase inductance for different B_{s0} and h_{s0}. A similar trend is seen as for the h_{s0}; the inductance is proportional to h_{s1}, but the variation is less significant. The difference between analytical calculation and 2-D

FEM analysis is slightly bigger especially for a higher h_{s1}. The big difference may be attributed to the overestimation of leakage inductance coming from slot wedge area.

7.5.4 Calculation of 3-phase SC current and braking torque

As depicted in the previous section, the impact of slot opening on the armature inductance is significant, which provides a way to adjust the SC current and SC braking torque by controlling the slot opening dimensions.

Figure 7.21 depicts the variation of average torque and torque ripple of the EMA motor against B_{s0}. The impact of B_{s0} on the average torque is less significant compared to its impact on torque ripple and on phase inductance as in Figure 7.21 (b) and Figure 7.18; the average torque increases when B_{s0} changing from 0.5 to 3mm, and then decreases, with maximum value at B_{s0}=3mm. The torque ripple is varying considerably, with two locally minimum torque ripple at B_{s0}=1mm and 3mm, respectively, but the torque ripple is well below 1.2% all the time.

(a) Average torque	(b) Torque ripple
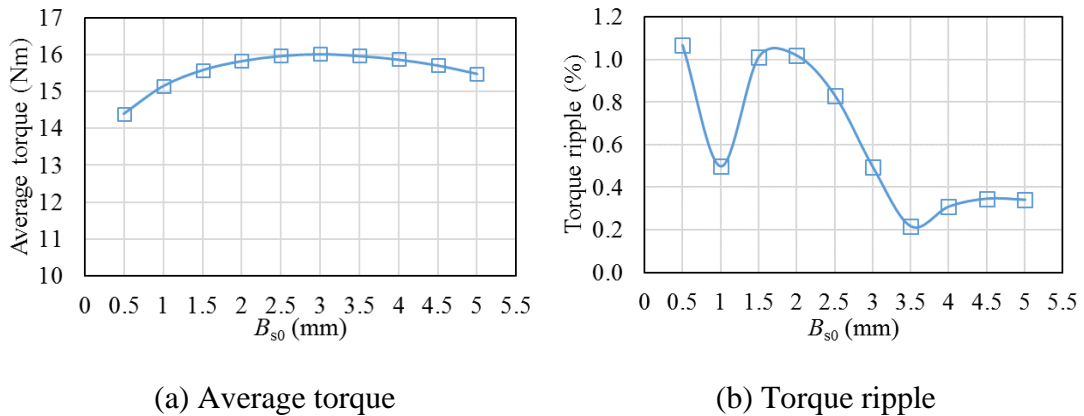
Figure 7.21 Average torque and torque ripple of dual 3-phase EMA motor with different B_{s0} when h_{s0}=1mm, h_{s1}=1mm

The single 3-phase winding SC characteristics of the dual 3-phase EMA motor with different B_{s0} are plotted in Figure 7.22, including critical speed, maximum SC torque, maximum SC current, and minimum output torque under SC fault. The calculated value using the analytical expression in Section 7.5.1 is presented for comparison. Generally, the analytical results agree well with the simulation results. When B_{s0} increases, the phase inductance decreases; it is evident that both the critical speed and the maximum SC current increase when B_{s0} increases as shown in Figure

7.22(a) and (b), which can be easily explained from the expression of (7.4) and (7.7). It should be noted that the critical speed is normally relatively low. The higher the maximum SC current, the higher the maximum SC braking torque (the braking torque is in negative direction), as in Figure 7.22(c). Thus, the resulting minimum output torque under SC fault occurring at critical speed is decreasing when B_{s0} increases, as in Figure 7.22(d).

(a) Critical speed

(b) Maximum SC current

(c) Maximum SC braking torque

(d) Minimum output torque under SC fault
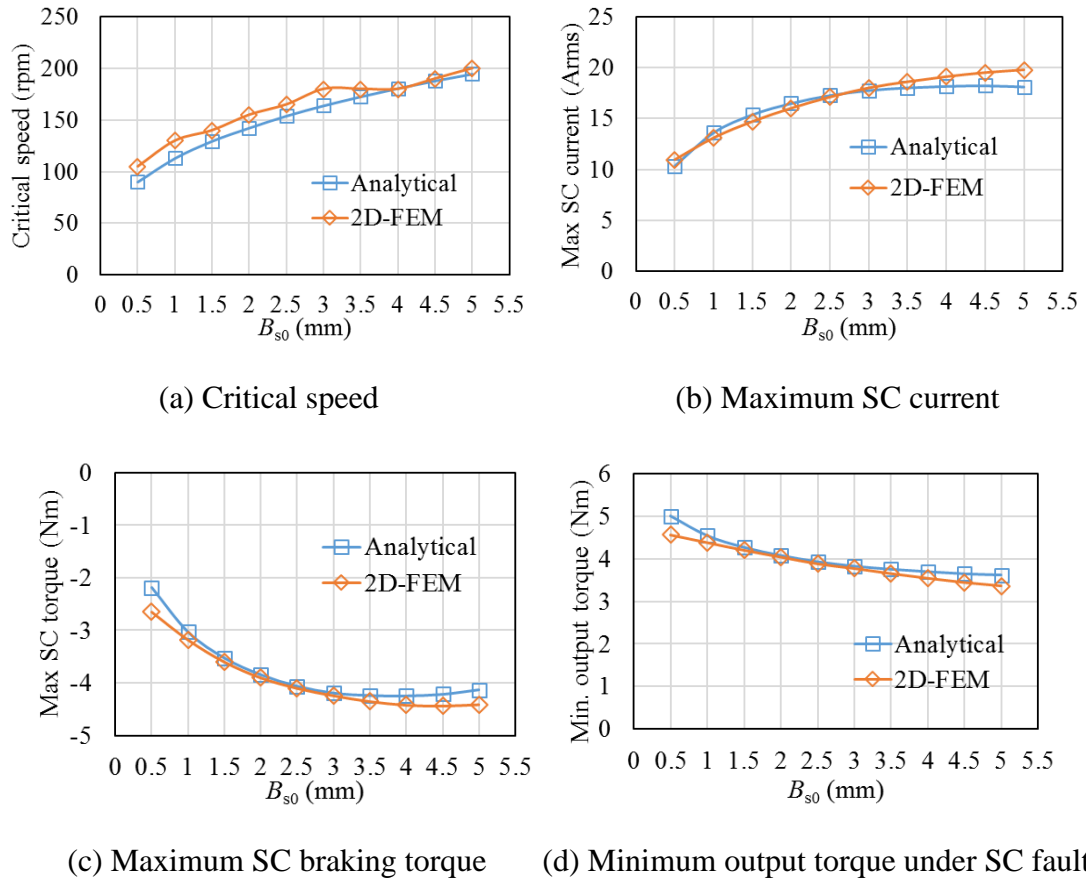
Figure 7.22 One 3-phase SC characteristic of dual 3-phase EMA motor with different B_{s0} when h_{s0}=1mm, h_{s1}=1mm

On the other hand, the per-unit inductance design can be realized when B_{s0}=2.5mm as the maximum SC current is equal to the designed peak current of 17Arms. In this case, the minimum output torque under one 3-phase SC fault is 3.9Nm. However, for B_{s0}<2.5mm case, the phase inductance is higher than per-unit inductance and thereby a higher minimum output torque can be achieved. This provides an opportunity to increase the resulting output torque capability under SC fault by having a phase inductance that is higher than per-unit inductance. This is interesting as in

many cases it is the output torque capability under SC fault condition that determines the overall sizing factor of a fault-tolerant motor [61].

For example, when B_{s0}=1mm, the resulting torque under SC fault is 4.4 Nm which is 12.8% higher than the resulting torque of 3.9Nm when B_{s0}=2.5mm (per-unit inductance design), while the average torque when B_{s0}=1mm under healthy condition is only reduced by 5% compared to B_{s0}=2.5mm counterpart. However, B_{s0} cannot be too small otherwise it is difficult to insert the coil into the slot unless a segmented modular tooth method is used. Therefore, B_{s0}=1.5mm is selected under which the resulting minimum output torque under SC fault is 4.2 Nm which is 7.7% higher compared to the case of B_{s0}=2.5mm, with average torque under healthy condition reduced by only 3%.

The impact of h_{s0} and h_{s1} can also be easily achieved from the analytical expression. Increasing h_{s0} and h_{s1} will increase the slot leakage inductance and thereby reduce maximum SC current and maximum SC braking torque, which helps to improve output torque capability under SC fault. On the other hand, increasing h_{s0} and h_{s1} will reduce slot area. Thus, both h_{s0}=1mm and h_{s1}=1mm are kept.

7.6   Final design and 3-D FEM verification

7.6.1   Final design geometry

The 2-D FEM analysis results have shown that the dual 3-phase EMA motor is able to deliver more than 15Nm of torque and meet the requirement under both OC and SC fault conditions. However, due to the short axial length of 20mm, the 3-D end effect on the torque capability might be considerable. An extra 10% of axial length, viz., 2mm, is added to compensate the torque reduction due to the 3-D end effect. The outer diameter is changed from of 136mm to 140mm to facilitate the keyway on the outside stator surface. On the other hand, to facilitate the fixation of surface-mounted magnet, a small notch feature is added to the rotor lamination surface, as in Figure 7.23 (b). The final design geometry data and specifications are summarized in Table 7.9.

(a) Before (b) Final
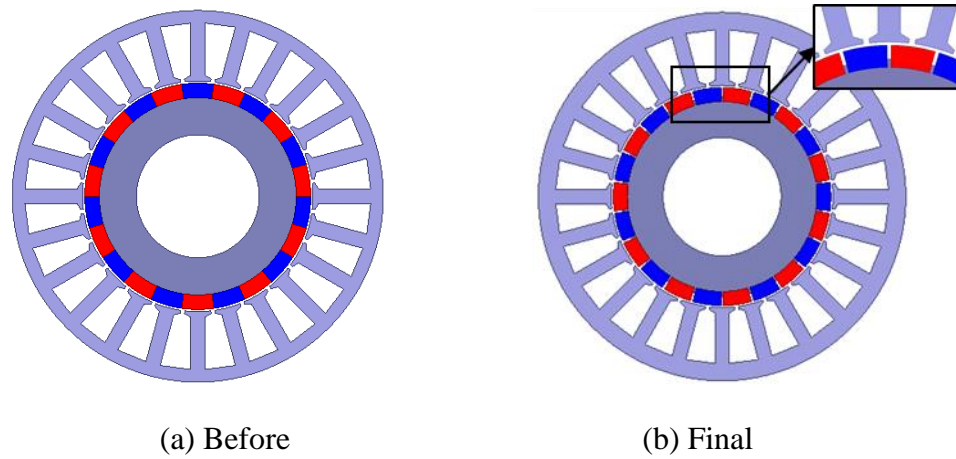
Figure 7.23 Dual 3-phase EMA motor before and after adjustment

Table 7.9 Main specifictaions of the dual 3-phase 24S-22P EMA motor

Parameter	Data	Parameter	Data
D_o (mm)	140	a_{pm}	0.917
D_i (mm)	84.4	Turns per coil	54
L_{ef} (mm)	22	Stator core material	Vacoflux-50
w_t (mm)	5.4	Rotor core material	DW270-35
h_{s0} (mm)	1	Magnet material	N45SH
h_{s1} (mm)	1	Max current (Arms)	17
h_{s2} (mm)	19	Max current density (A/mm2)	12
B_{s0} (mm)	1.5	Peak torque (Nm)	15
g (mm)	0.8	Peak torque under OC fault (Nm)	7.5
h_m(mm)	5.3	Peak torque under SC fault (Nm)	3.75

(a) Full motor (b) Rotor
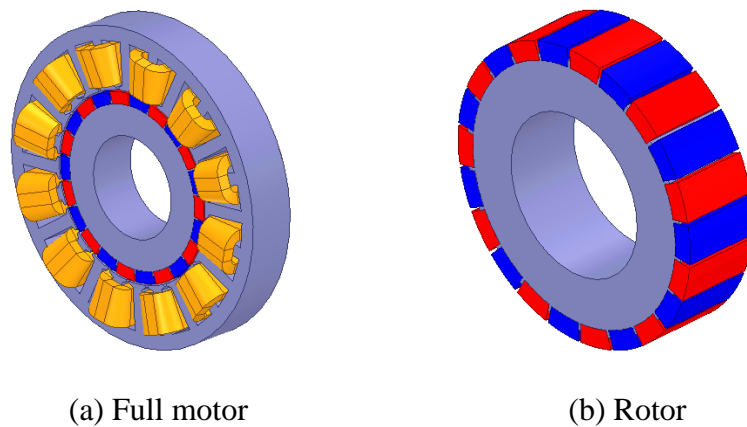
Figure 7.24 3-D geometry model of dual 3-phase EMA motor

7.6.2 3-D FEM verification

It is necessary to investigate the torque and fault-tolerant capability of the dual 3-phase EMA motor with 3-D FEM analysis due to the short axial length. The 3-D FEM model is plotted in Figure 7.24.

7.6.2.1 EM performance under healthy condition

The phase EMF comparison of the dual 3-phase EMA motor calculated from 2-D and 3-D FEM are plotted in Figure 7.25. It is evident that the difference between them is small. FFT analysis shows that the fundamental EMF of 3-D FEM result is 3% less compared to 2-D FEM result.

(a) Phase EMF   (b) FFT spectrum of phase EMF
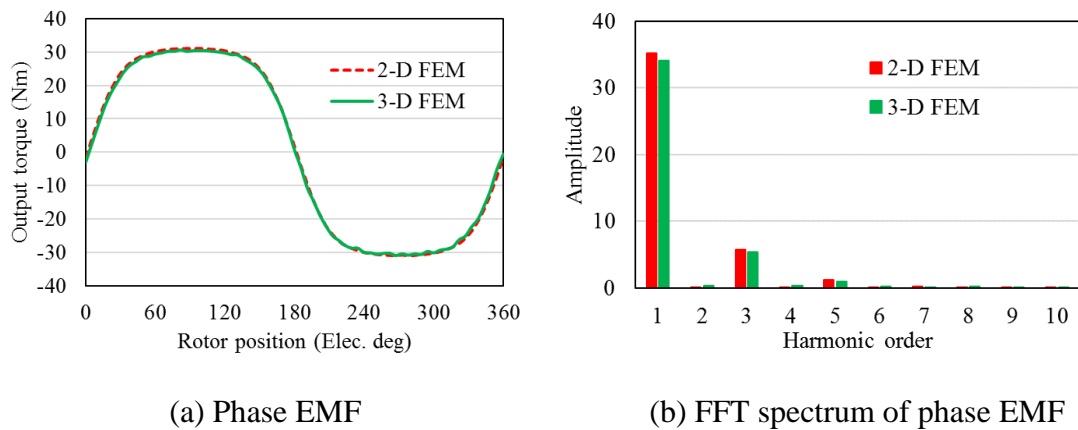
Figure 7.25 No-load phase EMF of dual 3-phase EMA motor @1320rpm

(a) Peak torque waveform   (b) Torque vs current
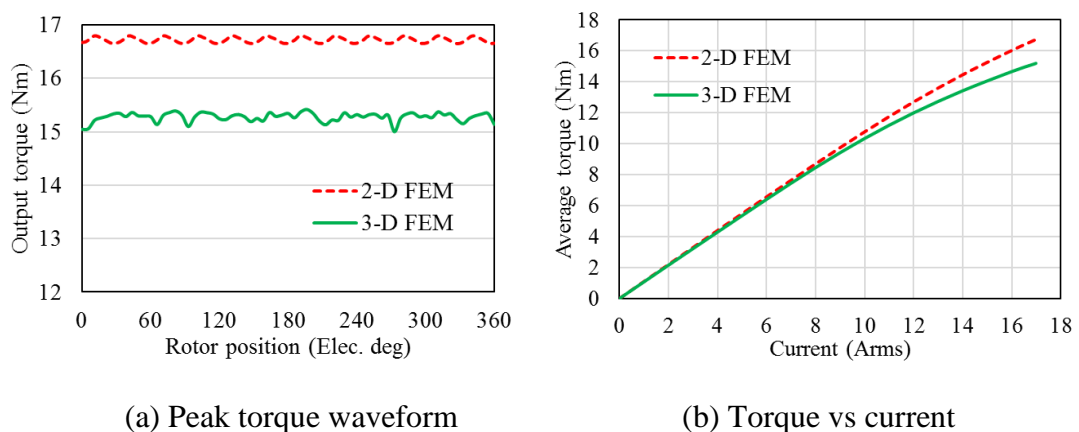
Figure 7.26 EM torque characteristics of dual 3-phase EMA motor under healthy condition

Figure 7.26 depicts the EM torque characteristics of the dual 3-phase EMA motor under healthy conditions. The peak torque waveform (with peak current density of 12A/mm^2) in Figure 7.26 (a) shows that the 3-D FEM calculated torque is about 15.2Nm which can meet the target torque of 15Nm and is 9.9% lower than that of 2-D FEM due to the 3-D effect. Figure 7.26 (b) depicts the comparison of torque current characteristics. It is evident that only when current is higher than 9Arms, the 3-D effect becomes considerable. This is reasonable that due to the increasing electrical loading, the stator core is becoming more saturated which leads to an increase of the end-winding leakage flux.

7.6.2.2 Inductance calculation

The inductance under no-load condition is calculated, as shown in Figure 7.27. As can be seen, the self-inductance is almost constant. The 3-D FEM inductance is 1.515mH which is 0.334mH higher than that of 2-D FEM results; the difference is attributed to the end-winding leakage inductance.

(a) 2-D FEM   (b) 3-D FEM
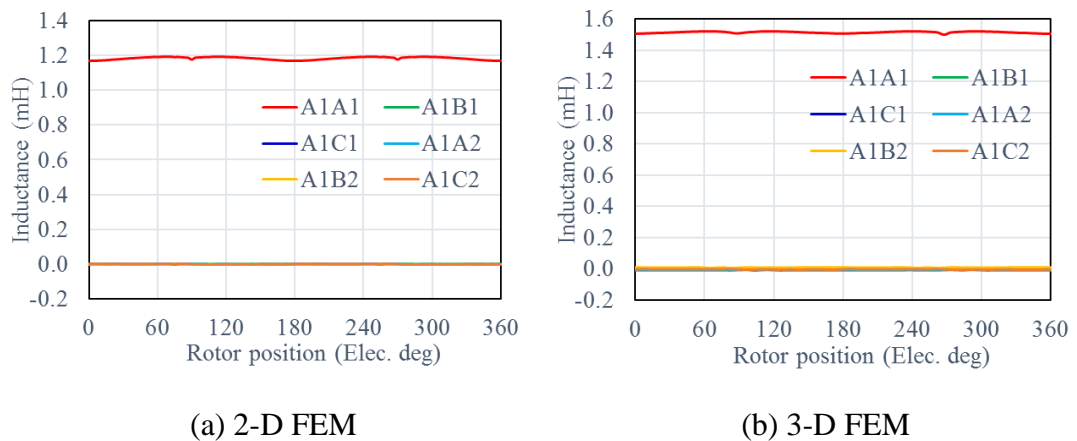
Figure 7.27 Inductance waveform of the dual 3-phase EMA motor

Table 7.10 Average value of inductances of dual 3-phase EMA motor

	L_{A1A1} (mH)	L_{A1B1} (mH)	L_{A1C1} (mH)	L_{A1A2} (mH)	L_{A1B2} (mH)	L_{A1C2} (mH)
2-D FEM	1.183	0.000	0.000	-0.001	0.001	0.000
3-D FEM	1.515	0.001	0.001	-0.009	0.009	0.000

In addition, the mutual-inductance between different phases is negligible compared to the self-inductance, as shown in Table 7.10, which implies magnetic isolation between phases and so is beneficial to the fault-tolerant operation of the dual 3-phase EMA motor as the faulty windings would not affect the operation of remaining healthy windings.

7.6.2.3 EM performance under open-circuit (OC) fault condition

The EMF of the OC fault phase of the dual 3-phase EMA motor operating at peak speed when the remaining healthy phase is loaded with peak current (1320rpm, 17Arms) is plotted in Figure 7.28. Compared to Figure 7.25, it is evident that voltage of OC phase under one 3-phase loaded with peak current is almost the same as the no-load phase voltage. This confirms that the mutual-coupling between the two 3-phase winding sets is negligible.

(a) Phase EMF   (b) FFT spectrum of phase EMF
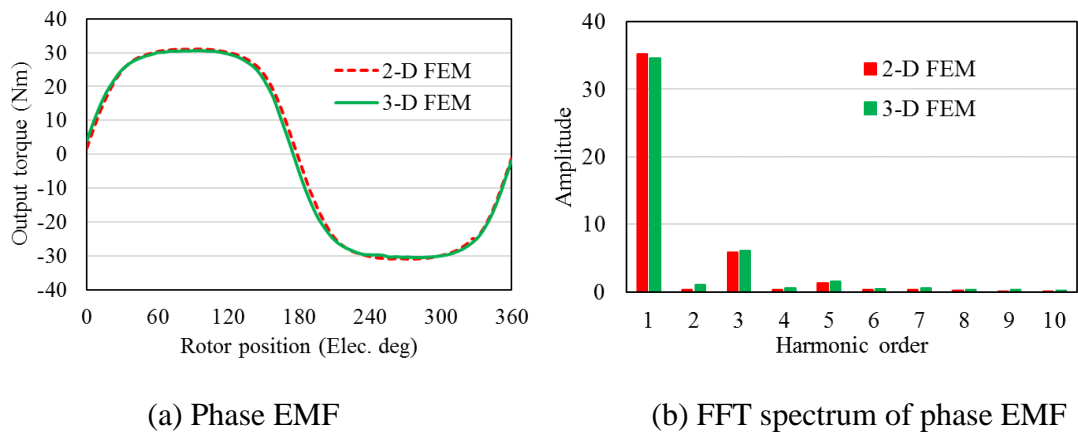
Figure 7.28 EMF of OC phase of dual 3-phase EMA motor under load

(a) Torque waveform   (b) Torque vs current
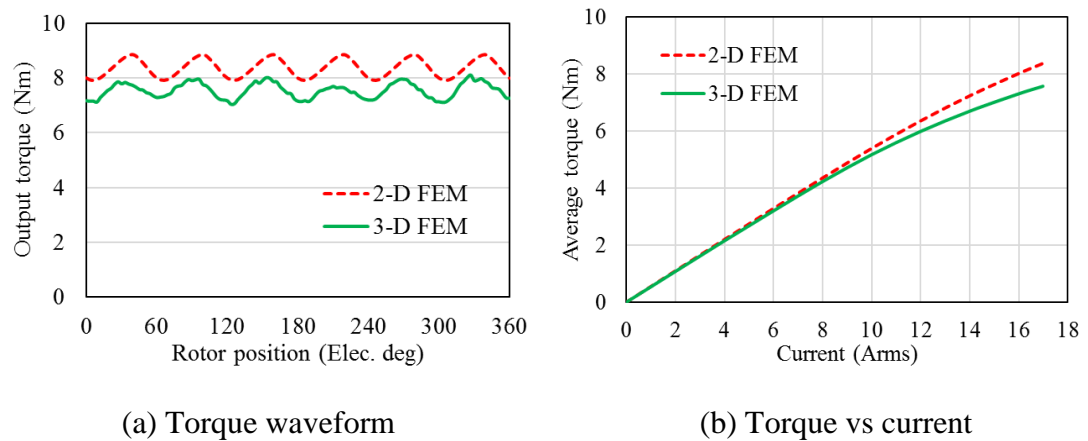
Figure 7.29 Torque of dual 3-phase EMA motor @OC fault condition

Figure 7.29(a) plots the peak EM torque waveform when one 3-phase winding is in OC fault condition and the remaining healthy 3-phase is fed with corresponding peak current. Again, lower peak torque is seen in 3-D FEM analysis. The torque current characteristics under OC fault condition is depicted in Figure 7.29(b). Similar to the healthy condition, when current is higher than 9Arms, the 3-D effect on reducing average torque becomes considerable.

7.6.2.4 EM performance under short-circuit (SC) fault condition

The comparison of SC current and braking torque waveform under one 3-phase SC fault at 1320rpm has been calculated using 2-D and 3-D FEM, and is shown in Figure 7.30. A lower steady-state SC current and braking torque is seen in the 3-D FEM result due to the high inductance attributing to to the end-winding effect. This is advantagous in terms of reducing temperature rise coming from SC current and reducing SC braking torque.

The behavior of the one 3-phase SC current and SC braking torque versus speed is calculated, as shown in Figure 7.31. A much lower SC braking torque can be observed in 3-D FEM analysis. The output torque under one 3-phase SC fault condition is quite similar for both 2-D and 3-D FEM analysis. The minimum output torque with peak current under one 3-phase SC condition for 3-D FEM analysis is 4.8Nm which is much higher than the design requiremnt of 3.75Nm.
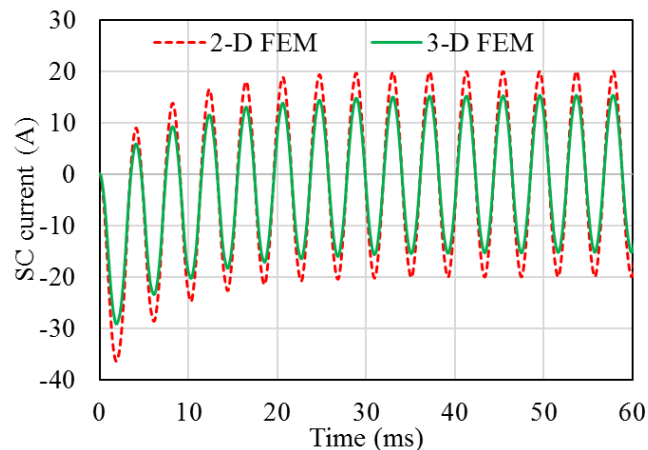
(a) SC current
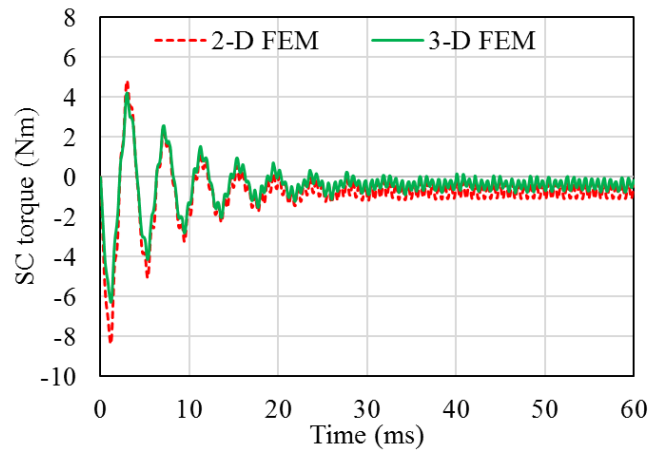
(b) SC braking torque

Figure 7.30 SC characteristics of dual 3-phase EMA motor @1320rpm
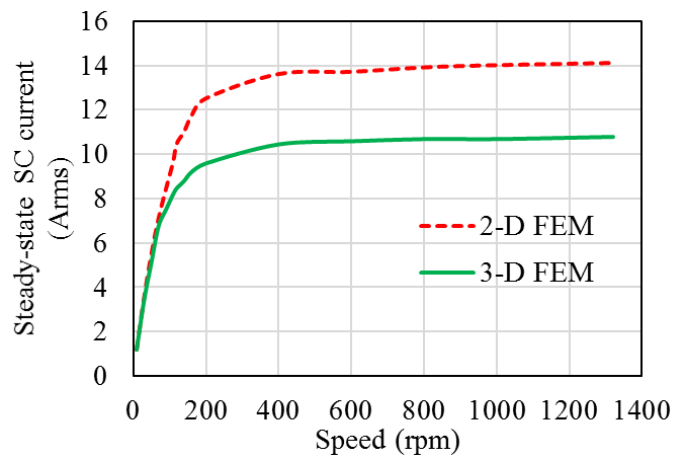
(a) SC current
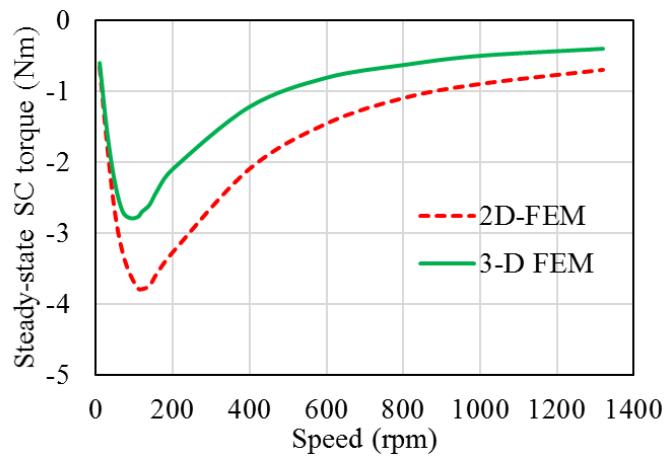
(b) SC braking torque
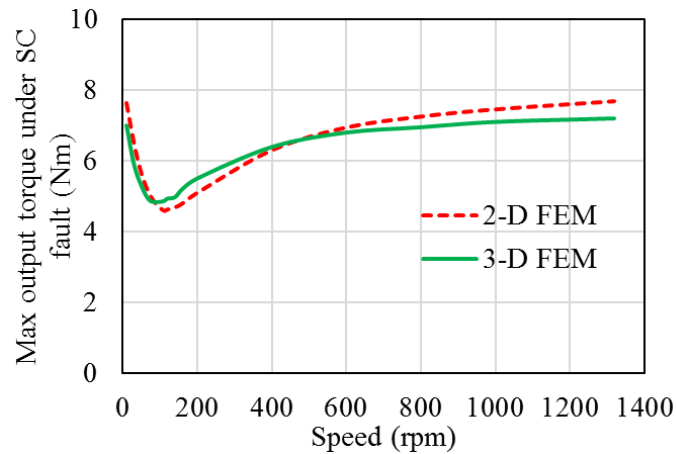
(c) Output torque with peak current under SC fault

Figure 7.31 Steady-state SC fault characteristics of dual 3-phase EMA motor

(a) Radial direction   (b) Axial direction
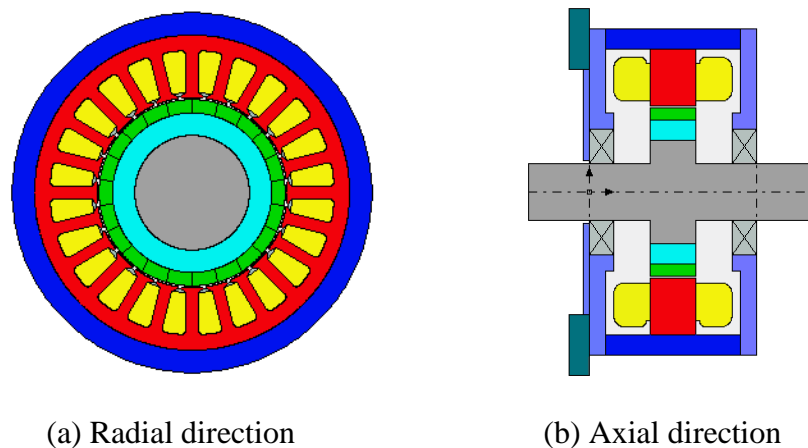
Figure 7.32 Thermal model built in Motor-CAD

7.7 Thermal analysis

As has been discussed in Section 6.6.2, the EMA must meet the thermal requirements under the designed duty cycle. The duty cycle of two minutes on with peak torque demand and one minute off repeating 3 times as in Figure 6.17 is used for thermal performance evaluation. The Motor-CAD model for thermal performance evaluation is shown in Figure 7.32, with basic input data summarized in Table 7.11.

The loss data of the dual 3-phase EMA motor calculated from 3-D FEM analysis with the worst scenario of peak speed and peak load (1320rpm, 17Arms) is

summarized in Table 7.12. It is evident that the dominant loss is copper loss, which accounts for more than 90% of total loss. It should be noted that the AC copper loss is neglected due to the low speed characteristic.

Table 7.11 Basic input data to Motor-CAD model for thermal analysis

Parameter	Value
Enclosure type	Totally Enclosed Non-Ventilated (TENV)
Housing outer cooling	Natural convection
Interface gap between stator lamination and housing	0.03mm
Ambient air temperature	60°C
Air gap thermal model type	Convection

Table 7.12 3-D FEM calculated loss data of the EMA motor

Copper loss @60°C (W)	Stator iron loss (W)	Rotor iron loss (W)	Total Iron loss (W)	Magnet loss (W)	Total loss (W)
311.3	13.0	5.6	19.4	4.6	335.3

The model of mechanical loss including bearing friction loss and windage loss is complicated. Normally the bearing friction loss can be estimated using SKF bearing estimator tool [169] or empirical formulas [168]. The windage loss can be estimated using (7.24) given in [170]. Since the dual 3-phase EMA motor is characterized by small size and low speed, both the windage loss and friction loss are negligible.

$$P_f = K C_f \pi \rho \omega^3 r^4 l_{ef} \tag{7.24}$$

where K is the roughness coefficient; ρ is the mass density of fluid; The friction coefficient C_f depends on many factors and it is often empirically determined [170].

7.7.1 Thermal duty cycle analysis

The transient thermal analysis is carried out for the dual 3-phase EMA motor with the duty cycle provided in Figure 6.17, with the results summarized in Figure 7.33.
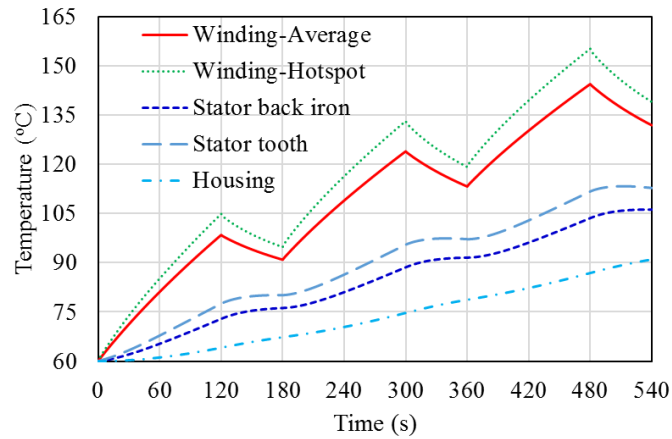
(a) Stator components
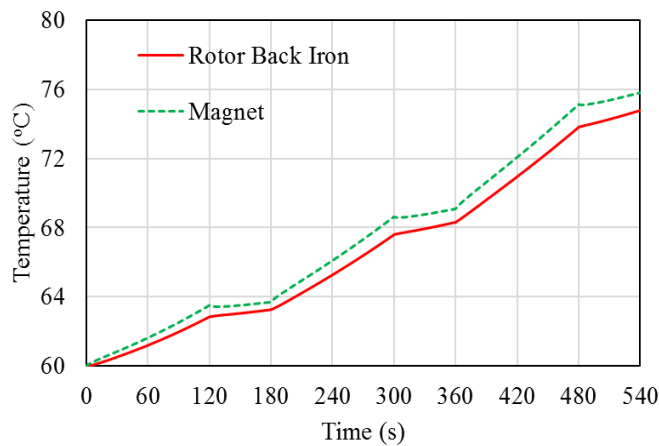
(b) Rotor components

Figure 7.33 Transient thermal characteristics of the EMA motor with duty cycle operation

As can be seen that with the duty cycle of two minutes on and one minute off repeating three times, the maximum winding average temperature at each two-minutes on and one-minute off operation reaches 98ºC, 123.9ºC, and 144.4ºC, respectively; the temperature rise at each two-minutes on operation is 38.4ºC, 33ºC, and 31.2ºC, respectively, and temperature drop at each one-minute off operation is 7.5ºC, 10.7ºC, and 12.6ºC, respectively. The maximum hotspot temperature of the winding reaches 155.2 ºC, which is 10.8ºC higher than corresponding average winding temperature and is within the safety temperature limit of winding insulation (200ºC). Stator tooth and stator back iron tend to have a lower temperature compared to winding. The maximum housing temperature is about 90ºCafter the duty cycle operation.

Since there is not much rotor loss and the thermal resistance between stator and rotor is high due to the existence of air, the rotor temperature is under 80°C which is much lower compared to stator components and compared to the magnet maximum allowable temperature of 150°C, but it is slowly monotonously increasing during the duty cycle operation because there is constant heat transferred from stator through airgap due to the high temperature difference between stator and rotor. It is evident that the rotor is less demanding in terms of thermal dissipation.

Figure 7.34 plots the loss behaviour during the duty cycle operation. One can note that the copper loss is dominant, and it increases when temperature rises.
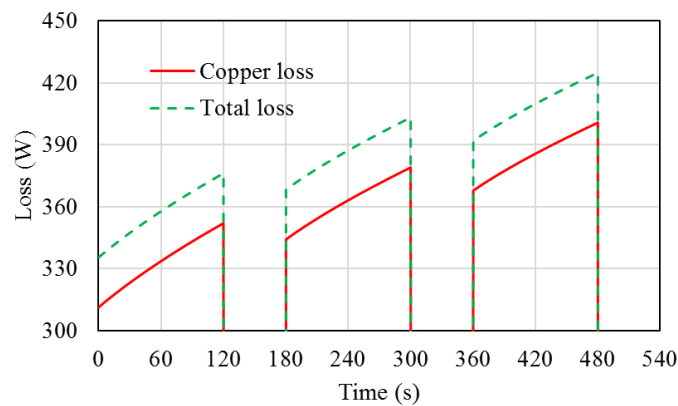
Figure 7.34 Loss behavior of the EMA motor with duty cycle operation

7.7.2 Sensitivity studies of motor thermal behavior

The accurate modelling and simulation of the thermal behaviour of the motor is complicated, and depends on many factors including losses estimation, material properties, assembly tolerance, and motor geometrical parameters. This section deals with sensitivity studies on the motor thermal behaviour.

7.7.2.1 Sensitivity of input losses

Both the machining and assembly process make it difficult to accurately predict both the copper loss and iron loss. By increasing both copper loss and iron loss with a ratio, the sensitivity of these losses with regards to the motor temperature can be studied for the duty cycle operation. Table 7.13 summarizes the maximum temperature of stator

and rotor components for different input loss combinations. The temperature characteristics of duty cycle operation are shown in Figure 7.35.

Table 7.13 Maximum temperature of the EMA motor for different loss combinations

#	Copper loss @60 °C	Iron loss	Housing (°C)	Winding average (°C)	Winding hotspot (°C)	Magnet (°C)
1st	100%	100%	91	144.4	155.2	75.8
2nd	105%	120%	91.9	148.6	160.0	77.2
3rd	110%	140%	93.9	154.0	166.0	78.5
4th	115%	160%	95.9	159.5	172.2	79.9
5th	120%	180%	97.9	165.1	178.4	81.4
6th	125%	200%	100	170.8	184.8	82.8
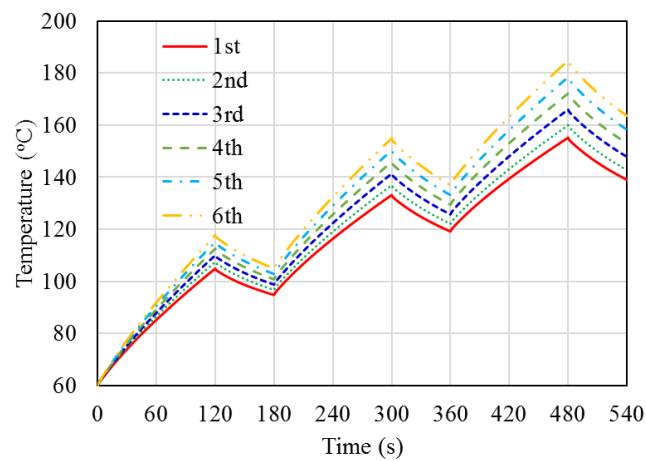
(a) Winding hotspot temperature
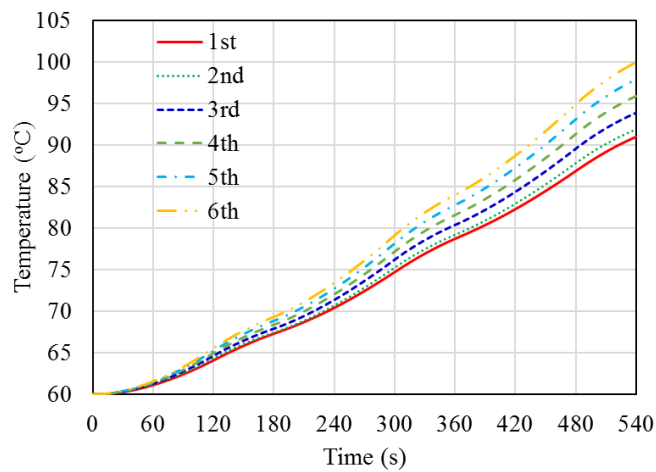
(b) Housing temperature
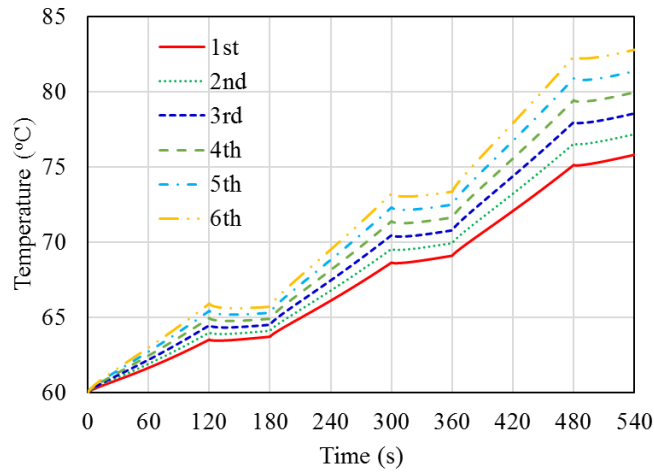
(c) Magnet temperature

Figure 7.35 Thermal behavior of the dual 3-phase EMA motor with different losses combinations

Table 7.14 Maximum temperature of the EMA motor for difference interface gaps between stator lamination and housing

Interface gap (um)	Housing (^{o}C)	Winding average (^{o}C)	Winding hotspot (^{o}C)	Magnet (^{o}C)
0	93.7	137.1	148.7	74.9
10	92.4	139.4	150.7	75.3
30	91	144.4	155.2	75.8
60	86.7	147.7	157.8	76.4
90	84.1	150.9	160.6	76.9

It can be observed that with 125% copper loss and 200% iron loss, the winding hotspot temperature and average temperature are 184.8^{o}C and 170.8^{o}C, respectively, which both are well below safety limit of 200°C. Magnet temperature is still very low. Maximum housing temperature just reaches 100°C.

7.7.2.2 Sensitivity of interface gap between stator and housing

The interface gap between stator core and housing results in different thermal resistance between stator and housing, which may have a considerable impact on the temperature distribution as the housing is the main heat dissipation path.
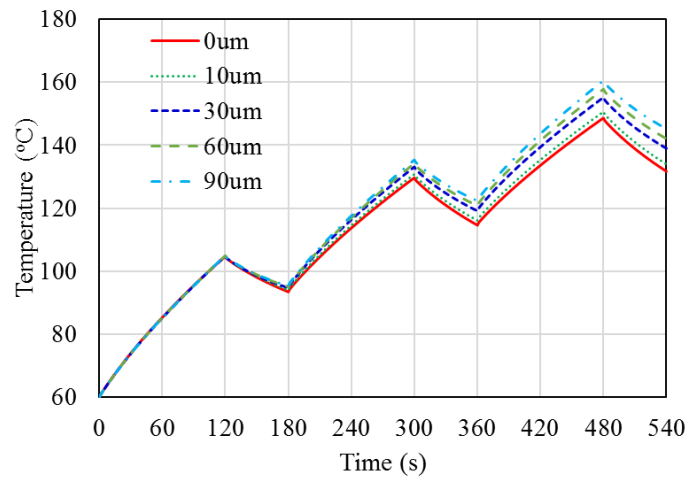
(a) Winding hotspot temperature
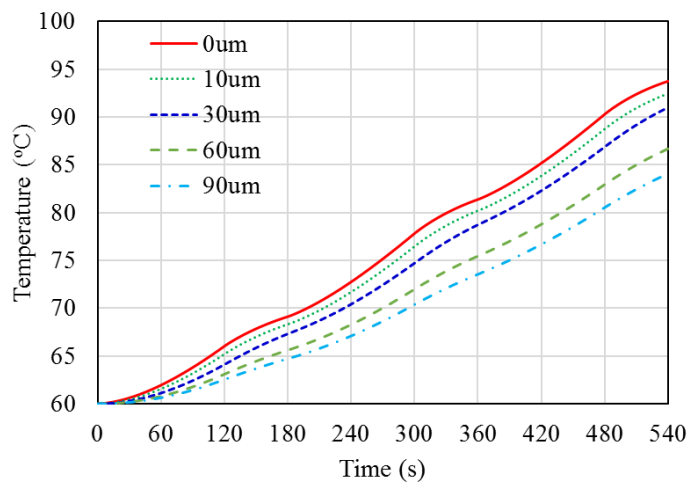
(b) Housing temperature
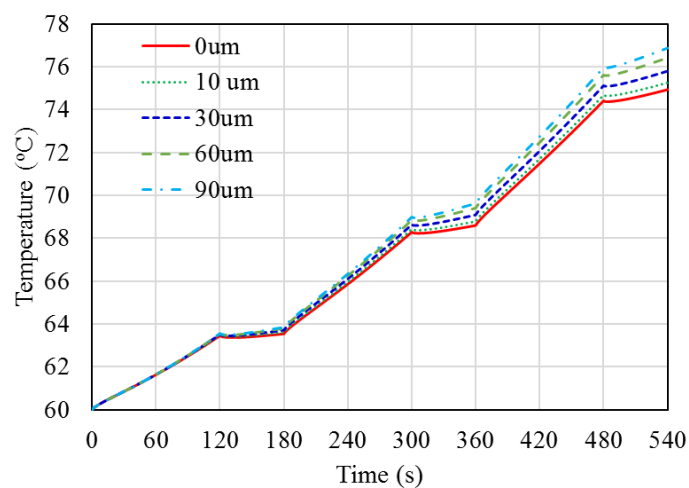
(c) Magnet temperature

Figure 7.36 Thermal behavior of the EMA motor with different interface gap

between stator lamination and housing

Table 7.14 and Figure 7.36 shows the temperature variation of the dual 3-phase EMA motor with different interface gaps between stator core and housing under the duty cycle operation. The average interface gap of 30um is the reference design that the prototype can achieve. It suggests that a perfect surface contact between stator and housing will give temperatures that 12℃ and 13.8℃ lower in winding hotspot and average temperature respectively, compared to the poor surface contact with 90um interface gap.

7.8   Chapter summary

In this chapter, a fault-tolerant EMA motor with a high level of physical, electrical, magnetic, and thermal isolation is identified. Firstly, the modular structure design of the EMA motor is presented to facilitate the modular EMA configuration. Secondly, the 24 slots, 22 poles single-layer winding SPM motor with excellent fault-tolerant capability and torque capability is identified as the candidate for the modular EMA motor. Performance improvement of the EMA motor is achieved through using a parallel magnetization pattern, high-performance cobalt-iron steel, and a dual 3-phase winding. The identified dual 3-phase winding configuration with 30^0 shift in time exhibits an improved torque performance in the healthy condition and the most symmetrical magnetic field and so no UMP in both healthy and fault conditions.

The armature inductance is analytically calculated and compared with 2-D FEM to evaluate the motor performance under 3-phase SC fault conditions. The steady-state SC current and maximum SC braking torque are optimized to acceptable levels by controlling slot opening dimensions. An interesting finding is that by having an inductance higher than one per-unit, the motor output torque capability under SC fault can be considerably improved without sacrificing considerable torque capability in the healthy condition.

Thermal evaluation of the dual 3-phase EMA motor under the designed duty cycle operation shows it can safely operate and the hotspot is in the winding. Sensitivity study on the losses suggests that the EMA motor has enough thermal margin.

Chapter 8

Prototyping and Experimental Validation

This chapter presents the prototype manufacturing and experiment tests undertaken to validate the design and analysis presented in the previous chapters. The first part of the chapter deals with the experimental verification of the 24 slots, 14 poles IPM traction motor presented in Chapter 5. The manufacturing process and test rig are presented. The static parameters including resistance, inductance, and EMF and performance under both normal and fault conditions have been tested; and the results are used to compare with the predicted results in Chapter 5.

The second part is concerned with the modular EMA motor (24 slots, 22 poles SPM motor) of Chapter 6 and Chapter 7. Two prototypes are built. The manufacturing challenges in stator winding and consideration for modular design are presented. The static characteristics under both normal and fault conditions of the single motor, and the modular performance with two interconnected motors assembled together have been tested. The experimental results are compared to the predicted results in Chapter 6 and Chapter 7.

8.1   24 slots, 14 poles IPM motor

To validate the design and analysis of the 24 slots, 14 poles IPM motor presented in Chapter 5, a prototype motor has been built. The manufacturing and testing of the IPM motor are tackled in this section.

8.1.1 Manufacturing and assembly

The general assembly drawing of the IPM motor is shown in Figure 8.1. Figure 8.2 shows the components and assembly of the IPM motor prototype. The stator and rotor are laminated stacks. The stator is wound with the proposed 24 slots, 14 poles topology with double-layer (DL) winding in Section 4.2.2. The resulting copper slot fill factor is 43.4%. With a dual 3-phase winding configuration, 2 terminals of each phase winding come out and therefore 12 terminals come out in total.
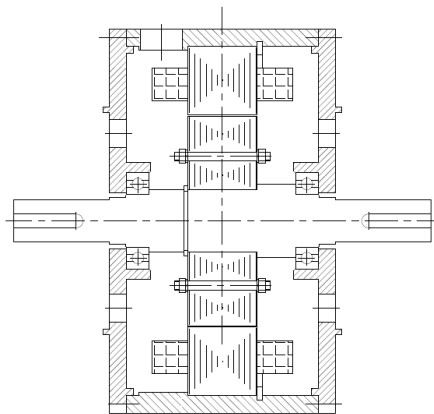
Figure 8.1 General assembly drawing of the IPM traction motor

Due to the limitations of the lead time and cost, a water jacket housing was not adopted, the motor instead relied on passive air cooling via the housing. The rotor uses V-shaped structure with a single-layer of magnets and has internal arc ducts to minimize weight.
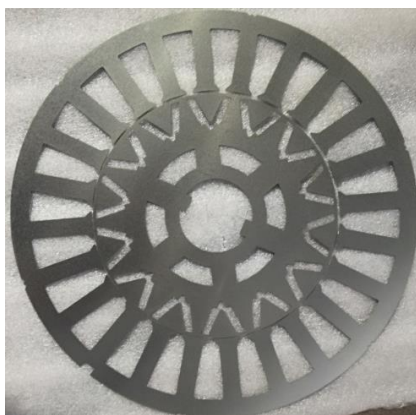
(a) Stator and rotor lamination
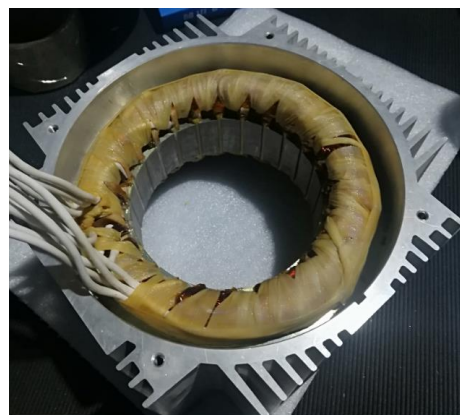
(b) Stator assembly

| (c) Rotor assembly | (d) Prototype assembly |

Figure 8.2 Components and assembly of the IPM traction motor prototype
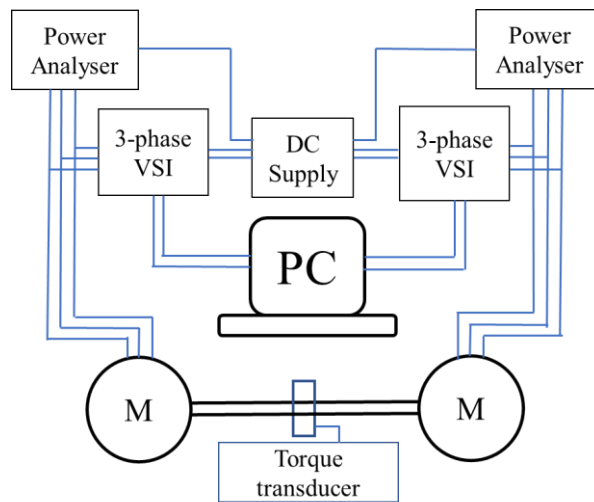
Figure 8.3 Schematic view of motor testing setup

8.1.2 Experimental test

8.1.2.1 Test rig setup

To test the performance of the motor under different representative operating conditions, the test rig is developed, and its schematic is shown in Figure 8.3.

The experimental test rig setup is shown in Figure 8.4. A PMSM servo motor is adopted as the load motor. Torque is measured with an HBM torque transducer. The control is realized by a back-to-back 3-phase voltage source inverters (VSI); one for the load motor, and another for the tested IPM motor.

(a) Back-to-back 3-phase voltage source inverters (VSI)
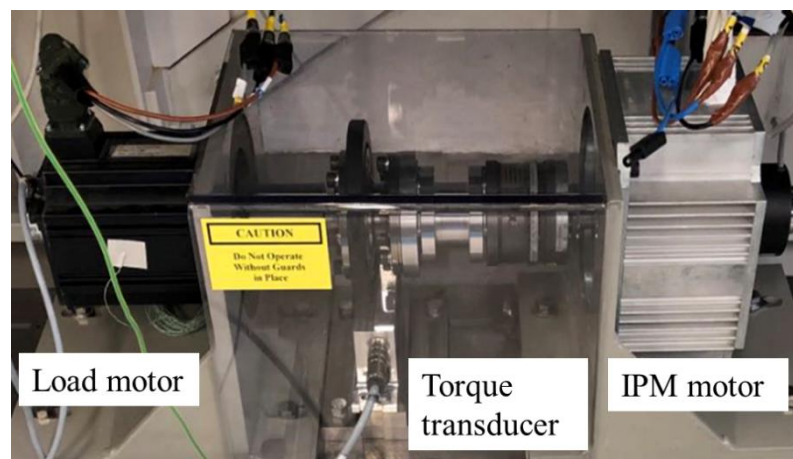
(b) Motor test rig

Figure 8.4 IPM traction motor testing setup

8.1.2.2 Resistance measurement

The resistance is measured at room temperature (20°C) using a DC current method. Due to the small phase resistance, an additional resistor is in series connected to limit the current to acceptable levels, as depicted in Figure 8.5. The measured results are summarized in Table 8.1. The resistance per phase is consistent, and the difference between the calculated and measured value is about 11%. The discrepancy may be attributed to the connections between different coils and the terminal leads.
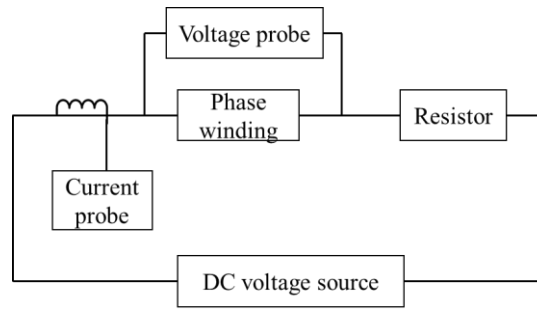
Figure 8.5 Schematic of phase resistance measurement

Table 8.1 Measured phase resistance of the IPM traction motor at 20$^{\text{o}}$C

	Calc.	Measured					
		A1	B1	C1	A2	B2	C2
Value (ohm)	0.0753	0.0845	0.0838	0.0836	0.0836	0.0835	0.0833
Ratio	-	1.12	1.11	1.11	1.11	1.11	1.11

8.1.2.3 No-load test

The no-load voltage was measured at room temperature (20$^{\text{o}}$C) when the IPM motor is driven by the load motor operating at different speeds. Figure 8.6 shows the no-load phase voltage when the IPM traction motor is configured as dual 3-phase winding operating at base speed of 1910rpm and its FFT spectrum. Table 8.2 summarizes the amplitude and RMS value of fundamental harmonic of the no-load phase voltage obtained from the experiment test with those of predicted by 3-D FEM calculation. It is worth noting that the 3-D FEM model is updated for the room temperature (20$^{\text{o}}$C).

As can be seen, the measured phase voltage is 4.7% lower than that of 3-D FEM results. This may be attributed to many factors, including the magnet dimension tolerance for inserting magnets into the rotor which can result in variations in magnet volume. In addition, the difference in B-H characteristic curves for both magnet and steel may also contribute to the difference. In addition, a 30^{0} shift in time between the two 3-phase windings can also be observed, as would be expected from the novel winding layout.

When the dual 3-phase winding configuration are configured as a single 3-phase winding configuration via series connection as in Figure 8.7, the corresponding no-load phase voltage is shown in Figure 8.8 and Table 8.2(b). Again, a lower measured value is observed.
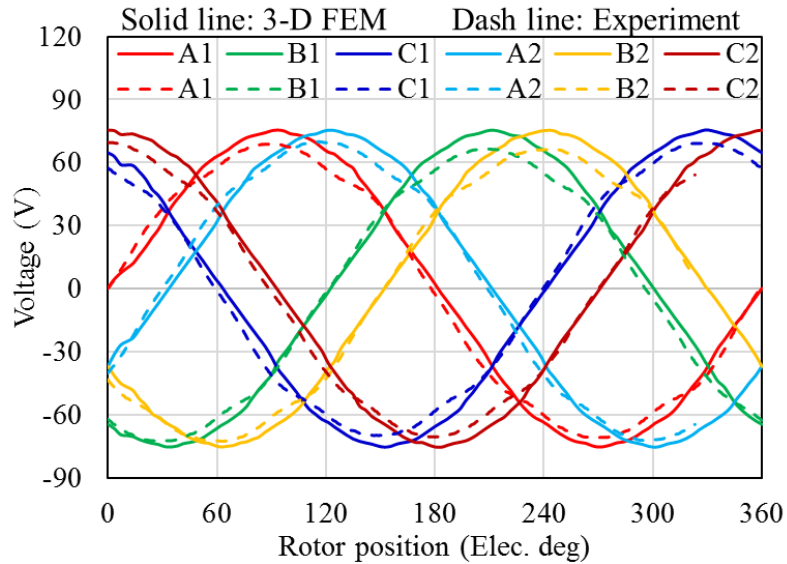
(a) Waveform
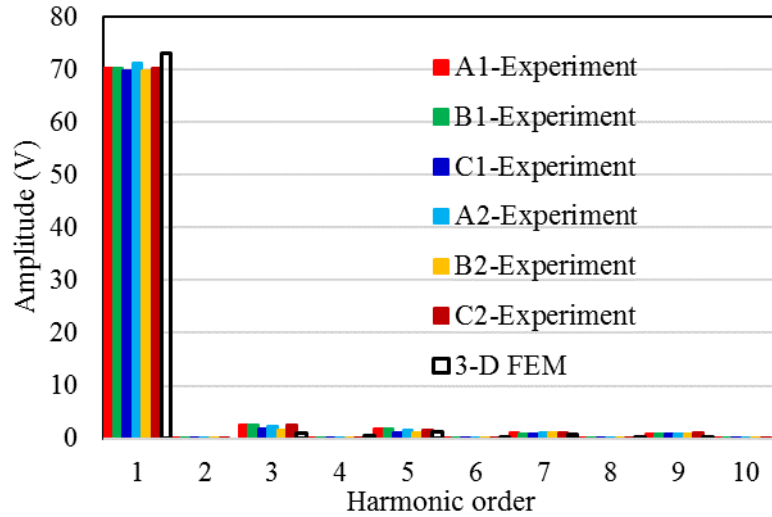
(b) FFT spectrum

Figure 8.6 Comparison of measured and predicted phase voltage of IPM motor @1910rpm for dual 3-phase configuration

(a) Coil phasor diagram   (b) Physical connection
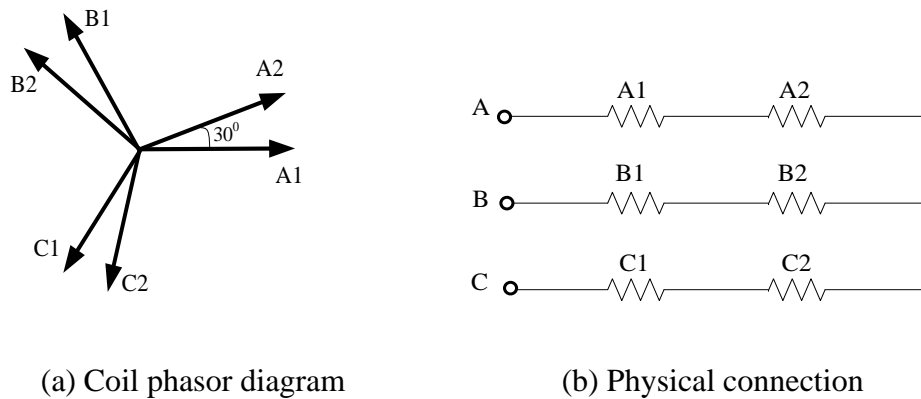
Figure 8.7 Winding configurated as a single 3-phase connection

Table 8.2 Measured and predicted EMF of IPM motor @1910rpm

(a) Dual 3-phase configuration

Fundamental voltage	Calc.	Measured					
		A1	B1	C1	A2	B2	C2
Amplitude (V)	73	70.2	70.2	69.9	71.3	69.9	70.3
RMS (Vrms)	51.6	49.7	49.7	49.4	50.4	49.4	49.7
Ratio (measured to calc.)	-	0.962	0.962	0.957	0.977	0.957	0.963

(b) Single 3-phase configuration

Fundamental voltage	Calc.	Measured		
		AB	BC	CA
Amplitude (V)	139.8	135.2	133.7	134.6
RMS (Vrms)	98.8	95.6	94.5	95.2
Ratio (measured to calc.)	-	0.967	0.957	0.963
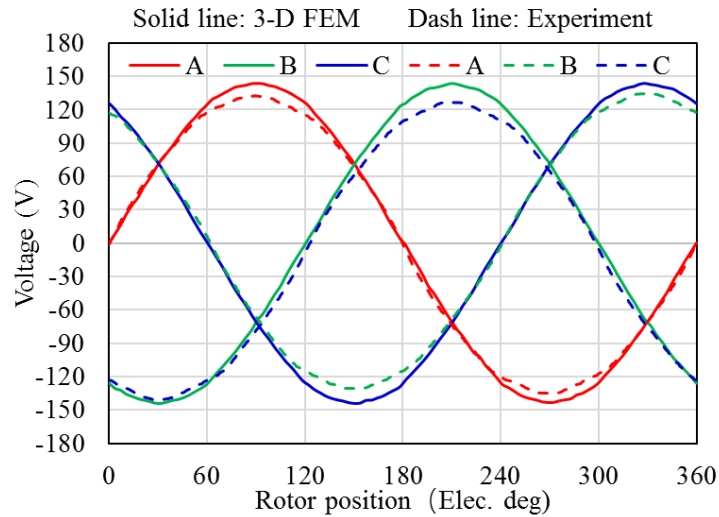
(a) Waveform
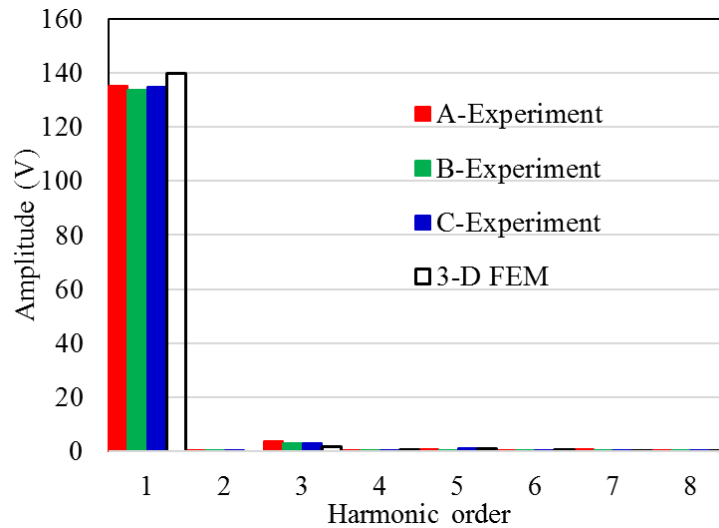
(b) FFT spectrum

Figure 8.8 Comparison of measured and predicted phase voltage of IPM motor
@1910rpm for single 3-phase configuration

8.1.2.4 Load test

Due to the limitations of the control drive, the control of dual 3-phase with 30^0 shift in time from each other, as in Figure 8.9, cannot be implemented. Thus, the dual 3-phase windings are configured as a single 3-phase winding driven by a 3-phase voltage source inverter, as in Figure 8.10. Due to the torque limitation of the load motor, the full torque and power speed characteristics of the IPM motor cannot be completely

tested. Due to the absence of water jacket, to avoid overheating of the motor, the testing was done in a short period of time.
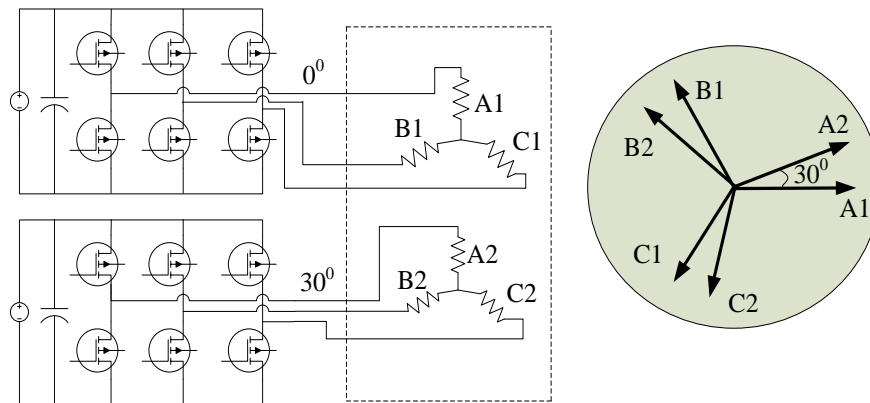
Figure 8.9 Dual 3-phase winding configuration driven by two 3-phase VSIs
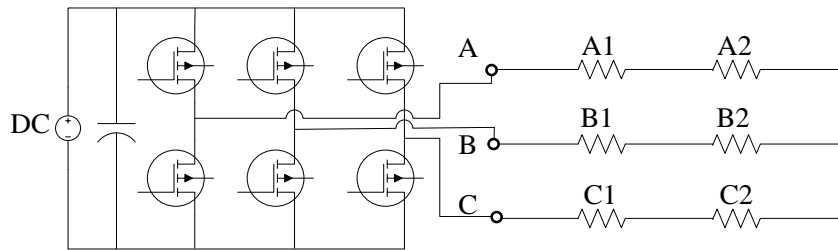
Figure 8.10 Single 3-phase winding configuration driven by a 3-phase VSI

8.1.2.4.1 Measurement of *d*- and *q*- inductance

The IPM traction motor is a salient pole synchronous motor where EM torque generated includes magnet torque and reluctance torque, as indicated in (3.45). The reluctance torque depends on the difference between *d*- and *q*- inductance. Thus, it is necessary to measure the *d*- and *q*- inductance versus different *d*- and *q*- axis current.

The parameter measurement method presented in [171] is used, which is based on the steady-state voltage and current waveform and rotor position because at steady state the derivative items in the voltage equations are zero, as indicated in (3.45). The corresponding steady-state phasor diagram is shown in Figure 8.11.

In this method, the motor is operating at certain steady speed. The motor speed should be selected carefully. The speed should be high enough to minimize the effect of resistive drop to the machine voltage drop. On the other hand, the speed cannot be

too high such that the current gets distorted due to the high back EMF of the motor at high speeds. Therefore, a speed of 1000rpm is selected, which is lower than the base speed of 1910rpm. The motor is in current control mode and the inverter is controlled to feed the machine with different d- and q- axis current. The phase current is measured with a current probe, and the phase terminal voltage is measured with a differential probe. Due to the PWM switching and stator slotting effect, the voltage is not sinusoidal. Since only the fundamental component is concerned, the FFT is applied to the voltage and current waveform to extract the fundamental amplitude and phase angle information. The measured fundamental voltage and current with their phase angle information can then be used to calculate the d- and q- axis flux linkage using (8.1). Finally, the d- and q- axis inductance can be calculated using (8.2).

It should be noted that the rotor position is not known. However, as the motor is in current control model, d- and q- axis current commands are given, so the measured current can be used to calculate the rotor position reference. The angle φ between current and q-axis can be easily calculated through the given d- and q- axis current command using (8.3); the angle between current and voltage can then be obtained by taking the difference between the phase angle of the fundamental voltage and the phase angle of the fundamental current. Then, the angle δ between the terminal voltage and q-axis can be achieved.
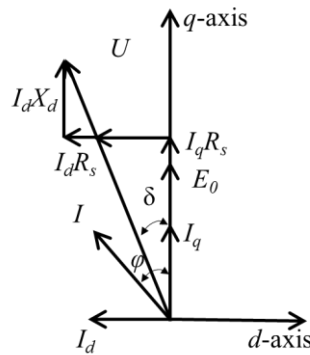
Figure 8.11 Phasor diagram under load condition

$$\begin{aligned} U_d &= I_d R_s - \omega_e \lambda_q \\ U_q &= I_q R_s + \omega_e \lambda_d \end{aligned} \qquad (8.1)$$

$$L_d = \frac{\lambda_d - \lambda_f}{I_d}$$
$$L_q = \frac{\lambda_q}{I_q} \tag{8.2}$$

$$\varphi = \tan^{-1}\left(\frac{I_d}{I_q}\right) \tag{8.3}$$

Figure 8.12 and Figure 8.13 shows the measured d- and q- axis inductance compared with 3-D FEM results. For the q-axis inductance, the measured results are higher than predicted results. However, as the q-axis current increases, the difference between them decreases. When I_q=24A, the difference is only about 4%. The significant errors at low q-axis current may be attributed to the high error in calculating the amplitude and phase angle of phase current as δ is relatively small which is more sensitive to the angle calculation error, while for higher q-axis current, the impact of the angle calculation error on δ becomes small. The manufacturing, material characteristics tolerance, and the effect of magnet temperature may also contribute to the difference.

A similar trend can be observed in the d-axis inductance. The measured results are generally higher than the 3-D FEM predicted results, and the difference is from 10% to 30%. Again, as the current increase, the difference decreases. More results are presented in Appendix B.
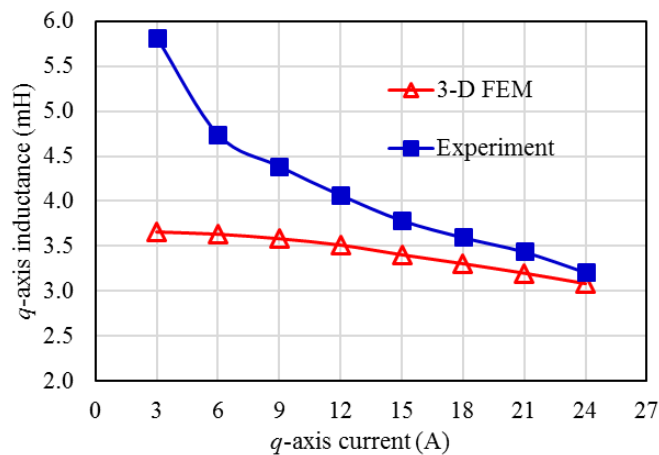
Figure 8.12 q-axis inductance versus different q-axis current when I_d=0A
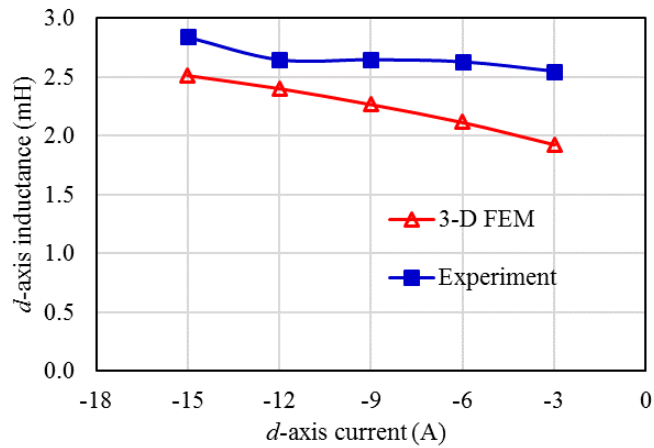
Figure 8.13 d-axis inductance versus different d-axis current when I_q=6A.
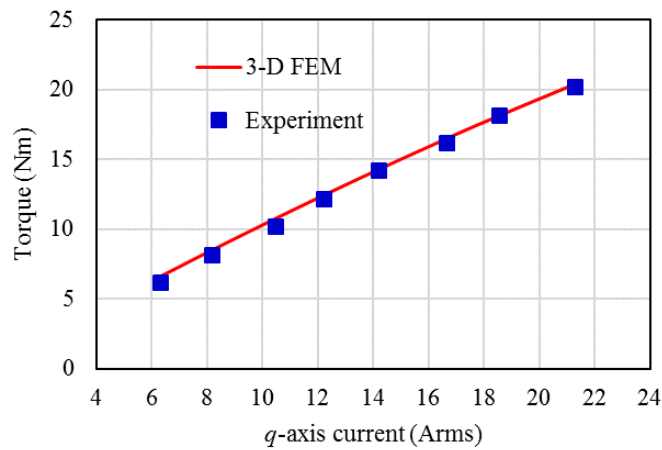
Figure 8.14 Comparison of measured and predicted torque of the IPM motor
@1000rpm

8.1.2.4.2 Efficiency measurement

The efficiency measurement of the IPM traction motor is carried out under current control mode when the load motor is controlled under speed control mode. For simplicity, the I_d=0A control strategy is adopted.

Figure 8.14 shows the comparison of measured and predicted torque current characteristics when the IPM motor is controlled at 1000rpm. As can been seen, the measured torque is generally lower than the predicted results, with the difference within 5%. This may be attributed to the lower amplitude of no-load measured back

EMF. Factors such as material tolerance, manufacturing and magnet temperature may also contribute to it.

The comparison of measured and predicted efficiency at different load conditions when the motor is operating at 1000rpm is plotted in Figure 8.15. The measured efficiency is lower than that of predicted and the difference between them varies from 1 to 1.6%, demonstrating a good level of accuracy. The difference between them is reasonable as the accurate estimation of losses is complicated. The winding temperature, magnet temperature and material loss data discrepancy may also contribute to it.
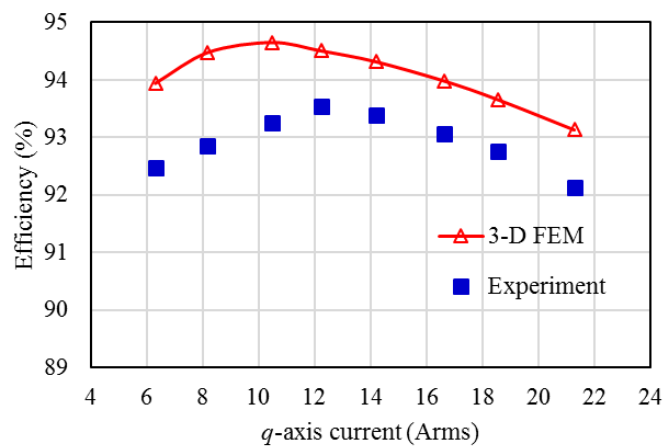
Figure 8.15 Comparison of measured and predicted efficiency of the IPM motor @1000rpm

8.1.2.5 Fault-tolerant capability test

8.1.2.5.1 Three-phase open-circuit (OC) fault test

The fault-tolerant capability test of the IPM motor under one 3-phase winding open-circuit (OC) fault is carried out under current control mode when the load motor is controlled at speed mode operating at 1000rpm. To avoid the overheat of the motor, the test is done in a short period of time. For simplicity, the I_d=0A control strategy is adopted.

Figure 8.16 depicts the comparison of the measured and predicted torque current characteristics when only A1B1C1 is loaded whilst A2B2C2 is open-circuit at

1000rpm. As can be seen, the measured results agree well with the 3-D FEM results, and the difference between them is about 4-9%.
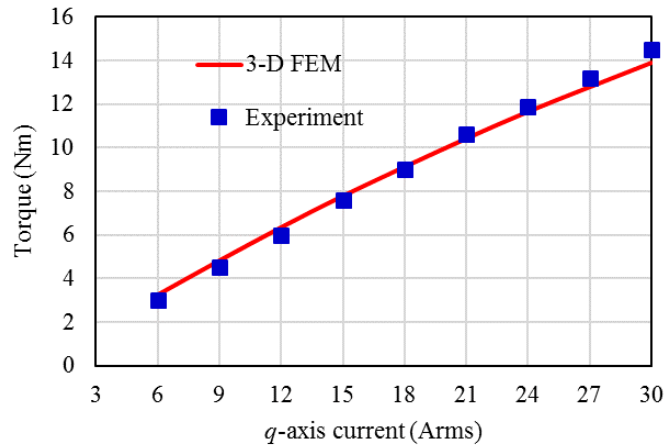
Figure 8.16 Comparison of measured and predicted torque current characteristics of the IPM motor under OC fault @1000rpm

8.1.2.5.2 Three-phase short-circuit (SC) fault test

The fault-tolerant capability test of the IPM motor under short-circuit (SC) fault is carried out when the motor is driven by the load motor operating at different speeds.

The comparison of measured and predicted steady-state SC characteristics when only A1B1C1 winding is short-circuited whilst A2B2C2 winding is open-circuit is plotted in Figure 8.17. As can be seen, the steady-state SC current increases when speed increases, approaching a constant value at high speed. The measured maximum steady-state SC current is about 21.7Arms which is smaller than 25.5Arms predicted from 3-D FEM; this may be attributing to the prototype's higher end-winding leakage inductance and the lower no-load EMF coming from the negative impact of material and manufacturing tolerance. The critical speed where the maximum steady-state SC braking torque (negative torque) occurs at is 80rpm, as in Figure 8.17 (b). The measured maximum steady-state SC braking torque is 8.5Nm (negative) which is smaller than 9.7Nm predicted from 3-D FEM.
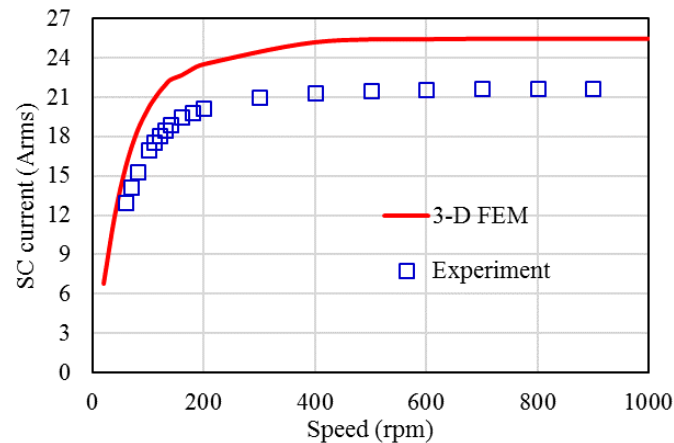
(a) Steady-state SC current
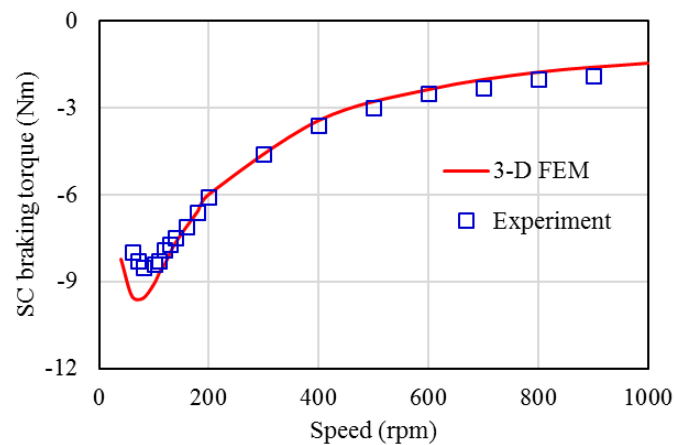
(b) Steady-state SC braking torque

Figure 8.17 Comparison of measured and predicted steady-state SC characteristics
when only one 3-phase A1B1C1 winding is short-circuited

To validate the output torque capability of the IPM motor under one 3-phase SC fault, the output torque of the IPM motor operating at the critical speed of 80rpm when the A1B1C1 winding is short-circuited and A2B2C2 winding is loaded with different currents (I_d=0A control strategy is used) is tested, and the comparison with 3-D FEM simulation results is depicted in Figure 8.18. A good agreement is observed between experimental test and 3-D FEM results. It is worth noting that, the steady-state SC braking torque (negative value) reaches maximum value at the critical speed of 80rpm, thus the result shows the minimum output torque when one 3-phase is short-circuited, and the other 3-phase is loaded with different currents. It shows that the IPM motor

can still maintain some output torque capability even under the most extreme conditions of low speed SC operation.

Finally, the steady-state SC characteristics of the IPM motor when the two 3-phase windings are short-circuited (Two 3-phase windings are connected in series as in Figure 8.7(b)) is carried out, and the result is shown in Figure 8.19. As can be seen, the steady-state SC current is the quite similar to the case when one 3-phase winding is short-circuited, while the steady-state SC braking torque is almost doubled. The measured steady-state SC braking torque is lower than that of 3-D FEM result. Again, the difference between them may be attributing to the prototype's higher end-winding leakage inductance and the lower no-load EMF coming from the negative impact of material and manufacturing tolerance.
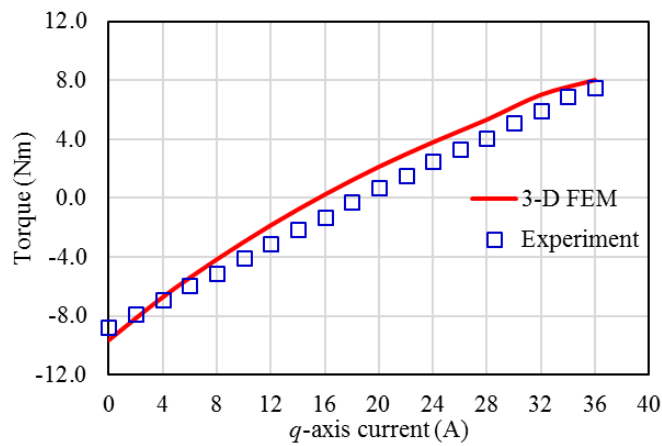
Figure 8.18 Comparison of measured and predicted output torque of the IPM motor when A1B1C1 short-circuit and A2B2C2 loaded with different current at 80rpm
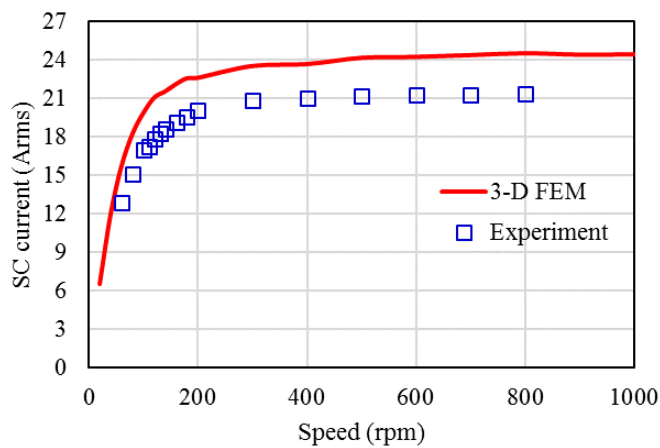
(a) Steady-state SC current
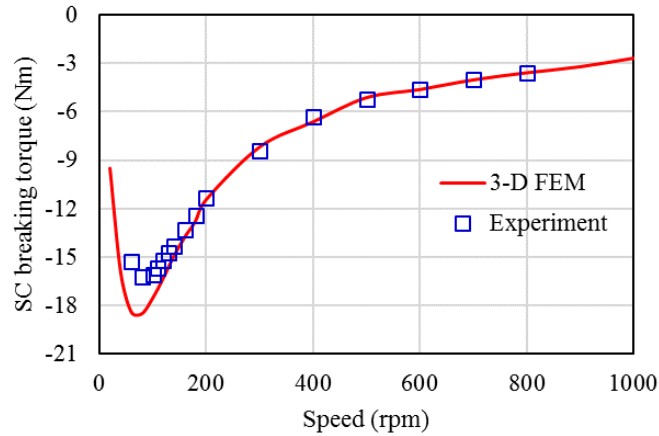
(b) Steady-state SC braking torque

Figure 8.19 Comparison of measured and predicted steady-state SC characteristics when two 3-phases are short-circuit (Two 3-phase windings are connected in series)

8.1.3 24 slots, 14 poles IPM motor summary

Although the full torque-speed characteristic of the IPM motor cannot be fully tested due to the limitations of test rig, the performance comparison at no-load and light load condition illustrates the similarities between the 3-D FEM predicted and the prototype's results. The performance under both 3-phase OC and SC fault conditions have been tested and compared to the predicted results, which demonstrates the excellent fault-tolerant capability of the IPM motor. All this demonstrates the applicability and prospect of the proposed 24S-14P IPM motor in the fault-tolerant traction motor applications.

8.2 24 slots, 22 poles EMA motor

To validate the design and analysis of the EMA motor presented in Chapter 6 and Chapter 7, two prototypes of the 24 slots, 22 poles EMA motor have been built. The manufacturing and testing of the EMA motor are detailed in this section.

8.2.1 Manufacturing and assembly

The stator core pack with a single-layer winding for the EMA motor is shown in Figure 8.20. Due to the narrow slot opening of 1.5mm, it is difficult to insert a coil into the slot and the end-winding projection is larger than expected. The resulting copper slot fill factor is 47%. It suggests that in the future a segmented modular tooth structure is preferable to facilitate the coil winding. This will reduce end-winding projection, increase the fill factor, improve the contact between wires and thereby improve the heat transfer between winding and stator core pack. In addition, a preformed wound coil can be pressed with certain pressure to further increase fill factor and improve heat transfer, as depicted in Section 3.2.5. With the dual 3-phase winding configuration, 2 terminals of each phase come out and therefore 12 terminals come out in total.

Figure 8.20 Laminated stator core with winding of the EMA motor

Table 8.3 Material of EMA prototype

Parameter	Designed	Prototype
Stator core material	Vacoflux-50	DW270-35
Rotor core material	DW270-35	DW270-35
Magnet material	N45SH	N45SH

It should be noted that due to a cost and lead time issue during the prototype construction, the cobalt-iron alloys: Vacoflux-50 was not available; instead, the DW270-35 was used for both stator and rotor core manufacturing, as summarized in

Table 8.3. This will inevitably decrease the motor torque capability which will be presented in the next section.

Figure 8.21 shows the rotor assembly of the EMA motor with and without rotor sleeve. Glass fiber is used for rotor sleeve to contain the surface-mounted magnets due to the low-speed characteristic. The rotor has a hollow shaft, as in Figure 8.21(b), to allow coupling the rotors of two motors when assembling two motors together. A removable shaft can be used for mounting an encoder if needed, as in Figure 8.21(a). Figure 8.22 depicts the EMA motor prototype assembly with encoder and flange.

(a) Rotor without sleeve   (b) Rotor without encoder-mounting shaft
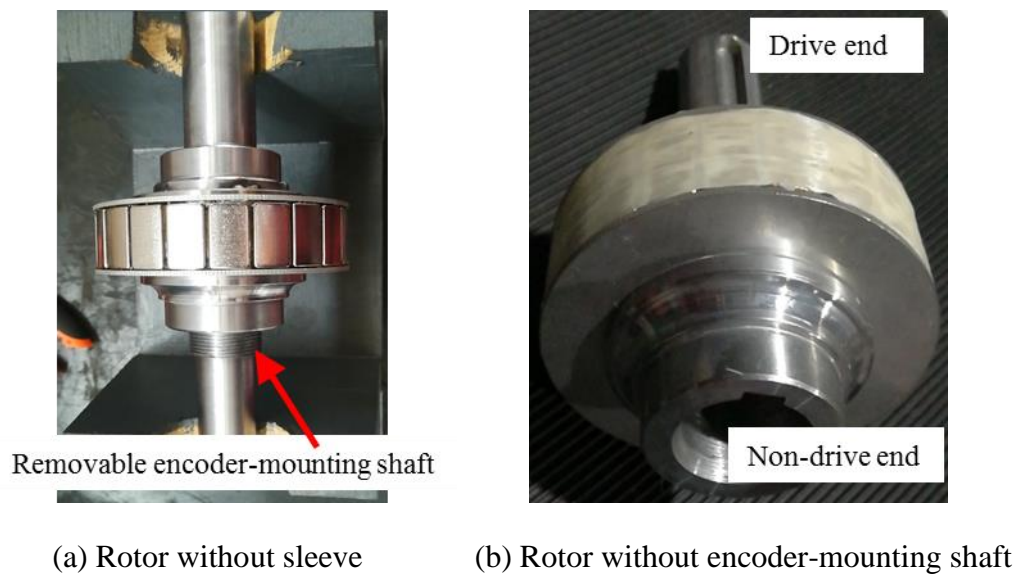
Figure 8.21 Rotor assembly of the EMA motor

Figure 8.22 EMA motor prototype assembly

8.2.2 Modularity check

Modularity in the prototype construction design was considered. The housing and endcap are designed to fit each other when assembling the unit motors together. The shaft extension part is designed to fit with the hollow part to facilitate the coupling of two shafts, as in Figure 8.21.

To make sure the torque generated in the assembled two motors are not cancelled out from each other, the relative position between coils and magnets in the two motor units when rotating is required to be the same. To achieve this, the coil position relative to stator lamination keyway and the relative position between N-pole magnet and rotor keyway are fixed, as depicted in Figure 8.23.

(a) Stator coil position   (b) Rotor magnet and keyway position
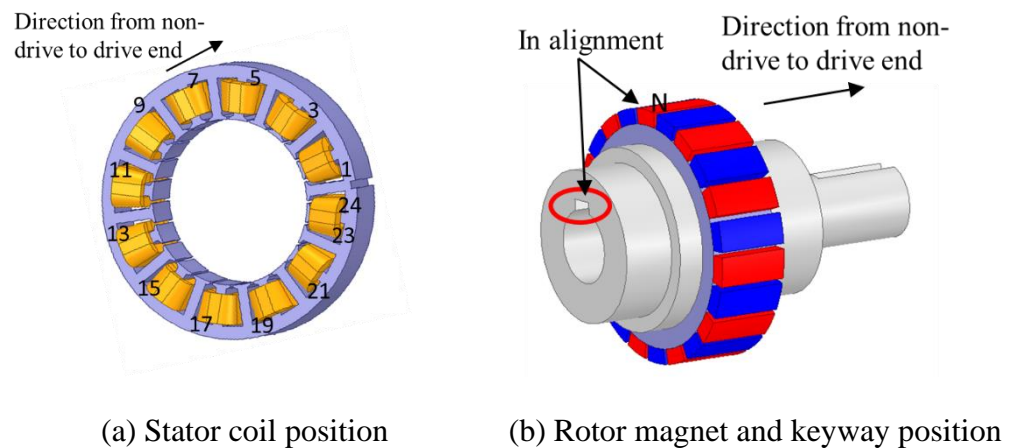
Figure 8.23 Description of coil and magnet position relative to stator and rotor keyway

Figure 8.24 Two interconnected EMA motors assembled together

With the modular mechanical design, two EMA motors can be assembled and one set of endcap and bearings between the two motors can be removed, as in Figure 8.24. This demonstrated the feasibility of the modular EMA motor design concept.

8.2.3 Experimental test: Single EMA motor

8.2.3.1 Test rig setup

The experimental testing rig is shown in Figure 8.25. A PMSM servo motor is adopted as the load motor. Torque is measured with an HBM torque transducer. The control is again realized by a back-to-back 3-phase voltage source inverters; one for the load motor, and the other for the EMA motor. The schematic of test rig is the same as the IPM motor test rig in Figure 8.3.
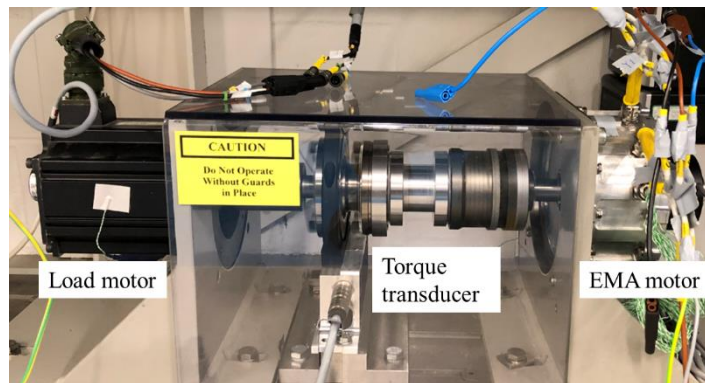
Figure 8.25 EMA motor testing setup

Table 8.4 Measured phase resistance of the EMA motor at 20°C

	Calc.	Measured					
		A1	B1	C1	A2	B2	C2
Value (ohm)	0.1376	0.1549	0.1571	0.1568	0.1535	0.1542	0.1562
Ratio	-	1.13	1.14	1.14	1.12	1.12	1.14

8.2.3.2 Resistance and inductance measurement

The resistance is measured at room temperature (20°C) using the DC current method depicted in Section 8.1.2.2. The measurement results are summarized in Table 8.4. The phase resistance is consistent, but the difference between the calculated and

measured value is significant. As pointed out before, due to the narrow slot opening, the end-winding is not well shaped while inserting into slot, and therefore lead to a much longer end-winding projection. This is the source of the significant discrepancy between the calculated and measured value.

Since the EMA motor has surface-mounted magnets, the inductance is almost a constant if not considering the magnetic saturation. The phase self-inductance is measured using AC current method as illustrated in Figure 8.26. A small AC current of 0.5Arms is fed into the winding and the self-inductance is then calculated through the measured voltage and current waveform, as summarized in Table 8.5. As can be seen that the measured phase self-inductance is 1.636mH which is about 13.2% higher than the predicted result of 1.445mH. This is reasonable, and the difference may be attributed to the prototype's higher end-winding leakage inductance.

Table 8.5 Measured phase inductance of the EMA motor at 20°C

	Experiment	3-D FEM
Phase-inductance (mH)	1.636	1.445
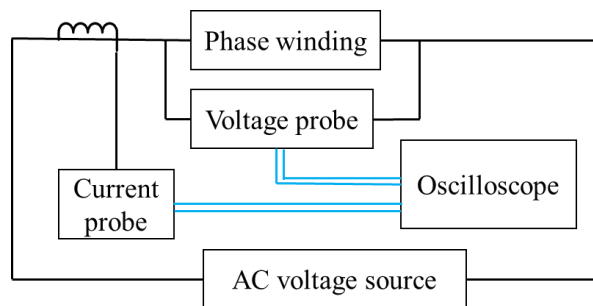
Figure 8.26 Schematic of self-inductance measurement

8.2.3.3 No-load test

The no-load back phase voltage of all phases was measured at room temperature (20^{0}C) when the EMA motor was driven by the load motor operating at 1320rpm. Figure 8.27 and Figure 8.28 depict the measured no-load phase voltage and its FFT spectrum for the dual 3-phase and single 3-phase configuration, respectively. Table 8.6 summarizes the amplitude and RMS value of the fundamental harmonic of the no-load phase voltage obtained from the experimental test, compared to predicted values.
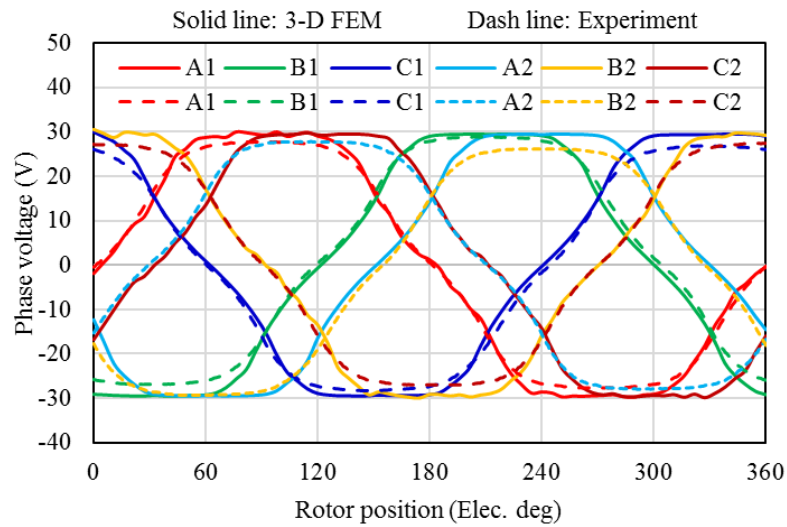
(a) Waveform
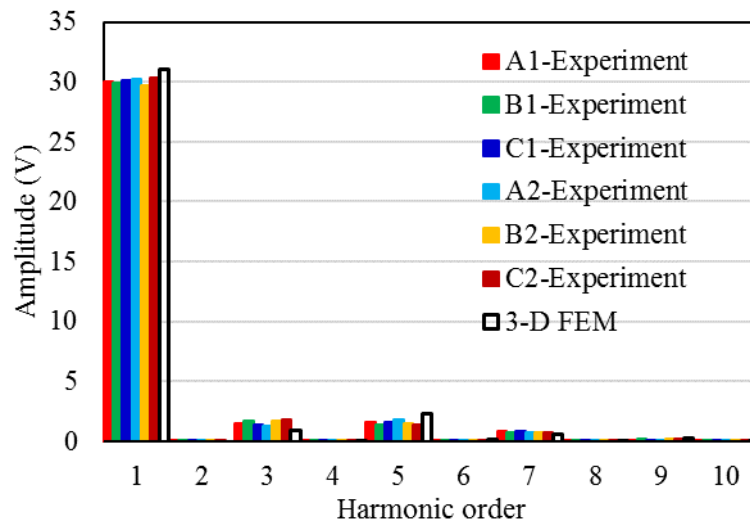
(b) FFT spectrum

Figure 8.27 Comparison of measured and predicted phase EMF of EMA motor @1320rpm for dual 3-phase configuration

As can be seen from Figure 8.27 and Table 8.6(a), the measured phase voltage is slightly lower than 3-D FEM calculated value by about 2.6%, which may be attributed to the impact of material tolerance, steel machining process, lamination stacking factor and assembly tolerance. Their harmonic distributions are similar. A 30^0 shift between the two 3-phase windings can be observed, as would be expected with the designed winding layout.
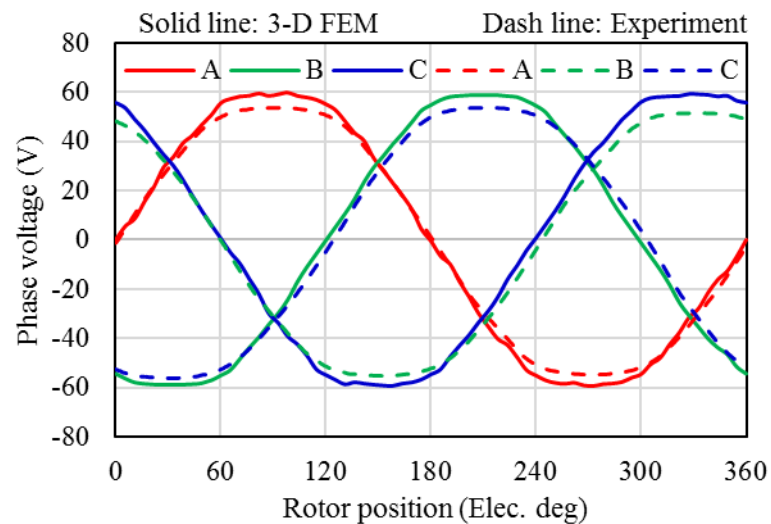
(a) Waveform
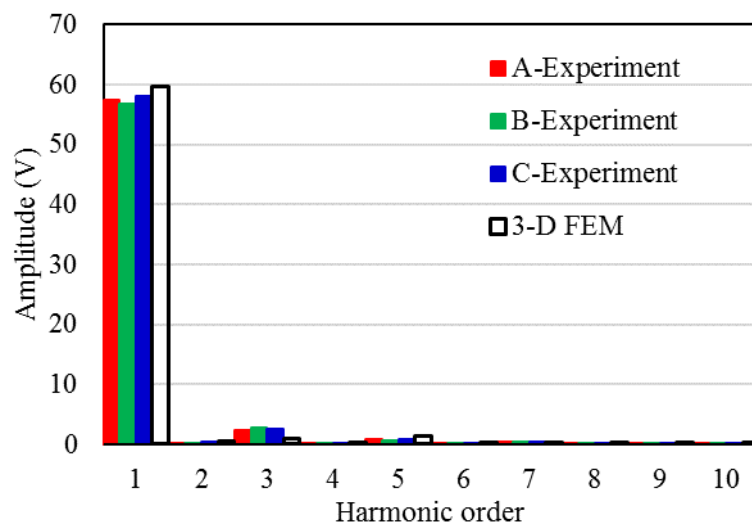
(b) FFT spectrum

Figure 8.28 Comparison of measured and predicted phase EMF of EMA motor
@1320rpm for single 3-phase configuration

Like the IPM motor, when the two 3-phase windings are configured as a single
3-phase winding through series connection as in Figure 8.7, the corresponding no-load
phase voltage is shown in Figure 8.28 and Table 8.6 (b). A 3.6% lower measured value
is observed.

Table 8.6 Measured and predicted EMF of EMA motor @1320rpm

(a) Dual 3-phase configuration

Fundamental voltage	Calc.	Measured					
		A1	B1	C1	A2	B2	C2
Amplitude (V)	30.9	30.0	29.9	30.1	30.3	29.7	30.4
RMS (Vrms)	21.8	21.2	21.1	21.3	21.4	21.0	21.5
Ratio (measured to calc.)	-	0.972	0.969	0.976	0.981	0.963	0.984

(b) Single 3-phase configuration

Fundamental voltage	Calc.	Measured		
		A	B	C
Amplitude (V)	59.6	57.4	56.9	58.2
RMS (Vrms)	42.2	40.6	40.2	41.1
Ratio (measured to calc.)	-	0.963	0.954	0.975

8.2.3.4 Load test

The load test is done to the EMA motor under current control mode when the load motor is controlled under speed mode. Due to the limitations of the drive, the control of dual 3-phase with 30^0 shift in time from each other cannot be implemented. Thus, like the IPM motor, the dual 3-phase windings are configurated as a single 3-phase winding driven by a 3-phase voltage source inverter, as in Figure 8.10. Since, the EMA motor has surface-mounted magnets, there is no reluctance torque and thus I_d=0A control strategy is adopted. To maintain thermal stability, the testing was carried out over a short period of time.

Figure 8.29 depicts the comparison of measured and predicted torque current characteristics when the EMA motor is operating at based speed of 660rpm. The measured torque is 7-8% lower than predicted with the same q-axis current excitation. This may be attributed to lower measured value of the no-load phase voltage. In addition, the difference may also be attributed to the factors such as material tolerance and magnet temperature. When loaded with 24A of q-axis current which is corresponding to 17Arms, the measured peak torque is 11.7Nm.
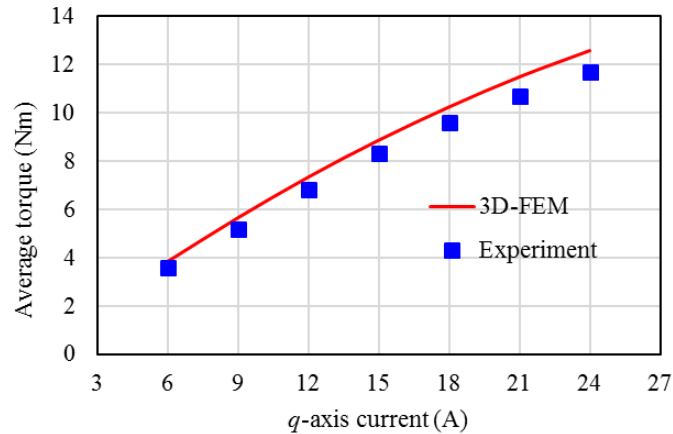
Figure 8.29 Comparison of measured and predicted torque of EMA motor @660rpm
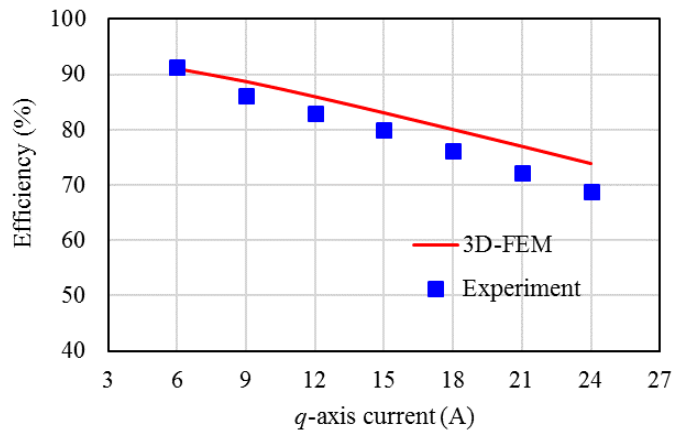
Figure 8.30 Comparison of measured and predicted efficiency of EMA motor @660rpm

The efficiency comparison of experiment and predicted result is plotted in Figure 8.30. The measured efficiency is lower than the 3-D FEM predicted result, with the difference to be 3-8%. The higher the q-axis current, the higher the difference between measured and predicted efficiency. This difference may be attributed to the drop in the measured no-load back EMF and the tolerance between the predicted and practical iron losses. Both the increasing magnet temperature and coil temperature during test are also the contributing factors. In addition, both the friction loss and windage loss are neglected in the predicted results, which may also contribute to the difference.

8.2.3.5 Fault-tolerant capability test

The EMA motor is designed with a dual 3-phase winding configuration. The fault-tolerant capability when one 3-phase winding is under fault conditions is detailed in this section.

8.2.3.5.1 Three-phase open-circuit (OC) fault test

The fault-tolerant capability test of the EMA motor under one 3-phase winding open-circuit (OC) fault is carried out under current control mode when the load motor is controlled as speed mode operating at base speed of 660rpm. Again, the I_d=0A control strategy is adopted. To maintain the thermal stability, the test was carried out over a short period of time.

Figure 8.31 depicts the comparison of the measured and predicted torque current characteristics when only one 3-phase winding (A1B1C1) is operating whilst the other one (A2B2C2) is open-circuit operating at 660rpm. The measured results are about 6% lower than that of 3-D FEM results. This may be attributed to the lower measured no-load phase voltage. In addition, the material and manufacturing tolerance may also contribute to the difference.

In addition, the torque when only A1B1C1 is loaded with 24A q-axis current (peak 17Arms) is 6.1 Nm, which is 52.1% of the torque when both A1B1C1 and A2B2C2 are loaded with the same 24A q-axis current. This confirms that the EMA motor can keep 50% output torque capability when one 3-phase winding is open-circuit, as specified in Table 7.8.
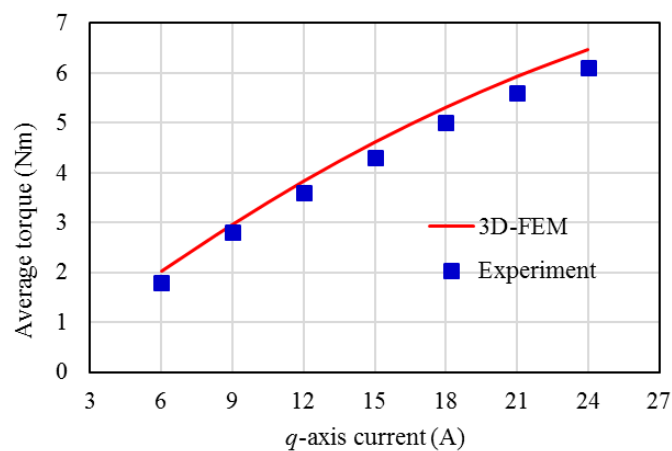
Figure 8.31 Comparison of measured and predicted torque current characteristics under OC fault @660rpm

8.2.3.5.2 Three-phase short-circuit (SC) fault test

The fault-tolerant capability test of the EMA motor under SC fault is carried out when the motor is driven by the load motor.
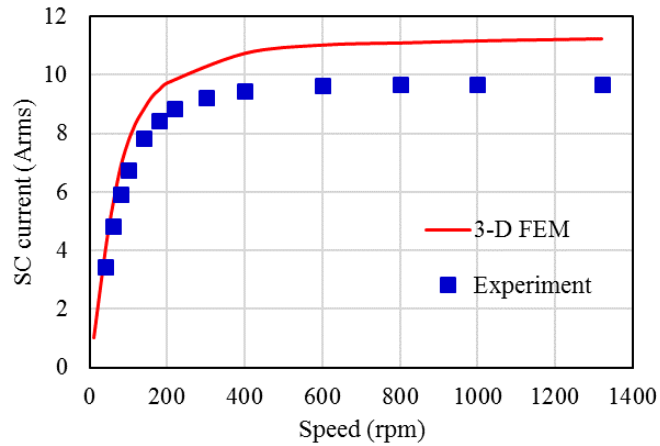
(a) Steady-state SC current
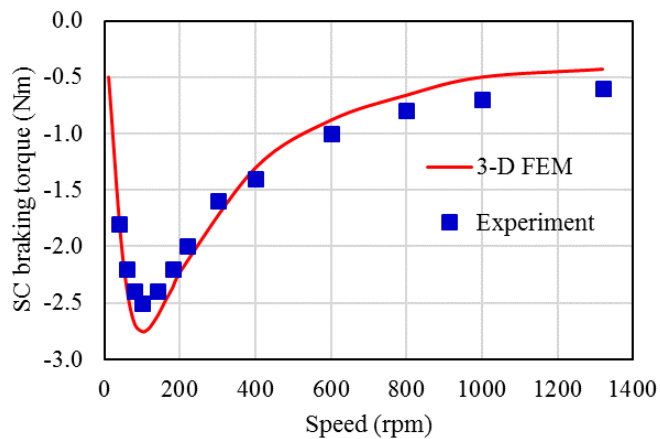
(b) Steady-state SC braking torque

Figure 8.32 Comparison of measured and predicted steady-state SC characteristics when one 3-phase A1B1C1 winding is short-circuited

The comparison of measured and predicted steady-state SC characteristics when A1B1C1 winding is open-circuit while A2B2C2 is short-circuited is plotted in Figure 8.32. It can be seen that the steady-state SC current increases when speed increases, approaching a constant value at high speed. The measured maximum steady-state SC current is about 9.7Arms which is smaller than 11.2Arms predicted from 3-D FEM which may be attributed to the prototype's higher end-winding leakage inductance and

the lower no-load phase voltage coming from material and manufacturing tolerance. The critical speed where the maximum steady-state SC braking torque (negative torque) occurs at is 100rpm, as in Figure 8.32(b). The measured maximum steady-state SC braking torque is 2.5Nm which is smaller than 2.8Nm predicted from 3-D FEM.

In addition, the measured SC braking torque of 2.5Nm is about 21.4% of the measured peak torque of 11.7Nm. This confirms that the EMA motor can maintain a SC braking torque less than 25% of peak torque when only one 3-phase winding is short-circuited, as specified in Table 7.8.

To validate the output torque capability of the EMA motor under one 3-phase SC fault, the output torque of the EMA motor operating at the critical speed of 100rpm when the A1B1C1 winding is short-circuited and A2B2C2 is loaded with different current (I_d=0A control strategy is used) is tested, and the comparison with 3-D FEM simulation results is plotted in Figure 8.33. A good agreement is observed between experimental test and 3-D FEM results. It is worth noting that, the steady-state SC braking torque (negative value) reaches maximum value at the critical speed of 100rpm, thus the result shows the minimum output torque when one 3-phase is short-circuited and the other one is loaded.
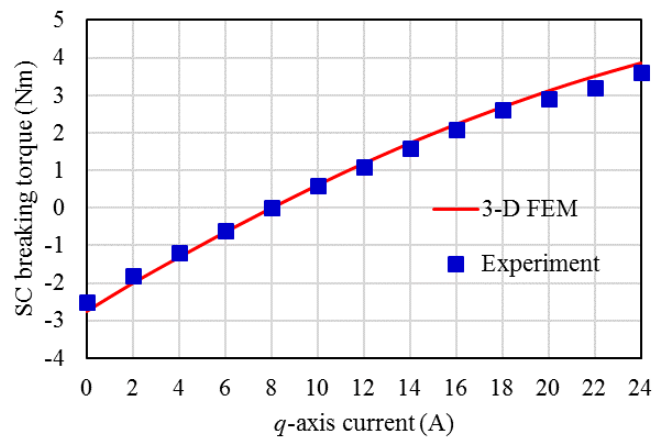
Figure 8.33 Comparison of measured and predicted output torque of the EMA motor when A1B1C1 short-circuit and A2B2C2 loaded with different current at 100rpm

In addition, the EMA motor can generate a maximum torque of 3.6Nm (peak current of I_q=24A) under one 3-phase SC fault at the critical speed of 100rpm, which

is about 30.8% of the peak torque of 11.7Nm when the motor is in normal operation. This confirms that the EMA motor can keep 25% output torque capability when one 3-phase winding is short-circuited, as specified in Table 7.8.
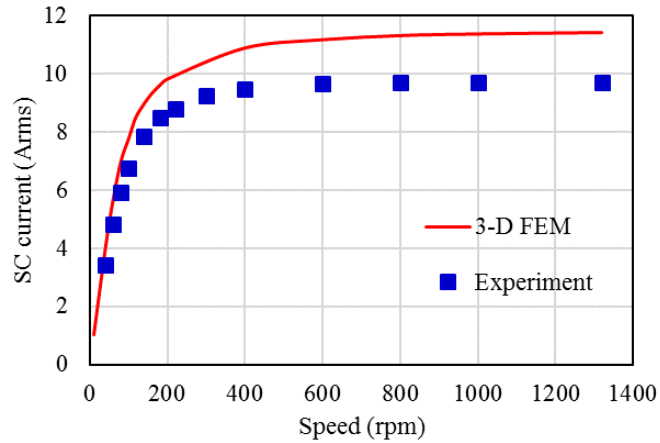
(a) Steady-state SC current
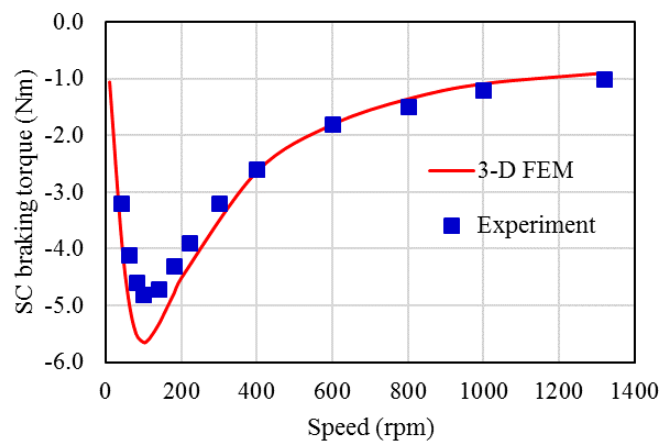
(b) Steady-state SC braking torque

Figure 8.34 Comparison of measured and predicted steady-state SC characteristics of the EMA motor when the two 3-phase windings are short-circuit, respectively

Finally, the steady-state SC characteristics of the EMA motor when the two 3-phase windings are both short-circuited was carried out, and the result is shown in Figure 8.34. As can be seen, the steady-state SC current is the same as the case when one 3-phase winding is short-circuited, whilst the steady-state SC braking torque is doubled. The measured steady-state SC braking torque is lower than that of 3-D FEM. Again, the difference between them may be attributing to the prototype's higher end-

winding leakage inductance and the lower no-load EMF coming from the impact of material and manufacturing tolerance.

In addition, the maximum SC braking torque is 4.8Nm, which is about 41% of the peak torque of 11.7Nm. This confirms that EMA motor can meet the requirement that the maximum SC braking torque when the two 3-phase windings are both short-circuit should be less than 50% of the peak torque, as specified in Table 7.8.

8.2.3.6 Thermal duty cycle test

The thermal transient test of duty cycle operation of Figure 6.17, was carried out with 660rpm, 17Arms of q-axis current at 25 $^{\circ}$C. Four K-type thermocouples are placed on the winding to measure temperature, with their position summarized in Table 8.7. The rotor temperature is not measured due to the test rig limitations.

To maintain consistency, the winding resistance in the thermal model is updated with measured value in Table 8.4. Table 8.8 summarizes the input loss data for the duty cycle thermal evaluation, where the iron loss and magnet loss are predicted using 3-D FEM analysis.

Figure 8.35 shows the comparison of measured and predicted winding temperature values. The measured temperature tends to be higher than the predicted winding average temperature. The peak temperature difference in each cycle of 180 seconds is getting smaller. The measured temperature in TC2, TC3, and TC4 reaches to peak 111.6°C at 480 seconds, which is 4.3°C higher than the predicted winding hotspot temperature at that point. Compared to the predicted winding average temperature, the measured peak temperature in the winding during the duty cycle operation is about 13.2 $^{\circ}$C higher. The higher measured temperature may be attributing to many factors. For instance, the material parameters discrepancy and the manufacturing tolerance may result in underestimated losses and different thermal conduction from practical condition. In addition, good contact between wires in each coil is assumed in the simulation, while in the prototype it may not be the case.

The simulation results in Section 7.7.1 shows that the maximum winding average temperature is 144.4°C. Considering the difference of 13.2 $^{\circ}$C between simulation and experiment results, a winding with insulation class of 200°C still have

enough margin in terms of thermal perspective. This demonstrates that the EMA motor can meet the duty cycle operation requirement.

Table 8.7 Position of thermocouples

Item	Location
TC1	End winding, phase A1
TC2	In-slot winding, phase A2
TC3	In-slot winding, phase C1
TC4	End winding, phase B2

Table 8.8 Input data for thermal evaluation

Copper loss @25°C (W)	Stator iron loss (W)	Rotor iron loss (W)	Magnet loss (W)	Total loss (W)
273.4	8.5	0.4	0.9	283.2
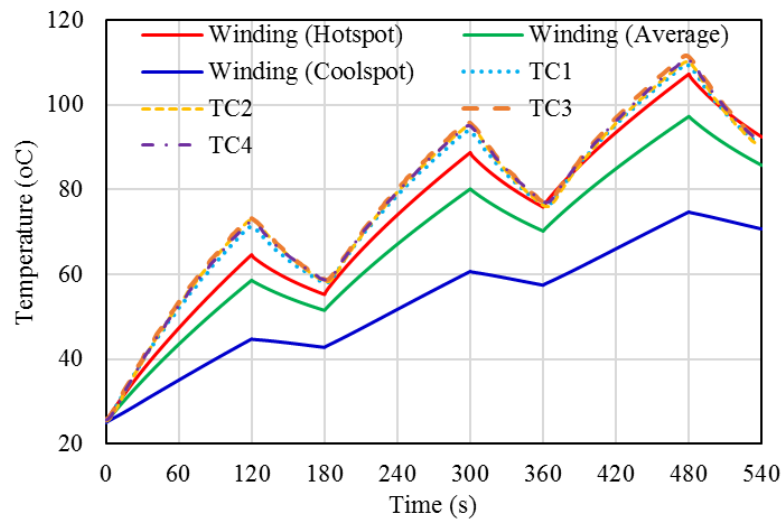
Figure 8.35 Comparison of measured and predicted temperature behaviour @660rpm

8.2.4 Experimental test: Two EMA motors assembled

As mentioned before, the EMA motor features a modular structure. For higher power/torque requirement, a few of unit EMA motors can be assembled. In this thesis, two EMA motors are built and assembled to demonstrate the modular feature of the

EMA motor. Therefore, this section deals with the functional validation of the assembled two EMA motors by testing only no-load and load performance.

8.2.4.1 Test rig setup

The experimental testing rig is shown in Figure 8.36. A PMSM servo motor is adopted as the load motor. Torque is measured with an HBM torque transducer. The control is again realized by a back-to-back 3-phase voltage source inverters; one for the load motor, and the other for the EMA motor.
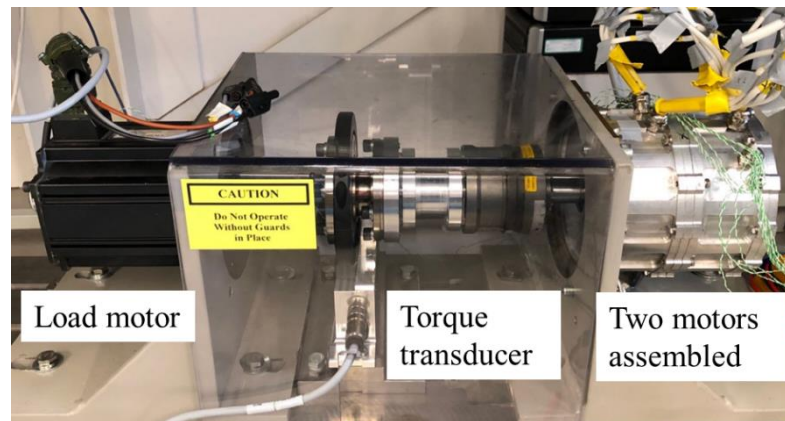
Figure 8.36 Test rig setup for the assembled two EMA motors
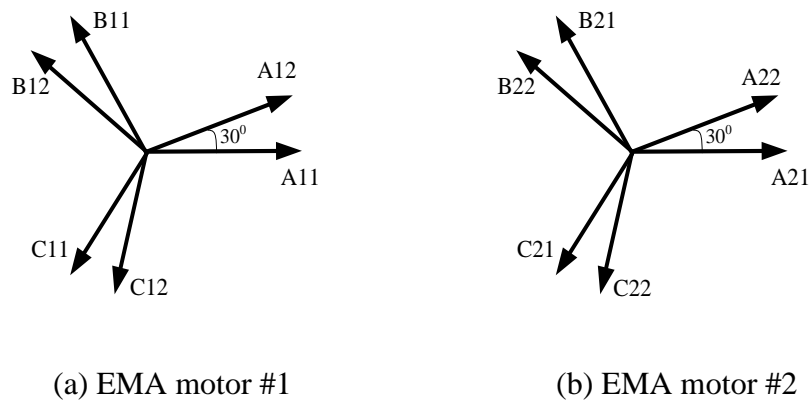
(a) EMA motor #1   (b) EMA motor #2

Figure 8.37 Coil phasor diagram for the two EMA motors

8.2.4.2 Winding configurations

There are two EMA motors and their winding coil phasor diagram are depicted in Figure 8.37. To form a dual 3-phase winding configuration, there are two kinds of

connection method, as detailed in Figure 8.38, resulting different shift angle in time between A1B1C1 and A2B2C2. In this thesis, the dual 3-phase winding configuration with 30^0 shift in time was identified as the solution for EMA application. Therefore, the winding configuration in the Figure 8.38 (b) is selected.
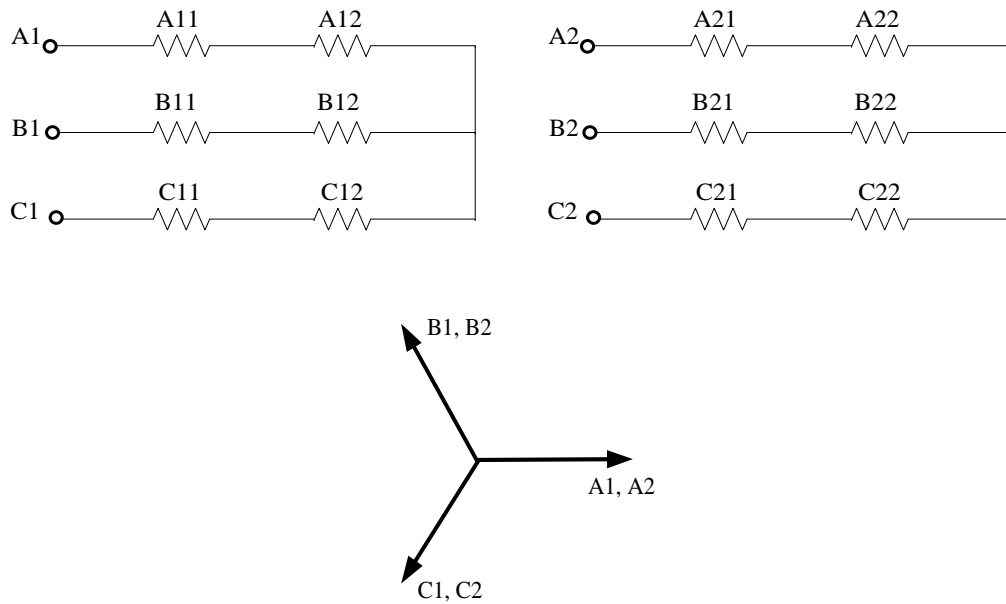
(a) 0^0 shift between A1B1C1 and A2B2C2
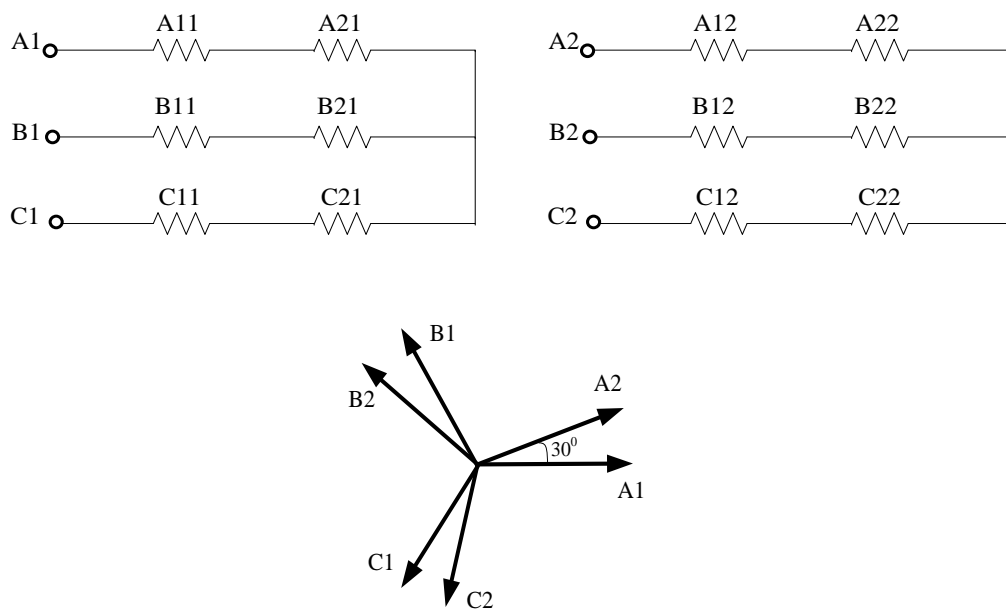
(b) 30^0 shift between A1B1C1 and A2B2C2 (selected)

Figure 8.38 Winding configuration for the assembled two EMA motors

8.2.4.3 No-load test

The no-load voltage was measured at room temperature (20°C) when the motor is driven by the load motor. Figure 8.39 shows the no-load phase voltage when the two EMA motor assembly is configured as a dual 3-phase winding as in Figure 8.38 (b) operating at 1320rpm and its FFT spectrum. Table 8.9 summarizes the amplitude and RMS value of fundamental harmonic of the no-load phase voltage obtained from the experiment test with those predicted by 3-D FEM calculation.

As can be seen, the no-load phase voltage of the two EMA motor assembly is doubled compared to the single EMA motor. The measured phase voltage is 3% lower than that of 3-D FEM results. This may be attributed to many factors, including the magnet dimension tolerance and the difference in B-H characteristic curves for both magnet and steel. On the other hand, the tolerance when assembling these two EMA motors together may also contribute to the difference.

Table 8.9 Comparison of measured and predicted phase voltage of the two EMA
motors assembled @1320rpm

Fundamental voltage	Calc.	Measured					
		A1	B1	C1	A2	B2	C2
Amplitude (V)	61.7	60.0	59.7	59.7	60.2	59.8	59.8
RMS (Vrms)	43.6	42.5	42.2	42.2	42.5	42.3	42.3
Ratio (measured to calc.)	--	0.973	0.968	0.968	0.975	0.969	0.969
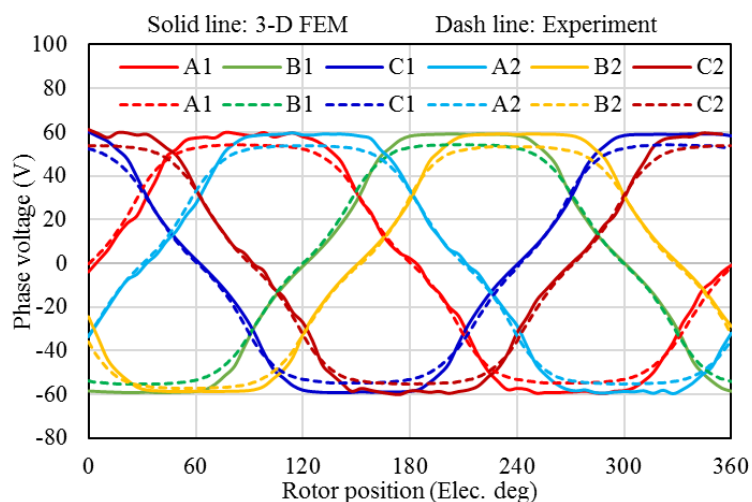
(a) Waveform
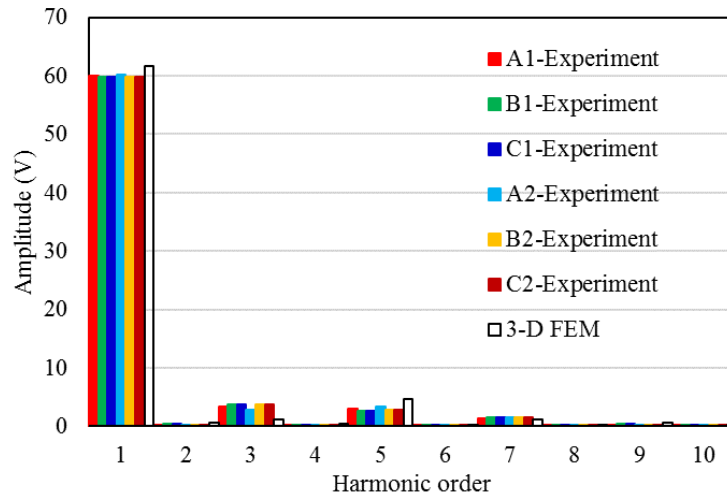
(b) FFT spectrum

Figure 8.39 Comparison of measured and predicted phase voltage of the two EMA motors assembled @1320rpm

8.2.4.4 Load test

The load test is done to the EMA motor under current control mode when the load motor is controlled as speed mode. Again, due to the limitations of control drive, the control of dual 3-phase with 30^0 shift in time from each other cannot be implemented. Thus, the dual 3-phase windings are configured as a single 3-phase winding driven by a 3-phase voltage source inverter, as in Figure 8.40. The I_d=0A control strategy is adopted. To maintain thermal stability, the testing was carried out over a short period of time.
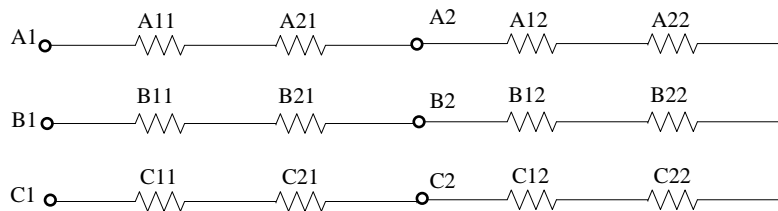
Figure 8.40 Single 3-phase winding configuration driven by a 3-phase VSI for the two interconnected EMA motors assembled
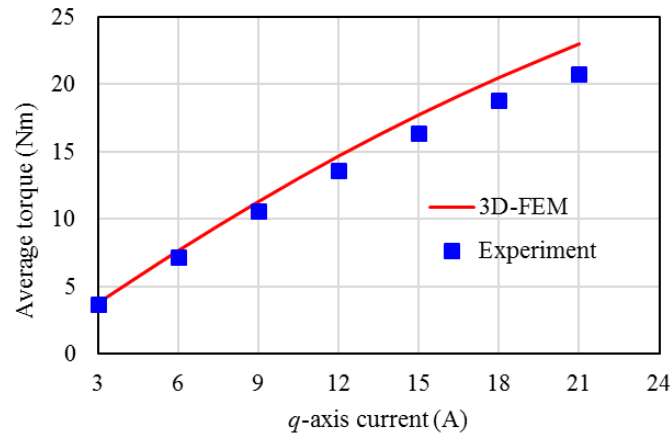
Figure 8.41 Comparison of measured and predicted torque of the two interconnected EMA motors assembled

Figure 8.41 plots the comparison of measured and predicted torque current characteristics when the two EMA motor assembly is operating at a base speed of 660rpm. The measured torque is about 7-11% lower than predicted with the same q-axis current excitation. This may be attributed to lower measured value of the no-load phase voltage. In addition, the difference may also be attributed to the factors such as material tolerance and magnet temperature. On the other hand, the tolerance when assembling these two EMA motors together may also contribute to the difference.

The general agreement between the measured and predicted results for the two EMA motor assembly demonstrates the feasibility and functionality of the modular structure of EMA motor.

8.2.5 24 slots, 22 poles EMA motor summary

The experimentally measured and predicted results of the EMA motor are summarized in Table 8.10. General agreement between the model predicted and the prototype's results can be observed considering the material and manufacturing tolerance. The modularity of the EMA motor is also validated through two EMA motor assembly. The winding hotspot temperature operating under extreme duty cycle condition is proved to be whithin the limit of the insultaion class. All this confirms the applicability and satisfactory implementation of the modular EMA motor for aircraft actuation system applications.

Table 8.10 Comparison of measured and predicted results of the EMA motor

	3-D FEM	Experiment
Peak current (Arms)	17	17
Peak Torque @ healthy (Nm)	13	11.8
Peak Torque @OC fault (Nm)	6.6	6.2
Max SC current (Arms)	11.4	9.7
Critical speed (rpm)	100	100
Max braking torque when one 3-phase SC fault (Nm)	-2.75	-2.50
Max braking torque when two 3-phase SC fault (Nm)	-5.65	-4.80
Min output torque when one 3-phase SC fault @critical speed (Nm)	3.86	3.60

Chapter 9

Conclusions

The research work and main contributions of this thesis are concluded in this chapter. The limitations and the potential future scope of work are also included.

9.1 Conclusions

A comprehensive literature review on state-of-the-art technologies has been presented for two topics, including traction motor for electric vehicles (EV) and electromechanical actuator (EMA) applications for aircraft actuation systems. It is inferred that the PM synchronous motor with FSCW configuration is a potential candidate for electric traction applications due to its high torque/power density, excellent fault-tolerance, high reliability and easy manufacturing. However, the issue of significant stator MMF harmonics in FSCW motor may cause some undesired effects, including high rotor losses at high speed, localized saturation, and unbalanced radial force. For electromechanical actuator (EMA) applications, the use of PM synchronous motors with FSCW configuration are dominant. The issue of significant stator MMF harmonics in FSCW motor is not that crucial, while the torque density and fault-tolerance are the critical concerns for a direct-drive electric motor for EMA applications.

After systematically analysing the principle of stator MMF harmonics in the FSCW motor using the winding function method and comparing different stator MMF

harmonic reduction techniques, a novel 24 slots, 14 poles FSCW topology with reduced stator space MMF harmonics was proposed using winding shifting concepts. Unlike the early winding shifting method which normally requires a two-slot pitch winding, non-overlapping or concentrated winding characteristics can be kept in the proposed winding. It has been shown that the novel winding configurations can cancel out all harmonics except for working harmonic and its slot harmonics. The main drawback is the lower winding factor compared to its counterpart. This, however, can be compensated by the reduced magnetic saturation level, improved overload capability and improved reluctance torque capability for IPM motors attributing to the reduced stator MMF harmonics. This method can also be extended to different slot/pole combinations with different phase numbers to facilitate different application requirements.

The novel 24 slots, 14 poles FSCW topology has been applied to an IPM motor designed for an electric traction applications. The performance including torque capability, rotor saliency, flux-weakening capability, efficiency and fault-tolerant capability have been evaluated. High efficiency can be observed in most of the operation area and it can maintain an efficiency higher than 94% in the high speed zone. The torque ripple is very low which means no extra measures like rotor skewing that may induce additional cost and negatively impact on average torque are required. The proposed 24 slots, 14 poles IPM motor with a dual 3-phase with 30^0 shift winding was proved to exhibit the best torque performance under healthy conditions while maintaining a higher output torque with higher torque ripple under fault conditions, and no significant UMP under both healthy and fault conditions. A terminal short-circuit (SC) current lower than rated current was observed which indicates that the motor can maintain continuous terminal SC fault without overheating the motor.

The 24 slots, 14 poles IPM motor prototype was built. The full torque-speed characteristic of the prototype cannot be fully tested due to the limitation of test rig. However, the performance comparison at no-load and light load conditions gives a clear convergence between the 3-D FEM predictions and the testing results. The performance under both OC and SC fault conditions have been tested and compared to the predicted results, which demonstrate the excellent fault-tolerant capability of the IPM motor. All this demonstrates the applicability and prospect of the proposed 24 slots, 14 poles IPM motor in the fault-tolerant traction motor applications.

The second topic focuses on developing a modular EMA capable of meeting a diverse range of requirements for aircraft actuation systems. The concerns of the electromechanical actuator (EMA) including actuation system architecture and actuator configurations have been evaluated, in terms of weight, reliability, size, efficiency and cost. The EMA scheme of a fault-tolerant rotary motor plus a mechanical roller screw has been identified as a promising EMA solution. The reliability analysis of the actuation system architecture and actuator configurations have confirmed the best configuration of two anti-jamming EMAs in parallel connection, with each EMA equipped with a dual three-phase drive. This configuration meets the requirements of safety-critical actuation applications.

A modular fault-tolerant 24 slots, 22 poles SPM motor with a high level of physical, electrical, magnetic, and thermal isolation was developed for the EMA application. The modular mechanical structure, detailed electromagnetic design, and thermal management are fully discussed. Performance improvement is achieved through using parallel magnetization methods, high performance steel, and a dual 3-phase winding with 30^0 shift. Analysis of motor fault conditions and the calculation of armature inductance have given a guideline for selecting appropriate slot dimensions to achieve the desired short-circuit (SC) current and braking torque under short-circuit (SC) fault conditions. An interesting finding was that by having an armature inductance higher than one per-unit, the motor output torque capability under SC fault can be considerably improved without sacrificing considerable torque capability in the healthy condition. In addition, the thermal evaluation under the designed extreme duty cycle operation shows that the EMA motor can safely operate and the hotspot is in the winding. Sensitivity studies on the losses suggests that it has enough thermal margin even in the winding hotspot position.

The experimental results of the 24 slot, 22 pole motor prototypes agree well with the model predicted results. The steady-state SC current and braking torque is slightly lower than predicted, and the output torque under one 3-phase OC or one 3-phase SC fault is quite close to the predicted results, which demonstrate its fault-tolerant capability. The slight mismatch is likely due to the material and manufacturing tolerances. The winding hotspot temperature operating under extreme duty cycle conditions is proved to be within the limit of the insulation class. In addition, the modularity of the EMA motor is also validated through two interconnected motors

assembled, and the measured performance under this configuration agrees well with the predicted results. All this confirms the applicability and satisfactory implementation of the modular EMA motor for aircraft actuation system applications.

9.2 Future scope of work

There are some limitations of the research work presented in this thesis, which indicates various potential further research works, as outlined below:

- Applying the proposed winding designs with reduced stator MMF harmonics to synchronous reluctance motor (SynRM) which has multi-layer flux barriers rotor to achieve high saliency ratio.

- Application of the proposed FSCW topologies in multi-phase motors.

- Investigation of the demagnetization withstand capability of PM synchronous motor with proposed FSCW topologies under various operating conditions including post-fault operations.

- In the designing of fault tolerant motors in this thesis, only open-circuit (OC) and terminal short-circuit (SC) faults are considered. Investigation on some other fault scenarios such as SC fault in a single turn, or in a few turns, and the corresponding remedial actions can be explored in the future.

- Due to the limited cooling options for EMA motor, end-winding potting techniques could be adopted as a potential way to improve the heat dissipation from winding to housing and hence improve the electric loading and torque density. Further investigations on this could be undertaken.

- Due to the limitations of time and cost, a complete EMA prototype including rotary to linear translator is not built in this thesis. In the future, it is expected that the EMA motor can be integrated with a mechanical screw part so that the full functional test of an EMA can be implemented and evaluated.

Appendix A

Winding distribution of multi-phase FSCW motor with reduced stator MMF harmonics

A.1.   Four-phase, 16 slots, 10 poles (16S-10P) winding configurations

The four-phase, 16 slots, 10 poles (16S-10P) winding motor can be obtained by doubling the slot numbers of an 8 slots, 10 poles (8S-10P) winding motor.

In fact, there is an angular difference between coil phasors of each phase in a four-phase, 16S-10P motor. Therefore, similar to 3-phase FSCW motors, if a multiple four-phase winding with an appropriate shift angle is used, all the harmonics except for working harmonic and its slot harmonic can be eliminated [117]. More details will not be further discussed in this thesis.
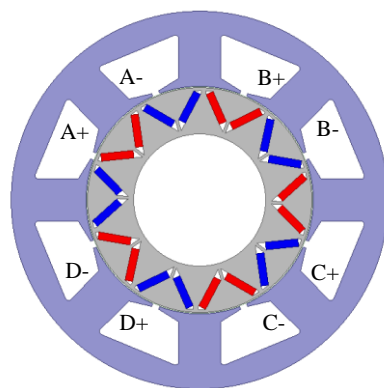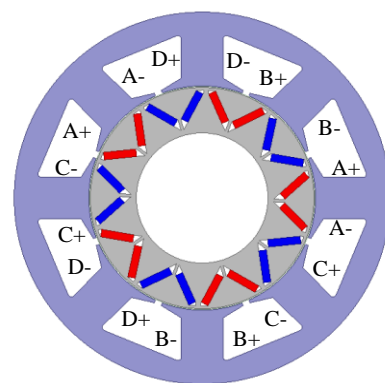
(a) 8S-10P-SL   (b) 8S-10P-DL

Conventional four-phase 8 slots, 10 poles (8S-10P) FSCW topology
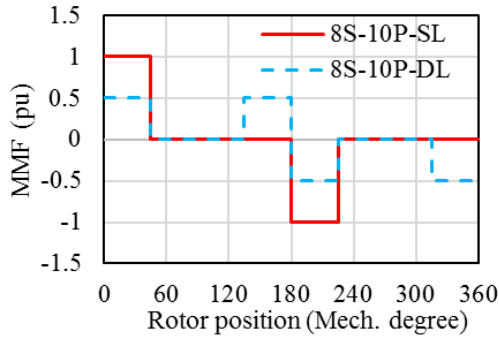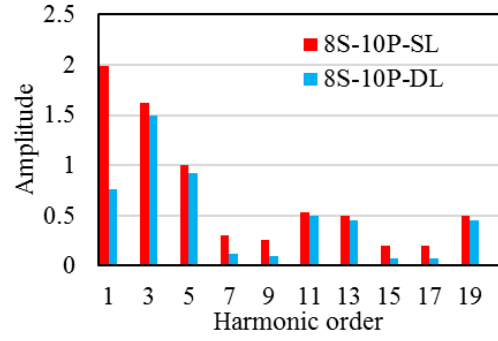
(a) MMF waveform

(b) FFT spectrum

MMF waveform and FFT spectrum comparison of conventional 8S-10P with SL and DL winding topology
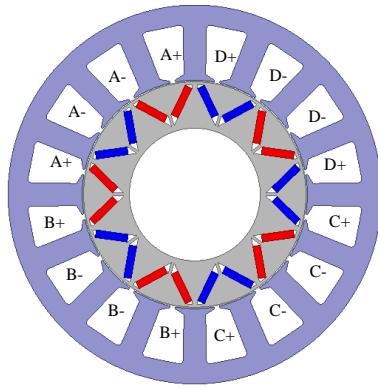
(a) 16S-10P-SL
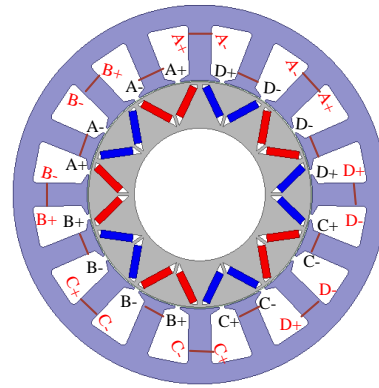
(b) 16S-10P-DL

Proposed four-phase 16S-10P FSCW topology
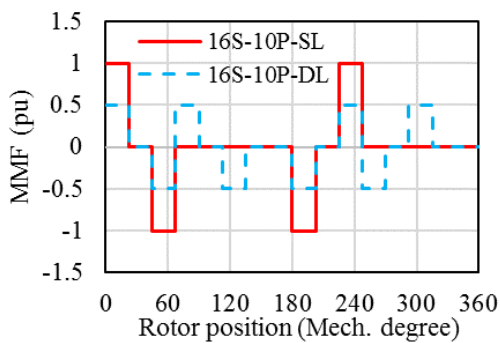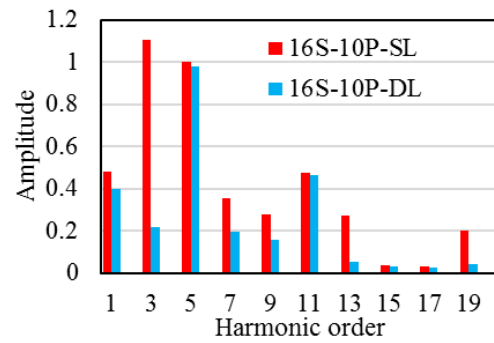
(a) MMF waveform

(b) FFT spectrum

MMF waveform and FFT spectrum comparison of proposed four-phase 16S-10P with SL and DL winding topology

A.2. Five-phase, 20 slots, 12 poles (20S-12P) winding configurations

The five-phase, 20 slots, 12 poles (20S-12P) winding motor can be obtained by doubling slot numbers of a 10 slots, 12 poles (10S-12P) winding motor.

Again, the concept of multiple *m*-phase winding configurations [117] can be used to cancel out the sub-harmonics. More details will not be further discussed in this thesis.
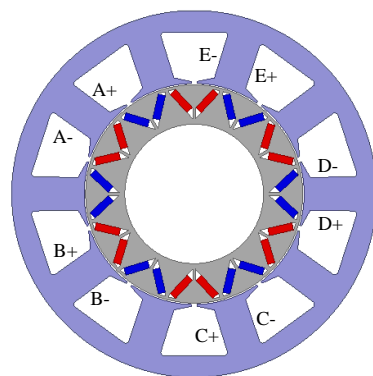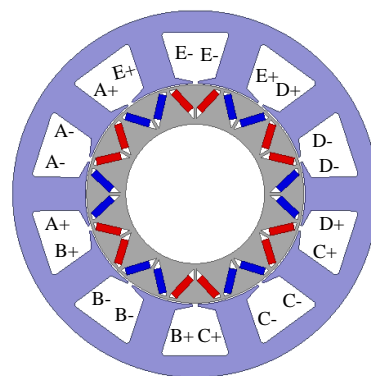
(a) 10S-12P-SL   (b) 10S-12P-DL

Conventional five-phase 10S-12P FSCW topology
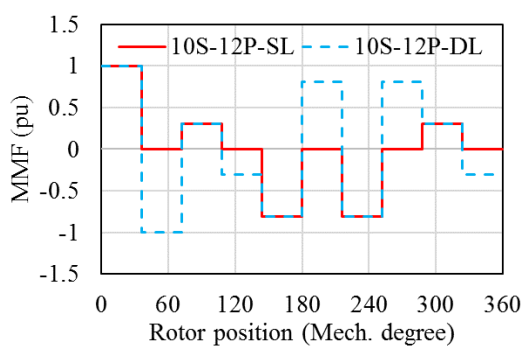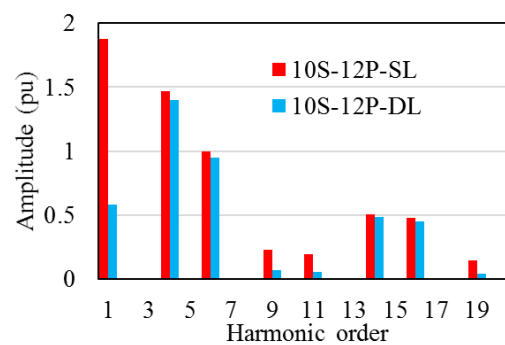
(a) MMF waveform   (b) FFT spectrum

Comparison of MMF waveform and FFT spectrum of conventional five-phase 10S-12P with SL and DL winding topology
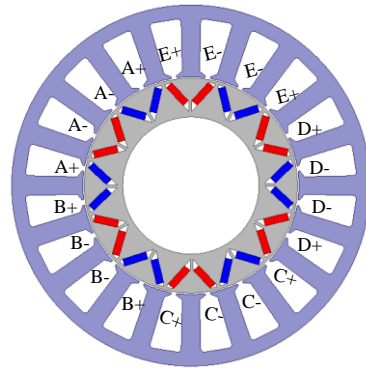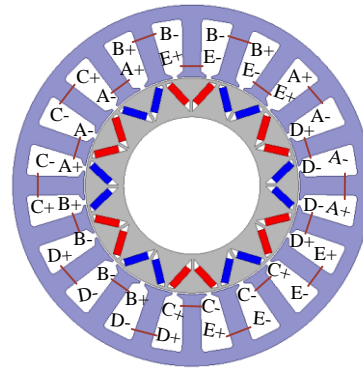
(a) 20S-12P-SL   (b) 20S-12P-DL

Proposed five-phase 20S-12P FSCW topology
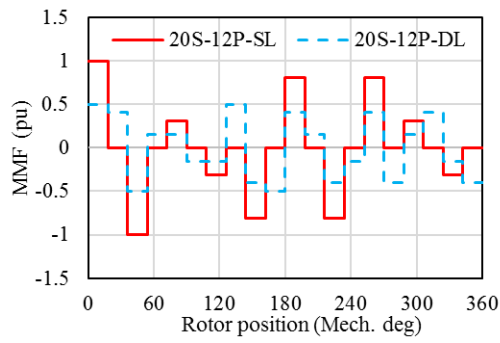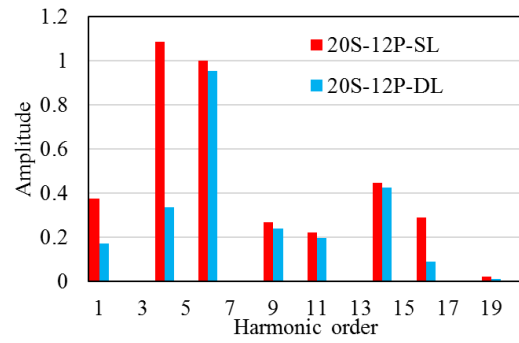
(a) MMF waveform   (b) FFT spectrum

MMF waveform and FFT spectrum comparison of proposed five-phase 20S-12P
with SL and DL winding topology

Appendix B

Comparison of inductance and torque of the 24 slots, 14 poles IPM motor

(a) I_d=0A

I_d (A)	I_q (A)	Measured			3-D FEM		
		L_d (mH)	L_q (mH)	Torque (Nm)	L_d (mH)	L_q (mH)	Torque (Nm)
0	3	-	5.82	3.0	-	3.66	3.2
0	6	-	4.74	6.0	-	3.63	6.2
0	9	-	4.39	8.8	-	3.58	9.3
0	12	-	4.07	11.6	-	3.51	12.2
0	15	-	3.79	14.2	-	3.40	15.0
0	18	-	3.60	16.6	-	3.30	17.6
0	21	-	3.44	18.8	-	3.20	20.1
0	24	-	3.21	21.0	-	3.08	22.4

(b) I_d=-3A

I_d (A)	I_q (A)	Measured			3-D FEM		
		L_d (mH)	L_q (mH)	Torque (Nm)	L_d (mH)	L_q (mH)	Torque (Nm)
-3	3	2.33	6.09	3.6	1.98	4.10	3.6
-3	6	2.55	4.98	6.6	1.93	3.91	6.9
-3	9	2.94	4.60	9.6	1.98	3.77	10.1
-3	12	3.64	4.27	12.4	2.12	3.67	13.2
-3	15	4.49	3.93	15.2	2.34	3.58	16.1
-3	18	5.32	3.69	17.6	2.66	3.44	18.9
-3	21	6.01	3.52	20	3.04	3.32	21.5

(c) I_d=-6A

I_d (A)	I_q (A)	Measured			3-D FEM		
		L_d (mH)	L_q (mH)	Torque (Nm)	L_d (mH)	L_q (mH)	Torque (Nm)
-6	3	2.53	6.13	0.8	2.17	4.52	0.6
-6	6	2.63	5.02	4	2.12	4.15	4.1
-6	9	2.72	4.77	7.2	2.11	3.99	7.5
-6	12	3.03	4.41	10.4	2.15	3.85	10.9
-6	15	3.39	4.09	13.4	2.24	3.70	14.1
-6	18	3.54	3.92	16.2	2.36	3.57	17.2
-6	21	3.87	3.67	18.8	2.53	3.44	20.0

Appendix B

(d) I_d=-9A

I_d (A)	I_q (A)	Measured			3-D FEM		
		L_d (mH)	L_q (mH)	Torque (Nm)	L_d (mH)	L_q (mH)	Torque (Nm)
-9	3	2.73	6.99	4.4	2.32	4.93	4.6
-9	6	2.65	5.13	7.8	2.27	4.35	8.2
-9	9	2.74	4.85	11	2.24	4.17	11.6
-9	12	2.75	4.42	14.2	2.24	4.01	15.0
-9	15	3.10	4.25	17.2	2.26	3.86	18.2
-9	18	3.09	3.97	19.9	2.32	3.70	21.1

(e) I_d=-12A

I_d (A)	I_q (A)	Measured			3-D FEM		
		L_d (mH)	L_q (mH)	Torque (Nm)	L_d (mH)	L_q (mH)	Torque (Nm)
-12	3	3.54	6.56	4.9	2.46	5.25	5.0
-12	6	2.65	5.39	8.3	2.40	4.59	8.7
-12	9	2.80	4.84	11.7	2.38	4.38	12.3
-12	12	2.84	4.52	14.9	2.34	4.15	15.8
-12	15	2.82	4.26	18.1	2.34	3.98	19.1
-12	18	3.03	4.00	20.9	2.35	3.82	22.2

(f) I_d=-15A

I_d (A)	I_q (A)	Measured			3-D FEM		
		L_d (mH)	L_q (mH)	Torque (Nm)	L_d (mH)	L_q (mH)	Torque (Nm)
-15	3	2.75	6.87	5.3	2.57	5.68	5.5
-15	6	2.84	5.44	8.9	2.51	4.81	9.3
-15	9	2.75	4.93	12.3	2.47	4.47	13.0
-15	12	2.90	4.60	15.7	2.44	4.26	16.6
-15	15	2.88	4.37	18.9	2.41	4.08	20.0
-15	18	2.86	4.10	21.9	2.40	3.91	23.2

Bibliography

[1] D. Spratt and I. Dunlop, "Existential climate-related security risk: A scenario approach," *National Centre for Climate Restoration*, June 2019.

[2] M. Muntean, R. V. Dingenen, F. Monforti, and N. Scarlat, "Identifying key priorities in support to the EU Macro-regional Strategies implementation," *European Commission JRC Technical Reports*, JRC110395, 2019.

[3] Greenhouse gas emissions from transport, Last modified 30 Nov 2018. Available: https://www.eea.europa.eu.

[4] Electric vehicles from life cycle and circular economy perspectives, *EEA Report No 13/2018*. Available: https://www.eea.europa.eu.

[5] B. Sarlioglu and C. T. Morris, "More electric aircraft: Review, challenges, and opportunities for commercial transport aircraft.," *IEEE Transactions on Transportation Electrification*, vol. 1, no.1, pp.54-64, 2015.

[6] Electric ferries and joined-up shipping to turn sea travel green. Available: https://phys.org/news.

[7] P. Harrop and K. Ghaffarzadeh, "Electric Motors for Electric Vehicles: Land, Water, Air 2020-2030," Available: https://www.idtechex.com/en/research-report.

[8] L. Parsa, and H.A. Toliyat, "Fault-tolerant interior-permanent-magnet motors for hybrid electric vehicle applications," *IEEE Transactions on Vehicular Technology*, vol. 56, no. 4, pp.1546-1552, 2007.

[9] G. J. Atkinson, J. W. Bennett, B. C. Mecrow, D. J. Atkinson, A. G. Jack, and V. Pickert, "Fault-tolerant drives for aerospace applications," In 6th *IEEE International Conference on Integrated Power Electronics Systems*, pp. 1-7, March 2010.

[10] N. Bianchi, B. Silverio, M. Dai Pre, and G. Grezzani, "Design considerations for fractional-slot winding configurations of synchronous motors," *IEEE Transactions on Industry Application*, vol. 42, no. 4, pp. 997-1006, 2006.

[11] C. Gerada and Keith J. Bradley, "Integrated PM motor design for an aircraft EMA," *IEEE Transactions on Industrial Electronics*, vol. 55, no.9, pp. 3300-3306, 2008.

[12] S. Zhu, T. Cox, Z. Xu, and C. Gerada, "Novel 24-slots14-poles fractional-slot concentrated winding topology with low-space harmonics for electrical motor," *The Journal of Engineering*, vol. 2019, no. 17, pp. 3784-3788, 2019.

[13] I. Boldea, L.N. Tutelea, L. Parsa, and D. Dorrell, "Automotive electric propulsion systems with reduced or no permanent magnets: An overview," *IEEE Transactions on Industrial Electronics*, vol. 61, no.10, pp. 5696-5711, 2014.

[14] S. Morimoto, S. Ooi, Y. Inoue, and M. Sanada, "Experimental evaluation of a rare-earth-free PMASynRM with ferrite magnets for automotive applications," *IEEE Transactions on Industrial Electronics*, vol. 61, no.10, pp. 5749-5756, 2014.

[15] F. Un-Noor, S. Padmanaban, L. Mihet-Popa, M. Mollah, and E. Hossain, "A comprehensive study of key electric vehicle (EV) components, technologies, challenges, impacts, and future direction of development," Energies, vol. 10, no.8, 1217, 2017.

[16] K. T. Chau, C. C. Chan, and C. Liu, "Overview of permanent-magnet brushless drives for electric and hybrid electric vehicles," *IEEE Transactions on Industrial Electronics*, vol. 55, no.6, pp. 2246-2257, 2008.

[17] R. Cao, C. Mi, and M. Cheng, "Quantitative comparison of flux-switching permanent-magnet motors with interior permanent magnet motor for EV, HEV, and PHEV applications," *IEEE Transactions on Magnetics*, vol. 48, no. 8, pp.2374-2384, 2012.

[18] "Q&A with Tesla's lead motor engineer (Full Interview)," January 6, 2016, Available: https://chargedevs.com/.

[19] K. Culmer, "Throwback Thursday: 1996 General Motors EV1 first drive," November 2017, Available: https://www.autocar.co.uk.

[20] M. Zeraoulia, M. E. H. Benbouzid, and D. Diallo, "Electric motor drive selection issues for HEV propulsion systems: A comparative study," *IEEE Transactions on Vehicular technology*, vol. 55, no. 6, pp.1756-1764, 2006.

[21] https://www.wieland.com/en/components-for-emobility.

[22] J. D. Widmer, R. Martin, and M. Kimiabeigi, "Electric vehicle traction motors without rare earth magnets," *Sustainable Materials and Technologies*, vol. 3, pp.7-13, 2015.

[23] https://www.byd.com/en/index.html

[24] B. Sarlioglu, C. T. Morris, D. Han, and S. Li, "Benchmarking of electric and hybrid vehicle electric motors, power electronics, and batteries," In *IEEE International Conference on Optimization of Electrical & Electronic Equipment (OPTIM)*, pp. 519-526, September 2015.

[25] T. Burress, "Benchmarking state-of-the-art technologies," Report by Oak Ridge National Laboratory, 2012.

[26] T. A. Burress, S. L. Campbell, C. Coomer, C. W. Ayers, A. Wereszczak, J. P. Cunningham, L. Marlino, L. E. Seiber, and H. T. Lin, "Evaluation of the 2010 Toyota Prius hybrid synergy drive system," Report by Oak Ridge National Laboratory, 2011.

[27] T. Burress, "Electrical Performance, Reliability Analysis, and Characterization," U.S. DOE Vehicle Technologies Office Annual Merit Review, 2017.

[28] "What Engineers Found When They Tore Apart Tesla's Model 3," Bloomberg Technology, Available: www.youtube.com.

[29] https://www.nio.com/.

[30] N. Zabihi, and R. Gouws, "A review on switched reluctance motors for electric vehicles," In *25th IEEE International Symposium on Industrial Electronics (ISIE)*, pp. 799-804, June 2016.

[31] E. Bostanci, M. Moallem, A. Parsapour, and B. Fahimi, "Opportunities and challenges of switched reluctance motor drives for electric propulsion: A comparative study," *IEEE Transactions on Transportation Electrification*, vol. 3, no. 1, pp.58-75, 2017.

[32] A. G. Jack, B. C. Mecrow, and J. A. Haylock, "A comparative study of permanent magnet and switched reluctance motors for high-performance fault-tolerant applications," *IEEE Transactions on Industry Applications*, vol. 32, no. 4, pp. 889-895, 1996.

[33] M. M. Beno, N. S. Marimuthu, and N. A. Singh, "Improving power factor in switched reluctance motor drive system by optimising the switching angles," *IEEE Region 10 International Conference TENCON*, Hyderabad, pp. 1-5, 2008.

[34] Y. A. Kwon, K. J. Shin, and G. H. Rim, "SRM drive system with improved power factor," in *23rd International Conference on Industrial Electronics, Control, and Instrumentation*, vol.2, pp. 541-545, 1997.

[35] R. Suryadevara and B. G. Fernandes, "Control techniques for torque ripple minimization in switched reluctance motor: An overview," in 8th *IEEE International Conference on In Industrial and Information Systems*, pp. 24-29, 2013.

[36] http://www.srdrives.com/land-rover.shtml.

[37] C. Rossi, D. Casadei, A. Pilati, and M. Marano, "Wound rotor salient pole synchronous motor drive for electric traction," in *IEEE Industry Applications Society Annual Meeting*, pp. 1235-1241, 2006.

[38] I. Boldea, G. D. Andreescu, C. Rossi, A. Pilati, and D. Casadei, "Active flux based motion-sensorless vector control of dc-excited synchronous motors," in *IEEE Energy Conversion Congress and Exposition*, pp. 2496-2503, 2009.

[39] J. D. Santiago, H. Bernhoff, B. Ekergård, S. Eriksson, S. Ferhatovic, R. Waters, and M. Leijon, "Electrical motor drivelines in commercial all-electric vehicles: A review," *IEEE Transactions on Vehicular Technology*, vol. 61, no.2, pp.475-484, 2011.

[40] S. Masahiro, "Self-Excited Wound-Field Synchronous Motors for xEV," *SAE International Journal of Alternative Powertrains*, vol. 6, no. 2, 2017.

[41] E.M. Illiano, "Design of a highly efficient brushless current excited synchronous motor for automotive purposes," Ph.D. dissertation, ETH Zurich, 2014.

[42] A. A. AbdElhafez and A. J. Forsyth, "A Review of More-Electric Aircraft," *13th International Conference on Aerospace Sciences & Aviation Technology*, May 26-28, 2009.

[43] G. L. Fronista and G. Bradbury, "An electromechanical actuator for a transport aircraft spoiler surface," in *IEEE Thirty-Second Intersociety Energy Conversion Engineering Conference*, vol. 1, pp. 694-698, 1997.

[44] I. Chakraborty, D. N. Mavris, M. Emeneth, and A. Schneegans, "A methodology for vehicle and mission level comparison of More Electric Aircraft subsystem solutions: Application to the flight control actuation system," *Journal of Aerospace Engineering*, vol. 229, no. 6, 1088-1102, 2015.

[45] S. Zhu, T. Cox, Z. Xu, C. Gerada, and C. Li, "Design Considerations of Fault-tolerant Electromechanical Actuator Systems for More Electric Aircraft (MEA)," in *IEEE Energy Conversion Congress and Exposition*, pp. 4607-4613, 2018.

[46] P. W. Wheeler, J. C. Clare, A. Trentin, and S. Bozhko, "An overview of the more electrical aircraft. Proceedings of the Institution of Mechanical Engineers," *Journal of Aerospace Engineering*, vol. 227, no.4, pp. 578-585, 2013.

[47] https://en.wikipedia.org/wiki/Airbus_E-Fan_X

[48] https://www.aviationtoday.com/2019/03/28/utc-hybrid-ev-regional/

[49] https://edition.cnn.com/2019/06/20/business/electric-planes-paris-air-show/index.html

[50] M. Christmann, S. Seemann, and P. Jänker, "Innovative approaches to electromechanical flight control actuators and systems," in *International Conference on Recent Advances in Aerospace Actuation Systems and Components*, pp. 17-23, 2010.

[51] P. B. Reddy, A. E. Refaie, K.-K. Huh, J. K. Tangudu, and T. M. Jahns, "Comparison of interior and surface PM machines equipped with fractional-slot concentrated windings for hybrid traction applications," In *IEEE Energy Conversion Congress and Exposition*, pp. 2252-2259, 2011.

[52] Renault Fluence Z.E. and Kangoo Express Z.E.: finalized designs revealed and pre-reservations open. Press Release, Renault. 15 April 2010.

[53] A. Boglietti, A. Cavagnino, M. Pastorelli, and A. Vagati, "Experimental comparison of induction and synchronous reluctance motors performance," In *14th IEEE Industry Applications Annual Conference*, vol. 1, pp. 474-479, October 2005.

[54] M. Ansari, W. A. Cronje, and A. Meyer, "Evaluation of a Reluctance Synchronous Motor: For use in an Electric Mine Shuttle Vehicle (EMSV)," *IEEE International Electric Vehicle Conference*, pp. 1-6, March 2012.

[55] M. Ruba, F. Jurca, C. Martis, R. Martis, and P. F. Piglesan, "Analysis of maximum torque per ampere control strategy for variable reluctance synchronous motors for traction applications," In *IEEE International Conference and Exposition on Electrical and Power Engineering*, pp. 322-326, October 2014.

[56] https://drivesncontrols.com/news/fullstory.php/aid/4727/Synchronous_reluctan ce_EV_motor_avoids_rare_earths.html

[57] N. Bianchi, S. Bolognani, E. Carraro, M. Castiello, and E. Fornasiero, "Electric vehicle traction based on synchronous reluctance motors," *IEEE Transactions on Industry Application*s, vol. 52, no. 6, pp.4762-4769, 2016.

[58] S. Ooi, S. Morimoto, M. Sanada, and Y. Inoue, "Performance evaluation of a high-power-density PMASynRM with ferrite magnets," *IEEE Transactions on Industry Applications*, vol. 49, no. 3, pp.1308-1315, 2013.

[59] D. G. Dorrell, A. M. Knight, M. Popescu, L. Evans, and D. A. Staton, "Comparison of different motor design drives for hybrid electric vehicles," In *IEEE Energy Conversion Congress and Exposition*, pp. 3352-3359, 2010.

[60] H. Neudorfer, N. Wicker, and A. Binder, "Comparison of three different electric powertrains for the use in hybrid electric vehicles," in *4th IET Conference on Power Electronics, Machines and Drives*, pp. 510-514, 2008

[61] J. W. Bennett, B. C. Mecrow, D. J. Atkinson, and G. J. Atkinson, "Safety-critical design of electromechanical actuation systems in commercial aircraft," *IET electric power applications*, vol. 5 no. 1, pp. 37-47, 2011.

[62] J. C. Derrien, and S. D. Sécurité, "Electromechanical actuator (EMA) advanced technologies for flight controls," *International Congress of the Aeronautical Sciences*, pp. 1-10, 2012.

[63] A. Turner, K. Ramsay, R. Clark, and D. Howe, "Direct-drive electromechanical linear actuator for shift-by-wire control of an automated transmission," In *IEEE Vehicle Power and Propulsion Conference*, pp. 1-6, 2006.

[64] N. Ziegler, D. Matt, J. Jac, T. Martire, and P. Enrici, "High force linear actuator for an aeronautical application. Association with a fault-tolerant converter," In *IEEE International Aegean Conference on Electrical Machines and Power Electronics*, pp. 76-80. 2007.

[65] S. C. Jensen, G. D. Jenney, and D. Dawson, "Flight test experience with an electromechanical actuator on the F-18 systems research aircraft," in *19th IEEE Digital Avionics Systems Conference*, vol. 1, 2000.

[66] A. Garcia, I. Cusido, J. A. Rosero, J. A. Ortega, and L. Romeral, "Reliable electro-mechanical actuators in aircraft," in *IEEE Aerospace and Electronic Systems Magazine*, vol. 23, no. 8, pp. 19-25, 2008.

[67] L. De Lillo, L. Empringham, P. Wheeler, J. Clare, and K. Bradley, "A 20 KW matrix converter drive system for an electro-mechanical aircraft (EMA) actuator," in *IEEE European Conference on Power Electronics and Applications*, pp. 1-6, 2005.

[68] M. Aten, C. Whitley, G. Towers, P. Wheeler, J. Clare, and K. Bradley, "Dynamic performance of a matrix converter driven electro-mechanical actuator for an aircraft rudder," in *Second IET International Conference on Power Electronics, Motors and Drives*, vol. 1, pp. 326-331, 2004.

[69] J. C. Derrien, P. Tieys, D. Senegas, and M. Todeschi, "EMA aileron COVADIS development," *SAE Technical Paper*, 2011.

[70] M. Villani, M. Tursini, G. Fabri and L. Castellini, "Electromechanical actuator for helicopter rotor damper application," *IEEE Transactions on Industry Application, vol.* 50, no. 2, pp. 1007-1014, 2013.

[71] M. Tursini, G. Fabri, E. D. Loggia, and M. Villani, "Parallel positioning of twin EMAs for Fault-Tolerant flap applications," in *IEEE Conference on Electrical Systems for Aircraft, Railway and Ship Propulsion*, pp. 1-6, 2012.

[72] L. Castellini, M. Andrea, and N. Borgarelli, "Analysis and design of a linear electro-mechanical actuator for a high lift system," in *International IEEE Symposium on Power Electronics, Electrical Drives, Automation and Motion*, pp. 243-247, 2014.

[73] M. Rottach, C. Gerada, and P. W. Wheeler, "Design optimisation of a fault-tolerant PM motor drive for an aerospace actuation application," in *7th IET International Conference on Power Electronics, Machines and Drives*, 2014.

[74] https://cordis.europa.eu/docs/results/323/323318/final1-flight-ema-cs-publishable-summary.pdf

[75] R. Arriba1 and A. Gallego, "Health and Usage Monitoring System (HUMS) Strategy to enhance the Maintainability & Flight Safety in a Flight Control Electromechanical Actuator (EMA), in *Third European Conference of the Prognostics and Health Management Society*, 2016.

[76] US patent, Jam-tolerant rotary actuator, US5518466A.

[77] J. W. Bennett, B. C. Mecrow, A. G. Jack, and D. J. Atkinson, "A prototype electrical actuator for aircraft flaps," *IEEE Transactions on Industry Applications*, vol. 46, no. 3, pp. 915-921, 2010.

[78] J. W. Bennett, "Fault-tolerant electromechanical actuators for aircraft," Ph.D. dissertation, Newcastle University, 2010.

[79] S. Rivera and A. Andreou, "Rotary Actuator for Retractable Landing Gear Systems," in *International Conference on Recent Advances in Aerospace Actuation Systems and Components*, Toulouse, France, March 2016.

[80] M. Villani, M. Tursini, G. Fabri, and L. Castellini, "High Reliability Permanent Magnet Brushless Motor Drive for Aircraft Application," *IEEE Transactions on industrial electronics*, vol. 59, pp. 2073- 2081, 2012.

[81] M. Villani, M. Tursini, G. Fabri and L. Castellini, "Multi-phase permanent magnet motor drives for fault-tolerant applications," in *IEEE International Electric Motors & Drives Conference*, pp. 1351-1356, 2011.

[82] P. C. Krause, O. Wasynczuk, S. D. Sudhoff, "Analysis of Electric Machinery and Drive Systems, New York: IEEE Press, 2013

[83] S. M. Raziee, O. Misir, and B. Ponick, "Winding function approach for winding analysis," *IEEE Transactions on Magnetics*, vol. 53, no. 10, pp.1-9, 2017.

[84] T. A. Lipo, "Analysis of synchronous machines," CRC Press, 2017.

[85] https://mathworld.wolfram.com/FourierSeries.html

[86] T. A. Lipo, "Introduction to AC Machine Design," John Wiley & Sons, 2017.

[87] H. Ge, "Fractional slot concentrated winding interior permanent magnet motors with reluctance torque: inductance-based methodology for comprehensive analysis, design, and control," Ph.D. dissertation, McMaster University, 2016.

[88] N. Bianchi, and M. D. Prè, "Use of the star of slots in designing fractional-slot single-layer synchronous motors," *IEE Proceedings-Electric Power Applications*, vol. 153, no. 3, pp. 459-466, 2006.

[89] J. Cros and P. Viarouge, "Synthesis of high performance PM motors with concentrated windings," *IEEE Transactions on Energy Conversion*, vol. 17, no. 2, pp. 248-253, June 2002.

[90] B. Aslan, E. Semail, J. Korecki, and J. Legranger, "Slot/pole Combinations Choice for Concentrated Multiphase Motors dedicated to Mild-Hybrid Applications," in *IEEE International Conference on Industrial Applications of Electronics*, pp.3698-3703, 2011.

[91] F. Magnussen and C. Sadarangani, "Winding factors and Joule losses of permanent magnet motors with concentrated windings," in *IEEE International Electric Motors and Drives Conference,* vol. 1, pp. 333-339. 2003.

[92] N. Bianchi and S. Bolognani, "Design techniques for reducing the cogging torque in surface-mounted PM motors," *IEEE Transactions on Industry Applications*, vol. 38, no. 5, pp.1259-1265, 2002.

[93] A. E. Refaie, Z. Q. Zhu, T. M. Jahns, and D. Howe, "Winding inductances of fractional slot surface-mounted permanent magnet brushless motors," in *IEEE Industry Applications Society Annual Meeting*, pp. 1-8, 2008.

[94] J. Soulard and F. Meier, "Design guidelines and models for PMSMs with non-overlapping concentrated windings," *COMPEL-The international journal for computation and mathematics in electrical and electronic engineering*, vol. 30, no. 1, pp. 72-83, 2011.

[95] W. Soong and T.J.E. Miller, "Field weakening performance of brushless synchronous AC motor drives," *IEE Proceedings-Electric Power Applications*, vol. 14, no. 6, pp. 331-340, 1994.

[96] F. Magnussen, P. Thelin, and C. Sadarangani, "Performance evaluation of permanent magnet synchronous motors with concentrated and distributed windings including the effect of field-weakening," *Proc. of IEE International Conference on Power Electronics and Electrical Motors*, vol.2, pp. 679-685, 2004.

[97] P. B. Reddy, A. M. El-Refaie, K. K. Huh, J. K. Tangudu, and T. M. Jahns, "Comparison of interior and surface PM motors equipped with fractional-slot concentrated windings for hybrid traction applications," *IEEE Transactions on Energy Conversion*, vol. 27, no. 3, pp. 593-602, 2012.

[98] B. C. Mecrow, A. G. Jack, D. J. Atkinson, S. R. Green, Gl. J. Atkinson, A. King, and B, Green, "Design and testing of a four-phase fault-tolerant permanent-magnet motor for an engine fuel pump," *IEEE Transactions on Energy Conversion*, vol. 19, no. 4, pp. 671-678, 2004.

[99] J. Dusek, P. Arumugam, C. Brunson, E. K. Amankwah, T. Hamiti, and C. Gerada, "Impact of slot/pole combination on inter-turn short-circuit current in fault-tolerant permanent magnet motors," *IEEE Transactions on Magnetics*, vol. 52, no. 4, pp. 1-9, 2015.

[100] A. M. El-Refaie, "Fractional-slot concentrated-windings synchronous permanent magnet motors: Opportunities and challenges," *IEEE Transactions on Industrial Electronics*, vol. 57, no. 1, 107-121, 2009.

[101] J. Shen, C. Wang, D. Miao, M. Jin, D. Shi, and Y. Wang, "Analysis and optimization of a modular stator core with segmental teeth and solid back iron for pm electric motors," in *IEEE International Electric Motors & Drives Conference*, pp. 1270-1275, 2011.

[102] M. Galea, "High performance, direct drive motors for aerospace applications," Ph.D. dissertation, University of Nottingham, 2013.

[103] H. Akita, Y. Nakahara, N. Miyake, and T. Oikawa, "New core structure and manufacturing method for high efficiency of permanent magnet motors," in *IEEE Industry Applications Society Annual Meeting*, vol. 2, pp. 367-372. Oct. 2003.

[104] C. M. Spargo, B. C. Mecrow, J. D. Widmer, C. Morton, and N. J. Baker, "Design and validation of a synchronous reluctance motor with single tooth windings," *IEEE Transactions on Energy Conversion*, vol. 30, no. 2, pp. 795-805, June 2015.

[105] G. Jack, B. C. Mecrow, P. G. Dickinson, D. Stephenson, J. S. Burdess, N. Fawcett, and J. T. Evans, "Permanent magnet motors with powdered iron cores and pressed windings," *IEEE Transactions Industry Application*, vol. 36, no. 4, pp. 1077-1084, July/August 2000.

[106] F. Magnussen and H. Lendenmann, "Parasitic effects in PM motors with concentrated windings," *IEEE Transactions on Industry Applications*, vol. 43, no. 5, pp. 1223-1232, 2007.

[107] Y. S. Chen, Z. Q. Zhu, and D. Howe, "Vibration of PM brushless motors having a fractional number of slots per pole," *IEEE Transactions on Magnetics*, vol. 42, no. 10, pp. 3395-3397, 2006.

[108] E. Fornasiero, N. Bianchi, and S. Bolognani, "Slot harmonic impact on rotor losses in fractional-slot permanent-magnet motors," *IEEE Transactions on Industrial Electronics*, vol. 59, no. 6, pp. 2557-2564, 2011.

[109] G. Dajaku and D. Gerling, "Eddy current loss minimization in rotor magnets of PM motors using high-efficiency 12-teeth/10-slots winding topology," in *International Conference on Electrical Motors and Systems*, pp. 1-6, 2011.

[110] G. Dajaku and Dieter Gerling, "A novel 12-teeth/10-poles PM motor with flux barriers in stator yoke," In *XXth IEEE International Conference on Electrical Motors*, pp. 36-40, 2012.

[111] P. B. Reddy, A. M. El-Refaie, and K. Huh, "Effect of number of layers on performance of fractional-slot concentrated-windings interior permanent

magnet motors," *IEEE Transactions on Power Electronics*, vol. 30, no. 4, pp. 2205-2218, 2015.

[112] G. Dajaku and D. Gerling, "A novel 24-slots/10-poles winding topology for electric motors," In *IEEE International Electric Motors & Drives Conference*, pp. 65-70, 2011.

[113] H. Kim, D. Kim, and J. Hong, "Characteristic analysis for concentrated multiple-layer winding motor with optimum turn ratio," *IEEE Transactions on Magnetics*, vol. 50, no. 2, pp. 789-792, 2014.

[114] A. Tessarolo, M. Mezzarobba, and N. Barbini, "Improved four-layer winding design for a 12-slot 10-pole permanent magnet motor using unequal tooth coils," In *42nd IEEE Industrial Electronics Society Annual Conference*, pp. 1686-1691, October 2016.

[115] M. V. Cistelecan, F. J. T. E. Ferreira, and M. Popescu, "Three phase tooth-concentrated multiple-layer fractional windings with low space harmonic content," in *IEEE Energy Conversion Congress and Exposition*, pp. 1399-1405, 2010.

[116] A. S. Abdel-Khalik, S. Ahmed, and A. M. Massoud, "Effect of multilayer windings with different stator winding connections on interior PM motors for EV applications," *IEEE Transactions on Magnetics*, vol. 52, no. 2, pp. 1-7, 2016.

[117] L. Alberti and N. Bianchi, "Theory and design of fractional-slot multilayer windings," *IEEE Transactions on Industry Applications*, vol. 49, no. 2, pp. 841-849, 2013.

[118] A. S. Abdel-Khalik, S. Ahmed, and A. M. Massoud, "Low space harmonics cancelation in double-layer fractional slot winding using dual multiphase winding," *IEEE Transactions on Magnetics*, vol. 51, no. 5, 8104710, 2015.

[119] X. Chen, J. Wang, V. I. Patel, and P. Lazari, "A nine-phase 18-slot 14-pole interior permanent magnet motor with low space harmonics for electric vehicle applications," *IEEE Transactions on Energy Conversion*, vol. 31, no. 3, pp. 8104710,2016.

[120] X. Chen, J. Wang, and V. I. Patel, "A generic approach to reduction of magnetomotive force harmonics in permanent magnet motors with concentrated

multiple three-phase windings," *IEEE Transactions on Magnetics*, vol. 50, no. 11, 8103604, 2014.

[121] Z. Pan, and R. A. Bkayrat, "Modular motor/converter system topology with redundancy for high speed, high-power motor applications," *IEEE Transactions on Power Electronics*, vol. 25, no. 2, pp. 408-416, 2009.

[122] V. I. Patel, J. Wang, W. Wang, and X. Chen, "Six-phase fractional-slot-per-pole-per-phase permanent-magnet motors with low space harmonics for electric vehicle application," *IEEE Transactions on Industry Applications*, vol. 50, no. 4, pp. 2554-2563, 2014.

[123] A. S. Abdel-Khalik, S. Ahmed, and A. M. Massoud, "A six-phase 24-slot/10-pole permanent-magnet motor with low space harmonics for electric vehicle applications," *IEEE Transactions on Magnetics*, vol. 52, no. 6, 8700110, 2016.

[124] P. B. Reddy, K. Huh, and A. M. El-Refaie, "Generalized approach of stator shifting in interior permanent-magnet motors equipped with fractional-slot concentrated windings," *IEEE Transactions on Power Electronics*, vol. 61, no. 9, pp. 5035-5046, 2014.

[125] T. D. Cox, "Development of novel linear drive motors," Ph.D. dissertation, University of Bath, 2008.

[126] J. F. Eastham, T. Cox, and J. Proverbs, "Application of planar modular windings to linear induction motors by harmonic cancellation," *IET Electric Power Applications*, vol. 4, no. 3, pp. 140-148, 2010.

[127] M. Rottach, C. Gerada, T. Hamiti, and P. W. Wheeler, "A computationally efficient design procedure for actuator motors using magnetic reluctance-and thermal resistance network models," In *XXth IEEE International Conference on Electrical Motors*, pp. 2526-2532, 2012.

[128] P. Zheng, F. Wu, Y. Lei, Y. Sui, and B. Yu, "Investigation of a novel 24-slot/14-pole six-phase fault-tolerant modular permanent-magnet in-wheel motor for electric vehicles," *Energies*, vol. 6, no. 10, pp. 4980-5002, 2013.

[129] V. Patel, "Novel 6-phase fractional-slot permanent magnet machine for electric vehicle applications," PhD dissertation, University of Sheffield, 2014.

[130] J. Krotsch and B. Piepenbreier, "Radial forces in external rotor permanent magnet synchronous motors with non-overlapping windings," *IEEE Transactions on Industrial Electronics*, vol. 59, no. 5, pp. 2267-2276, May 2012.

[131] B. Cassoret, J. P. Lecointe, and J. F. Brudny, Power Electronics and Motor Drives. Boca Raton, FL, USA: CRC 2011.

[132] K. Wang, Z. Q. Zhu, Y. Ren, and G. Ombach, "Torque Improvement of Dual Three-Phase Permanent-Magnet Machine with Third-Harmonic Current Injection," *IEEE Transactions on Industrial Electronics*, vol. 62, no. 11, pp. 6833-6844, 2015.

[133] J. Goss, R. Wrobel, P. Mellor, and Dave Staton, "The design of AC permanent magnet motors for electric vehicles: A design methodology," In *IEEE International Electric Machines & Drives Conference*, pp. 871-878, 2013.

[134] N. Bianchi, M. D. Pre, and S. Bolognani, "Design of a fault-tolerant IPM motor for electric power steering," *IEEE Transactions on Vehicular Technology*, vol. 55, no. 4, pp. 1102-1111, 2006.

[135] T. Jahns, "Design, analysis, and control of interior PM synchronous machines," in *IEEE Industrial Application Society Annual Meeting*, Tutorial Course Notes, October 2004.

[136] S. H. Han, T. M. Jahns, and W. L. Soong, "Torque ripple reduction in interior permanent magnet synchronous machines using the principle of mutual harmonics exclusion," in *IEEE Industry Applications Annual Meeting*, pp. 558-565, 2007.

[137] P. Xu, J. H. Feng, S. Y. Guo, S. Feng, W. Chu, Y. Ren, and Z. Q. Zhu, "Analysis of dual three-phase permanent-magnet synchronous machines with different angle displacements," *IEEE Transactions on Industrial Electronics*, vol. 65, no. 3, pp. 1941-1954, 2018.

[138] Z. Q. Zhu, D. Ishak, D. Howe, and J. Chen, "Unbalanced magnetic forces in permanent-magnet brushless machines with diametrically asymmetric phase windings," *IEEE Transactions on Industry Applications,* vol. 43, no. 6, pp. 1544-1553, 2007.

[139] M. Recksiek, "Advanced high lift system architecture with distributed electrical flap actuation," in *2nd International Workshop on Aircraft System Technologies*, pp. 49-60, 2009.

[140] Airbus Current Market Outlook 2019-2038, Available: https://www.airbus.com/

[141] C. P. Lawson, and J. M. Pointon, "Thermal management of electromechanical actuation on an all-electric aircraft," in *26th International Congress of Aeronautical Sciences*, pp. 14-19, 2008.

[142] F. Meng, "Actuation system design with electrically powered actuators, Cranfield University, Master thesis, 2011.

[143] P Zheng, S Zhu, B Yu, L Cheng, and Y Fan, "Analysis and optimization of a novel tubular staggered-tooth transverse-flux PM linear motor," *IEEE Transactions on Magnetics*, vol. 51, no. 11, 8111304, 2015.

[144] J. Wang, G. W. Jewell, and D. Howe, "A general framework for the analysis and design of tubular linear permanent magnet motors," *IEEE Transactions on Magnetics*, vol. 35, no. 3, pp. 1986-2000, 1999.

[145] www.skf.com › binary › 14489-EN---Roller-screw-catalogue

[146] R. K. Holm, N. I. Berg, M. Walkusch, P. O. Rasmussen, and R. H. Hansen, "Design of a magnetic lead screw for wave energy conversion," *IEEE Transactions on Industry Applications*, vol. 49, no. 6, pp. 2699-2708, 2013.

[147] S. Pakdelian, N. W. Frank, and H. A. Toliyat, "Magnetic design aspects of the trans-rotary magnetic gear," *IEEE Transactions on Energy Conversion*, vol. 30, no. 1, pp. 41-50, 2015.

[148] N. I. Berg, R. K. Holm, and P. O. Rasmussen, "Theoretical and experimental loss and efficiency studies of a magnetic lead screw," in *IEEE Energy Conversion Congress and Exposition*, pp. 2185-2192, 2013.

[149] H. Qi, T. Fu, X. Qi, and Y. Lang, "Architecture optimization of more electric aircraft actuation system," *Chinese Journal of Aeronautics*, vol. 24, no. 4, pp. 506-513, 2011.

[150] L. Xue, "Actuation technology for flight control system on civil aircraft," Cranfield University, Master thesis, 2009.

[151] A. Landi and M. Nicholson, "ARP4754A/ ED-79A - Guidelines for Development of Civil Aircraft and Systems - Enhancements, Novelties and Key Topics," *SAE International Journal of Aerospace*, vol. 4, no. 2, pp. 871-879, 2011.

[152] I. Moir and A. Seabridge, "Aircraft Systems: Mechanical, Electrical and Avionics Subsystems Integration," New York: Wiley, 2008.

[153] Junxiang Chen, "Study of 270VDC System Application," Cranfield University, Master thesis, 2010

[154] P. C. Lemor, "The roller screw, an efficient and reliable mechanical component of electro-mechanical actuators," in *31st IEEE Intersociety Energy Conversion Engineering Conference*, vol. 1, pp. 215-220, 1996.

[155] P. J. Tavner and J. P. Hasson, "Predicting the design life of high integrity rotating electrical motors," in *9th International Conference on Electrical Machines and Drives*, pp. 286-290, 1999.

[156] T. Sadeghi and A. Lyons, "Fault-tolerant EHA architectures," *IEEE Aerospace and Electronic Systems Magazine*, vol. 7, no. 3, pp. 32-42, March 1992.

[157] Nonelectronic Parts Reliability Data (NPRD-2011), 2011.

[158] V. Vitkovskii, I. R. Kirillov, P. Yu Chaika, E. A. Kryuchkov, V. M. Poplavskii, Yu V. Nosov, and N. N. Oshkanov, "Performance-based reliability assessment of electromagnetic pumps," *Atomic Energy*, vol. 102, no. 2, pp. 122-128, 2007.

[159] L. Ferraris, P. Ferraris, E. Pošković, and A. Tenconi, "Comparison between parallel and radial magnetization in PM fractional machines," In *37th Annual Conference of the IEEE Industrial Electronics Society*, pp. 1776-1782, 2011.

[160] H. N. Phyu, C. Bi, and Q. Jiang, "Effect of magnetization on torque pulsation of the PM BLDC motor," In *IEEE International Conference on Electrical Machines and Systems*, pp. 3685-3690, 2008.

[161] L. Ferraris, P. Ferraris, E. Pošković, and A. Tenconi, "PM fractional machines adopting bonded magnets: Effect of different magnetizations on the energetic performance," In *IEEE International Energy Conference and Exhibition*, pp. 113-120, 2012.

[162] G. Lee, S. Kim, J. Hong and J. Bahn, "Torque Ripple Reduction of Interior Permanent Magnet Synchronous Motor Using Harmonic Injected Current," *IEEE Transactions on Magnetics*, vol. 44, no. 6, pp. 1582-1585, June 2008.

[163] B. C. Mecrow, A. G. Jack, J. A. Haylock, and J. Coles, "Fault-tolerant permanent magnet machine drives," *IEE Proceedings-Electric Power Applications*, vol. 143, no. 6, pp. 437-442, 1996.

[164] C. Gerada, K. Bradley, and M. Summer, "Winding turn-to-turn faults in permanent magnet synchronous machine drives," In *14th IEEE Industry Applications Annual Meeting*, vol. 2, pp. 1029-1036, 2005.

[165] Z. Sun, J. Wang, D. Howe, and G. Jewell, "Analytical prediction of the short-circuit current in fault-tolerant permanent-magnet machines," *IEEE Transactions on Industrial Electronics*, vol. 55, no. 12, pp. 4210-4217, 2008.

[166] P. Ponomarev, Y. Alexandrova, I. Petrov, P. Lindh, E. Lomonova, and J. Pyrhönen, "Inductance calculation of tooth-coil permanent-magnet synchronous machines," *IEEE Transactions on Industrial Electronics*, vol. 61, no. 11, pp. 5966-5973, 2014.

[167] G. Huth, "Permanent-magnet-excited AC servo motors in tooth-coil technology," *IEEE Transactions on Energy Conversion*, vol. 20, no. 2, pp. 300-307, 2005.

[168] J. Pyrhönen, T. Jokinen, and V. Hrabovcova, "Design of Rotating Electrical Machines," John Wiley & Sons, 2013.

[169] https://www.skfbearingselect.com

[170] J. Saari, "Thermal analysis of high-speed induction machines", Ph.D. Dissertation, Helsinki University of Technology, 1998.

[171] K. M. Rahman, and S. Hiti, "Identification of machine parameters of a synchronous motor," *IEEE Transactions on Industry Applications*, vol. 41, no.2, pp. 557-565, 2005.